In situ STM study of the growth and dissolution processes on bimetallic Pd/Au(111) substrates and of ultrathin alloy layers on Au(111)

Alexis Damian

Thèse présentée pour obtenir le grade de

DOCTEUR DE L'ECOLE POLYTECHNIQUE

Spécialité : Physique

par

Alexis DAMIAN

In Situ STM Study of the Growth and Dissolution Processes on Bimetallic Pd/Au(111) Substrates and of Ultrathin Alloy Layers on Au(111)

Soutenue le 23 septembre 2009 devant le jury composé de :

Prof . Dr. Olaf Magnussen	Christian-Albrechts-Universität zu Kiel	Rapporteur
Dr. Sylvie Rousset	Université Paris Diderot	Rapporteur
Dr. Fabienne Berthier	Université Paris-Sud	Examinateur
Dr. François Ozanam	Ecole Polytechnique	Examinateur
Dr. Fouad Maroun	Ecole Polytechnique	Co-Directeur
Dr. Philippe Allongue	Ecole Polytechnique	Directeur

Remerciements

J'ai réalisé mon doctorat à l'Ecole Polytechnique, au sein du laboratoire de Physique de la Matière Condensée (PMC) avec un financement du Ministère de l'Enseignement Supérieur et de la Recherche, d'Octobre 2006 à Septembre 2009. Je tiens à remercier au travers de ces quelques lignes les différentes personnes qui ont grandement participé au bon déroulement de ce projet.

En premier lieu, je souhaite remercier mon directeur de thèse, Philippe Allongue, de m'avoir accueilli dans son équipe et d'avoir ainsi satisfait mon souhait d'étudier par microscopie à effet tunnel les mécanismes fondamentaux de l'électrodépôt. Je lui suis grandement reconnaissant pour la confiance qu'il m'a toujours accordé et ce dès nos premiers contacts alors que j'étais encore à l'Université McGill (Canada) et qui s'est traduite par une grande liberté scientifique pour effectuer ce travail. C'est dans ce cadre privilégié que j'ai pu pleinement collaborer avec Fouad Maroun, mon co-directeur de thèse. Au cours de mes trois années passées à PMC, nous avons appris à nous connaître et à nous apprécier. Dynamique, sympathique et « engagé », Fouad a contribué de manière déterminante à la réussite de ce projet de doctorat par un encadrement irréprochable. Son soutien et ses encouragements constants pour participer à des conférences ou aller faire des séminaires en France ou à l'étranger, me faire rencontrer des chercheurs, publier les résultats, m'ont permis d'être en mesure de pleinement choisir, à la fin de ma thèse, entre la poursuite d'une carrière académique (e.g. post-doc) et celle d'une carrière dans l'industrie. Je l'en remercie très sincèrement et lui souhaite une longue et fructueuse carrière avec l'encadrement d'un grand nombre de thésards !

Ensuite, je tiens à exprimer ma reconnaissance envers les membres du jury qui m'ont fait l'honneur de juger ce travail. Tout d'abord, François Ozanam, directeur de recherche à l'Ecole Polytechnique, pour avoir accepté de présider ce jury. Je souhaite également le remercier pour son écoute et ses nombreux conseils précieux sur la gestion de mon projet de thèse en tant que directeur de PMC. Olaf Magnussen, professeur au département de Physique Expérimentale et Appliquée de l'Université de Kiel (Allemagne) ainsi que Sylvie Rousset, directrice du laboratoire Matériaux et Phénomènes Quantiques (MPQ) de l'Université Paris Diderot, pour leur lecture attentive de mon manuscrit en tant que rapporteurs. Enfin, je remercie chaleureusement Fabienne Berthier, directeur de recherche au Laboratoire d'Etude des Matériaux Hors Equilibre (LEMHE) de l'Université d'Orsay, qui a examiné avec minutie mon travail et pour sa participation active lors de la soutenance.

Je remercie de la même manière Isabelle Braems du LEMHE avec qui j'ai collaboré dans le cadre de l'ANR SEAMAN. Son apport conceptuel et théorique quant à l'interprétation des phénomènes de croissance sélective sur substrat bimétallique et de dissolution d'alliage a été déterminant.

J'aimerais exprimer ma gratitude envers l'ensemble des chercheurs et techniciens du laboratoire avec qui j'ai pu interagir et plus particulièrement envers ceux du groupe « Electrochimie et Couches Minces » : Catherine Henry de Villeneuve pour son soutien, son aide fréquente et utile au laboratoire, Jean-Noël Chazalviel pour sa disponibilité et sa patience pour répondre, de manière toujours très pédagogique, à mes nombreuses questions, Robert Cortès pour sa gentillesse et nos nombreuses discussions passionnées lors du déjeuner, Ionel Solomon pour sa bonne humeur et ses petites blagues d'une grande finesse. Ensuite, je souhaite remercier mes camarades doctorants et post-doctorants, Nicolas Tournerie, Gregory Savidand, Oscar de Abril et Hugo Feitosa, avec qui j'ai grandement collaboré et apprécié de travailler au quotidien. J'élargis mes remerciements aux « jeunes » chercheurs du laboratoire à savoir Isabelle Maurin, Sandrine Perruchas, Denis Grebenkov et Alistair Rowe qui ont été pour moi une source d'inspiration constante par leur dynamisme, leur engagement et leurs compétences.

Je souhaite faire des remerciements particuliers à l'ensemble des doctorants de PMC que j'ai pu côtoyer pendant mon doctorat pour leur implication forte dans la vie du laboratoire au travers des séminaires thésards, pots de thèse, visites de laboratoires, etc… et avec qui j'ai pu nouer des liens d'amitié forts et durables. Je pense notamment à Morgane Presle, Nayeli Panier, Amélie Revaux, Aurélie Fouquier, Joëlle Corde, Morgan Gohin, François Guillemot, Filippo Fabri, Vincent Tariel, Geneviève Mialon, Gabriel Freiman, Sabrina Sam, Vu Dsuong, Lin Xiaoxin, Amel Slimani, Lynda Amirouche, Mathieu Bérard, Caroline Bertail. Un grand merci également à mes compagnons des jours de galère, Frédérique Roux, Larbi Touahir et Driss Lamine dont la présence au laboratoire les soirs de semaines ou les week ends nous ont amené à partager des moments qui me laisseront des souvenirs impérissables. J'espère grandement que nous saurons perpétuer ces relations privilégiées qui nous unissent au sein du groupe X-Recherche et plus généralement de l'AX.

Enfin, je remercie toute ma famille et en particulier ma femme Maïlis pour m'avoir « supporté » et encouragé sans relâche au cours de ces trois années.

Contents

1 Introduction **1**

2 Electrochemical Growth and Dissolution: Fundamentals and Experimental **7**
2.1 Electrochemical fundamentals 7
2.1.1 The metal-electrolyte interface *7*
2.1.2 The Nernst equation *9*
2.1.3 Electrode kinetics *12*
2.2 Electrodeposition process 14
2.3 Experimental and technical details 15
2.3.1 Electrochemical instrumentation: the potentiostat *15*
2.3.2 Electrodes, chemicals and solutions *16*
2.3.3 Scanning tunneling Microscopy (STM) *16*
References 17

3 Experimental Procedures for the Preparation of Bimetallic Substrates and Monolayer Alloy Films **19**
3.1 Preparation and characterization of the Au(111) surface 19
3.1.1 Introduction *19*
3.1.2 Au(111) single crystal *20*
3.1.3 Au/mica *20*
3.1.4 Atomic structure of the Au(111) surface *21*
3.1.5 Electrochemical characterization *24*
3.2 Preparation and characterization of the bimetallic Pd/Au(111) substrate 26
3.2.1 Introduction *26*
3.2.2 Pd electrodeposition on Au(111) *27*
a) Brief overview 27
b) Deposition procedure 29
c) Morphology of Pd adlayer on Au surfaces 29
3.2.3 Characterization of the Pd/Au(111) surface properties *33*
a) Cyclic voltammetry 34
b) STM 35
3.3 Electrodeposition procedures of ultrathin alloy films 37
3.3.1 Introduction *37*
3.3.2 The 1st deposition procedure *40*
3.3.3 The 2nd deposition procedure *41*
References 46

4 Electrochemical Growth and Dissolution of Ni and Co on Bimetallic Pd/Au(111) Substrates **51**
4.1 Introduction 51
4.2 Electrochemical study of Ni and Co deposition and dissolution on Au(111) and Pd(1ML)/Au(111) surfaces 53
4.2.1 Cyclic voltammetry *53*
4.2.2 Nickel and cobalt growth rates *57*
a) Au(111) surface 58
b) Pd(1ML)/Au(111) surface 60

c) Influence of H re-adsorption on Pd(1ML)/Au(111) surface 61
4.2.3 Dissolution curves *64*
a) Nickel dissolution 64
b) Cobalt dissolution 65
4.2.4 Discussion of the electrochemical data *66*
a) Origin of the substrate dependent growth kinetics of Ni monolayer 68
b) Mechanism of H-desorption during deposition 71
4.2.5 Conclusions of electrochemical measurements *72*
4.3 Nucleation and growth processes of Ni and Co on bimetallic Pd/Au(111) surfaces 72
4.3.1 Overview of the Ni and Co growth on monometallic Au(111) *73*
4.3.2 Nucleation and monolayer growth of Ni on bimetallic Pd/Au(111) surface *76*
4.3.3 Multilayer Ni growth on bimetallic Pd/Au(111) *82*
4.3.4 Quantitative analysis of Ni growth on bimetallic Pd/Au(111) surface *83*
4.3.5 Co deposition on bimetallic Pd/Au(111) surface *85*
4.4 Ni Dissolution process on bimetallic Pd/Au(111) surfaces 87
4.4.1 Dissolution of Ni monolayer on bimetallic Pd/Au(111) surface *87*
4.4.2 Influence of anions *90*
4.4.3 Dissolution of multilayer Ni films on bimetallic Pd/Au(11) surface *91*
4.4.4 Quantitative analysis of Ni dissolution on bimetallic Pd/Au(111) surface *94*
4.5 Discussion 95
4.5.1Interpretation of the substrate dependence of the Ni monolayer deposition/dissolution onset potential *96*
a) Theoretical considerations 96
b) Discussion of E_{bind} 98
c) Role of the H-monolayer adsorbed on the Pd islands 100
4.5.2 Explanation of the absence of selective Co deposition/dissolution process *101*
4.6 Conclusion 102
References 103

5 Growth and Dissolution of Two-Dimensional Binary Ultrathin Alloy Films on Au(111) 109
5.1 Introduction 109
5.2 Growth of Ni-based ultrathin alloy films 114
5.2.1 Growth of Ni_xPd_{1-x} ultrathin films *115*
a) Morphologies of Ni_xPd_{1-x} monolayer alloys 115
b) Moiré structure of the NiPd alloys 117
c) Conclusions 119
5.2.2 Growth of Ni_xAu_{1-x} ultrathin films *120*
a) Morphology of Ni-rich alloy 120
b) Morphology of Au-rich alloy 122
c) Conclusions 124
5.3 Selective dissolution of Ni from NiAu and NiPd ultrathin alloy films 125
5.3.1 Dissolution of Ni from NiPd ultrathin films *125*
a) Dissolution of $Ni_{88}Pd_{12}$ monolayer alloy 125
b) Dissolution of $Ni_{70}Pd_{30}$ monolayer alloy 127
c) Dissolution of $Ni_{51}Pd_{49}$ monolayer alloy 130
d) Dissolution of $Ni_{24}Pd_{76}$ monolayer alloy 133
e) Conclusions 135
5.3.2 Dissolution of Ni from NiAu ultrathin films *135*
a) Dissolution of Ni-rich alloy 135
b) Dissolution of Au-rich alloy 140
c) Conclusions 142

5.4 Monte Carlo simulations of alloy dissolution 142
5.4.1 Model description *143*
a) Dissolution step 143
b) Diffusion step 144
c) A brief description of the program 146
5.4.2 Simulation results *147*
a) Summary of the characteristics of the experimental alloy dissolution morphology 147
b) Dependence of the calculated morphology on the simulation parameters 148
c) Dissolution of segregated alloys 156
d) Influence of defects in the alloy layer 159
5.4.3 Conclusions *160*
5.5 Discussion 161
5.5.1 General remarks *161*
5.5.2 NiAu monolayer alloys *161*
5.5.3 NiPd monolayer alloys *163*
5.6 Conclusion 169
References 171

6 Conclusions **177**

Chapter 1

Introduction

Metal electrodeposition has attracted a lot of interest because of its practical use and versatility for plating large surfaces. A renew of interest grew up since the late 80th, which has been brought up by the development of STM in electrolyte and the setting up of cleaning procedures allowing to maintain single crystal surfaces in electrolytes for hours with a low number of impurities. A lot of the electrodeposition processes were understood before the STM invention, achieved by using macroscopic in situ measurements (current/voltage, impedance, and microbalance measurements …) and ex situ characterizations using X−Ray diffraction, electron microscopes… Moreover, the developed theoretical aspects of electrodeposition, although partly phenomenological, allowed fitting reasonably well the electrochemical characterizations of several systems. However, the understanding of the basic processes at the atomic scale was missing, because of the lack of techniques allowing the visualization of the deposit morphology at the atomic scale. In particular, the nucleation and growth processes were described by mean field laws, with no hint regarding the processes at the atomic scale.

Since then, and since the intensive use of STM in ultra high vacuum (UHV) and in electrochemistry to observe the deposit morphology, the gain insight into atomic scale processes is tremendous and changes completely our understanding of the correlation between the atomic scale dynamics, binding energies and morphology. Experiments using STM to observe deposit morphologies have first been achieved in UHV. The possibility of observing deposits, a fraction of monolayer (ML) thick, prepared at different temperature allowed a detailed atomic scale theoretical description of the nucleation and growth processes and the derivation of atomic scale parameters like diffusion coefficients and detachment energies [1-4]. Similar progress has been achieved in the electrochemical environment [5-7], where the same processes are present in addition to electrochemically specific ones (direct deposition, anion adsorption). Anion adsorption [8] on the substrate and/or on the deposited film, as well as the presence of charges and counter-ions at the deposit interface appeared to influence dramatically the deposit morphology. The number of examples is tremendous where the morphology obtained by electrodeposition is different from that obtained in UHV, although, in some cases similar morphologies may be obtained. In the case of Ni growth on Au, both situations are possible depending on the electrodeposition conditions [9]. The case of Co on Au(111) is also similar [10,

11]. One case among others where the influence of anions on metal electrodeposition is often very important is the underpotential deposition (UPD) process [12]. It consists in the deposition of a single (sometimes a double) monolayer of a metal on a foreign substrate in conditions (at an electrode potential) not allowed by thermodynamics. The driving force for this process is generally the difference between the deposit and the substrate surface energies, and also the interaction energy between the deposit and the substrate. In addition, anion co-adsorption is often involved in UPD processes, as it is the case for Cu UPD on Au [13].

In parallel to these studies, a regain of interest appeared in the last decade for understanding the nucleation and growth of bimetallic alloys, in particular in a thin layer geometry. Indeed, such alloys usually have interesting physical and chemical properties, for example magnetic or catalytic. Proper understanding of the latter properties necessitates the knowledge of the alloy structure and composition at the atomic scale, motivating microscopic studies of alloy growth. Preparing a bimetallic alloy film with a desired composition in UHV might be tricky and time consuming, because annealing is often necessary (for flattening the deposit surface and increasing the homogeneity of the alloy composition), which results in changing the alloy surface composition. In spite of these difficulties, the use of atomic resolution STM with chemical contrast allowed several research group to completely characterize the surface of the alloy they prepared in UHV (in the case of PtRh bulk alloys, see for example [14], and in the case of CuPd monolayer alloys see [15]). Bimetallic alloy films may be also prepared by co-electrodepositing both metals. Such technique was successfully used to prepare thick alloy film [16]. However these experimental conditions were not adapted for preparing alloy film of few monolayers thick. A more judicious approach for electrodepositing ultrathin AB alloy films is to use the "atomic layer epitaxy" technique, which consists in adsorbing and reducing one monolayer of A, then one monolayer of B, etc…[17]. However, this technique suffers from different handicaps: the deposit flatness is very good for few A adsorption/B adsorption cycles only; the atom intermixing is perpendicular to the film plane only, and it is difficult to vary at wish the alloy composition. Recently, another electrodeposition procedure, inspired by the metal growth in UHV, was used to prepare monolayer thick PdAu alloys with different alloy composition [18]. Atomic scale STM imaging with chemical contrast operated in solution allowed complete characterization of the deposited alloy and demonstrated that this electrodeposition procedure is suited for preparing ultrathin alloy films forming a solid solution phase.

From the theoretical point of view, the importance of a good description of atomic scale processes appeared crucial to explain correctly the macroscopic characteristics of electrodeposits. For example, Berthier et al. succeeded, using Monte Carlo simulations, in describing correctly the

dynamic process of monolayer electrodeposition at the atomic scale and relating such information to macroscopic behavior [19]. Other calculations, using embedded atom method potential, focused on predicting the deposition potential shift of a metal as a function of the metallic substrate [20]. In the case of alloys, DFT calculations were undertaken to determine the dissolution potential of solute atom as function of the host nature [21]. Moreover, using phase field modeling, Karma et al. succeeded to describe properly the morphology of an alloy upon selective dissolution of the less noble metal [22].

In the first part of this work, we studied the electrochemical growth and dissolution of Ni ultrathin film on specific bimetallic Pd/Au substrate. Our aim is to investigate the influence of the substrate on a deposition/dissolution procedure which does not present a UPD process. For this purpose we studied by in situ STM the growth and dissolution morphologies as a function of the deposition and dissolution potentials and in the presence of different anions in the solution. The results are analyzed and discussed in connection with the different Ni-Pd and Ni-Au interaction energies. In the second part, we investigated the growth and dissolution of NiPd and NiAu monolayer alloys on Au(111). Our aim is to characterize their structure, their phase and their atomic arrangement. We also aim at understanding their growth mechanism in relationship with (*i*) their tendency to form a solid solution or a segregated phase, (*ii*) their interaction with the substrate, and (*iii*) the possible presence of strain in the film plane. We also study the morphology of the monolayer alloys during Ni selective dissolution and performed Monte Carlo simulations to understand the experimentally obtained morphologies.

The manuscript is divided into six chapters. In chapter 2, we describe the experimental techniques used in this work. In chapter 3, the experimental procedures for preparing bimetallic substrates and monolayer alloy films are presented. In chapter 4, the growth and dissolution of Ni on Pd/Au bimetallic substrate is presented and discussed. Finally, chapter 5 is dedicated to the growth and dissolution of NiPd and NiAu alloys deposited on Au(111). The general conclusion is presented in chapter 6.

References

1. Brune, H., *Microscopic view of epitaxial metal growth: Nucleation and aggregation.* Surface Science Reports, 1998. **31**(3-4): p. 125-229.
2. Brune, H., *Metals on Metals*, in *Landolt Börnstein series: Physics of Covered Solid Surfaces*, H.P. Bonzel, Editor. 2001, Springer: Berlin. p. 217-258.
3. Evans, J.W., Thiel, P.A., and Bartelt, M.C., *Morphological evolution during epitaxial thin film growth: Formation of 2D islands and 3D mounds.* Surface Science Reports, 2006. **61**(1-2): p. 1-128.
4. Hwang, R.Q. and Bartelt, M.C., *Scanning tunneling microscopy studies of metal on metal epitaxy.* Chemical Reviews, 1997. **97**: p. 1063-1082.
5. Nichols, R.J., Ross, R.N., and Lipkowski, J., *Imaging metal electrocrystallization at high resolution*, in *Imaging of surfaces and interfaces*. 1999, VCH: New York.
6. Gewirth, A.A. and Niece, B.K., *Electrochemical applications of in situ scanning probe microscopy.* Chemical Reviews, 1997. **97**: p. 1129-1162.
7. Allongue, P. and Maroun, F., *Metal electrodeposition on single crystal metal surfaces mechanisms, structure and applications.* Current Opinion in Solid State and Materials Science, 2006. **10**(3-4): p. 173-181.
8. Magnussen, O.M., *Ordered Anion Adlayers on Metal Electrode Surfaces.* Chemical Reviews, 2002. **102**: p. 679-725.
9. Magnussen, O.M. and Behm, R.J., *Structure and growth in metal epitaxy on low-index Au surfaces - a comparison between solid-electrolyte and solid-vacuum interfaces.* Journal of Electroanalytical Chemistry, 1998. **467**: p. 258-269.
10. Allongue, P., Cagnon, L., Gomes, C., Gundel, A., and Costa, V., *Electrodeposition of Co and Ni/Au(1 1 1) ultrathin layers. Part I: nucleation and growth mechanisms from in situ STM.* Surface Science, 2004. **557**(1-3): p. 41-56.
11. Repain, V., Berroir, J.M., Rousset, S., and Lecoeur, J., *Growth of self-organized cobalt nanostructures on Au(111) vicinal surfaces.* Surface Science, 2000. **447**: p. L152-L156.
12. Herrero, E., Buller, L.J., and Abruna, H.D., *Underpotential Deposition at Single Crystal Surfaces of Au, Pt, Ag and Other Materials.* Chemical Reviews, 2001. **101**(7): p. 1897-1930.
13. Möller, F.A., Magnussen, O.M., and Behm, R.J., *In situ STM studies of Cu underpotential deposition on Au(100) in the presence of sulfate and chloride anions.* Physical Review B, 1995. **51**(4): p. 2484.

14. Hebenstreit, E.L.D., Hebenstreit, W., Schmid, M., and Varga, P., *$Pt_{25}Rh_{75}$(111), (110), and (100) studied by scanning tunnelling microscopy with chemical contrast.* Surface Science, 1999. **441**: p. 441-453.
15. Hoster, H.E., Filonenko, E., Richter, B., and Behm, R.J., *Formation and short-range order of two-dimensional Cu_xPd_{1-x} monolayer surface alloys on Ru(0001).* Physical Review B, 2006. **73**(16): p. 165413-11.
16. Andricacos, P.C., Romankiw, L.T., Gerischer, H., and Tobias, C., *Magnetically soft materials in data storage: Their properties and electrochemistry.* 1990, VCH: New York. p. 230-321.
17. Gregory, B.W. and Stickney, J.L., *Electrochemical atomic layer epitaxy (ECALE).* Journal of Electroanalytical Chemistry, 1991. **300**: p. 543-561.
18. Maroun, F., Ozanam, F., Magnussen, O.M., and Behm, R.J., *The role of atomic ensembles in the reactivity of bimetallic electrocatalysts.* Science, 2001. **293**(5536): p. 1811-1814.
19. Berthier, F., Braems, I., Creuze, J., Tetot, R., and Legrand, B., *Voltammetry and electrodeposition in the presence of attractive interactions: I. a mean-field approach.* Journal of the Electroanalytical Chemistry, 2004. **573**: p. 365-376.
20. Oviedo, O.A., Leiva, E.P.M., and Rojas, M.I., *Energetic and entropic contributions to the underpotential/overpotential deposition shifts on single crystal surfaces from lattice dynamics.* Electrochimica Acta, 2006. **51**(17): p. 3526-3536.
21. Greeley, J. and Nørskov, J.K., *Electrochemical dissolution of surface alloys in acids: Thermodynamic trends from first-principles calculations.* Electrochimica Acta, 2007. **52**(19): p. 5829-5836.
22. Erlebacher, J., Aziz, M.J., Karma, A., Dimitrov, N., and Sieradzki, K., *Evolution of nanoporosity.* Nature, 2001. **410**: p. 450-453.

Chapter 2

Electrochemical Growth and Dissolution: Fundamentals and Experimental

The first part of this chapter gives a brief description of the fundamentals of metal electrodeposition. The different terms as well as the electrochemical concepts employed in this work are introduced. Starting with the structure of the metal-electrolyte interface, we will then define the Nernst equation followed by explanation on the electrode kinetics. In the second part, we will present some experimental and technical details related to this work, concerning the instrumentation, the electrochemical cell and solutions employed.

2.1 Electrochemical Fundamentals

2.1.1 The metal-electrolyte interface

Electrochemical reactions take place at the interface between an electronic conductor (a metal electrode), and an ionic conductor (an electrolyte which contains ions). The present paragraph will only give some basic considerations concerning the metal-electrolyte interface. Further information can be found in Refs. [1-4].

The metal-electrolyte interface has been shown experimentally to behave like a plate capacitor of molecular thickness. Indeed, the metal electrode may carry an excess charge located at the surface, which is compensated by an ionic excess charge on the solution side of the interface. As illustrated in Fig. 2.1, one side of the capacitor is the metal surface, the other side is built by solvated ions from the electrolyte at a distance of closest approach equal to the radius of their solvation shell (~ 3 Å). This distance defines the so-called outer Helmholtz plane (OHP). The whole array of charged species and oriented dipoles existing at the metal-electrolyte interface is called the *electrical double layer*.

A more comprehensive model of the double layer takes into account thermal diffusion of the ions. Consequently, the ionic counter charge is located in a *diffuse layer* located in the vicinity of the interface. The thickness of this layer depends on the ion concentration and is typically 1 nm for 0.1 M ion concentration.

Because of the small "capacitor plate distance" of ~ 10 Å, the capacity of the electric double layer is extremely high and varies typically from 10 to 40 $\mu F.cm^{-2}$ but its value changes with the applied potential with a minimum around the so-called potential of zero charge (pzc, the potential at which no excess charge is present on the electrode surface).

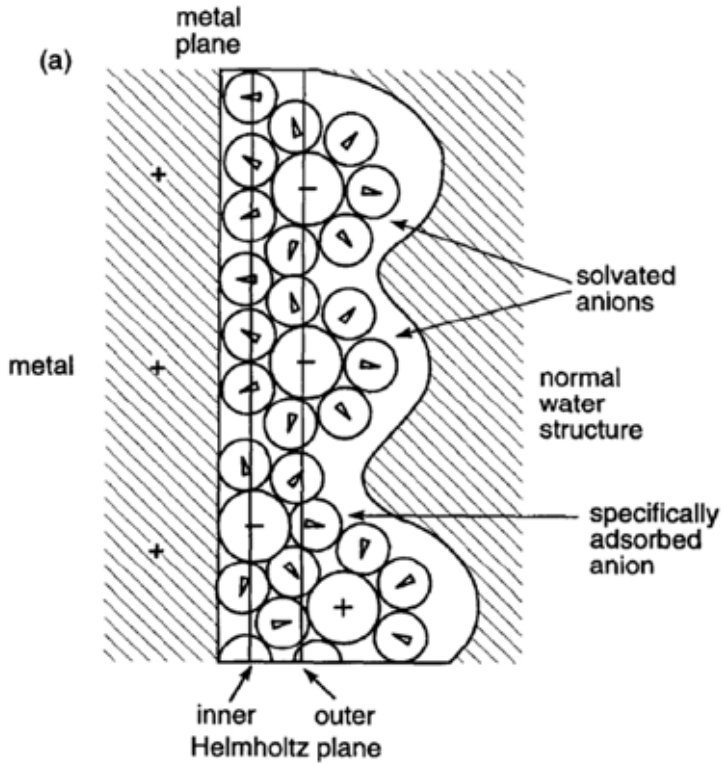

Figure 2.1: Model of the metal-electrolyte interface (electrical double layer) under conditions where anions are specifically adsorbed. Adapted from Ref. [5].

The solvated ions at the OHP which interact with the electrode surface by electrostatic forces only, are said to *adsorb nonspecifically*. These are ions with strongly bound solvation shells such as most cations or F^-. Other ions, mostly anions like Cl^-, Br^- or I^- with relatively weakly bound solvation water, may partly strip their solvation shell in the double layer and directly bind to the electrode surface. The position of these chemisorbed or *specifically adsorbed ions* defines the so-called inner Helmholtz plane (see Fig. 2.1). The lateral arrangement and the coverage of specifically adsorbed ions depend markedly on the electrode potential, the substrate structure and crystallographic orientation. [6].

In the following, deposition and dissolution processes of metals will be considered. As we will see, the main control parameter of these processes is the potential drop between the electrode and the electrolyte. However, a potential may be applied only between two electrodes immersed in the same electrolyte, the electrode of interest and a counter electrode. This makes the potential drop between the electrode of interest and the solution not easily defined. One way

to overcome this problem is to use an auxiliary electrode (reference electrode), a potentiostat (see Sec. 2.3.1) and a relatively concentrated supporting electrolyte. The latter does not participate to deposition and dissolution reactions. It ensures that the potential drop in the electrolyte bulk remains negligible and defines the diffuse layer independently from the presence of metal cations.

2.1.2 The Nernst equation

At the electrochemical interface between a metal electrode (labeled M) and a solution containing metallic ions (labeled M^{z+}), the following equilibrium sets up:

$$M^{z+} + ze^- \rightleftarrows M \qquad \text{(Eq. 2.1)}$$

where z is the charge of the ions in the electrolyte. From the equilibrium condition expressed as the equality between the electrochemical potentials of both phases (M and M^{z+}), we can deduce the Nernst equation which gives the equilibrium potential U_{eq} (V) of the redox process of Eq. 2.1:

$$U_{eq} = U^{\circ}_{M^{z+}/M} + \frac{RT}{zF}\ln\left(\frac{a_{M^{z+}}}{a_M}\right) \qquad \text{(Eq. 2.2)}$$

where $U^{\circ}_{M^{z+}/M}$ is the standard electrode potential (i.e. established in the standard conditions: T = 298 K, P = 10^5 Pa, c = 1 mol.l^{-1}), R is the standard gas constant (R = 8.314 J.mol^{-1}.K^{-1}), T is the absolute temperature (K), F is the Faraday constant (F = 96485 C.mol^{-1}), $a_{M^{z+}}$ and a_M are the activities of the metal and ions species. As the reduced species is in the pure metal phase, its activity a_M is equal to unity. For low concentration (< 1 mol.l^{-1}), the activity a is equal to the concentration c. The oxidized species are the metal ions in the solution $c_{M^{z+}}$. Hence, the Nernst equation can be written to the following expression (Eq. 2.3) where the equilibrium potential depends on the concentration of the ions in solution:

$$U_{eq} = U^{\circ}_{M^{z+}/M} + \frac{RT}{zF}\ln(c_{M^{z+}}) \qquad \text{(Eq. 2.3)}$$

The values of the standard electrode potentials in aqueous solution for different redox couples (M^{z+}/M) are tabulated in text books [7] and are usually given versus the normal hydrogen electrode (NHE) in standard conditions. This reference electrode, which is not handy (since it requires the use of a platinum wire immersed in acidic solution of pH = 0 in which purified hydrogen gas is bubbling) was replaced in our studies by a commercial, saturated mercury/mercurous sulfate reference electrode (MSE). In the following of this work, all potentials will be quoted against MSE. Table 2.1 displays a few values for redox couples used in the thesis. The electrode potentials recorded using NHE can be converted into potentials versus MSE according to:

$$U_{(\text{V vs. MSE})} = U_{(\text{V vs. NHE})} - 0.640 \qquad \text{(Eq. 2.4)}$$

Table 2.1: Standard potentials for different redox couples. Adapted from Ref. [7].

Redox Couple	Electrode Reaction	$U°$ / V_{NHE}	$U°$ / V_{MSE}
Co^{2+}/Co	$Co^{2+} + 2e^- \leftrightarrow Co$	-0.277	-0.917
Ni^{2+}/Ni	$Ni^{2+} + 2e^- \leftrightarrow Ni$	-0.257	-0.897
H_2/H^+	$H_2 + 2e^- \leftrightarrow 2H^+$	0	-0.64
MSE electrode Hg_2SO_4 /Hg	$Hg_2SO_4 + 2e^- \leftrightarrow 2Hg + SO_4^{2-}$	0.64 (saturated KCl)	0
$PdCl_4^{2-}/Pd$	$PdCl_4^{2-} + 2e^- \leftrightarrow Pd$	0.64	0
$AuCl_4^-/Au$	$AuCl_4^- + 3e^- \leftrightarrow Au$	1.002	0.362

The Nernst potential can be thus calculated for different metal ion concentrations. If the potential U applied to the electrode M is different from U_{eq} then metal bulk phase can be deposited ($U < U_{eq}$) while dissolved ($U > U_{eq}$). Therefore, the Nernst equilibrium potential represents the upper limit of the stability range of a metal bulk phase. The magnitude of the deviation of the electrode potential U from the equilibrium value U_{eq} is termed the overpotential, defined as:

$$\eta = U - U_{eq} \qquad \text{(Eq. 2.5)}$$

and its sign is obviously determined whether U is lower than (cathodic overpotential) or greater than (anodic overpotential) U_{eq}. For $\eta < 0$, the growth process is called overpotential deposition (OPD).

However, when metal deposition takes place on a foreign substrate S, the experimentally observed deposition potential is often different from the thermodynamically calculated value for various reasons. (*i*) The onset of metal deposition can be shifted to more negative deposition potentials than the equilibrium U_{eq} owing either to limitations due to charge transfer or nucleation (see Sec. 2.1.3 and Refs. [4, 8] for further details) or to undesired side reactions (such as solvent decomposition). (*ii*) Deposition can also take place at potentials more positive than the Nernst potential. This effect is termed underpotential deposition (UPD) and concerns the first (or the first two) deposit monolayer [9, 10]. Experimentally, the UPD process is characterized by one or more sharp and narrow current peaks in the voltammogram at potentials more positive than the current associated with the onset of bulk deposition of M (i.e. in the OPD regime). Extensive studies have tried to rationalize the existence of such deposition process using models ranging from rather phenomenological approaches to very sophisticated quantum-mechanical calculations [10-12]. A meaning-full parameter of the UPD process is the so-called underpotential shift, $\Delta U_{UPD} = U^{M/S} - U^{M/M}$, which is defined as the potential difference between the desorption peak of a monolayer of a metal M adsorbed on a foreign substrate S ($U^{M/S}$) and the Nernst potential of the redox couple of M^{z+}/M. First, a systematic investigation of ΔU_{UPD} for different pairs of M and S has shown a strong correlation with the difference in electronic work functions $\Delta\Phi$ for the two metals. It indicates that UPD takes place when the substrate work functions is larger than that of the deposit inducing partial charge transfer from the adlayer to the substrate. Second, thermodynamic interpretation of the underpotential shift allowed to consider the existence of UPD through the excess of binding energy, indicating that such growth process occurs when the interaction of the admetal with the substrate are stronger than the admetal-admetal interaction. UPD processes have been widely studied by means of in situ methods to complement the classical, current- and voltage-based techniques such as X-ray diffraction and scanning tunneling microscopy. The most studied systems are Cu/Au(111)[13-16], Ag/Au(111) [17], Ag/Pt(111) [18] and Pb/Ag(111) [19]. An analogy may be drawn between the UPD process and the presence, in some cases, of a shift in the desorption temperature (in temperature desorption spectroscopy (TDS) in UHV) of a monolayer metal film, as compared to a multilayer one, deposited on a foreign substrate. In this case, the desorption peak of the last film monolayer during a positive temperature ramp is positioned at higher temperature than that of the rest of the film [20].

2.1.3 Electrode kinetics

The deposition reaction ($M^{z+} + ze^- \rightarrow M$) depends on two main processes (see Fig. 2.2a): (*i*) the diffusion of electroactive species from the bulk solution to the electrode surface (mass transport step) and (*ii*) the electron transfer at the electrode (charge transfer or discharge step).

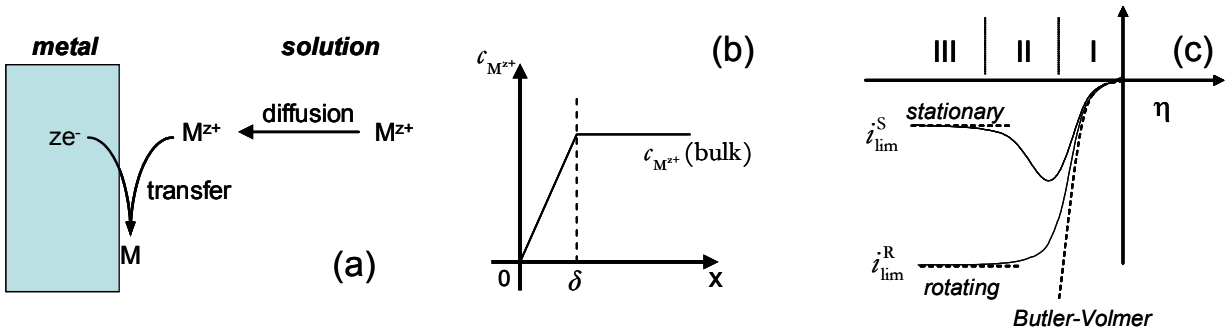

Figure 2.2: (a) Schematic representation of the two main processes governing the electrochemical charge transfer for the process $M^{z+} + ze^- \rightarrow M$. (b) Concentration profile and diffusion layer approximation (dashed line). x = 0 corresponds to the electrode surface and δ is the diffusion layer thickness. (c) Shape of linear sweep voltammogram recorded either on stationary electrode (SE) or on a rotating disc electrode (RDE).

For the discharge of metal ions, electrons have to cross the phase boundary between ion conductor (i.e. the electrolyte) and the electron conductor (i.e. the metal electrode). See Sec. **2.1.1** for details. It involves the change in the structure of the ions, such as partial removal of the hydrate shell or geometric deviations from the situation in the bulk solution. The charge transfer reaction corresponds to a thermally activated process for which the activation energy barrier varies with the applied electrode potential. For further details see textbooks [4]. The exchange of electrons due to an electrochemical process occurring at the electrode surface gives rises to a current, which is a measure of the reaction rate taking place at the electrode. A mathematical relationship between the current density *i* (expressed in $A.cm^{-2}$) and the applied overpotential η is given by the Butler-Volmer equation [4]:

$$i = i^+ + i^- = i_o \left[\exp\left(\frac{(1-a)zF}{RT} \eta \right) - \exp\left(\frac{-azF}{RT} \eta \right) \right] \qquad \text{(Eq. 2.6)}$$

The overall current density *i* is actually the sum of the partial current densities related to the anodic (metal dissolution) and cathodic (metal deposition) partial reactions (i^+ and i^-,

respectively). The electrochemical charge transfer coefficient a is a measure of the symmetry of the activation barrier ($0 < a < 1$). i_o corresponds to the exchange current density and is related to reaction kinetics.

The Butler-Volmer equation reveals that the current density varies exponentially with the applied overpotential η. Let us focus on the case of electrodeposition. At small negative values of η, the electrochemical transfer is limited by the discharge step and the concentration of M^{Z+} at the electrode surface ($c_{M^{z+}}(0)$) will remain roughly equal to the one in the bulk solution (i.e. far from the electrode, $c_{M^{z+}}(\text{bulk})$). This deposition regime is usually defined as the *kinetic regime*. However, at larger negative η, the reactive species are consumed so fast that the reaction rate will be partially *limited by the diffusion* of these species from the bulk solution to the electrode surface. The consumption of M^{z+} ions leads to the formation of a concentration profile, which extends from the electrode surface to the solution by an amount δ termed the diffusion layer thickness (see **Fig. 2.2b**), and the current density is thus given by the Fick's law. At sufficiently large negative overpotentials, $c_{M^{z+}}(0)$ decreases to zero and the current density is no longer determined by the electron transfer rate and becomes entirely limited by the rate of diffusion. In that case, the limiting value is called diffusion-limited current (i_{lim}) and is expressed by:

$$i_{lim} = -zFD\frac{c_{M^{z+}}(\text{bulk})}{\delta} \qquad \text{(Eq. 2.7)}$$

where D is the diffusion coefficient of M^{z+} in the electrolyte (~ 10^{-5} $cm^2.s^{-1}$).

The expression of δ depends on the hydrodynamic conditions in the cell [4]. In unstirred solutions, the value of δ is time dependent and increases until it reaches an approximately constant value at around 100 μm due to microscopic convection effects. Reaching the steady state is likely to take up to one minute. When a rotating disc electrode (RDE) is used, convective flow is imposed and δ takes a well-defined value of the order of 10 μm (given by the Levich equation, see textbooks for details [4]). A steady state is attained within few seconds.

According to the concepts exposed above, the shape of current-potential curves (also called linear sweep voltammograms (LV)), in a potential range where deposition takes place, can be predicted. Fig. 2.2c models the shape of LV of a stationary electrode or of a rotating disc electrode (RDE) in case of a deposition process. It can be seen that, at low $|\eta|$ (region I), the current density decreases exponentially on both type of electrodes i.e. follows the Butler-Volmer equation (represented by the dashed line). As $|\eta|$ increases, there is a transition (region II) in which both electron transfer and mass-transport rates play a role. Finally, at large $|\eta|$ (region III),

the diffusion-limiting region is reached. It is straightforward to observe that the shape of LV strongly differ between RDE and stationary electrode. Contrary to the case of RDE, the decrease of the current density after reaching a peak on stationary electrode reflects the fact that the diffusion layer thickness still increases toward the bulk solution and does not yet reach a steady state value.

2.2 Electrodeposition processes

The growth process in the electrochemical environment and the resulting morphology requires knowledge of both *thermodynamics* and *kinetics*. Contrary to gas phase deposition in the ultra high vacuum environment (UHV), the electrodeposition is ruled by the value of the applied overpotential (η) which not only determines the kinetics of the ion transfer reaction (see Sec. 2.1.2) but also may affect the deposition process by changing the electrode surface properties (anion co-adsorption, surface reconstruction). As mentioned above, the metal species are dissolved in solution in form of solvated cations or complexes. On the atomic scale (see Fig. 2.3), the electrodeposition process implies the loss of the surrounding shell and the creation of an adsorbed cation (step 1, $M_{sol}^{z+} \rightarrow M_{ad}^{z+}$). The electrochemical discharge of the adsorbed cation $M_{ad}^{z+} + ze^- \rightarrow M$ (step 2) creates an adatom.

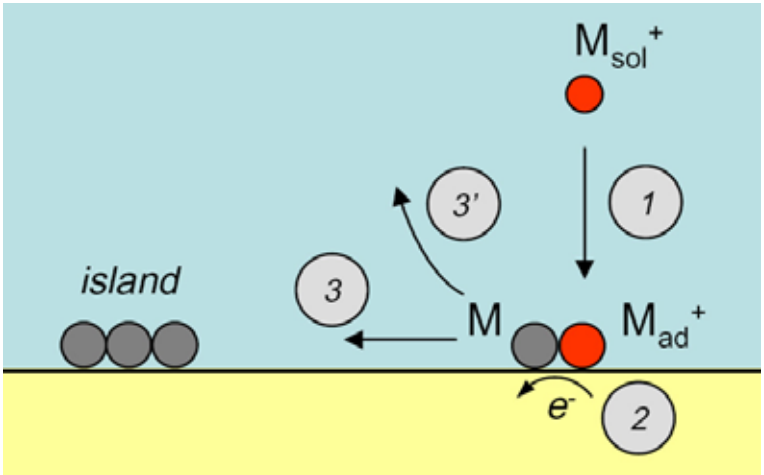

Figure 2.3: Elementary steps in electrodeposition. Adapted from Ref. [21].

Close to the equilibrium potential, at $\eta \sim 0$, the adatom is unstable on a defect free region and it can be redissolved in solution (step 3'). In that case the description of the growth process relies on the classical *thermodynamic* theory to epitaxial thin film growth. This approach takes into account the energetics of the substrate, of the deposited metal and of the boundary between the

substrate and the adlayer. It leads to the definition of the so-called growth modes: (*i*) Frank-van der Merwe (FM) growth mode (layer-by-layer or step-flow growth), (*ii*) Volmer-Weber (VW) growth mode (island growth), (*iii*) Stranski-Kranstanov (SK) growth mode (initially step-flow growth and after critical thickness, island growth). Further details concerning the thermodynamic aspects of growth process can be found in the following references [8, 22, 23]. Moreover, in the electrochemical environment, the deposition occurs by direct discharge of the cation on energetically favorable sites (e.g. steps) with essentially no surface mobility. This later process is analog to site sensitive chemical vapor deposition (CVD) in UHV.

At large enough $|\eta|$, the growth process occurs far from equilibrium implying that the formed adatom is stabilized on the surface (redissolution back into the electrolyte is negligible). Then, it diffuses on the surface (step 3) to aggregate into islands with other adatoms. Hence, the obtained morphology is influenced by kinetics (i.e. the path taken by adatoms onto the surface) rather than by thermodynamics (i.e. deposition and desorption) and the term *growth mode* should now be replaced by *growth morphologies*. In this case, classical theory of nucleation and growth applies. This process resembles to the situation found for molecular beam epitaxy (MBE) with the existence of the same elementary steps involved during the growth (such as adsorption potential, surface diffusion barrier, Ehrlich-Schwoebel barrier). For a given flux, the density of islands depends on the surface diffusion coefficient of the adatoms which may vary with η, via co-reactions, structural changes or changes in surface chemistry [24]. Changing the anions may for instance induce dramatic effects: the addition of sulfamates to Watts solution promotes UPD of nickel [25] and the addition of thiocyanates (SCN^-) promotes UPD of cobalt [26].

2.3 Experimental and technical details

2.3.1 Electrochemical instrumentation: the potentiostat

The potentiostat corresponds to an electronic hardware required to control a three electrode cell (defined below) and perform electrochemical measurements such as linear sweep voltammetry (LV), cyclic voltammetry (CV), and controlled-potential electrolysis. Its role is to control the potential of the working electrode (WE) with respect to the reference electrode (RE) by adjusting the electrical current which passes between the working electrode and the counter electrode (CE). No current passes through the reference electrode. In this work we used a home made potentiostat while the data acquisition was done by means of a home made labview program.

2.3.2 Electrodes, chemicals and solutions

In this work, the electrochemical measurements were conducted in a standard three-electrode cell. The working electrode was a Au(111) substrate. Two types of Au substrates were used depending on the experimental techniques employed: (*i*) a cylindrical Au(111) single crystal electrode (5 mm diameter) purchased by MaTeck for in situ scanning tunneling microscopy (STM) experiments, (*ii*) thin Au films evaporated on mica for measurements in the conventional electrochemical cell. The experimental procedures used to prepare these Au samples are described in the Chapter 3 (Sec. 3.1). The reference electrode was a commercially available, mercury / mercurous sulfate electrode (MSE; saturated KCl; +0.64 V vs. NHE), and all potentials in this work are quoted against MSE. The counter electrode was a platinum wire of high purity (99.99 %, Johnson-Matthey), which was cleaned in aqua regia (mixture of concentrated nitric acid (HNO_3) and concentrated hydrochloric acid (HCl), in a volumetric ratio of 1:3 respectively) and stored in piranha solution (mixture of concentrated sulfuric acid (H_2SO_4) and 30% hydrogen peroxide solution (H_2O_2) in a volumetric ratio of 3:1 respectively). In the conventional electrochemical cell only, the counter electrode was separated from the main cell compartment by a glass frit and the electrolyte was deaerated by high-purity Ar gas before and during the measurements.

All solutions were prepared using ultra-pure deionized water (resistivity of 18.2 MΩ.cm), produced using a Milli-Q Millipor system with reagent grade chemicals. $NiSO_4$ and $CoSO_4$ were purchased by Merck; K_2PdCl_4, $PdSO_4$, $HAuCl_4$, $HClO_4$ K_2SO_4 and KCl were purchased by Sigma-Aldrich; H_2SO_4 and HCl were purchased by Carlo Erba Company. The supporting electrolyte (SE) used in this work was 0.1 M K_2SO_4 + 1 mM KCl + 1 mM H_2SO_4 of pH ~ 3.

2.3.3 Scanning Tunneling Microscopy (STM)

In situ electrochemical STM experiments were performed with a home built scanning tunneling microscope, described in detail in Ref. [27]. Tunneling tips were prepared by electrochemical etching of W wire in 2M NaOH and coated with Apiezon wax. Tip and sample potentials were kept independently under potential control by using a bipotentiostat, with the tip potential kept typically at -0.6 V. STM images were obtained in constant current mode with tunneling currents between 1–10nA. They are presented as top view images with darker colors corresponding to lower surface areas. The electrochemical cell employed during in situ STM measurements was a small volume cell (~ 300 μl) made of Teflon.

References

1. Grahame, D.C., *The electrical double layer and the theory of electrocapillarity.* Chemical Reviews, 1947. **41**: p. 441-542.
2. Parsons, R., *Electrical double layer: Recent experimental and theoretical developments.* Chemical Reviews, 1990. **90**(5): p. 813-826.
3. Schmickler, W., *Interfacial electrochemistry*. 1996, New York-Oxford: Oxford University Press.
4. Bard, A.J. and Faulkner, L.R., *Electrochemical Methods: Fundamentals and Applications, 2nd Edition*. 2001, New York: John Wiley & Sons.
5. Kolb, D.M., *Reconstruction phenomena at metal-electrolyte interfaces.* Progress in Surface Science, 1996. **51**(2): p. 109-173.
6. Magnussen, O.M., *Ordered Anion Adlayers on Metal Electrode Surfaces.* Chemical Reviews, 2002. **102**: p. 679-725.
7. Bard, A.J., Parsons, R., and Jordan, J., *Standard Potential in Aqueous Solutions*. 1985, New York: Marcel Dekker.
8. Budevski, E., Staikov, G., and Lorenz, W.J., *Electrochemical phase formation and growth.* Advances in Electrochemical Science and Engineering, ed. R. Alkire, H. Gerischer, D.M. Kolb, and C.W. Tobias. 1996, Weinheim: VCH.
9. Herrero, E., Buller, L.J., and Abruna, H.D., *Underpotential Deposition at Single Crystal Surfaces of Au, Pt, Ag and Other Materials.* Chemical Reviews, 2001. **101**(7): p. 1897-1930.
10. Leiva, E., *Recent developements in the theory of metal upd.* Electrochimica Acta, 1996. **41**: p. 2185-2206.
11. Kolb, D.M., Przasnyski, M., and Gerischer, H., *Underpotential deposition of metals and work function differences.* Electroanalytical Chemistry and Interfacial Electrochemistry, 1974. **54**: p. 25-38.
12. Kolb, D.M., Gerischer, H., and Tobias, C., *Physical and electrochemical properties of metal monolayers on metallic substrates*, in *Advances in electrochemistry and electrochemical engineering*. 1978, Wiley-Interscience: New York. p. 125-271.
13. Magnussen, O.M., Hotlos, J., Nichols, R.J., Kolb, D.M., and Behm, R.J., *Atomic structure of Cu adlayers on Au(100) and Au(111) electrodes observed by in situ scanning tunneling microscopy.* Physical Review Letters, 1990. **64**: p. 2929-2932.
14. Batina, N., Will, T., and Kolb, D.M., *Study of the initial stages of copper deposition by in situ Scanning Tunneling Microscopy.* Faraday Discussions, 1992. **94**: p. 93-106.

15. Watanabe, M., Uchida, H., Miura, T., and Ikeda, N., *Electrochemical quartz crystal microbalance study of copper ad-atoms on highly ordered Au(111) electrodes in sulfuric acid.* Journal of Electroanalytical Chemistry, 1995. **384**: p. 191-195.
16. Hölzle, M.H., Zwing, V., and Kolb, D.M., *The influence of steps on the deposition of Cu onto Au(111).* Electrochimica Acta, 1995. **40**(10): p. 1237-1247.
17. Ogaki, K. and Itaya, K., *In situ scanning tunneling microscopy of underpotential and bulk deposition of silver on gold(111).* Electrochimica Acta, 1995. **40**(10): p. 1249-1257.
18. Kimizuka, N. and Itaya, K., *In situ scanning tunnelling microscopy of underpotential deposition: Silver adlayers on Pt(111) in sulfuric acid solutions.* Faraday Discussions, 1992. **94**: p. 117-126.
19. Obretenov, W., Schmidt, U., Lorenz, W.J., Staikov, G., Budevski, E., Carnal, D., Müller, U., Siegenthaler, H., and Schmidt, E., *Underpotential depostion and electrocrystallisation of metals: an in situ scanning tunneling microscopy study with lateral atomic resolution.* Faraday Discussions, 1992. **94**: p. 107-116.
20. Guan, J., Campbell, R.A., and Madey, T.E., *Ultrathin metal films on W(111): morphology and faceting reconstruction.* Surface Science, 1995. **341**(3): p. 311-327.
21. Allongue, P., Maroun, F., Jurca, H.F., Tournerie, N., Savidand, G., and Cortes, R., *Magnetism of electrodeposited ultrathin layers: Challenges and opportunities.* Surface Science, 2009. **603**: p. 1831-1840.
22. Brune, H., *Growth Modes*, in *Encyclopedia of Materials: Science of Technology, Sect. 1.9, Physical Properties of Thin Films and Artificial Multilayers*, K. Samwer, Editor. 2001, Pergamon press. p. 3683-3693.
23. Michely, T. and Krug, J., *Islands, Mounds, and Adatoms: Patterns and Processes in Crystal Growth Far from Equilibrium*. 2004, Berlin: Springer.
24. Krug, K., Stettner, J., and Magnussen, O.M., *In Situ Surface X-Ray Diffraction Studies of Homoepitaxial Electrochemical Growth on Au(100).* Physical Review Letters, 2006. **96**(24): p. 246101-4.
25. Bubendorff, J.L., Cagnon, L., Costa-Kieling, V., Bucher, J.P., and Allongue, P., *Anion promoted Ni-underpotential deposition on Au(111).* Surface Science, 1997. **384**: p. L836-L843.
26. Cagnon, L., Gundel, A., Devolder, T., Morrone, A., Chappert, C., Schmidt, J.E., and Allongue, P., *Anion effect in Co/Au(111) electrodeposition: structure and magnetic behavior.* Applied Surface Science, 2000. **164**(1-4): p. 22-28.
27. Allongue, P., Costa-Kieling, V., and Gerischer, H., *Etching of silicon in NaOH solutions. I. In situ scanning tunneling microscopic investigations of n-Si(111).* Journal of the Electrochemical Society, 1993. **140**: p. 1009-1018.

Chapter 3

Experimental Procedures for the Preparation of Bimetallic Substrates and Monolayer Alloy Films

This chapter describes the experimental procedures used to prepare the metallic surfaces employed in this work. The first part (section 3.1) will be dedicated to the Au(111) surface which corresponds to the common substrate used in each section of the thesis. After describing the preparation procedures of the different types of Au samples, a brief description of the Au(111) atomic structure will be given. Then, in section 3.2, we will present the preparation of bimetallic Pd/Au(111) surface used as substrate in Chapter 4 to study the growth/dissolution processes of Ni and Co ultrathin layers. The early stages of Pd deposition on Au surface will be first detailed followed by characterization of the Pd(1ML)/Au(111) surface properties. Finally, in section 3.3, we will detail the different procedures employed in Chapter 5 to electrodeposit the Ni-based ultrathin alloy films on Au(111).

3.1 Preparation and characterization of the Au(111) surface

3.1.1 Introduction

Gold (Au) is of particular interest to electrochemists because of its inertness and the wide polarizable potential ranges accessible in aqueous media. In addition, ordered single crystal Au surfaces can be easily prepared by "flame annealing treatment" applied in an analogous fashion to that used originally for ordered platinum electrodes [1]. Contrary to Pt single crystal, the cooling down process for a Au annealed surface can be done in ambient environments. Moreover, Au films can also be easily evaporated on mica substrates. Au is the only face-centered cubic (fcc) metal that exhibits a reconstruction of the hexagonal close-packed (111) surface at room temperature. Various structural aspects and details of the Au(111) reconstruction based on results from UHV experiments [2] are valid also in the electrochemical conditions [3, 4]. In this work, two types of Au(111) substrates were used: (*i*) single crystal and (*ii*) thick gold film deposited on mica. The following sections describe their preparation and characterization.

3.1.2 Au(111) single crystal

For in situ Scanning Tunneling Microscopy (STM) experiments, a cylindrical Au(111) single crystal electrode (5 mm diameter) was used. The Au(111) single crystal was purchased from MaTeck, already aligned and mechanically polished. To remove the defects left from this treatment (scratches and damages in the upper layer), the sample has been electropolished in cyanide solution. This step was only done once before using the crystal for the first time. Usually, the surface of single crystal is prepared before each experiment and consists, first, in electrochemical oxidation of the Au surface in 1 M $HClO_4$ (1 min) followed by chemical dissolution of the oxide in 10% HCl (10 s) to remove possible organic impurities. Then, the Au(111) single crystal is flamed annealed for around 5 min in a butane flame composed of 82% butane and 18% propane to obtain smooth steps and defect-free terraces due to the increased mobility of the surface atoms. After cooling down in air, the crystal was mounted in the electrochemical cell and immersed in electrolyte under potential control. For instance, surface immersion at potential below -0.4 V ensures that the reconstruction will not be lifted (see below).

3.1.3 Au/mica

For measurements in the conventional electrochemical cell, highly (111) textured and epitaxial thin Au films deposited on mica were used. They were prepared by resistive evaporation in a chamber under secondary vacuum (1 to 5 x 10^{-5} Torr) onto freshly cleaved mica with the following growth conditions: $T_{substrat}$ = 360°C and deposition rate of 1.5 - 2 $A.s^{-1}$. Film thickness typically ranges between 600 and 800 Å. Au/mica substrate morphology was systematically checked by atomic force microscopy (AFM) whereas X-ray diffraction (XRD) indicates that the grains are (111) textured [full width at half maximum (FWHM) = 0.5°] and aligned in plane with respect to the lattice of mica (FWHM = 7°). Similarly to Au(1111) single crystal, Au/mica can be flame annealed to get flat terraces and smooth step edges. Fig. 3.1 shows an AFM image of the Au/mica film after flame annealing which reveals a quasi-continuous 2D film composed of relatively flat area separated by steps. The profile corresponding to the black cross-section line in the bottom of AFM image indicates that mounds exhibit typical height ranging between 0.5 and 1 nm. Au/mica substrates present the advantages to be more flexible in use than Au(111) single crystal. Indeed, the deposition process of Au by evaporation allows one to prepare "large" Au coated mica wafers (~ 20 cm^2), which provide disposable and versatile Au surface. Au/mica is well suited to get tailor-made substrate for electrochemical measurements performed in the

conventional cell. However, such Au films are not suitable to STM measurements since terrace width is too small to perform proper growth studies. In both cases, the Au(111) surface displays reconstruction patterns which correspond to a rearrangement of the surface atoms' positions driven by a lowering of the surface energy. Since electrochemical reactions often depend markedly on the surface structure, a detailed knowledge of the latter is desirable and the subsequent section will give a brief overview of the atomic structure of the reconstructed Au(111) surface.

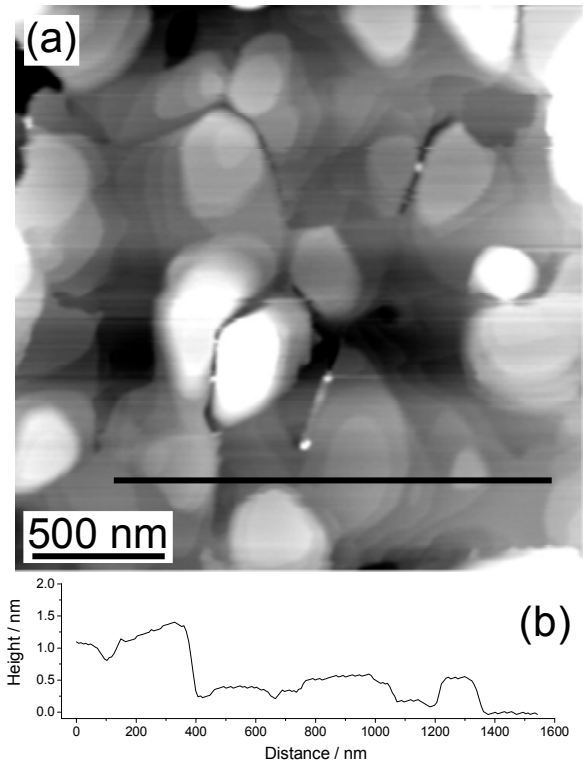

Figure 3.1: (a) ex situ AFM image (2000 x 2000 nm^2) of the (111) textured Au/mica film after flame annealing. (b) Profile representing the cross-section along the black line at the bottom of (a).

3.1.4 Atomic structure of the Au(111) surface

The structure of Au(111) surfaces, used as substrate in each chapter of the thesis, has been studied extensively under ultrahigh vacuum (UHV) conditions [2, 5-7] as well as in the electrochemical environment [3, 4, 8-10]. Clean Au(111) crystals in UHV exhibit a surface reconstruction, where the atoms in the Au surface layer are contracted uniaxially by ~ 4% along the $<1\bar{1}0>$ direction. This leads to a complex structure of the topmost layer, the so-called herringbone reconstruction. The same surface reconstruction is observed on Au(111) samples

prepared by annealing in the flame of a Bunsen burner and subsequently immersed into acidic or salt solutions at potentials negative of a critical potential (see below), which is determined by the anion species of the electrolyte [3, 4, 8-10]. Fig. 3.2 shows a STM image of the surface of the Au(111) single crystal after flame annealing, recorded in 0.1 M H_2SO_4 at U = -0.6 V. This image is composed of terraces (the largest extends over many hundred of angstroms) separated by monoatomic steps of ~ 2.35 Å height as shown in the profile. It can be observed that the terraces exhibit a long-range periodic pattern of pairwise-arranged, parallel corrugation lines which change their orientation in a zigzag pattern by ± 120° and thus form a periodic sequence of domains boundaries, characteristic for the 22 x √3 reconstruction of the Au(111) surface. The distance between neighbored pairs in the $<1\bar{1}0>$ direction is equal to 63 Å while the vertical corrugation amplitude of the modulation pattern amounts to 0.20 Å [2, 6]. Moreover, it can be observed that all of the line pairs pass through the steps without any apparent lateral displacement or even a change in direction at the step edges.

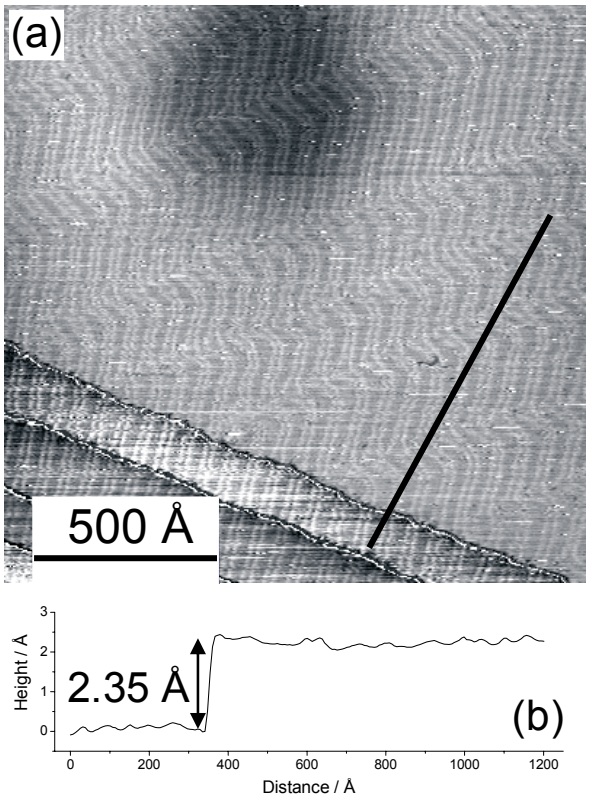

Figure 3.2: (a) STM image (160 x 160 nm²) of the Au(111) surface after flame annealing recorded in 0.1 M H_2SO_4 at U = -0.6 V. Pairwise-arranged, parallel corrugation lines forming a zigzag pattern can be observed on terraces. This structure is characteristic of the 22 x √3 reconstruction of the Au(111) surface. (b) Profile representing the cross-section along the black line at the bottom of (a).

Figure 3.3 shows high-resolution STM image of the 22 x √3 reconstructed Au(111) stretching over two pairs of lines (white) surface. In the figure, the rectangle corresponds to the (22 x √3)-unit cell of the reconstructed surface, which is modeled in Figure 3.4. The 4% compression is achieved by two partial dislocations per (22 x √3)-unit cell. In the top layer one extra atom is inserted resulting in 23 atoms on top of 22 bulk atoms in the second layer. This leads to a compression along the $<1\bar{1}0>$ direction. Due to the additional atom in the first layer not only fcc sites are occupied, but also, the energetically less favorable bridge sites as well as the hcp sites. The change from fcc to hcp sites, with narrower hcp areas, results in a pairwise arrangement of domains walls with a lateral displacement of ~ 0.9 Å. These are aligned along the $<11\bar{2}>$ direction. The higher population of the fcc sites compare to hcp sites is caused by energetic differences. In order to achieve a more isotropic distribution of stress caused by the unidirectional compression, the domain walls are bent by ± 120° reflecting the threefold symmetry of the fcc(111) substrate [2].

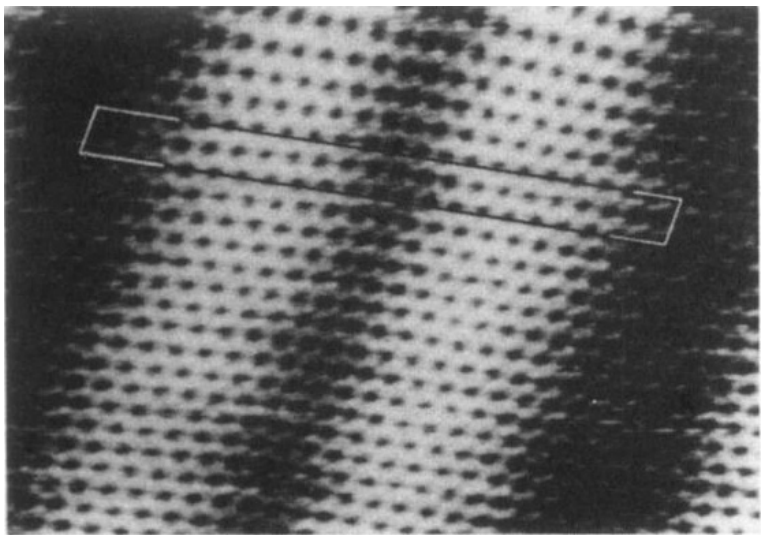

Figure 3.3: Atomic resolution STM image (85 x 60 Å^2) of the 22 x √3 reconstructed Au(111) stretching over two pairs of corrugation lines (white) surface; the unit cell is marked in the figure. Adapted from [2].

At the bending points ("elbows"), the topmost Au layer contains dislocations, resulting in a distortion of the Au lattice at these positions. A model of the atomic structure of reconstruction near the elbows has been detailed by Chambliss et al. [6, 11]. The energetic conditions of surface atoms at the elbows differ from the other surfaces sites. Hence, these elbows can become preferential sites for exchange and nucleation processes. Indeed, there are already a number of cases, as for Ni, Co and Ru, where the impact of surface reconstruction on electrochemical

parameters is clearly stated [12-15]. For this reason it is important to know the electrochemical parameters such as electrode potential and electrolyte composition, for which a reconstructed surface is stable.

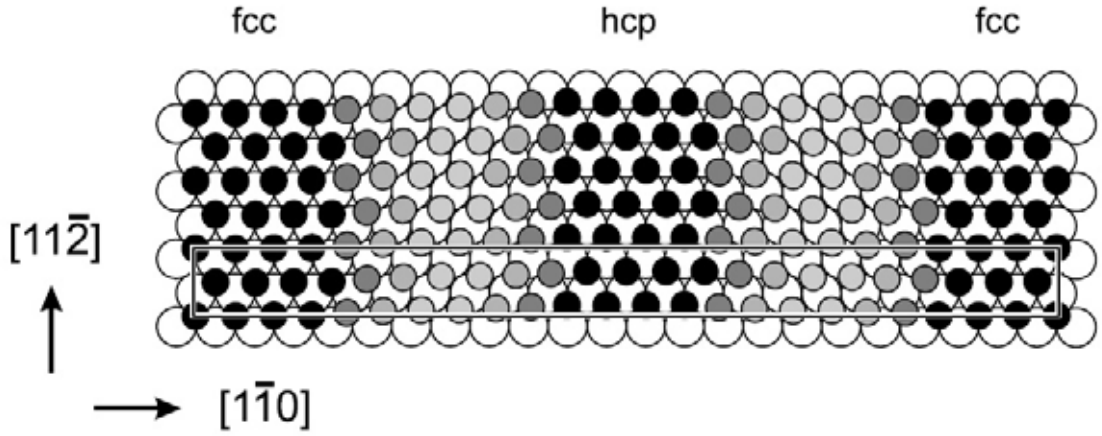

Figure 3.4: Atomic model of the reconstructed Au(111) surface with the unit cell represented by the rectangle: atoms in the topmost layer are represented by the smaller, filled circles, whereas the second layer is symbolized by the larger, open circles. The height modulation is represented by different grey tones. Adapted from Ref. [16].

3.1.5 Electrochemical characterization

In the electrochemical environment, the stability of the (22 x √3) reconstruction of the Au(111) depends on the potential applied to the electrode. The transition between reconstructed and unreconstructed surface can be easily induced by changing the electrode potential [4]. Fig. 3.5 shows the cyclic voltammogram (CV) of a freshly-prepared, reconstructed Au/mica film immersed at rather negative potential into 0.1 M K_2SO_4 + 1 mM KCl + 1 mM H_2SO_4, which corresponds to the supporting electrolyte (SE) used in this work, and recorded at a scan rate (*sr*) of 10 mV.s^{-1}. In this work, we used a saturated mercury / mercurous sulfate electrode (MSE) and all potentials in this work are quoted against MSE. The (22 x √3) → (1 x 1) structural transition is reflected in a pronounced current peak on the anodic scan at U = -0.15 V, indicating that the surface is reconstructed at potential more negative than this value. Then, the broad peaks between 0 and +0.15 V corresponds to the sulfate adsorption on the (1 x 1) - Au(111) surface while the current spikes at U = 0.4 V are due to structural transition within the sulfate adlayer [17]. At potential more positive than 0.4 V, the sulfate anion adlayer is ordered in a (√3 x √7) structure due to strong electrostatic forces between the positively charged surface and the negatively charged anions. Below 0.4 V, the adlayer/substrate interaction decreases and the

anions become disordered and highly mobile due to repulsive electrostatic forces between sulfate anions. By decreasing the electrode potential close to the point of zero charge (pzc, see Sec. 2.1 for definition) which is close to U = -0.15 V, the anions desorbs entailing the beginning of the surface reconstruction process. Finally, the shape of the CV recorded on the flame-annealed Au/mica substrate is very similar to the one obtained on Au(111) single crystal [4, 17], demonstrating the crystalline quality of the thin Au film evaporated on mica substrates.

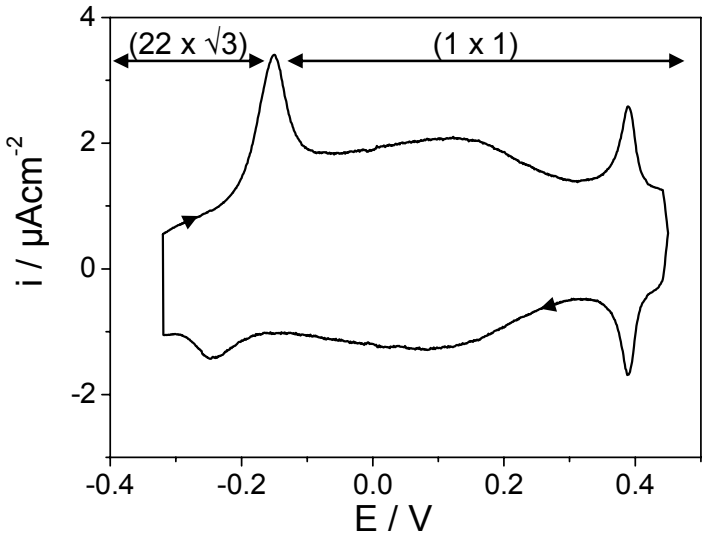

Figure 3.5: Cyclic voltammogram of (111)-textured Au/mica in 0.1 M K_2SO_4 + 1 mM KCl + 1 mM H_2SO_4, starting at -0.3 V. sr = 10 mV.s^{-1}. Lifting of the 22 x √3 reconstruction during the positive scan due to anion adsorption is seen by a pronounced current peak at -0.15 V.

Since the reconstructed surface is compressed by ~ 4%, material is expelled from the top Au layer during the lifting of the reconstruction, resulting in the incorporation of additional Au atoms at steps and in the creation of islands. The change from (22 x √3) to (1 x 1) takes place in the order of minutes [16]. The unreconstructed surface is stabilized by the adsorption of species (e.g., anions, organic molecules) present in the solution [18]. The lifting process can be reversed by sweeping the potential to more cathodic values. Below $U \leq$ -0.2 V, the islands originating from the lifing begins to dissolve and the reconstruction is re-formed. However, the resulting, potential-induced, reconstruction differs from the one obtained by flame annealing (not shown). The characteristic long range order of the very regular herringbone phase is lost and is replaced by a rather randomly arranged pattern of the typical double stripes [3, 4, 8, 9, 19].

3.2 Preparation and characterization of the bimetallic Pd/Au(111) substrate

3.2.1 Introduction

The thin monolayer used in Chapter 4 to prepare the bimetallic substrate had to fulfill the following points: (*i*) present a noble-metal character in order to study the dissolution process of less noble metals deposited on it (such as Ni or Co); (*ii*) own proper electrochemical growth properties which allow us to deposit wide monolayer thick islands as well as flat monolayer thin film; (*iii*) do not form alloy upon deposition at room temperature either with the substrate (Au in our case) or with the overlayer (e.g. Ni and Co); and (*iv*) exhibit the same crystalline structure than the substrate.

There are several noble metals that could be considered as possible overlayer to modify the Au(111) surface, such as platinum (Pt), ruthenium (Ru), rhodium (Rh), silver (Ag) and palladium (Pd). However, most of them show growth properties that are not compatible with the mentioned prerequisite. For instance, Pt electrodeposition onto unreconstructed Au(111) leads to the formation of three-dimensional (3D) clusters with a cauliflower and rough appearance [20, 21], which hampers monolayer formation. In the case of Ru, the nucleation process leads to the formation of high-density monoatomic thick islands of small dimensions (~15 Å). Ru islands coalesce at higher coverage forming large ramified aggregates and finally a highly defective monolayer [22]. Then, concerning Rh, it has been shown that the growth process on Au(111) begins by forming *bilayer* fractal-shaped islands [23]. Even if further growth allowed one to cover almost completely the gold surface, the fact that the adlayer is composed of two atomic layers is not appropriated for our study. In contrast, Ag upd on Au(111) allows us to deposit one monoatomic thick and flat layer [24, 25], which is suitable to our bimetallic model system. In addition, silver surface do not reveal strong interactions with aqueous solutions such as chemisorption of hydrogen or specific adsorption of anions as for the platinum group (see Sec. 3.2.3). However, Ag substrate is known to severely restructure during the deposition of an overlayer, especially with Ni adatoms via intermixing and encapsulation reactions [26, 27]. Thus, due to substrate restructuring, Ag surface is not stable, which hinders its use in the case of bimetallic surface. Finally, Pd upd onto Au(111)-(1x1) carries out in a layer-by-layer mode up to the completion of the second layer, which enables one to deposit wide monatomic Pd islands [28, 29]. No alloy formation between Pd monolayer and Au(111) surface was detected under electrochemical conditions at room temperature by STM and SXS measurements [28-30] contrary

to the case of Pd deposited on Au(111) in UHV [31]. Even if Pd films exhibit strong interactions with hydrogen which is not the case for Au surface, the hydrogen absorption does not occur for films thinner than 3 ML [32]. Moreover, it has been proved by STM and SXS experiments [28, 30] that Pd grows pseudomorphically with Au(111) surface up to the fifth layers (see below for explanations). This point ensures that Pd monoatomic thick islands exhibit the same in-plane lattice parameters than Au(111).

Thus, Pd has been chosen to modify the Au(111) surface. In the following, the electrochemical growth properties of Pd onto Au(111) surface as well as the experimental procedure used to prepare it will be described in details.

3.2.2 Pd electrodeposition on Au(111)

a) Brief overview

Pd can be electrodeposited by using different Pd salts. Most of the electrochemical studies of the initial stages of Pd deposition onto Au(111) have been performed with tetrachloropalladate(II) salt i.e. with K_2PdCl_4 [28-30, 33, 34], since noble metals are commonly deposited from their stable chloride compounds. The nucleation and growth processes of Pd have also been studied by using palladium sulphate ($PdSO_4$ [35]) and palladium nitrate ($Pd(NO_3)_2$ [36]) salts. All these studies were performed on unreconstructed Au(111) by means of cyclic voltammetry (CV), in situ STM and also structure sensitive in situ technique such as Surface X-ray Diffraction (SXD). It has been shown that the deposition of the first Pd monolayer onto Au(111) begins always at underpotentials, whereby Pd nucleates exclusively at surface defects such as monoatomic high steps of terraces or at the monoatomic rims of islands in chloride [28], sulphate [35] and nitrate [36] containing electrolytes. Only in the case of higher overpotentials, deposition starts also on terraces [29]. The nature of the spectator ions contained in the electrolyte has no effect on the nucleation behavior. However, anions (i.e. SO_4^{2-}, NO_3^- and $[PdCl_4]^{2-}$) seem to play a crucial role during the growth and in the shape of the emerging islands, due to specific adsorption which varies with the nature of the Pd salt. In chloride-containing electrolytes, the $[PdCl_4]^{2-}$ anions are adsorbed over a wide potential range, between 0 and 0.4 V, both on Au(111) surface and on the Pd layers [28, 29]. Hence, Pd deposition occurs via reductive discharge of the adsorbed Pd chloro complex. At the opposite, in sulphate and nitrate electrolytes, Pd^{2+} ions are dissolved in the electrolyte while SO_4^{2-} and NO_3^- anions are

adsorbed on Au(111) and on the Pd layers during the reduction reaction in the underpotential region. It is assumed that the adsorbed anions ($[PdCl_4]^{2-}$, SO_4^{2-} or NO_3^-) affect differently the surface mobility of either Pd or Au adatoms. According to Kibler et al. [28, 35, 36], the Pd islands vary from round shape in chloride solution to triangular shape in sulphate solution. In addition, it is well known that the surface mobility of gold adatoms is significantly increased in case of specific anion adsorption, especially in chloride containing solutions which corresponds to the so-called electrochemical annealing [37]. In the presence of adsorbed $[PdCl_4]^{2-}$ on Au(111), it has been observed that the lifting of the reconstruction yields monoatomic high gold islands that are larger in size but fewer than those in sulphate solution, i.e. the surface defect density is lower [35]. Hence, Au adatom diffusion is much lower in sulphate or nitrate containing solutions, resulting in a high number of small gold islands at which Pd will nucleate (see Fig. 3.9). Finally, in all three cases, the upd is two-dimensional (2D) up to the completion of the second Pd layer before turning to three-dimensional (3D) process for thicker films, regardless of the anion in solution. STM measurements concluded that the Pd grows epitaxially and pseudomorphically with the Au(111) substrate up to the end of the fourth layer. Since Pd atoms are about 4.8% smaller than Au atoms (a_{Pd} = 2.75 Å compared to a_{Au} = 2.88 Å), pseudomorphic growth involves that Pd atoms undergo tensile strain to adopt the Au in-plane lattice parameter, as described in Fig 3.6. Indeed, according to Kibler et al. [28], a hexagonal moiré pattern with 60-70 Å distances was observed from the fifth layer one. Such a pattern with a 57 Å periodicity is expected for a native Pd(111) monolayer on a Au(111) surface. Moreover, Takahasi et al. [30] confirmed from SXD measurements that the electrochemical deposition enables one to deposit pseudomorphic Pd monolayer on Au(111).

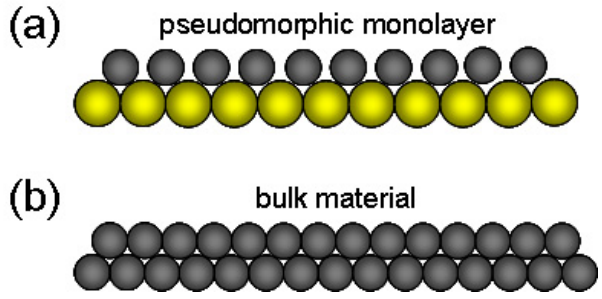

Figure 3.6: Hard sphere models of (a) a pseudomorphic monolayer deposited on a foreign metal substrate of larger lattice constant and (b) of the corresponding bulk metal surface. In case of Pd overlayer, the Pd bulk lattice parameter (2.75 Å) is ~ 4.8% lower than the one of Au (2.88 Å).

In this work, we used Pd amount varying from 0.4 to 1.3 monolayer (ML) to modify the Au(111) substrate. While bimetallic surfaces with submonolayer Pd coverage displayed morphological features very well-suited to make comparative growth STM study, substrates modified by a complete Pd monolayer are used for macroscopic electrochemical measurements.

b) Deposition procedure

The bimetallic Pd/Au(111) substrate was prepared by electrochemical Pd deposition on Au(111) at 0 V in 0.1 M H_2SO_4 + 0.1 mM K_2PdCl_4 (Sigma-Aldrich, 98 %) or, in 0.1 M H_2SO_4 + 0.1 mM $PdSO_4$ (Sigma-Aldrich, 98 %). The freshly prepared, flame-annealed Au(111) surface was immersed into the Pd containing solution at a positive potential (0.3 V) where Pd deposition does not yet occur and any surface oxidation of the substrate is prevented. At this potential, the surface reconstruction is lifted which could leave a surface with some monoatomic high Au islands (see Sec. 3.1.5). Then, the potential was stepped from 0.3 to 0 V where the Au(111) surface is still unreconstructed [4]. The deposited amount of Pd was controlled via the charge (ca. 445 $mC.cm^{-2}$ for one Pd monolayer). The experimental set up used to prepare the Pd/Au(111) substrate depends on the type of the experiment: (*i*) in the STM cell using the Au(111) single crystal for STM experiments and (*ii*) in the electrochemical cell using the Au/mica film for electrochemical characterization. In the STM cell, after a chosen deposition charge, the process at 0 V was stopped by exchanging under potential control the Pd-containing electrolyte with the supporting electrolyte (0.1 M K_2SO_4 + 1 mM H_2SO_4 + 1 mM KCl, pH = 3) which contained 1mM $NiSO_4$ or $CoSO_4$ for studying electrodeposition process on Pd modified Au(111) surface. At the end of the exchanging solution process, pH of the solution contained in the STM cell was again equal to 3. Then, tip was approached to the surface and STM study of deposition processes on Pd/Au(111) surface was carried out. For Au/mica film in the electrochemical cell, deposition was stopped by removing the sample from the deposition bath, rinsed carefully with Milli-Q water and transferred to another electrochemical cell for surface characterization or in the supporting electrolyte with metallic cations (Ni^{2+} or Co^{2+}).

c) Morphology of Pd adlayer on Au surfaces

Fig. 3.7 displays a series of STM images showing the Pd growth on the *Au(111) single crystal* from 0.1 M H_2S0_4 + 0.1 mM K_2PdCl_4 at 0 V by using the experimental procedure described above. Fig. 3.7a displays the Au(111) surface covered by ~ 0.4 ML of wide atomically flat Pd monolayer islands, which have mainly nucleated along the Au steps and also in the centre of large Au terraces. The white dashed lines served as landmark to locate the monoatomic step edges of

the Au terraces while black dashed lines highlight the rims of Pd islands in order to facilitate their identification. The obtained morphology is in agreement with the Pd growth process described in the literature [28, 29, 32]. Due to the pronounced height difference between Pd islands and the Au steps, the Au/Pd boundary can be clearly identified. In the STM image conditions (I_{tip} = 0.46 nA, U_{tip} = -0.52 V, U_{sample} = -0.6 V), Au terraces appear approximately 0.3 Å higher than Pd layers. The lower Pd apparent height (2 Å instead of 2.25 Å) may be explained by geometric considerations taking into account that Pd islands are pseudomorphic to the Au(111) substrate [28, 30] and/or by electronic effects (differences in the electronic local density of states). For longer deposition time, Pd progressively covers the whole Au surface with a uniform monolayer without any second layer island, as can be observed in Fig. 3.7b for which the Pd coverage (θ_{Pd}) is equal to 0.97 ML. Hence, the deposition of one Pd monolayer reproduces exactly the topography of the Au(111) substrate. Then, Fig. 3.7c shows that the second layer islands also nucleate either at the terrace step edges or in the middle of terraces, similarly to observations made for the nucleation of the first Pd layer islands (see Fig. 3.7a). Furthermore, third Pd layer islands are also visible on top of the second layer islands.

Concerning the morphology of Pd adlayers on *Au/mica substrates*, Fig. 3.8 shows ex situ AFM images of Pd/Au/mica surfaces obtained by electrodeposition in 0.1 M H_2SO_4 + 0.1 mM K_2PdCl_4 at 0 V for different deposition times. Compared to the bare substrate (see Fig. 3.1), the surface of Au/mica modified by submonolayer coverage of Pd (θ_{Pd} = 0.3) displays numerous islands which are homogeneously spread over the surface, as shown in Fig. 3.8a. Fig. 3.8b corresponds to the enlargement marked by the black square in image a. It reveals that the Pd islands have nucleated mainly at the Au step edges and that the Pd morphology is similar to that on the Au single crystal. Fig. 3.8b corresponds to another Au/mica substrate covered by a full Pd monolayer (θ_{Pd} = 1). It can be observed that the overall morphology of the Pd(1ML)/Au/mica is very similar to the one found in case of bare Au/mica substrate indicating that the Pd film perfectly replicates the entire surface structure, in full agreement with the 2D growth mode described above.

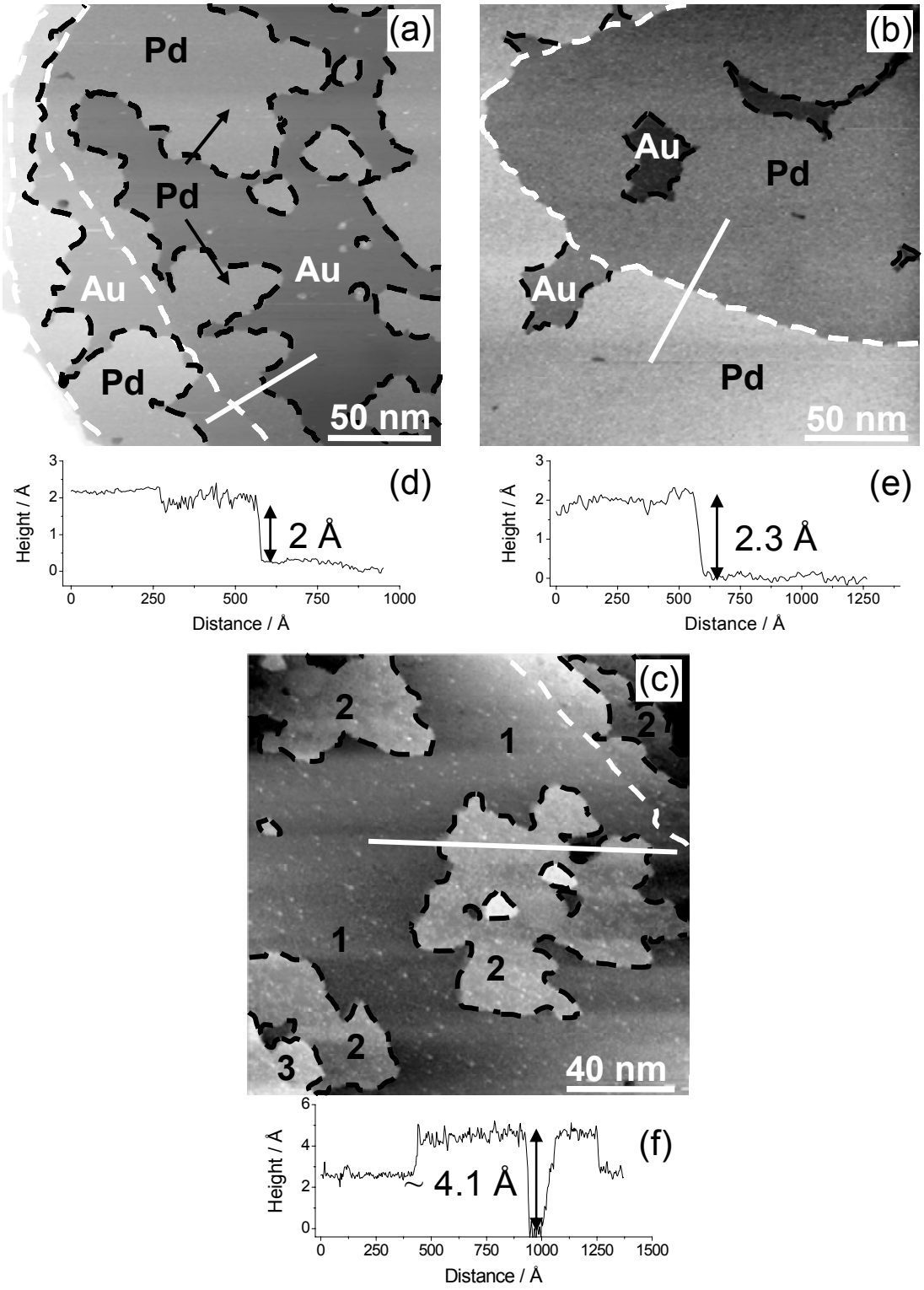

Figure 3.7: Sequence of STM images showing the growth of Pd on Au(111). The Pd adlayer was deposited in 0.1 M H_2SO_4 + 0.1 mM K_2PdCl_4 at 0 V. The Pd coverage (θ_{Pd}) varies from (a) 0.4, (b) 0.97 up to (c) 1.3 ML. The white dashed lines served as landmark to locate the monoatomic step edges of the Au terraces while black dashed lines highlight the rims of Pd islands. (a, b) 255 x 255 nm^2 and (c) 170 x 170 nm^2. (d,e,f) line scans at the bottom represent the cross-section along the white line in each figure. Numbers in image (c) refer to the Nth Pd atomic layer of the deposit.

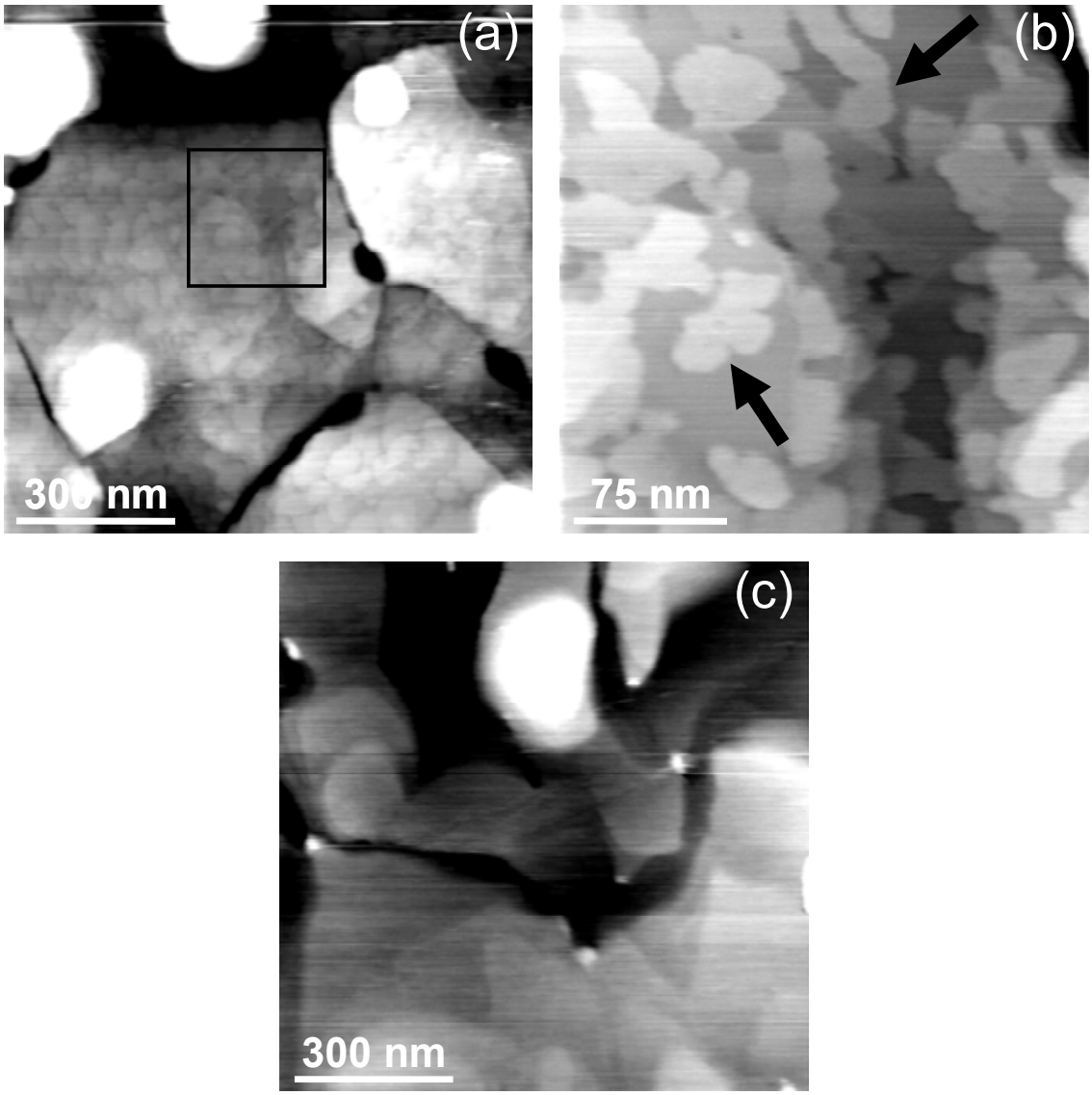

Figure 3.8: Ex situ AFM images showing the morphology of the Pd adlayer deposited on Au/mica in 0.1M H_2SO_4 + 0.1mM K_2PdCl_4 at 0 V for different deposition times. In images (a) and (c) (1000 x 1000 nm^2), the Pd coverage is equal to θ_{Pd} = 0.3 and θ_{Pd} = 1 respectively, while inset in (b) shows enlargement, marked by the black square, revealing the Pd islands deposited on the Au film surface (260 x 260 nm^2).

Finally, to illustrate the influence of the Pd salt on the island morphology, Fig. 3.9 shows a STM image of the Au(111) modified by 0.3 monolayer of Pd obtained by deposition in 0.1 M H_2SO_4 + 0.1 mM $PdSO_4$ at 0 V. It can be noticed that the morphology of the Pd islands clearly differs from the one found by using tetrachloropalladate(II) salt (compared Fig. 3.9 with Fig. 3.7a). In the present case, the islands have mainly nucleated on the Au terraces and exhibit a rounded shape with the presence of 2nd layer islands on top of them. Moreover, the island density is much higher than the one obtained by using K_2PdCl_4 and the average size is lower. As mentioned in Sec. 3.2.2, such variation in Pd island morphology could be explained by a higher

surface defect density, resulting from the lifting of the Au(111) reconstruction, when using $PdSO_4$ compared to the use of K_2PdCl_4 [35]. Hence, the present Pd/Au(111) morphology obtained with palladium sulphate salt ($PdSO_4$) yields much smaller Pd islands and is thus less suitable for studies of Chapter 4 than the one obtained with tetrachloropalladate(II) salt (K_2PdCl_4).

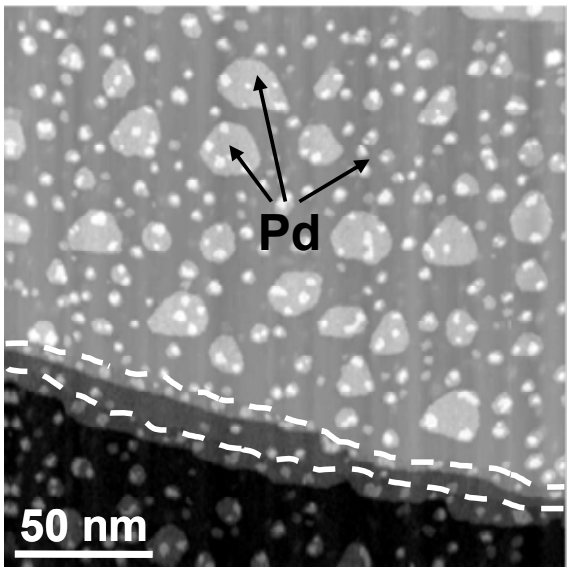

Figure 3.9: STM image (204 x 204 nm²) of the Au(111) single crystal modified by 0.3 monolayer of Pd. The Pd growth was performed in 0.1 M H_2SO_4 + 0.1 mM $PdSO_4$ at 0 V. Image was recorded in 0.1M K_2SO_4 + 1mM H_2SO_4 + 1mM KCl at -0.4 V.

3.2.3 Characterization of the Pd/Au(111) surface properties

Contrary to Au surface, it is well known that Pd surface exhibits strong affinity towards hydrogen species resulting in the existence of UPD of hydrogen [32]. The origin of such process is purely thermodynamic in the sense that, contrary to other transition metals, the electroadsorption of hydrogen species is energetically favorable on Pd [38]. This process is also known to occur on Pt, Rh, and Ir. In addition, Pd surface exhibit remarkable catalytic properties towards the hydrogen evolution reaction (HER), which takes place in the OPD range. Such electrocatalytic activity is expressed by a considerably smaller overpotential compared to the one on Au(111) electrode.

Since the electrodeposition of Ni and Co occurs in parallel to the hydrogen reduction process and in a potential range where UPD hydrogen layer is present on Pd, the present section will be devoted to characterize the adsorption of hydrogen on Pd monolayer by means of cyclic voltammetry and STM measurements.

a) Cyclic voltammetry

Fig. 3.10 shows the cyclic voltammograms recorded in the supporting electrolyte on bare (111)-textured Au/mica surface and on Pd(1ML)/Au/mica surface in a potential domain between -0.20 V and -0.80 V. The figure demonstrates that there is a significant difference between the two surfaces. For Pd(1ML)/Au (see solid curve), CV shows the characteristic peaks related to the interaction of palladium with hydrogen species present in the aqueous electrolyte, i.e. the UPD process. Indeed, the broad peaks, between -0.50 to -0.70 V, correspond either to the hydrogen adsorption process (C_{ads}) or to the H desorption (A_{des}). At slightly higher cathodic potential (< -0.70 V), the sharp decrease of the current density corresponds to the beginning of the hydrogen evolution reaction. There is no peak related to the H absorption process for the monolayer of Pd in agreement with results reported in the literature [32, 39]. In the case of Au(111) (see dashed curve), the shape of the cyclic voltammogram does not display such peaks.

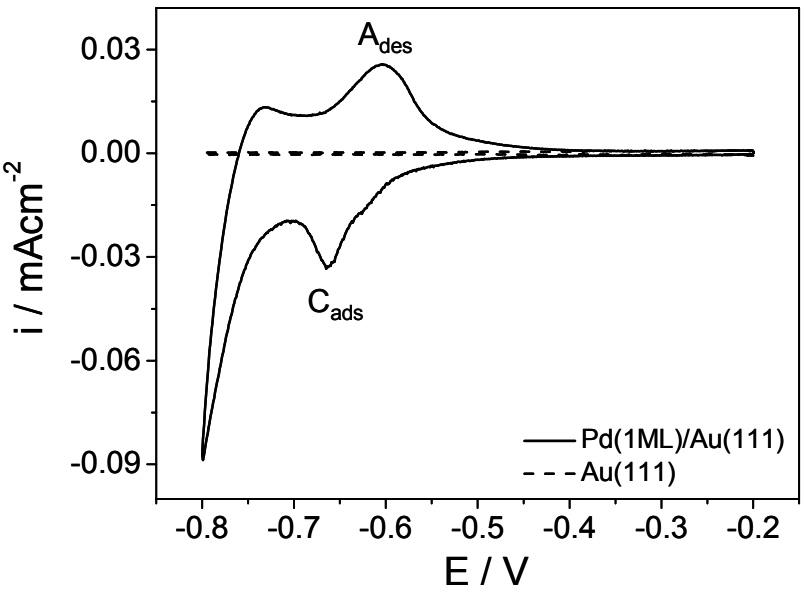

Figure 3.10: Cyclic voltammograms of Pd(1ML)/Au(111) (solid line) and bare Au(111) surface (dashed line) recorded in 0.1 M K_2SO_4 + 1 mM H_2SO_4 + 1 mM KCl. Scan rate: *sr* =10 $mV.s^{-1}$.

Integration of the cathodic peak (C_{ads}) was carried out between -0.50 V and -0.70 V with subtraction of the capacitive current assuming that capacitive current is independent of potential. We found a value roughly equal to 160 $\mu C.cm^{-2}$. This compares well with value of Baldauf and Kolb [32] (170 $\mu C.cm^{-2}$ for 1 ML).

b) STM

We also performed STM measurements between -0.40 V and -0.80 V to characterize the bimetallic Pd/Au(111) surface in this potential range. Fig. 3.11 displays the morphology of the same Pd islands polarized at U = -0.4 V (Fig. 3.11a) and at U = -0.8 V (Fig. 3.11b). According to the CV shown in Fig. 3.10, the Pd islands are H-free at -0.40 V while at -0.80 V, the Pd surface should be covered by a hydrogen layer. The aim of these experiments was to observe if any modification of the Pd island morphology occurred in the region where H is adsorbed.

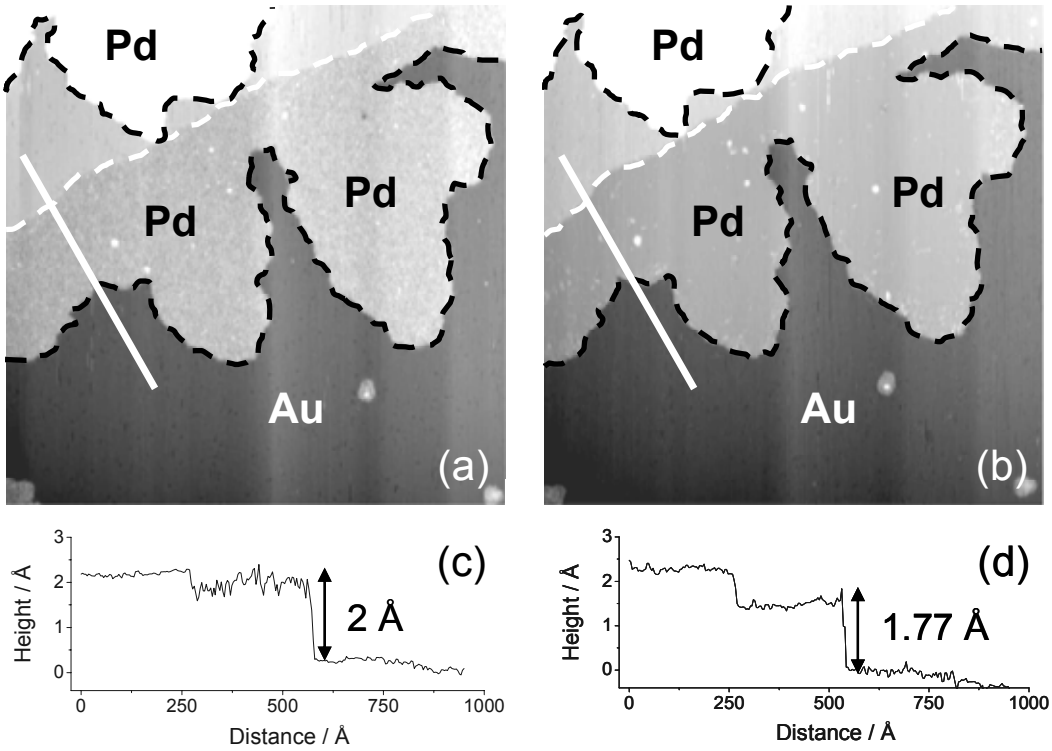

Figure 3.11: Series of STM images (124 x 124 nm^2) showing the variation of the Pd island height caused by the hydrogen adsorption. Images were recorded in 0.1M K_2SO_4 + 1mM H_2SO_4 + 1mM KCl at (a) -0.4 V and (b) -0.8 V. (c, d) line scans at the bottom represent the cross-section along the white line in each figure.

In Fig. 3.11a, it can be observed that the Pd surface is rougher than that of Au at U = -0.40 V. We could wonder whether this rough aspect is caused by the adsorption of residual $[PdCl_4]^{2-}$ anions (see Sec. 3.2.2). In order to check this hypothesis, we repeated the measurements by using Pd/Au(111) surface previously prepared in sulphate containing electrolyte i.e. in 0.1 M H_2SO_4 + 0.1 mM $PdSO_4$. As can be observed in Fig. 3.9 (Sec. 3.2.2), the surface of Pd islands displays the same rough appearance. Then by shifting the electrode potential to -0.8 V (Fig. 3.11b), it can be observed that the Pd islands apparent roughness

decreases and becomes similar to that of Au. Moreover, by comparing the profiles plotted in Figs. 3.11c and d, the Pd island height decreases of around 0.2 Å. Indeed, at U = -0.4 V, monoatomic thick Pd island is 1.99 ± 0.18 Å high while at U = -0.8 V, the height decreases to 1.77 ± 0.14 Å.

The difference in apparent roughness between Pd and Au may originate from anion adsorption. El-Aziz et al. [40] showed that the point of zero charge (pzc, see chapter 2 for definition) of Pd(1ML)/Au(111) is equal to -0.49 V while the one of Au(111) – (22 x √3) is -0.08 V, i.e. there is a shift in the pzc between Au(111) and Pd(1ML)/Au(111) of around 400 mV. Hence, it means that anions could be adsorbed on top of Pd islands at potentials where the Au is still reconstructed and bare of adsorbed species. Anions could be the ones contained in the electrolyte i.e. SO_4^{2-} or Cl^-. Changing K_2PdCl_4 by $PdSO_4$ allowed us to discard any adsorption of $\left[PdCl_4\right]^{2-}$ anions. Therefore, the existence of a rough appearance on top of the Pd islands compared to Au surface could be caused by the presence of adsorbed species on Pd. Then, the decrease of the apparent Pd step height could be linked to the anion desorption which is followed by the adsorption of hydrogen. However, the sharp decrease of the Pd island height (~ 0.2 Å) to a value much smaller than that estimated from geometric considerations suggests a strong change in the electronic properties of the Pd islands. Indeed, density functional theory (DFT) calculations showed that the presence of H layer adsorbed on Pd is expected to reduce the Pd density of states (DOS) near the Fermi level [41, 42].

3.3 Electrodeposition procedures of ultrathin alloy films

3.3.1 Introduction

Electrodeposition is a well-suited technique to deposit alloys and is widely employed in parallel to other deposition methods such as physical and chemical vapor deposition (PVC and CVD) [43]. The simplest preparation method is to electrodeposit simultaneously (i.e. co-deposit) the two alloy components which are both contained in a single electrolyte. Unfortunately, alloy electrodeposition is strongly dependent on a large number of experimental parameters such as metal-ion concentrations (bath composition), pH, deposition potential or current, anions, mass transport (stirring), which make difficult the reproducible and precise control of alloy composition and morphology in the ultrathin layer limit. Hence, changes in the experimental conditions may result in electrodeposits with different phase structures, even when they have the same chemical composition.

To be comprehensive, studies dealing with ultrathin alloy films require being able to control the thickness, the morphology and, especially, the surface stoichiometry. In this chapter, the procedure used to electrodeposit the Ni_xAu_{1-x} and Ni_xPd_{1-x} monolayer alloys is adapted from the one developed by Maroun and co-workers employed to grow Pd_xAu_{1-x} alloys on Au(111) in acidic media (0.1 M H_2SO_4) [44]. Their procedure involves (*i*) the use of a rotating disc electrode (RDE) to control the hydrodynamic conditions and establish a constant diffusion layer thickness δ near the electrode surface (steady-state regime), (*ii*) the co-deposition of both alloy components in a potential regime where the growth process is limited by the mass transport of the metal ions toward the surface (diffusion control) and (*iii*) the use of diluted solutions of the two metal salts to achieve low deposition rates increasing the adatom diffusion time to favor 2D morphology and to allow easy control of the alloy thickness. The general principle of their procedure is illustrated by Fig. 3.12a in the case of the deposition of an A_xB_{1-x} alloy where A could correspond to Au and B to Pd. The schemes in Fig. 3.12a show two linear sweep voltammograms (LV) in the RDE configuration corresponding to the reduction of two different redox species (note the existence of two different Nernst potentials $\phi_{Nernst}^{M_A}$ and $\phi_{Nernst}^{M_B}$). In the LVs, the variation of current density with electrode potential can be divided in three distinct regions. At low overpotentials, the current increases exponentially in agreement with the butler-volmer equation Then, as the overpotential increases, there is a transition region in which both electron transfer and mass transport rates play a role called mixed controlled region, before limiting-current region,

where only mass transport is rate determining. Thus, by choosing a sufficiently negative potential both metals can be deposited under mass transport limitations. In these conditions, the two partial metal deposition fluxes are potential independent and uniquely determined by the concentration of the metal species in solution (noted c_A or c_B), their (temperature-dependent) diffusion coefficients in the electrolyte (D_A or D_B), and the hydrodynamic conditions. The chemical composition of A_xB_{1-x} is given by $\frac{x}{1-x} \sim \frac{c_A D_A}{c_B D_B}$. Moreover, the metal ions or complexes in solution that arrive at the electrode surface are immediately discharged and redissolution back into the electrolyte is negligible (Fig. 3.12b). Thus, this deposition procedure allows one to get an accurate control of the composition and the amount of deposited material by simply adjusting the metal-ion concentrations and the deposition time. In diffusion-limited deposition at high overpotentials, the deposition process occurs under conditions far from equilibrium, which resembles the situation found for molecular beam epitaxy (MBE) growth under UHV conditions [45]. However in the electrochemical environment, the surface mobility of the deposited metal adatoms depends on the interface structure, which includes the presence of coadsorbed species (solvent molecules, anions), and on the surface charge.

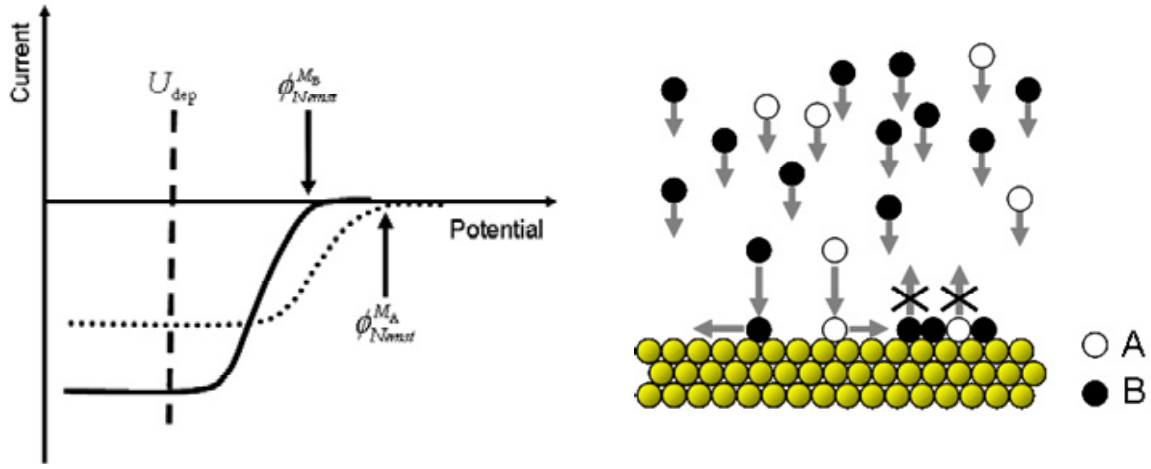

Figure 3.12: (a) Principle of deposition of an A_xB_{1-x} alloy (with predetermined composition) on a rotating disc electrode (RDE). This procedure was used by Maroun and coworkers [44] to electrodeposit ultrathin Pd_xAu_{1-x} alloy films. (b) At large negative overpotentials, the metal ions or complexes in solution that arrive at the electrode surface are immediately discharged and redissolution back into the electrolyte is negligible.

In the case of Ni-based alloys, several modifications to the Maroun's procedure had to be done. Concerning the rotating disc electrode (RDE), its use was excluded for two major reasons: (*i*) RDE's experimental set up requires the utilization of voluminous cell which is hardly compatible with the STM set up constraints, (*ii*) consequently the use of RDE for the growth step entails to transfer the sample, after depositing the thin films, into the STM cell for morphological investigations or into a separate cell for electrochemical measurements, which is excluded in the case of oxygen sensitive alloys such as Ni-based alloys. Fortunately, diffusion-limited electrodeposition had also been successively performed on static electrode in unstirred electrolyte [46, 47]. In totally quiescent solution, the diffusion layer in the vicinity of the surface should theoretically continue to grow with time after the beginning of the deposition process contrary to the case of stirred solution (achieved with a RDE for instance) for which the diffusion layer reaches a constant value (~ 10 μm for 2000 rpm). However, natural convection flows are always present in the electrochemical cell, even in quiescent solution, which leads ultimately to the establishment of a stable diffusion layer thickness around 100 μm. In addition, the use of diluted solutions of the two metal salts (≤ 200 μM) allowed us to decrease this initial transient period where the diffusion profile evolves in front of the surface before reaching a stable δ value and achieving a fixed deposition rate value. Hence, Fig. 3.13 shows the principle of our deposition procedure using a stationary electrode. The shape of LVs reflects the fact that the diffusion layer thickness varies after reaching the diffusion regime contrary to the case of LVs recorded on RDE explaining the current density decrease. Finally, the deposition method was elaborated considering the three following constraints. (*i*) The deposition potential U_{dep} has to be sufficiently negative in order to ensure that the growth process of the two components occurs under diffusion-controlled or at least that homogeneous nucleation is achieved. (*ii*) The deposition time t_{dep} must take into account that long deposition process at negative potential can modify pH in the near-surface region. (*iii*) After immersion into the deposition solution, the Au(111) substrate is covered by adsorbed chloro-complex of Pd and Au (i.e. $[PdCl_4]^{2-}$ and $[AuCl_4]^-$ anions). The procedure must take this experimental fact into consideration in order to avoid any influence of these adsorbed species on the initial stages of monolayer alloy growth.

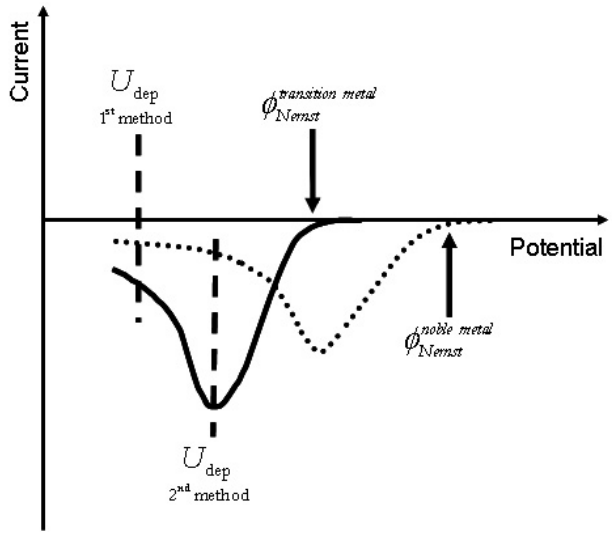

Figure 3.13: Principle of deposition of Ni-based monolayer alloys (Ni_xPd_{1-x} and Ni_xAu_{1-x}) on a stationary electrode. The Nernst potentials of, both, transition metal (i.e. Ni) and noble metals (Au and Pd) were positioned arbitrarily along the potential axis but their respective location reflects the existence of a large difference between them. Two different methods have been used to electrodeposit Ni-based monolayer alloys.

In this work, the deposition of Ni-based alloy films (NiPd and NiAu) on Au(111) single crystal has been carried out directly into the STM cell, which corresponds to a small volume cell (~ 300 µl) made of Teflon. The supporting electrolyte (SE) was 0.1 M K_2SO_4 + 1 mM H_2SO_4 + 1 mM KCl, similar to the one used in Chapter 4. The pH value of the deposition solution is equal to 3 which should prevent any Ni hydroxide formation during the growth or the dissolution processes [48]. Two different methods have been used to electrodeposit Ni-based alloy films.

3.3.2 The 1st deposition procedure

In the first one, deposition was done in highly diluted solutions i.e. in SE + x µM $NiSO_4$ + y µM K_2PdCl_4 (resp. $HAuCl_4$) for different ratio x/y and with the sum (x + y) ranging from 3 to 10 µM, at negative deposition potential (U_{dep} = -1.5 V), and for long deposition time (t_{dep} = 30 min). In these conditions, the corresponding deposition rate is around 0.03 - 0.05 ML.min^{-1}. The freshly prepared, flame-annealed Au(111) surface was immersed into the supporting electrolyte at -0.6 V. Then, the electrode potential is shifted to -1.5 V and a drop of 10 µl containing the metallic anions is added. At the end of the deposition time, the potential is stepped from U_{dep} to a stabilization potential (U_{stab}) (see Sec. 4.2) at which the Ni deposition process is stopped and no dissolution occurs. In parallel, the noble metal deposition is stopped by exchanging rapidly the alloy-containing electrolyte with the supporting electrolyte. These growth conditions present the

advantages that (*i*) the deposition occurs in diffusion-limited regime as schematized in Fig. 3.13, (*ii*) exclude any influence of chloro-complex adsorption process on the growth and the final stoichiometry and (*iii*) that the ultrathin alloy film thickness is well controlled. However, long deposition time at large negative U_{dep}, at which the hydrogen evolution reaction (HER) rate is high, could involve a rise of pH in the near-surface region and eventually lead to the formation of Ni hydroxides [49]. Indeed, in such experimental conditions, the Ni deposit morphology exhibits a less defined moiré pattern (not shown) and a lower island height (ranging from 1 to 1.3 Å). Hence, due to this major restriction, the use of this procedure has been restricted to the case of Au-rich NiAu (low Ni content) since Pd is well known to catalyze the HER.

3.3.3 The 2nd deposition procedure

The second deposition method allowed us to overcome the as-cited difficulties. The concentration of metallic anions has been increased to get higher deposition rates and, therefore, lower t_{dep}. In addition, U_{dep} has been shifted toward more positive value to limit the HER generation and the probable modification of pH. Finally, the potential sequence has been adapted to this new set of parameters. Indeed, the alloy growth has been performed in the supporting electrolyte (SE) which contains x mM $NiSO_4$ + y mM K_2PdCl_4 (resp. $HAuCl_4$) with x = 0.125 mM and y = 0.01, 0.02, 0.035, 0.05 mM. The chosen deposition potential is equal to U_{dep} = -1.24 V which is significantly negative of the Nernst potentials of the three redox couples considered here but less than in the first method. Typical deposition time ranges from 80 to 120 s corresponding to deposition rates of approximately 0.5 to 1 ML.min^{-1} which are much higher than the one obtained with the previous procedure. The freshly prepared, flame-annealed Au(111) surface was immersed into the solution at an appropriate potential, called "rest" potential, which depends on the nature of the noble component contained in the electrolyte. The rest potential was set to +0.30 V for NiPd containing electrolyte and +0.45 V for the NiAu one. At these rest potentials, the alloy deposition process does not yet occur (more positive than their respective Nernst potentials) and any surface oxidation of the substrate is prevented. Indeed, in standard conditions, the $Au/[AuCl_4]^-$ Nernst potential is equal to 0.3 V while the one of $Pd/[PdCl_4]^{2-}$ is equal to 0 V. Contrary to Ni^{2+} cations, $[PdCl_4]^{2-}$ and $[AuCl_4]^-$ anions are adsorbed on Au(111) when polarized at their respective rest potentials [28]. Hence, Pd and Au deposition first occurs via the reductive discharge of the Pd or Au tetrachloro complex. So, in

order to avoid any influence of these adsorbed species on the initial stages of monolayer alloy growth, the potential step program showed in Fig. 3.14 was used.

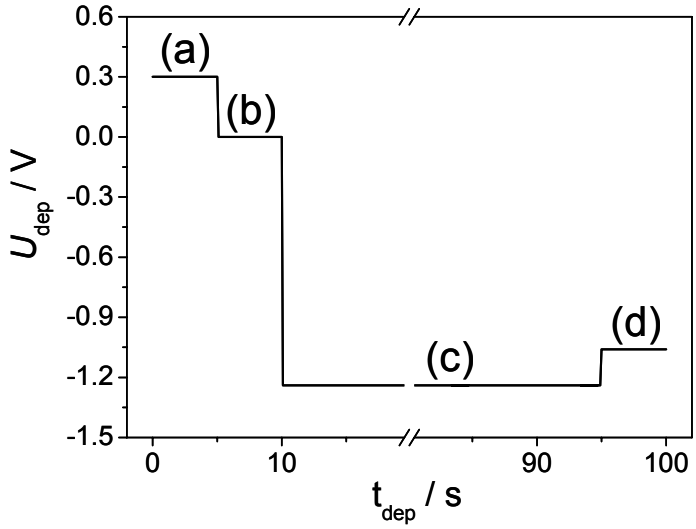

Figure 3.14: Potential step program used to deposit the Ni-based alloys (NiPd and NiAu).

Fig. 3.15 gives simplified illustrations of the surface processes associated with the potential step program used to electrodeposit NiPd alloys. Similar one could have been made for the deposition of NiAu alloys by changing $[PdCl_4]^{2-}$ for $[AuCl_4]^{-}$. In Fig. 3.15a, the Au(111) substrate is polarized at its rest potential and covered by a $[PdCl_4]^{2-}$ layer of which the surface coverage ($\theta_{[PdCl_4]^{2-}}$) depends on the K_2PdCl_4 concentration initially contained in the electrolyte. Then, a potential step was first applied to 0 V (see Fig. 3.14), where the Au(111) surface is still unreconstructed [4], for a short period of time (around 3-5 s) to discharge the Pd chloro complex. At 0 V, the growth morphology for Pd corresponds to a layer-by-layer growth [28, 47]. At the end of this sequence at 0 V (Fig. 3.15b), the Au(111) substrate is decorated by a small amount of Pd islands which have nucleated along the Au step edges and on the terraces i.e. correspond to a bimetallic Pd/Au(111) substrate similar to the ones displayed in Sec. 3.2. In the STM images presented in Chapter 5, the Pd monoatomic thick islands deposited on Au(111) originating from this stage of the procedure are clearly identified and usually surrounded with dashed lines of white or black color depending on the image contrast. In the case of NiAu alloys, the Au chloro complex discharge either simply modified the width of the Au terraces when nucleating at step edges or created monoatomic islands on terraces which are easily discernable and also surrounded by dashed line for clarity. Second, the potential was stepped from 0 V to

U_{dep} = -1.24 V at which the alloy growth will take place during different periods of time (t_{dep}) depending on the metal-ion concentration and on the expected thickness (Fig. 3.15c).

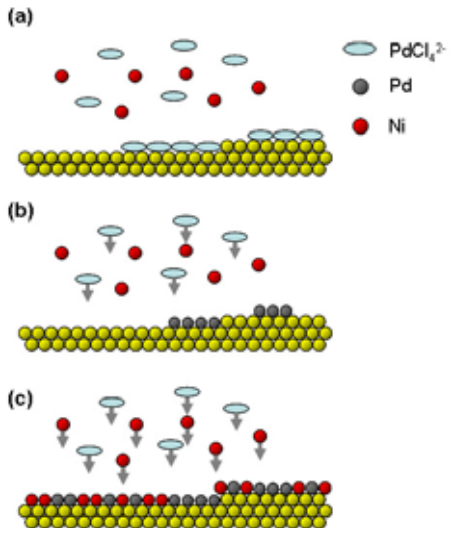

Figure 3.15: Illustration of the surface processes linked with the potential step program of Fig. 3.14 to deposit NiPd monolayer alloys. (a) The Au(111) surface is polarized at the rest potential at which $[PdCl_4]^{2-}$ anions are adsorbed. (b) Discharge of the Pd chloro complex at 0 V. (c) Alloy codeposition at U_{dep}.

At the end of t_{dep}, the deposition process is stopped by using the same procedure than the one employed in the first method: the potential is stepped from U_{dep} to a stabilization potential (U_{stab}) at which the Ni adatoms are stable while, in parallel, the noble metal deposition is stopped by diluting rapidly the alloy-containing electrolyte with the supporting electrolyte. The 2nd method presents a main drawback since both metals are not deposited under mass transport limitations at U_{dep} = -1.24 V. Indeed, the growth process of Ni does not occur under full diffusion controlled but rather in mixed controlled regime (kinetics + diffusion). Hence, the composition of the alloy film is no longer proportional to the respective concentration of Ni and Pd or Au. This difficulty is easily overcome considering that the respective compositions of ultrathin alloys can be determined by quantifying, from STM images, the noble metal surface coverage (wrote θ_M with M = Pd or Au) left on the Au(111) surface after selective dissolution of the Ni adatoms.

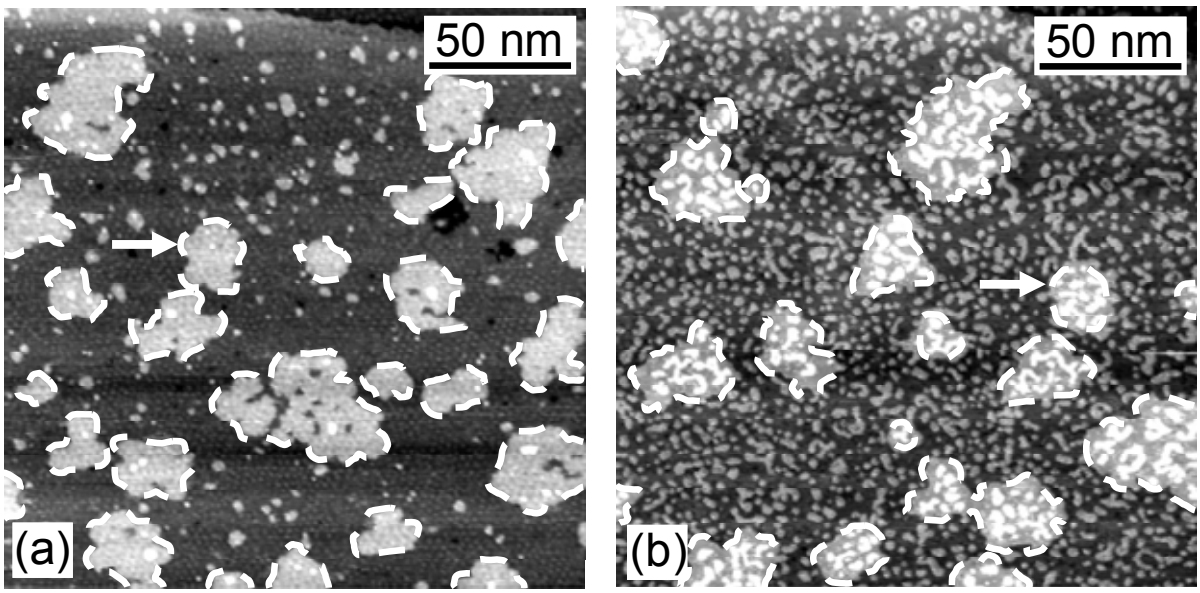

Figure 3.16: STM images (204 x 204 nm^2) showing (a) the morphology of NiPd ultrathin film obtained by using the 2nd deposition procedure and (b) the same surface area after selective dissolution of Ni. The remaining islands left on the bimetallic PdAu surface are composed of Pd. By quantifying the Pd surface coverage (wrote θ_{Pd}) in the STM image, the alloy monolayer composition can be determined. White dashed lines are used as a landmark to localize Pd islands electrodeposited during the 1st step of the alloy electrodeposition and white arrows point to the same position on the surface.

For instance, Fig. 3.16 shows the morphology of a NiPd monolayer alloy electrodeposited using the 2nd procedure before (Fig. 3.16a) and after (Fig. 3.16b) the selective dissolution of Ni. Pd alloy content can thus be estimated from Pd coverage in Fig. 3.16b (large islands excluded) and from alloy coverage in Fig. 3.16a. By increasing the concentration of K_2PdCl_4 contained in the deposition electrolyte, it can be observed in Fig. 3.17 that the Pd coverage on the Au(111) surface after the selective dissolution of Ni may be estimated allowing precise determination of the alloy composition. According to Fig. 3.18, Pd coverage increases linearly with the concentration of K_2PdCl_4. Similar results were obtained in case of NiAu ultrathin alloys.

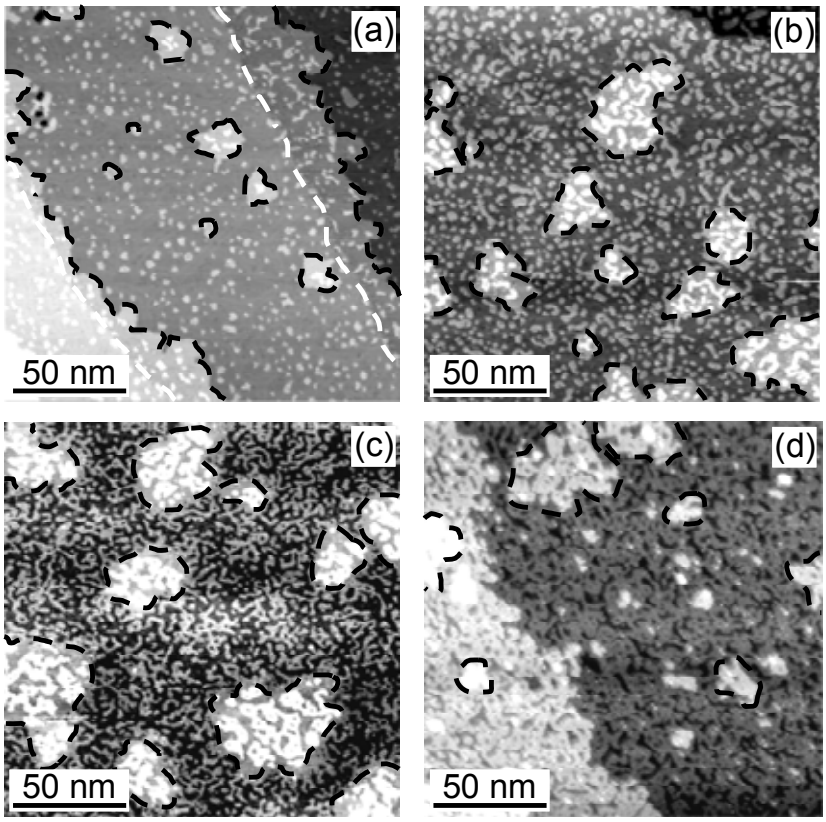

Figure 3.17: STM images (175 x 175 nm^2) showing the increase in the Pd coverage (θ_{Pd}), that remains on the Au(111) surface after the selective dissolution of Ni, by increasing the concentration of K_2PdCl_4 contained in the deposition electrolyte. The ultrathin NiPd alloys were deposited at U_{dep} = -1.24 V in 0.1 M K_2SO_4 + 1 mM H_2SO_4 + 1 mM KCl + 0.125 mM $NiSO_4$ which contains (a) 0.01 mM, (b) 0.02 mM, (c) 0.035 mM and (d) 0.05 mM of K_2PdCl_4. In each case, the deposition time (t_{dep}) was adjusted to obtain a coverage close to 1.

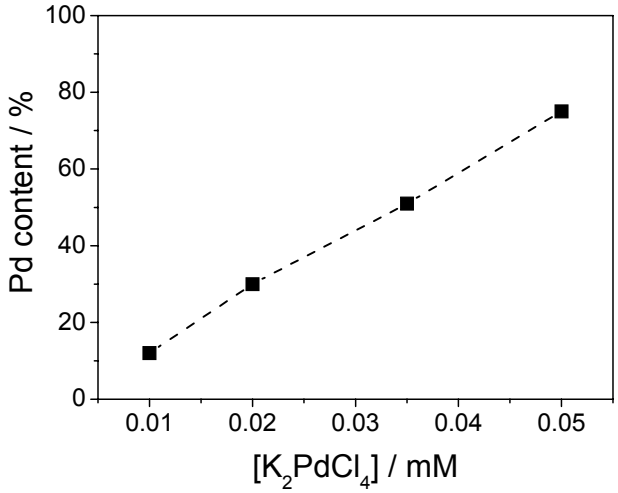

Figure 3.18: Dependence of the Pd content within the Ni_xPd_{1-x} ultrathin alloy film deposited at -1.24 V as a function of the concentration in K_2PdCl_4 contained in the deposition electrolyte

References

1. Clavilier, J., Faure, R., Guinet, G., and Durand, R., Journal of Electroanalytical Chemistry, 1980. **107**: p. 205.
2. Barth, J.V., Brune, H., Ertl, G., and Behm, R.J., *Scanning tunneling microscopy observations on the reconstructed Au(111) surface: Atomic structure, long-range superstructure, rotational domains, and surface defects.* Physical Review B, 1990. **42**: p. 9307-9318.
3. Wang, J., Ocko, B.M., Davenport, A.J., and Isaacs, H.S., *In situ X-ray-diffraction and -reflectivity studies of the Au(111)/ electrolyte interface: reconstruction and anion adsorption.* Physical Review B, 1992. **46**: p. 10321-10338.
4. Kolb, D.M., *Reconstruction phenomena at metal-electrolyte interfaces.* Progress in Surface Science, 1996. **51**(2): p. 109-173.
5. Wöll, C., Chiang, S., Wilson, R.J., and Lippel, P.H., *Determination of atom positions at stacking-fault dislocations on Au(111) by scanning tunneling microscopy* Physical Review B, 1989. **39**: p. 7988-7991.
6. Chambliss, D.D., Wilson, R.J., and Chiang, S., *Nucleation of ordered Ni island arrays on Au(111) by surface-lattice dislocations.* Physical Review Letters, 1991. **66**(13): p. 1721-1724.
7. Abernathy, D.L., Gibbs, D., Grübel, G., Huang, K.G., Mochrie, S.G.J., Sandy, A.R., and Zehner, D.M., *Reconstruction of the (111) and (001) surfaces of Au and Pt: thermal behavior.* Surface Science, 1993. **283**: p. 260-276.
8. Gao, X., Hamelin, A., and Weaver, M.J., *Atomic relaxation at ordered electrochemical surfaces probed by scanning tunneling microscopy: Au(111) in aqueous solution compared with ultrahigh-vacuum environments.* Journal of Chemical Physics, 1991. **95**: p. 6993-6996.
9. Tao, N.J. and Lindsay, S.M., *Kinetics of a potential induced 23x√3 to 1x1 transition of Au(111) studied by in situ scanning tunneling microscopy.* Surface Science, 1992. **274**: p. L546-L553.
10. Wang, J., Davenport, A.J., Isaacs, H.S., and Ocko, B.M., *Surface charge-induced ordering of the Au(111) surface.* Science, 1991. **255**: p. 1416-1418.
11. Chambliss, D.D., Wilson, R.J., and Chiang, S., *Ordered nucleation of Ni and Au islands on Au(111) studied by scanning tunneling microscopy.* Journal of Vacuum Science and Technology B, 1991. **9**(2): p. 933-937.
12. Strbac, S., Magnussen, O.M., and Behm, R.J., *Nanoscale pattern formation during electrodeposition: Ru on reconstructed Au(111).* Physical Review Letters, 1999. **83**: p. 3246-3249.

13. Möller, F., Magnussen, O.M., and Behm, R.J., *Overpotential-controlled nucleation of Ni island arrays on reconstructed Au(111) electrode surfaces.* Physical Review Letters, 1996. **77**: p. 5249-5252.
14. Takakusagi, S., Kitamura, K., and Uosaki, K., *In situ real-time monitoring of electrochemical Ag Deposition on a reconstructed Au(111) surface studied by scanning tunneling microscopy* Journal of Physical Chemistry C, 2008. **112**: p. 3071-3077.
15. Allongue, P. and Maroun, F., *Self-ordered electrochemical growth on single-crystal electrode surfaces.* Journal of Physics: Condensed Matter, 2006. **18**(13): p. S97-S114.
16. Magnussen, O.M., *In-situ Rastertunnelmikroskop-Untersuchungen zu Rekonstruktion, Anionenadsorption und Unterpotentialabscheidung auf Gold-Elektroden.* 1993, University Ulm.
17. Magnussen, O.M., Hageböck, J., Hotlos, J., and Behm, R.J., *In situ scanning tunnelling microscopy observations of a disorder-order phase transition in hydrogensulfate adlayers on Au(111).* Faraday Discussions, 1992. **94**: p. 329-338.
18. Wu, S., Lipkowski, J., Magnussen, O.M., Ocko, B.M., and Wandlowski, T., *The driving force for (px√3) <=>(1x1) phase transition of Au(111) in the presence of organic adsorption - a combined chronocoulometric and surface x-ray scattering study.* Journal of Electroanalytical Chemistry, 1998. **446**: p. 67-77.
19. Kolb, D.M. and Schneider, J., *Surface reconstruction in electrochemistry: Au(100)-(5x20), Au(111)-(1x23) and Au(110)-(1x2).* Electrochimica Acta, 1986. **31**: p. 929-936.
20. Waibel, H.F., Kleinert, M., Kibler, L.A., and Kolb, D.M., *Initial stages of Pt deposition on Au(111) and Au(100).* Electrochimica Acta, 2002. **47**(9): p. 1461-1467.
21. Uosaki, K., Ye, S., Naohara, H., Oda, Y., Haba, T., and Kondo, T., *Electrochemical epitaxial growth of a Pt(111) phase on an Au(111) electrode.* Journal of the Physical Chemistry B, 1997. **101**(38): p. 7566.
22. Strbac, S., Maroun, F., Magnussen, O.M., and Behm, R.J., *The structure, growth and reactivity of electrodeposited Ru/Au(111) surfaces.* Journal of Electroanalytical Chemistry, 2001. **500**(1-2): p. 479-490.
23. Kibler, L.A., Kleinert, M., and Kolb, D.M., *The initial stages of rhodium deposition on Au(111).* Journal of Electroanalytical Chemistry, 1999. **467**: p. 249-257.
24. Esplandiu, M.J., Schneeweiss, M.A., and Kolb, D.M., *An in situ scanning tunneling microscopy study of Ag electrodeposition on Au(111)* Physical Chemistry Chemical Physics, 1999. **1**: p. 4847-4854.
25. Ogaki, K. and Itaya, K., *In situ scanning tunneling microscopy of underpotential and bulk deposition of silver on gold(111).* Electrochimica Acta, 1995. **40**(10): p. 1249-1257.

26. Maroun, F., Morin, S., Lachenwitzer, A., Magnussen, O.M., and Behm, R.J., *Admetal-induced substrate restructuring during metal-on-metal electrochemical deposition studied by in situ scanning tunneling microscopy.* Surface Science, 2000. **460**: p. 249-263.
27. Lachenwitzer, A., Morin, S., Magnussen, O.M., and Behm, R.J., *In situ STM study of electrodeposition and anodic dissolution of Ni on Ag(111).* Physical Chemistry Chemical Physics, 2001. **3**(16): p. 3351-3363.
28. Kibler, L.A., Kleinert, M., Randler, R., and Kolb, D.M., *Initial stages of Pd deposition on Au(hkl) part I: Pd on Au(111).* Surface Science, 1999. **443**: p. 19-30.
29. Naohara, H., Ye, S., and Uosaki, K., *Electrochemical layer-by-layer growth of palladium on an Au(111) electrode surface: Evidence for important role of adsorbed Pd complex.* Journal of the Physical Chemistry B, 1998. **102**(22): p. 4366-4373.
30. Takahasi, M., Hayashi, Y., Mizuki, J., Tamura, K., Kondo, T., Naohara, H., and Uosaki, K., *Pseudomorphic growth of Pd monolayer on Au(111) electrode surface.* Surface Science, 2000. **461**(1-3): p. 213-218.
31. Koel, B.E., Sellidj, A., and Paffett, M.T., *Ultrathin fillms of Pd on Au(111): Evidence for surface alloy formation.* Physical Review B, 1992. **46**(12): p. 7846.
32. Baldauf, M. and Kolb, D.M., *A hydrogen adsorption and absorption study with ultrathin Pd overlayers on Au(111) and Au(100).* Electrochimica Acta, 1993. **38**(15): p. 2145-2153.
33. Naohara, H., Ye, S., and Uosaki, K., *Electrochemical deposition of palladium on an Au(111) electrode: effects of adsorbed hydrogen for a growth mode.* Colloids and Surfaces A: Physicochemical and Engineering Aspects, 1999. **154**: p. 201-208.
34. Quayum, M.E., Ye, S., and Uosaki, K., *Mechanism for nucleation and growth of electrochemical palladium deposition on an Au(111) electrode.* Journal of Electroanalytical Chemistry, 2002. **520**(1-2): p. 126-132.
35. Tang, J., Petri, M., Kibler, L.A., and Kolb, D.M., *Pd deposition onto Au(111) electrodes from sulphuric acid solution.* Electrochimica Acta, 2005. **51**: p. 125-132.
36. Kontje, C., Kibler, L.A., and Kolb, D.M., *Pd deposition onto Au(111) from nitrate solution.* Electrochimica Acta, 2009. **54**: p. 3830-3834.
37. Nichols, R.J., Magnussen, O.M., Hotlos, J., Twomey, T., Behm, R.J., and Kolb, D.M., *An in-situ STM study of potential-induced changes in the surface topography of Au(100) electrodes.* Journal of Electroanalytical Chemistry, 1990. **290**: p. 21-31.
38. Jerkiewicz, G., *Hydrogen sorption at/in electrodes.* Progress in Surface Science, 1998. **57**: p. 137-186.

39. Kibler, L.A., El Aziz, A.M., and Kolb, D.M., *Electrochemical behaviour of pseudomorphic overlayers: Pd on Au(111)*. Journal of Molecular Catalysis A: Chemical, 2003. **199**: p. 57-63.
40. El-Aziz, A.M., Kibler, L.A., and Kolb, D.M., *The potentials of zero charge of Pd(1 1 1) and thin Pd overlayers on Au(1 1 1)*. Electrochemistry Communications, 2002. **4**(7): p. 535-539.
41. Paul, J.F. and Sautet, P., *Density-functional periodic study of the adsorption of hydrogen on a palladium (111) surface*. Physical Review B, 1996. **53**(12): p. 8015.
42. Dong, W., Ledentu, V., Sautet, P., Eichler, A., and Hafner, J., *Hydrogen adsorption on palladium: a comparative theoretical study of different surfaces*. Surface Science, 1998. **411**(1-2): p. 123-136.
43. Osaka, T., Takai, M., Hayashi, K., Ohashi, K., Saito, M., and Yamada, K., *A soft magnetic CoNiFe film with high saturation magnetic flux density and low coercivity*. Nature, 1998. **392**: p. 796
44. Maroun, F., Ozanam, F., Magnussen, O.M., and Behm, R.J., *The role of atomic ensembles in the reactivity of bimetallic electrocatalysts*. Science, 2001. **293**(5536): p. 1811-1814.
45. Michely, T. and Krug, J., *Islands, Mounds, and Adatoms: Patterns and Processes in Crystal Growth Far from Equilibrium*. 2004, Berlin: Springer.
46. Sibert, E., Ozanam, F., Maroun, F., Behm, R.J., and Magnussen, O.M., *Diffusion-limited electrodeposition of ultrathin Au films on Pt(1 1 1)*. Surface Science, 2004. **572**(1): p. 115-125.
47. Krug, K., Stettner, J., and Magnussen, O.M., *In Situ Surface X-Ray Diffraction Studies of Homoepitaxial Electrochemical Growth on Au(100)*. Physical Review Letters, 2006. **96**(24): p. 246101-4.
48. Pourbaix, M., *Atlas of electrochemical equilibria in aqueous solutions*. Atlas of electrochemical equilibria in aqueous solutions. 1966, London: Pergammon Press. 387.
49. Ji, J., Cooper, W.C., Dreisinger, D.B., and Peters, E., *Surface pH measurements during nickel electrodeposition*. Jounal of Applied Electrochemistry, 1995. **25**: p. 642-650.

Chapter 4

Electrochemical Growth and Dissolution of Ni and Co on Bimetallic Pd/Au(111) Substrates

4.1 Introduction

The electrodeposition of metals on metallic substrates has been widely studied by in situ techniques, especially in the last two decades by scanning probe microscopy, in particular STM [1-3]. The aim of such investigations is to determine the morphology of a deposit, less than a few monolayers thick, as a function of different experimental conditions as: the substrate nature, its crystallographic orientation, the presence of defects on its surface like steps, the deposition potential, the presence of adsorbates, etc… The correlation of the deposit morphology with these parameters gave tremendous insight into the atomic processes governing the nucleation and growth in electrochemical conditions. One of the most studied parameter is the deposition potential. The case of Ni growth on Au(111) as a function of the deposition potential is almost an academic example, where three different morphologies may be obtained [4]: at *low* overpotential, Ni nucleation takes place preferentially on the elbows of the Au(111) reconstruction followed by the growth of monolayer thick islands; at *medium* overpotential, deposited Ni islands are monolayer thick and have a needlelike shape with a define width; at *high* overpotential, bi-dimensional growth of a Ni monolayer is observed. In this case, such morphological zoology appears richer than the one observed for the same system in ultra high vacuum (UHV) [5].

Among the electrochemical growth studies as a function of the deposition potentials, those where underpotential deposition (UPD) is involved have attracted a lot of attention [6]. In a UPD process, metal deposition takes place at a potential more positive than the Nernst potential (or equilibrium potential), whereas, in the absence of UPD, potentials more negative than the Nernst potential are necessary for the deposition. A UPD process is generally limited to the deposition of one monolayer. Its driving force is (*i*) a substrate surface energy larger than the deposit one, and (*ii*) a large interaction energy between the deposit and the substrate. In this case, the system energy is minimized when the substrate is completely covered by one (sometimes more) deposit monolayer. However, this description is rather simplified, because anions co-

adsorption is often involved in UPD process, as it is the case of Cu UPD on Au [7]. From the theoretical point of view, calculations have been performed to predict the system where UPD is present and to estimate the UPD onset potential [8]. This study uses a thermodynamic cycle where the difference between the Nernst potential and the UPD potential is directly related to different energies of the system and among them the deposit/substrate interaction (binding) energy. The latter energy is of fundamental interest because it plays a key role in a deposit morphology [9].

The determination of binding energies in the UHV environment, is usually done by thermal desorption spectroscopy (TDS) [10]. However, this technique is restricted to the use of heteroepitaxial systems that do not form bulk or surface alloys before reaching the desorption temperature. This condition is only achieved by using refractory metal substrates such as Ta, Mo, Ru, Re and W [11]. Calorimetry allows measuring binding energies, but its application to metal on metal epitaxy remains challenging [12]. It is therefore highly desirable to have a direct access to binding energies of metal adatoms on metallic substrates at room temperature. As explained above, in the electrochemical environment, binding energies may be obtained if a UPD process is present, because the difference between the Nernst potential and the UPD potential is in principle easy to measure precisely. However, in the absence of a UPD process, information on the deposit/substrate interactions has never been reported.

In this chapter, we study the influence of the substrate chemical nature on the heteroepitaxial deposition/dissolution reactions in the absence of UPD process. For this purpose, we prepare bimetallic Pd/Au(111) surface, which consists of a Au(111) substrate modified by monoatomic Pd overlayers of various coverage ranging from half a monolayer up to a full monolayer, and compare the deposition and dissolution of ultrathin films of nickel (Ni) and cobalt (Co) on these two surfaces. First, the electrochemical behavior of Ni and Co on *monometallic* Pd(1ML)/Au(111) will be characterized by cyclic voltammetry and compared to the one on Au(111). In addition, the deposition kinetics of Ni and Co on these two monometallic substrates will be determined. Second, we will investigate by in situ STM the deposition/dissolution morphology of Ni on *bimetallic* Pd/Au(111) surface, which allows us to compare directly these processes on two different surfaces. We will show that significant differences are present and correlate them to the difference in Ni-Pd and Ni-Au binding energies.

4.2 Electrochemical study of Ni and Co deposition and dissolution on Au(111) and Pd(1ML)/Au(111)

4.2.1 Cyclic voltammetry

Cyclic voltammetry was used to characterize the electrodeposition of Ni and Co on *monometallic* Au(111) and on Pd(1ML)/Au(111), separately. As mentioned above in Sec. 3.2, the electrodeposition properties of Pd onto unreconstructed Au(111) enable us to cover the Au substrate with a complete Pd monolayer [13]. In this study, Pd(1ML)/Au(111) surface is used as substitute of a Pd(111) single crystal. Even if the electronic structure of Pd(1ML)/Au(111) is different from the one of Pd(111) (see discussion in Sec. 4.5), a pseudomorphic Pd monolayer on Au(111) exhibits cyclic voltammograms for the UPD of H and Cu [14, 15], which are very similar to those of Pd(111) [16]. Figs. 4.1 and 4.2 shows the typical cyclic voltammograms (*i-U* curves) of Au(111) and Pd(1ML)/Au(111) substrates recorded at the scan rate of 50 $mV.s^{-1}$ in the supporting electrolyte, abbreviated SE, of composition 0.1 M K_2SO_4 + 1 mM H_2SO_4 + 1 mM KCl (dashed lines) and in the Co^{2+} or Ni^{2+} containing electrolytes (1 mM $CoSO_4$ or $NiSO_4$ were added, solid lines).

In the absence of metallic cations, the electrochemical responses of Au(111) and Pd(1ML)/Au(111) are clearly different. In the case of Au(111) (see Figs. 4.1a and 4.2a), the shape of the cyclic voltammogram (CV) displays only a single reduction peak (C_1) at -1.24 V, which corresponds to the hydrogen evolution reaction (HER). For Pd(1ML)/Au(111) (see Figs. 4.1b and 4.2b), the CV presents a more complex shape (see Sec. 3.2.3) with different waves of current corresponding to the following processes:

* The cathodic current measured for -0.85 V < *U* < -0.65 V is assigned to hydrogen adsorption (peak C_{ads}),

* The hydrogen evolution reaction for *U* < -0.90 V with a peak at -1.09 V (C_1). Notice that this peak is shifted by ~ 100 mV with respect to the one measured on the Au(111) electrode due to the catalytic properties of Pd towards the proton reduction.

* The oxidation of molecular dihydrogen (peak A_1) and hydrogen desorption (-0.7 to -0.35 V, A_{des}) on the return sweep of potential towards positive values.

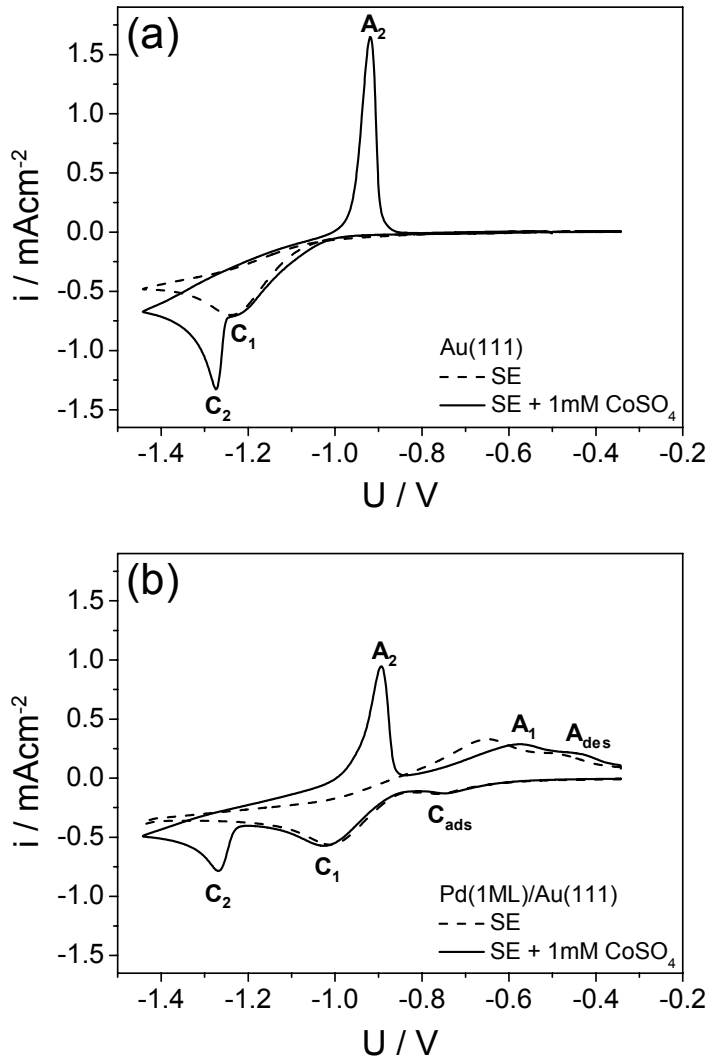

Figure 4.1: Cyclic voltammograms recorded in the supporting electrolyte (SE), 0.1 M K_2SO_4 + 1 mM H_2SO_4 + 1 mM KCl (pH 3), without (dashed line) and with (solid line) 1 mM $CoSO_4$ on (a) Au(111) and (b) Pd(1ML)/Au(111). Scan rate: sr = 50 mV.s^{-1}.

In the Co solution (Figs. 4.1a and 4.1b), supplementary peaks are observed on both surfaces. In the cathodic potential sweep, the presence of Co^{2+} in the solution alters neither the hydrogen adsorption process on Pd(1ML)/Au(111) nor the HER on both surfaces. Then, a new pronounced peak (C_2) is observed at -1.27 V on Au(111) as well as on Pd(1ML)/Au(111). CV measurements performed at lower scan rate (sr = 10 mV.s^{-1}, not shown) reveal that the peak is positioned at -1.24 V on both surfaces, which corresponds to an overpotential η = 240 mV with respect to the calculated Co^{2+}/Co Nernst potential (-1.00 V for 1 mM Co^{2+}). The absence of this peak in the Co-free solution clearly demonstrates that it is related to the cobalt deposition process. In the anodic sweep, cobalt stripping peak (A_2) is observed at -0.92 V on Au(111) (Fig. 4.1a) and at -0.90 V on Pd(1ML)/Au(111) (Fig. 4.1b). Peaks A_1 and A_{des} are slightly shifted

towards positive potentials, which could be caused either by the modification of the dihydrogen production at high negative potentials that occurs in parallel with the Co deposition process or by the influence of the Co dissolution reaction on the H_2 oxidation and hydrogen desorption processes. It may also be noticed that the anodic charge under the dissolution peak (noted $Q_{Dissolution}^{M/S}$ with M = Co or Ni and S = Au(111) or Pd(1ML)/Au(111)) is larger on Au(111) ($Q_{Dissolution}^{Co/Au(111)}$ = 1.29 mC.cm^{-2}) than on Pd(1ML)/Au(111) ($Q_{Dissolution}^{Co/Pd(1ML)/Au(111)}$ = 1.11 mC.cm^{-2}) although the same cathodic potential sweep was applied. This point will be commented later on.

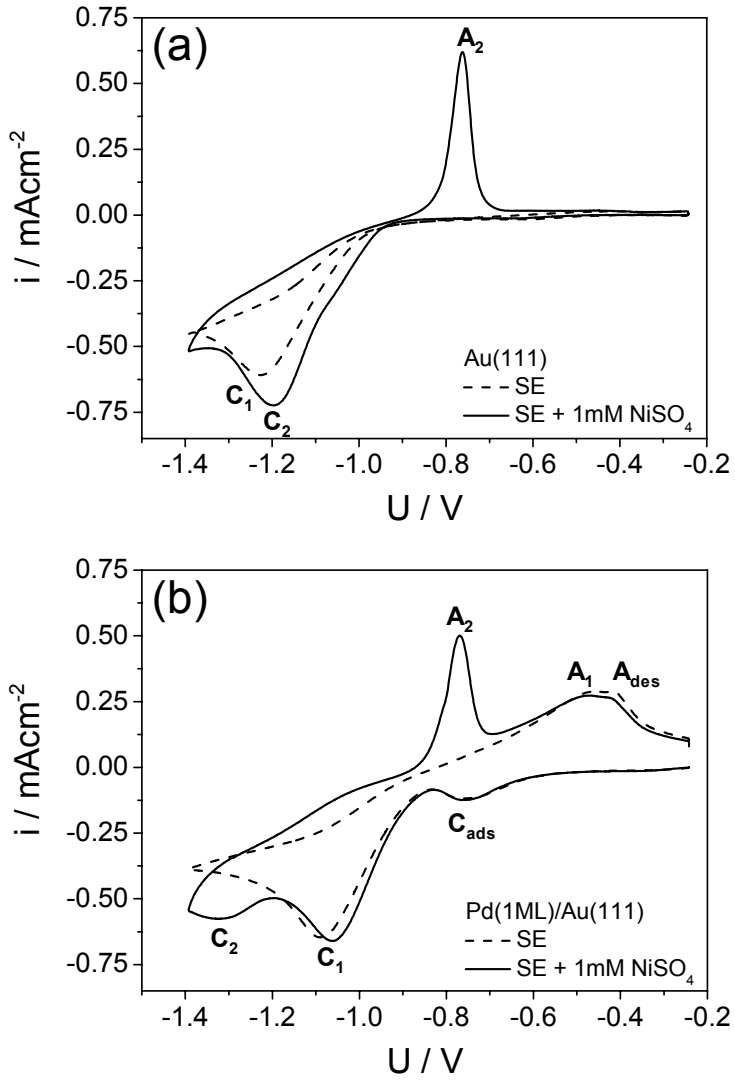

Figure 4.2: Cyclic voltammograms recorded in the supporting electrolyte (SE), 0.1 M K_2SO_4 + 1 mM H_2SO_4 + 1 mM KCl (pH 3), without (dashed line) and with (solid line) 1 mM $NiSO_4$ on (a) Au(111) and (b) Pd(1ML)/Au(111). Scan rate: *sr* = 50 mV.s^{-1}.

In the Ni solution, the response of Au(111) (Fig. 4.2a) displays a somewhat broader cathodic reduction wave which starts at a slightly more positive potential i.e. at -1.2 V than in the absence of Ni ions in solution. These changes suggest that the current peak corresponding to Ni deposition overlaps with that of the proton reduction. The onset potential of Ni deposition, is actually -1.01 V ($\eta \geq 30$ mV) compared to the calculated Ni^{2+}/Ni Nernst potential -0.98 V (for 1 mM Ni^{2+}) [4]. A shoulder on the right hand side of the current wave (- 1.05 V < U < -1.01 V) may be identified. In the positive sweep, the single oxidation peak (A_2) at -0.75 V is ascribed to the dissolution of metallic Ni into Ni^{2+} ions in the solution. Very similar voltammogram was reported for Ni deposition on Au(111) in modified Watts electrolyte [4]. On Pd(1ML)/Au(111) surface (Fig. 4.2b), Ni deposition is clearly associated with the broad cathodic peak (C_2) at -1.32 V. In the positive sweep, the nickel stripping peak is observed at -0.77 V that is slightly more negative than the peak potential value obtained on bare Au(111). As noticed above, the charge under the dissolution peak for Ni dissolution on Au(111) ($Q_{\text{Dissolution}}^{\text{Ni/Au(111)}} = 0.71$ mC.cm^{-2}) is larger than for Ni dissolution on Pd(1ML)/Au(111) ($Q_{\text{Dissolution}}^{\text{Ni/Pd(1ML)/Au(111)}} = 0.56$ mC.cm^{-2}).

To summarize, the above CVs show that Co and Ni deposition occurs at potential negative of the Nernst potential on Au(111) and on Pd(1ML)/Au(111). There is no evidence for any underpotential deposition processes, in agreement with previous works [4, 17]. It should again be recalled that Ni and Co growth on Pd(1ML)/Au(111) occurs on a hydrogenated Pd surface. Indeed H-adsorption takes place at potentials more positive than Ni or Co Nernst potential on this surface (see also Sec. 3.2.3). The presence of this H-adlayer seems to have no influence on Co deposition (peaks C_2 and A_2 are positioned at the same potential on both surfaces) whereas some differences are found in the position of the Ni peaks. In fact the position of peaks C_2 and A_2 are in this case slightly shifted on the Pd monolayer surface. To the best of our knowledge, no other voltammogram related to Ni or Co electrodeposition on Pd surface is available in the literature. Similarly, Gomez et al. [18] used a polycrystalline Pt surface, which exhibits strong interactions with hydrogen as Pd surface. They also observed a reduction peak at -1 V vs. Ag/AgCl (1 M) (i.e. -1.4 V_{MSE}) in high concentrated $NiCl_2$ electrolyte (0.5 M, pH 3) but any attempt of explanation about the origin of this peak is missing.

4.2.2 Nickel and cobalt growth rates

As seen on cyclic voltammograms, the partial electrochemical current related to Co or Ni deposition is mostly hidden by the HER current. This hinders the determination of the film thickness as well as the direct determination of the onset potential for deposition, especially in the case of nickel for which the two cathodic waves (HER and deposition) overlap. In order to get insights into the electrochemical growth rates of Co and Ni on *monometallic* Au(111) and Pd(1ML)/Au(111) surfaces, we used the charge measured under the dissolution peak, assuming that the process corresponds to the dissolution of the metal layer. Actually, under this assumption the film thickness, denoted $t_{M/S}$ with M the deposited metal (i.e. Co or Ni) and S the substrate i.e. Au(111) or Pd(1ML)/Au(111), can be determined from the electric charge under the dissolution peak ($\mathcal{Q}^{M/S}_{Dissolution}$) using the Faraday's law. By assuming that the anodic charge is arising from the dissolution reaction $M \rightarrow M^{2+} + 2e^-$ with M = Ni or Co, and considering the fact that Ni and Co films are actually (111)-oriented we find that the equivalence charge-to-thickness (in ML) is $\mathcal{Q}_{eq} = 0.59$ mC.cm^{-2} per monolayer (the surface atom density is 1.85 x 10^{15} atom.cm^{-2} and 2 electrons are exchanged per atom).

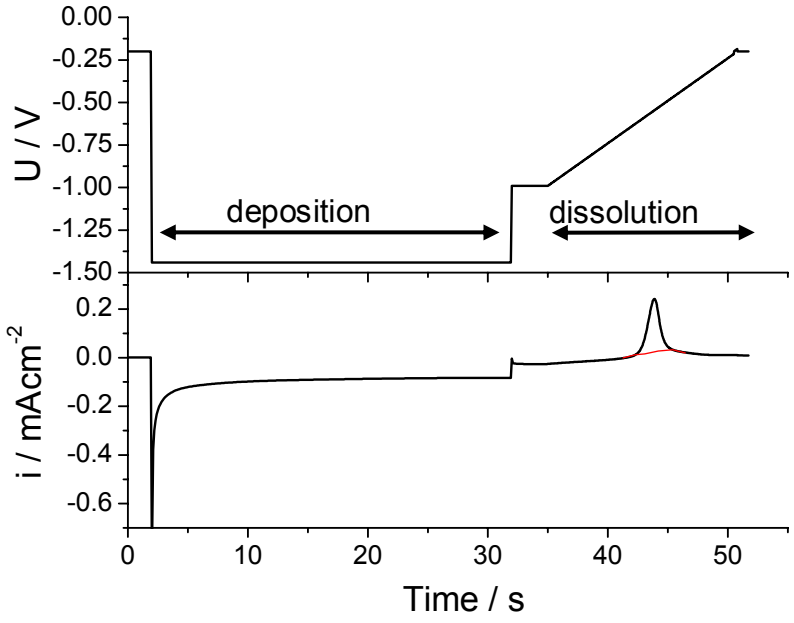

Figure 4.3: Sequence of potentials and corresponding current transient recorded on Au(111) in 0.1 M K_2SO_4 + 1 mM H_2SO_4 + 1 mM KCl + 1 mM $NiSO_4$. First, the electrode potential is stepped from -0.2 V to U_{dep} (equal to -1.44 V here) for a period (t_{dep}) ranging from few seconds to 150 s. Subsequently, the potential is held for ~ 5 s at the stabilization potential (U_{stab}) before applying a positive ramp of potential (sr = 50 mV.s^{-1}) to dissolve the deposited film. In parallel, the electrochemical current is recorded.

The principle of the method is described in Fig. 4.3 where we show the sequence of potentials used to grow and dissolve a film so as to determine the growth rates. A potential step is first applied from -0.2 V to the selected deposition potential (U_{dep}) for a certain time (t_{dep}). At the end of the deposition, the potential is stepped to a stabilization potential U_{stab}, during ~ 5 s. This so-called stabilization potential is carefully chosen such that neither significant dissolution nor further growth occurs. Experimentally, we found $U_{stab}^{Ni} = -1.07$ V for nickel and $U_{stab}^{Co} = -1.13$ V for cobalt. Then, a positive linear sweep of potential (sr = 50 mV.s^{-1}) is applied to dissolve the deposited film. The corresponding variations of the electrochemical current are shown at the bottom of Fig. 4.3. The figure is typical of Ni deposition/dissolution. The same kinds of plots are obtained in the case of cobalt. During deposition, the current density follows a Cottrell-like decay with time [19]. It can be shown that it is mainly due to proton reduction under mass transport limitations. During the anodic sweep of potential the peak of current corresponds to peak A_2 in the CV of Fig. 4.2a. It should be emphasized that the sharp decrease of i_{diss} on the right hand size of the peak arises from the complete consumption of Ni atoms deposited on the surface. Integration of this peak gives the average thickness of the deposit as explained above. The experiment was repeated by increasing the deposition times to obtain the plots shown in Figs. 4.4 and 4.5 which relate the variations of Co and Ni film thickness, deposited on *monometallic* Au(111) (circles) and Pd(1ML)/Au(111) (triangles), to the deposition time. Several deposition potentials are considered in the figures. The deposition rate $v_{dep}^{M/S}$, expressed in ML.s^{-1}, is directly inferred from the slope of the thickness plot vs. deposition time. It will be analyzed below.

a) Au(111) surface:

On Au(111), the plots of $t_{Co/Au}$ (Fig. 4.4a-c) and $t_{Ni/Au}$ (Fig. 4.5a-c) vs. deposition time display a similar shape for all the investigated U_{dep}, which is characterized by two different growth regimes. The first regime, observed for low deposition time, is characterized by a sharp increase of the film thickness i.e. a high growth rate followed by the second regime with a significantly lower growth rate. The crossover between the two growth regimes (obtained by intersecting the two linear parts of each plot) depends on the nature of the metallic overlayers. Remarkably, the average thickness value ($t^*_{M/S}$) related to the crossover between the two growth regimes was found equal to $t^*_{Ni/Au}$ ~ 1 ML for Ni and $t^*_{Co/Au}$ ~ 2 ML for Co. This observation is valid at all investigated potentials U_{dep}. Below t^* (i.e. in the first growth regime), the growth rate of Ni (resp. Co) on Au(111) ranges from 0.03 (0.20) up to 0.98 (0.39) ML.s^{-1} according to the applied potential. Above t^* (i.e. in the second growth regime), the nickel (resp. cobalt) growth rate slows

down and varies from 0.001 (0.01) to 0.11 (0.15) ML.s^{-1} depending on the applied potential. Such slow growth rates will allow one to control the surface coverage with a good accuracy. Concerning the growth of Ni, the present observations are in excellent agreement with previous works which showed that the kinetics of Ni monolayer growth is faster than Ni multilayer growth at moderate overpotential [20]. In the case of cobalt, $t^*_{Co/Au}$ is ~ 2 ML instead of 1 ML because a biatomic Co layer is first formed [17]. Finally, these electrochemical measurements for Ni and Co growth are also in full agreement with previous STM observations [17, 21-23] which showed that the second Ni monolayer (resp. the third Co monolayer) nucleates after completion of the first Ni monolayer (resp. Co biatomic layer).

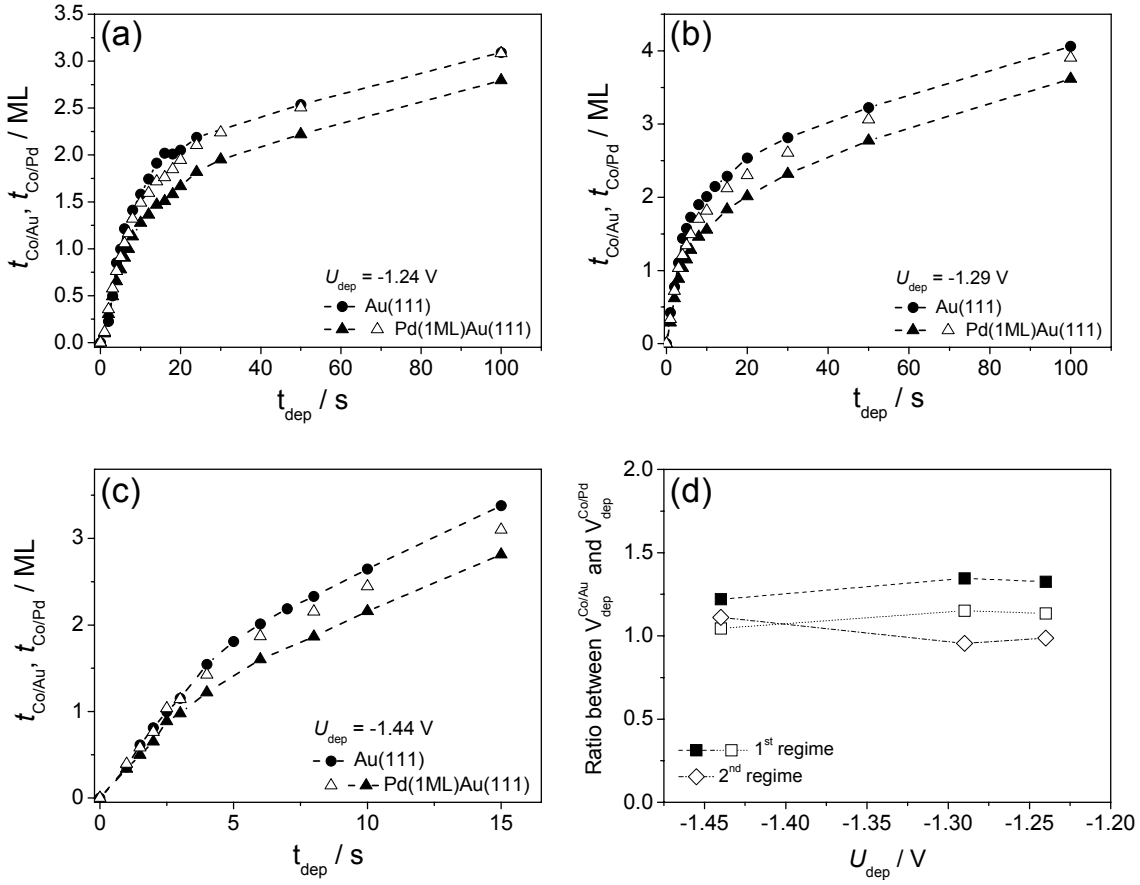

Figure 4.4: Variation of the Co thickness vs. deposition time on (●) Au(111) and (▲) Pd(1ML)/Au(111) at (a) U_{dep} = -1.24 V, (b) U_{dep} = -1.29 V and (c) U_{dep} = -1.44 V. The open triangles (Δ) correspond to the Co thickness on Pd(1ML)/Au(111) corrected by the H re-adsorption charge. (d) Variation of the ratios between the deposition rates of Co on Au(111) and on Pd(1ML)/Au(111) as a function of U_{dep} in the monolayer (■) and multilayer (◊) regimes. The open squares (□) in the Co first bilayer regime correspond to the ratios in which the deposition rates of Co on Pd(1ML)/Au(111) has been corrected by the H re-adsorption charge.

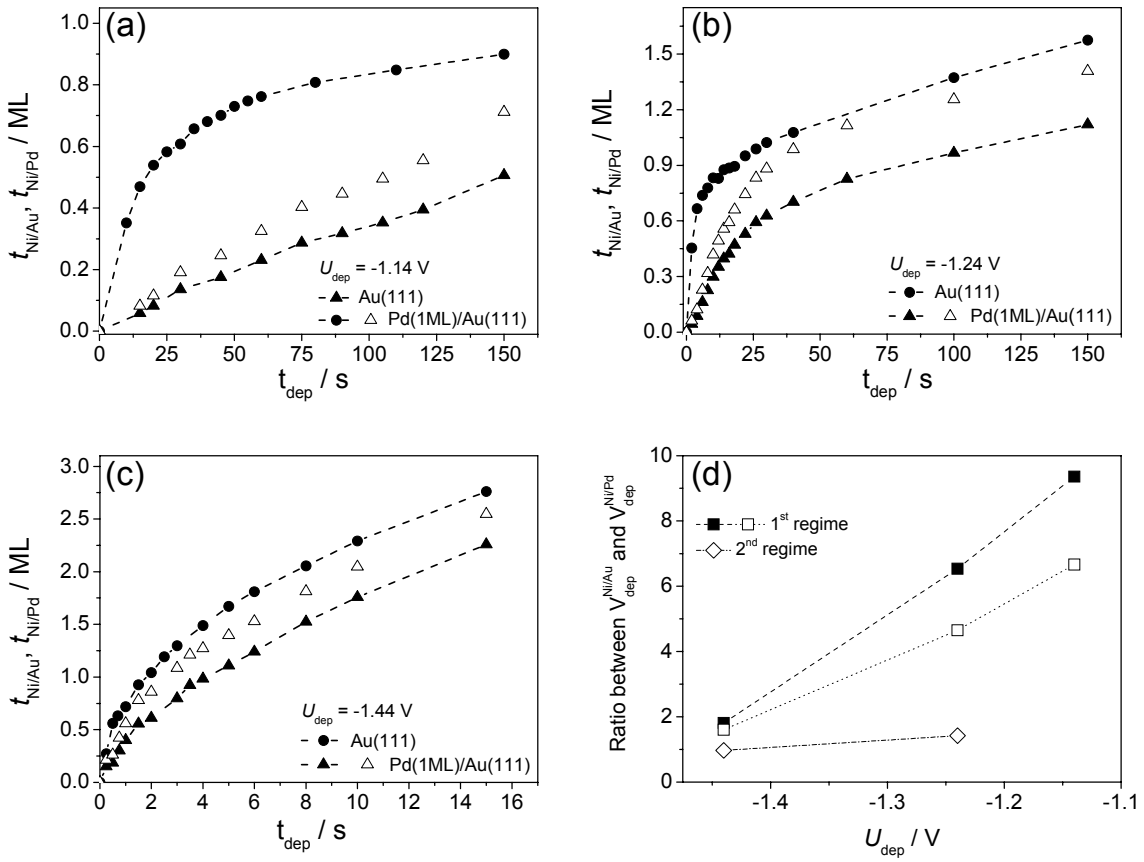

Figure 4.5: Variation of the Ni thickness vs. deposition time on (●) Au(111) and (▲) Pd(1ML)/Au(111) at (a) U_{dep} = -1.14 V, (b) U_{dep} = -1.24 V and (c) U_{dep} = -1.44 V. The open triangles (Δ) correspond to the Ni thickness on Pd(1ML)/Au(111) corrected by the H re-adsorption charge. (d) Variation of the ratios between the deposition rates of Ni on Au(111) and on Pd(1ML)/Au(111) as a function of U_{dep} in the monolayer (■) and multilayer (◊) regimes. The open squares (□) in the Ni first monolayer regime correspond to the ratios in which the deposition rates of Ni on Pd(1ML)/Au(111) has been corrected by the H re-adsorption charge.

b) Pd(1ML)/Au(111) surface:

Concerning the results on Pd(1ML)/Au(111), the variations of $t_{Co/Pd}$ (black filled triangles in Fig. 4.4) also exhibit two different kinetic regimes. For low deposition time, $t_{Co/Pd}$ increases with a slightly lower growth rate than $t_{Co/Au}$. Actually, $v_{dep}^{Co/Pd(1ML)/Au(111)}$ varies from 0.15 ML.s^{-1} at -1.24 V to 0.32 ML.s^{-1} at -1.44 V, that is in average 23% lower than the ones found on Au(111). Then, the crossover between the first and the second regime seems to begin at lower thicknesses than for Co on Au(111), involving the appearance of a shift between the variation of $t_{Co/Pd}$ and $t_{Co/Au}$. For instance, at U_{dep} = -1.24 V, $t^*_{Co/Pd}$ is found around 1.75 ML. Finally, in the second regime, the slopes related to the deposition of subsequent Co layers, i.e. from the growth of the

third layer on the already deposited bilayer, are parallel to the ones found for the similar processes using Au(111), meaning that the deposition rates in the multilayer regime are not dependent on the substrate. In the case of Ni, the variations of $t_{Ni/Pd}$ (black filled triangles in Fig. 4.5) depend on U_{dep} and change markedly compared to the ones plotted for $t_{Ni/Au}$. At -1.14 V (Fig. 4.5a), $t_{Ni/Pd}$ displays now only one deposition regime characterized by a very low deposition rate (0.0035 ML.s^{-1}). At $U_{dep} \geq$ -1.24 V (Figs. 4.5b and 4.5c), the existence of a transition between the first and the second kinetic regime is again observed but at lower thicknesses than on Au(111), similarly to the observations made for Co. For instance $t^*_{Ni/Pd} \sim 0.6$ ML in Fig. 4.5b at U_{dep} = -1.24 V. However, the influence of the Pd(1ML)/Au(111) surface on the decreasing of the growth rate appears much more pronounced than for Co. At -1.24 V, $v_{dep}^{Ni/Pd(1ML)/Au(111)}$ is found equal to 0.03 ML.s^{-1} in the first regime which is more than six times lower than on Au(111), 0.18 ML.s^{-1}, while at -1.44 V the difference between $v_{dep}^{Ni/Pd(1ML)/Au(111)}$ and $v_{dep}^{Ni/Au(111)}$ decreases but the former is still two times lower than the latter. The deposition of subsequent Ni layers occurs also at almost the same rates (parallel slopes) on both surfaces.

In Figs. 4.4d and 4.5d, the ratios between the deposition rates of Co or Ni on Au(111) and on Pd(1ML)/Au(111) are plotted as a function of U_{dep} in each kinetic regime. For Ni, it can be noticed that $v_{dep}^{Ni/Au(111)} / v_{dep}^{Ni/Pd(1ML)/Au(111)}$ in the first regime (black filled squares) decreases from 9.4 to 1.8 between -1.14 and -1.44 V. In the case of Co, Fig. 4.4d shows that $v_{dep}^{Co/Au(111)} / v_{dep}^{Co/Pd(1ML)/Au(111)}$ fluctuates between 1.33 at -1.24 V and 1.22 at -1.44 V going through 1.35 at -1.29 V, signifying that the growth kinetics of Co is less influenced by the chemical nature of substrate (since the deposition rates are almost similar on both surfaces) than Ni. In addition, the growth of Co on both substrates seems to be mainly limited by the diffusion transport of Co^{2+} cations from the solution towards the surface. Finally, for all U_{dep} and on both substrates, the deposition rates in the second regime (open diamonds) are identical for Au(111) and Pd(1ML)/Au(111).

c) Influence of H re-adsorption on Pd(1ML)/Au(111) surface

According to the results presented below, we found a systematic difference between the $t^*_{M/Pd}$ and $t^*_{M/Au}$ (with M = Ni or Co). The origin of this difference in t^* has to be explained since the STM observations, presented above in Sec. 4.3, will show that the growth morphology of these two metal overlayers is similar on Pd monolayer islands and on Au(111). Namely, a 2D growth occurs for Ni and Co deposition and similar in-plane atom spacing was found. As mentioned in Secs. 3.2.3 and 4.2.1, the Pd(1ML)/Au(111) surface is covered by an adsorbed

hydrogen layer in the Co and Ni deposition potential range, contrary to Au(111). One likely explanation for this discrepancy in t^* could be the re-adsorption of hydrogen on the Pd surface in the course of the Ni and Co stripping process. Naturally, this hypothesis assumes that the H-monolayer was *desorbed* upon deposition. Justifications for such hypothesis will be addressed in the paragraph dedicated to the general discussion of the electrochemical data (see Sec. 4.2.4). In the subsequent paragraph, we examine the influence of the H re-adsorption process on the plots of Figs. 4.4 and 4.5.

Assuming the hypothesis of H-desorption during metal deposition on Pd(1ML)/Au(111), we have to take into account that the re-adsorption of hydrogen during the metal overlayer dissolution is accompanied by a negative electrochemical current. Consequently, the resulting dissolution peak should be the balance between this negative current and the positive dissolution current, corresponding to the anodic charge, named Q_M (preciously called $Q^{M/S}_{Dissolution}$), that we measured. The measured anodic charge under peak A_2 is thus the sum of two contributions:

$$Q_A = Q_M - Q_{H\ re\text{-}ads} \qquad \text{(Eq. 4.1)}$$

Where Q_M corresponds to the true dissolution charge associated with the dissolution of the metal atoms ($M \rightarrow M^{2+} + 2e^-$) that we should obtained (i.e. corrected) in absence of the H concomitant adsorption process and $Q_{H\ re\text{-}ads}$ is the charge associated to the re-adsorption of H on the free Pd surface ($H^+ + e^- \rightarrow H_{ads}$). Since the process occurs during metal dissolution for which *the surface coverage is lower than unity*, we may write:

$$Q_{H\ re\text{-}ads} = Q^{ML}_{Hads} \times \theta_{M/Pd} = Q^{ML}_{Hads} \times \frac{Q_M}{Q_{eq}} \qquad \text{(Eq. 4.2)}$$

where Q^{ML}_{Hads} is the charge corresponding to one complete H-monolayer adsorbed on Pd(1ML)/Au(111), which is equal to 170 $\mu C.cm^{-2}$ in 0.1 M H_2SO_4 according to Baldauf and Kolb [14], $\theta_{M/Pd}$ corresponds to the surface coverage of the metal M on the Pd monolayer (M = Ni or Co) and Q_{eq} is the charge corresponding to one monolayer of metal (0.59 $mC.cm^{-2}$, see above). Combining both equations lead to:

$$Q_M = \frac{Q_A \times Q_{eq}}{Q_{eq} - Q^{ML}_{Hads}} \qquad \text{(Eq. 4.3)}$$

In the case of Ni monolayer, the corrected thickness corresponds to $t_{Ni/Pd} = \frac{Q_M}{Q_{eq}}$. Thus, we obtain:

$$t_{\mathrm{Ni/Pd}} = \frac{Q_{\mathrm{A}}}{(Q_{\mathrm{eq}} - Q_{\mathrm{Hads}}^{\mathrm{ML}})} \qquad \text{(Eq. 4.4)}$$

For Co, we have to take into account that the first growth regime corresponds to the initial formation of a biatomic layer (see Sec. 4.3). Therefore, the surface coverage of Co is two times lower than its respective thickness i.e. $\theta_{\mathrm{Co/Pd}} = \frac{Q_{\mathrm{M}}}{2Q_{\mathrm{eq}}} = \frac{t_{\mathrm{Co/Pd}}}{2}$ which leads to:

$$t_{\mathrm{Co/Pd}} = \frac{Q_{\mathrm{A}}}{(Q_{\mathrm{eq}} - \frac{Q_{\mathrm{Hads}}^{\mathrm{ML}}}{2})} \qquad \text{(Eq. 4.5)}$$

Thus, the variations of $t_{\mathrm{Co/Pd}}$ and $t_{\mathrm{Ni/Pd}}$ have been calculated again taking into account the correction corresponding to the concomitant H adsorption on Pd(1ML)/Au(111) and are added in Figs. 4.4 and 4.5. The results are symbolized by the open triangles on graphs (a-c) and by open squares on plots (d). The correction affects markedly the variations of $t_{\mathrm{Co/Pd}}$ and $t_{\mathrm{Ni/Pd}}$ by increasing the respective slope values in the first kinetic regime and, by consequence by operating merely a vertical shift of around 0.29 ML in the second regime. Therefore, only the corrected ratios in the first regime are modified as shown in Figs. 4.4d and 4.5d. For Ni (Fig. 4.5a-c), it can be observed that the crossover thickness $t^*_{\mathrm{Ni/Pd}}$ is now closer to 1 ML for $U \leq$ -1.24 V. For U = -1.14 V, the growth rate was very slow and the second regime was not reached. It is worth emphasizing that, despite the above correction, the Ni monolayer growth rate remains systematically smaller on Pd than on Au surfaces. Fig. 4.5d shows that the corrected ratio values are still high even decreasing from 6.7 to 1.6 between -1.14 and -1.44 V. This observed trend can be explained by the fact that, at large negative potentials, the electrochemical transfer becomes limited by mass transport in solution, a process which is independent of the electrode material. In the case of cobalt (Fig. 4.4a-c), the correction tends to reduce the difference in growth rates found between Pd and Au surfaces. Indeed, the corrected $t_{\mathrm{Co/Pd}}$ now almost overlaps with $t_{\mathrm{Co/Au}}$ as expressed by the ratio value which is close to unity in the bilayer regime (Fig. 4.4d).

To conclude this paragraph, the excellent agreement between the values of $t^*_{\mathrm{Ni/Pd}}$ derived from corrected plot with STM observations (see next section 4.3) comes into strong support of the proposed hypothesis. A further more refined argument, which will also discussed in the next section, is the excellent agreement found between the growth rate derived from electrochemical measurements and STM data. This plausible hypothesis calls however for an atomic scale mechanism accounting for the H-desorption or segregation during metal deposition. This point will be discussed later on.

4.2.3 Dissolution curves

Figs. 4.6 and 4.7 show several series of current density - potential curves corresponding to the dissolution of Ni and Co films, previously deposited on *monometallic* Au(111) and Pd(1ML)/Au(111) surfaces at U_{dep} = -1.24 V during different deposition times as indicated in the legends of the figures (i.e. by increasing thickness). In the case of deposition on Pd(1ML)/Au(111), the thickness was corrected from the H-adsorption as explained above. These curves were obtained according to the sequence of potentials illustrated in Fig. 4.3. The linear sweep voltammograms (LV) were corrected for the background current and the axis of both graphs in Figs. 4.6 and 4.7 used the same scale to facilitate the comparison between experiments done on Au(111) (panel (a)) and Pd(1ML)/Au(111) (panel (b)).

a) Nickel dissolution:

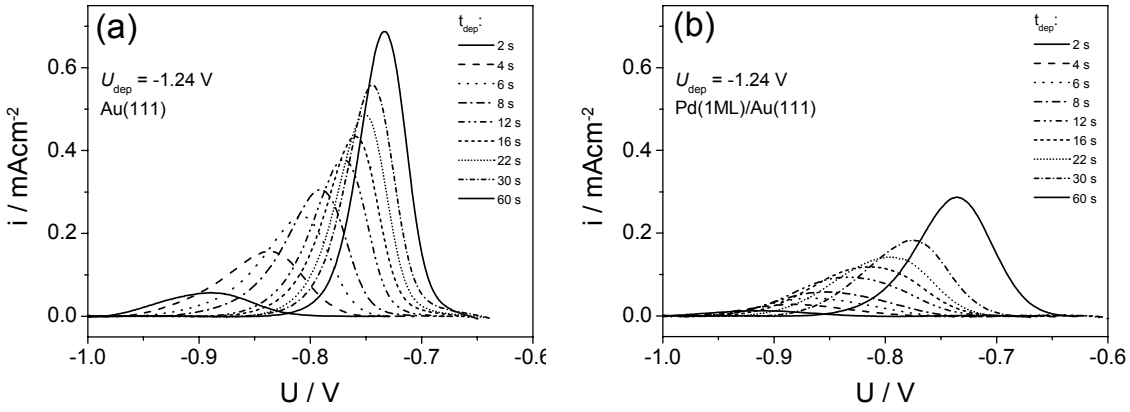

Figure 4.6: Series of current-potential curves showing the dissolution of the Ni film, previously deposited at U_{dep} = -1.24 V during different deposition times (see legend in the figure) on (a) Au(111) and (b) Pd(1ML)/Au(111) in 0.1 M K_2SO_4 + 1 mM H_2SO_4 + 1 mM KCl + 1 mM $NiSO_4$. The linear voltammograms were normalized for the background current. Scan rate: *sr* = 50 mV.s^{-1}.

The dissolution curves reported in Fig. 4.6 clearly show that the rise in the Ni dissolution current density on Au(111) as well as on Pd(1ML)/Au(111) shifts towards more positive potential values with increasing the Ni thickness. This behavior demonstrates that the kinetics of Ni dissolution depends on the film thickness even in the submonolayer range. Comparing the shapes of the dissolution curves between the two substrates, it can be noticed that the current rise is steeper on Au(111) than on Pd(1ML)/Au(111). The peak maximum is also remarkably lower for a given thickness. This behavior demonstrates that the dissolution kinetics of Ni depends on the substrate.

b) Cobalt dissolution:

In contrast to the case of nickel, Fig. 4.7 shows that the Co dissolution onset potential from Au(111) or Pd(1ML)/Au(111) is independent of the average thickness *below* 2 ML. Above this critical thickness the current rise is shifted anodically. Comparing the shapes of the dissolution curves between the two substrates, one notices that the onset potential of dissolution depends to a lesser extent on the substrate. Only the current rise is slower for Co stripping on Pd(1ML)/Au(111) than on Au(111), revealing a possible influence of the substrate on the dissolution kinetics.

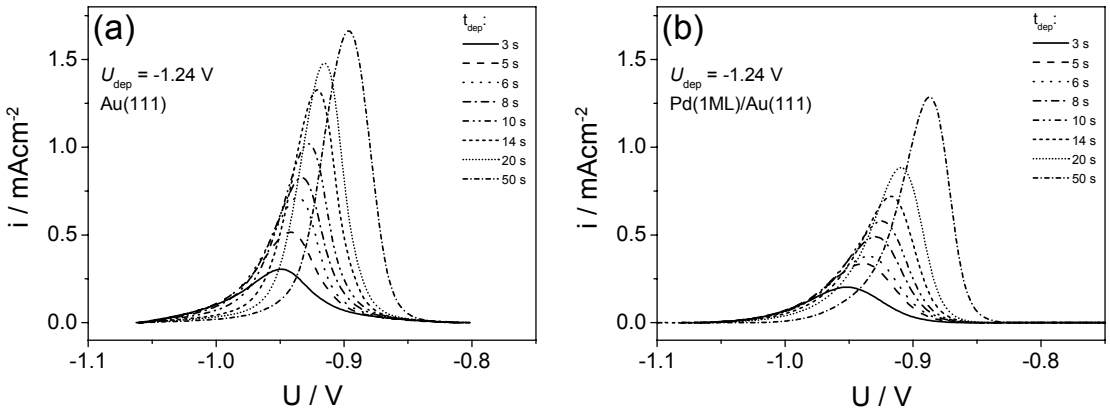

Figure 4.7: Series of current-potential curves showing the dissolution of the Co film, previously deposited at U_{dep} = -1.24 V during different deposition times (see legend in the figure) on (a) Au(111) and (b) Pd(1ML)/Au(111) in 0.1 M K_2SO_4 + 1 mM H_2SO_4 + 1 mM KCl + 1 mM $CoSO_4$. The linear voltammograms were normalized for the background current. Scan rate: sr = 50 mV.s^{-1}.

The above assessment about the electrochemical dissolution can be characterized more deeper by comparing the dissolution curves corresponding to the same metal thickness (i.e. accounting for the charge associated with the H-adsorption on the Pd(1ML)/Au(111) surface). Fig. 4.8 compares the dissolution of 2 ML-thick Co (panel a) and 1 ML-thick Ni films (panel b) on Au(111) (solid line) and Pd(1ML)/Au(111) (dashed line). First, the dissolution kinetics of both metallic deposits appeared to be more sluggish on Pd(1ML)/Au(111) than on Au(111) as demonstrated by the decreasing of the exponential rise steepness. Then, it can be observed in Fig. 4.8a that the Co bilayer dissolution process begins at the same potential on both substrates. On the contrary, according to Fig. 4.8b, there is an unambiguous shift of the Ni dissolution onset potential between Pd(1ML)/Au(111) and Au(111) substrates of around 90 mV.

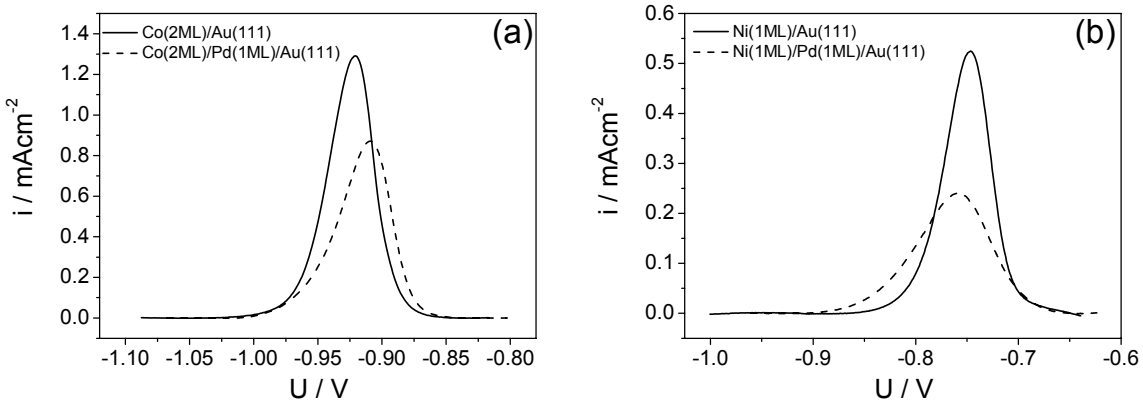

Figure 4.8: Current-potential curves showing the dissolution of (a) Co bilayer and (b) Ni monolayer, previously deposited at U_{dep} = -1.24 V on Au(111) (solid line) and Pd(1ML)/Au(111) (dashed line) in 0.1 M K_2SO_4 + 1 mM H_2SO_4 + 1 mM KCl + 1 mM $CoSO_4$ (resp. $NiSO_4$). The linear voltammograms were normalized for the background current. Scan rate: sr = 50 mV.s^{-1}.

4.2.4 Discussion of the electrochemical data

Before discussing the origin of these observations, the generally accepted mechanism to describe the electrodeposition of Ni [24-27] is going to be detailed. The validity of such mechanism has not been clearly established in the case of cobalt [28] because the pH-dependence of Co and Ni solutions is slightly different [29]. The mechanism involves two consecutive one-electron charge transfers and the participation of an anion with the formation of an adsorbed complex and can be represented by:

$$Ni^{2+} + X^- \rightarrow NiX^+ \qquad \text{(Eq. 4.6a)}$$

$$NiX^+ + e^- \rightarrow NiX_{ads} \qquad \text{(Eq. 4.6b)}$$

$$NiX_{ads} + e^- \rightarrow Ni + X^- \qquad \text{(Eq. 4.6c)}$$

in which X denotes a ligand, probably an anion (SO_4^{2-}, Cl^- or an OH^-) and NiX_{ads} corresponds to an adsorbed Ni species. The above electrochemical model was recently re-examined in light of in situ quartz crystal microbalance (QCMB) measurements, which showed that the deposition rate is greater at submonolayer coverage than in the multilayer deposition regime [20]. In this mechanism, step 2 (Eq. 4.6b) is considered as the rate-determining step with a Tafel slope of 120 mV/decade [30]. Due to large overpotential required to perform Ni deposition, the process is

also accompanied by simultaneous hydrogen reaction evolution (HER), i.e. the proton reduction ($2H^+ + 2e^- \rightarrow H_2$), described by the following well-known mechanism [31]:

$$M + H^+ + e^- \rightarrow M\text{-}H_{ads} \qquad \text{(Eq. 4.7a)}$$

$$M\text{-}H_{ads} + H^+ + e^- \rightarrow M + H_2 \qquad \text{(Eq. 4.7b)}$$

$$2M\text{-}H_{ads} \rightarrow 2M + H_2 \qquad \text{(Eq. 4.7c)}$$

where M represents the free metal surface site (e.g. substrate and/or Ni) and $M\text{-}H_{ads}$ the atomic hydrogen adsorbed on the metal surface (need to complete). Reaction (Eq. 4.7a) is an adsorption step in which a chemical bond $M\text{-}H_{ads}$ is formed and where M represents the free metal surface site (e.g. substrate and/or Ni, Co). The production of molecular H_2 follows a desorption stage according either to reaction (Eq. 4.7b) which implies that H_{ads} are mobiles on the surface, or to reaction (Eq. 4.7c) if a second proton is involved. It was assumed that the adsorbed Ni species catalyze H-adsorption [32].

With the aim of describing in greater details the differences found in growth and dissolution kinetics of Ni monolayer and Co bilayer between Au(111) and Pd(1ML)/Au(111) surfaces, the Butler-Volmer equation can be used. For the sake of clarity, only the equation part related to the dissolution process is given (see Sec. 2.1 for the complete expression of Butler-Volmer equation). The partial current density related to the dissolution can be expressed as:

$$i_{diss} = zFv_{diss} = zFK_{diss} \exp\left(\frac{\alpha_{diss} zF}{RT}\left(U - \phi^{M}_{Nernst}\right)\right) \qquad \text{(Eq. 4.8)}$$

where K_{diss} is the kinetic rate constants (in s^{-1}), U is the electrode potential (V) and ϕ^{M}_{Nernst} is the equilibrium potential (V) of the reaction $M \leftrightarrow M^{z+} + ze^-$ with M is the metal substrate and M^{z+} is the metallic cation dissolved in the electrolyte. According to this equation, the existence of slower electrochemical rate (i.e. lower current density) may be explained either by purely kinetic considerations (i.e. K depends on the electrode material) or by thermodynamic considerations (i.e. ϕ^{M}_{Nernst} depends on the substrate).

Taking into account the above deposition mechanism and the electrode kinetic equations, we will discuss the origin of the material dependent growth and dissolution kinetics observed in the case of Ni monolayer. Then, we will also briefly examine the possible mechanism describing the H-desorption process caused by the Ni deposition. It must be mentioned that the discussion related to (*i*) the Ni dissolution in multilayer regime and (*ii*) the dissolution of Co bilayer will be developed after the STM result descriptions since these processes are expected to be strongly dependent on the film morphology.

a) Origin of the substrate dependent growth kinetics of Ni monolayer

Influence of the point of zero charge (pzc):

We recall that the pzc is the potential at which the electrode surface presents no net charge. At potential negative of pzc, the surface is negatively charged and the amount of charge increases linearly (assuming that the interfacial capacitance is independent of the applied potential) with potential difference measured with respect to pzc. Hence, at a given potential, a difference in pzc may therefore influence the local concentration of ionic species close to the electrode surface due to different electrostatic interactions. Table 4.1 gives the pzc of several noble metal electrodes. It shows that the pzc is sensitive to the metal and, for a given metal, to its crystal orientation. The metal dependence of pzc approximately scales with the metal work function [33].

Table 4.1: Point of zero charge (pzc) values of selected single crystal electrode surfaces. Note the dependence of pzc with surface orientation. Note also that the pzc of one epitaxial monolayer is different of that of the bulk single crystal.

Metal	pzc (V_{MSE})	Ref.
Au(111)	-0.08	[34]
Au(100)	+0.30	[34]
Ag(111)	-1.10	[35]
Pd(111)	-0.52	[36]
Pd(1ML)/Au(111)	-0.49	[36]

The pzc value was invoked to explain the slower deposition rates of Ni on Ag(111) as compared to Ni growth on Au(111) in a modified Watts bath of composition 10^{-2} M H_3BO_3 + 10^{-4} M HCl + 10^{-3} M $NiSO_4$ [37, 38]. The pzc of Ag(111) which is 1.016 V more negative than that of Au(111) [34, 39] implies that the net negative surface charge at the Ni deposition potential is larger on Au(111) than that at the Ag(111) surface. Assuming first order reactions, this could increase the rate of step (Eq. 4.6a-b) on Au(111) because of a larger cation concentration in the close proximity of the Au surface.

El-Aziz et al. [36] showed that the pzc of the first, pseudomorphic Pd layer on Au(111) is 0.406 V more negative than that of Au(111). The argument developed above could again be used to explain that steps (1-2) are slower on Pd(1ML)/Au(111). However, our supporting electrolyte (K^+ and SO_4^{2-}) is 10 times more concentrated than the Watts solution used in Ref. 21. In addition the Ni^{2+} concentration is 100 times smaller than inert species carrying the current and its average

conductivity is more than 100 times that of Ni^{2+}. Therefore, the value of the pzc should, in our case, have a negligible effect on the Ni^{2+} concentration close to the electrode surface because other cations (e.g. K^+) will more efficiently screen the surface charge in the steady-state regime, i.e., after the typical time for building up the diffuse layer after a potential step. Therefore the difference in the electrode surface charge induced by the difference in the pzc of Pd(1ML)/Au(111) and Au(111) should not affect the Ni^{2+} concentration in the vicinity of the surface. Moreover, after the transient regime which lasts typically the time constant of the electrochemical cell, i.e., in our case, ~ 1 ms, the Ni surface coverage reaches at most (for the most negative deposition potential) few 10^{-3} ML, which is by far much smaller than the difference we observe. Therefore, the difference in the pzc between Au(111) and Pd(1ML)/Au(111) seems inappropriate to explain the observed difference in the Ni deposition kinetics.

Influence of the H-monolayer on Pd:

The slower growth rate of Ni monolayer on Pd(1ML)/Au(111) (Fig. 4.5) could be attributed to the presence of the H-UPD layer which is present on Pd in this region of potential. Such adlayer might affect the reaction kinetics.

From a mechanistic viewpoint, step (Eq. 4.6b) is rate determining in the case of Ni deposition on a Ni substrate [24-27]. However, it has been inferred from EQCM measurements that the step (Eq. 4.6c) becomes rate determining during the growth of the first Ni monolayer on Au(111) [40]. This change was attributed to the absence of adsorbate (H, OH or other ions) on Au(111) at potentials where Ni deposition takes place. It is indeed likely that Ni on Ni growth takes place on a nickel surface which is covered by H or OH species. In this case, the transfer of electron at step Eq. 4.6b is probably hindered (for the reasons exposed above). This change of rate determining step (*rds*) can be correlated with the existence of two growth regimes found for Ni/Au(111) growth, i.e. the *rds* of monolayer growth corresponds to step (Eq. 4.6c) and it is faster than the multilayer growth for which the *rds* is step (Eq. 4.6b) (Fig. 4.5). Therefore we can infer that Ni monolayer growth should be *slower* on H-terminated Pd(1ML)/Au(111) than on Au(111) because the former surface is covered by a UPD layer at potentials more positive than the Ni deposition onset potential. This conclusion is again in close agreement with observations, especially at potentials close to the Nernst potential of Ni^{2+}/Ni.

From a pure electrochemical transfer viewpoint, the presence of an adsorbed H-layer on Pd constitutes a steric barrier which increases the Ni^{2+} / Pd surface minimum approach distance. In case of similar activation energy, increasing the approach distance reduces the kinetic transfer [19]. In addition, the presence of the H-monolayer on Pd reduces the electron density of states

close to the Fermi level of the substrate (see Sec. 3.2) which also contributes to reducing the rate of the overall reaction.

Therefore, several explanations allowed one to correlate the observed slower discharge kinetics of Ni^{2+} ions at the Pd/Au(111) surface with the presence of the H-monolayer on this surface. However, some questions remain still open: (*i*) why the growth rate of Ni/Pd is faster than that of Ni/Ni while both surfaces are covered by H monolayer? In addition, the Pd-H bond strength is greater than the Ni-H one [41]. (*ii*) Why the Ni dissolution kinetics is slower on Pd(1ML)/Au(111)? According to Fig. 4.8b, K_{diss} and α_{diss} should be lower on Pd(1ML)/Au(111) than on Au(111) since the Ni dissolution kinetics is more sluggish on Pd(1ML)/Au(111) than on Au(111).

Thermodynamic considerations:

According to Eq. 4.8, the growth kinetic difference observed in Fig. 4.5 could also be explained by a negative shift of ϕ^{M}_{Nernst} on Pd(1ML)/Au(111) with respect to that on Au(111).

In practice, the Nernst potential of an electrochemical reaction may be estimated from different types of experiment. For a completely reversible system where both the oxidized and reduced species are ionic and in equal concentrations in the solution, the Nernst potential is usually determined from CV measurements and estimated as the median potential between the oxidation and reduction peaks. In systems where the reduced species is not ionic, such as in the case of electrodeposition, this method is not applicable. One must determine the current at the onset of deposition and dissolution and fit the plots using Butler-Volmer equation. However, the partial current linked to the Ni reduction process can not be determined in our case since it is masked by the HER reaction (see Fig. 4.2).

Another way to measure the Nernst potential is to find the potential for which the deposition current is equal to the dissolution current. This potential should coincide with stabilization potential used in Sec. 4.2.2. From such experiments we could not put in evidence a significant difference between the stabilization potential of a Ni monolayer on Au(111) and Pd(1ML)/Au(111). This is probably because the stabilization time (5 s) was quite short for practical reasons. In addition, for our system, additional oxydo–reduction reactions (e.g. H^+ and O_2 reductions) may influence the determination. We will see in Sec. 4.3 that in situ STM measurements allow one to perform potential-resolved measurements over long period of time and, thus, works close to the equilibrium conditions.

Hence, the Nernst potential on Pd(1ML)/Au(111) and on Au(111) can not be directly determined in the case of our study. However, the study related to the Ni dissolution curves on

the two different substrates gave us crucial information concerning the onset of the dissolution process on each substrate. As shown in Fig. 4.8b, there is an unambiguous shift of the Ni dissolution onset potential between Pd(1ML)/Au(111) and Au(111) substrates. Indeed, the dissolution onset of Ni(1ML) takes place on Pd(1ML)/Au(111) at $\phi_{Dissolution}^{Ni/Pd/Au(111)}$ = -0.90 V that is more negative than on Au(111) for which $\phi_{Dissolution}^{Ni/Au(111)}$ = -0.83 V ($\Delta\phi_{Dissolution}^{Ni} = \phi_{Dissolution}^{Ni/Au(111)} - \phi_{Dissolution}^{Ni/Pd/Au(111)}$ ~ 70 mV). However, $\Delta\phi_{Dissolution}^{Ni}$ has been determined by using a quasi-stationary method (i.e. LV) in which the conditions are fare from the equilibrium, source of possible discrepancy in their measured values. This apparent shift of the dissolution potential might also be caused by the electrochemical transfer kinetics.

Proving that $\Delta\phi_{Dissolution}^{Ni}$ really stems from a shift of the Nernst potentials requires independent experiments. Moreover, the current interpretation of the electrochemical data assumes that the Ni monolayer growth on Pd surface is also 2D. Even if this growth morphology was found in the case of Ni/Au(111) film, we have to check it on Pd(1ML)/Au(111). In other words, we have to ensure that the observed preferential behaviors cannot be attributed to different growth modes and structures of the Ni monolayer on Pd(1ML)/Au(111) compared to the ones for Ni(1ML) on Au(111). Consequently, at this moment, it is difficult to conclude on a possible shift in the Ni^{2+}/Ni Nernst potential. This point will be again addressed in the next section, based on STM investigations of the deposition and dissolution of metal monolayers.

b) Mechanism of H-desorption during deposition

In Sec. 4.2.2, we found that the crossover thickness $t^*_{Ni/Au}$ was roughly equal to 1 ML, in full agreement with previous STM observations [4, 17]. In the case of Ni growth on Pd(1ML)/Au(111), the values of $t^*_{Ni/Pd}$ were systematically found lower than 1 ML. While this discrepancy can not be rationalized in terms of growth morphology, we assumed that this point was correlated to the hydrogen re-adsorption process during the metal dissolution. Assuming this hypothesis allowed us to get acceptable results, in agreement with the Ni/Pd morphology determined by STM and presented below in Sec. 4.3. Obviously, the existence of such re-adsorption process requires that the H-monolayer was previously *desorbed* upon deposition. The following paragraph will detail the possible mechanism, at the atomic scale, accounting for the H-desorption or segregation during metal deposition.

Several mechanisms may be inferred. In the first one, the H-monolayer acts as a surfactant layer does in crystal growth. The H-monolayer is progressively transferred from the Pd surface on top of the Ni monolayer islands (or Co biatomic islands). A second possible

mechanism involves the existence of HER specific sites at the partially covered M/Pd surface. One may imagine that electrochemically reduced H^+ recombine with the H-adsorbed species present on the Pd surface to form molecular H_2 at the Ni or Co/Pd boundary (i.e. at the metal island steps). In both cases H-adsorption is expected to occur during the stripping of the metal adlayer because the protons in the solution can progressively react with the newly exposed Pd surface in the potential range where Ni or Co atoms are dissolved. More detailed (and also quite difficult) additional studies would be necessary to confirm such mechanisms.

4.2.5 Conclusions of electrochemical measurements

According to the above electrochemical characterizations, the growth kinetics of Co bilayer appears to be similar on Au(111) and Pd(1ML)/Au(111) surfaces (see Figs. 4.4) while the Ni monolayer growth is found to be *slower* on Pd(1ML)/Au(111) than on Au(111) (see Fig. 4.5). In the latter case, the observed difference in growth kinetics seems to decrease by applying a sufficiently negative potential, the electrochemical transfer becoming limited by the mass transport in solution. Concerning the dissolution process of Co bilayer and Ni monolayer (Fig. 4.8), it has been observed that the dissolution kinetics was lower on Pd(1ML)/Au(111) in both cases compared to the one on Au(111). In the specific case of Ni, we found that the dissolution process begins preferentially on Pd(1ML)/Au(111) but becomes slower than on Au(111) at sufficiently positive potential. Moreover, these data demonstrate that the multilayer growth of Ni (resp. Co) is *slower* than monolayer (resp. bilayer) growth. Similarly, the dissolution of Ni (resp. Co) multilayer films has also been found *slower* than the monolayer (resp. bilayer) dissolution process. Finally, the above data strongly suggest that the H-monolayer is *desorbed* from the Pd surface upon Ni or Co deposition.

4.3 Nucleation and growth processes of Ni and Co on *bimetallic* Pd/Au(111) surface

After a short review on the initial stages of Ni electrodeposition on Au(111) studied by STM, the following sections will focus on results of the study of Ni electrodeposition and dissolution on bimetallic Pd(*x*ML)/Au(111) substrate with *x* varying between 0.4 and 0.6 ML, abbreviated Pd/Au(111) hereafter, obtained by means of in situ STM measurements. The use of such bimetallic Pd/Au(111) substrate will allow one to compare directly the deposition and

dissolution of Ni ultrathin films on these two different surfaces and get better insight into the influence of the substrate chemical nature on the heteroepitaxial processes.

4.3.1 Overview of the Ni and Co growth on *monometallic* Au(111)

Nickel: Numerous in situ STM studies have shown that the nucleation and growth mechanism of Ni electrodeposition on Au(111) strongly depends on the applied overpotential and is furthermore influenced by the presence of the Au herringbone reconstruction [4, 17, 42, 43]. At a very small overpotential ($\eta \leq 80$ mV), the nucleation is driven by place exchange between Ni and Au surface atoms which occurs exclusively at the elbows of the reconstructed Au(111) (see Sec. 3.5.2). In the STM image of Fig. 4.9a (adapted from Ref. [4]), the embedded Ni atoms appear as small "holes" at the elbows (see black arrow). This direct deposition process is driven by a place exchange mechanism analogous to the one reported in UHV on the same surface [44]. Then, Ni monolayer islands are formed exclusively on top of the embedded Ni atoms and evolve to larger monolayer islands of compact, triangular shape pointed out by the white arrow in Fig. 4.9a. At an intermediate overpotential (100 mV $< \eta <$ 200 mV), the growth of Ni islands at the lower Au step edges begins (not shown) and presents a unique growth mechanism. As can be seen on image of Fig. 4.9b, the nickel growth proceeds via the formation of pseudomorphic, strongly anisotropic, needle-like monolayer islands (see white arrows), which are growing perpendicular to the pair of lines (domain walls) of the Au(111) reconstruction [42, 43]. These needles adopt a width of n x 11.5 Å, with $n \leq 5$, before strain relaxation occurs upon lateral expansion [43]. In these conditions, a full Ni monolayer may be deposited before the growth of subsequent layers. Since the characteristic features of the Ni growth behavior are solely related to effects unique to Ni/Au(111) i.e. the presence of the reconstruction, they find no analogue for Ni deposition on substrate which does no exhibit reconstruction phenomena such as on Ag(111) [38], or Cu(100) [45]. A slight increase of $\eta \sim 0.2$ V makes the above mechanism faster and a more classical isotropic step flow process is observed. At large overpotential ($\eta > 0.25$ V), homogeneous nucleation across the gold surface followed by layer-by-layer growth occurs as shown by in situ time resolved STM image of Fig. 4.9c. A rapid lateral expansion of the monatomic Ni islands proceeds up to full coverage of the gold surface and subsequent growth continues in a layer-by-layer mode [4, 17].

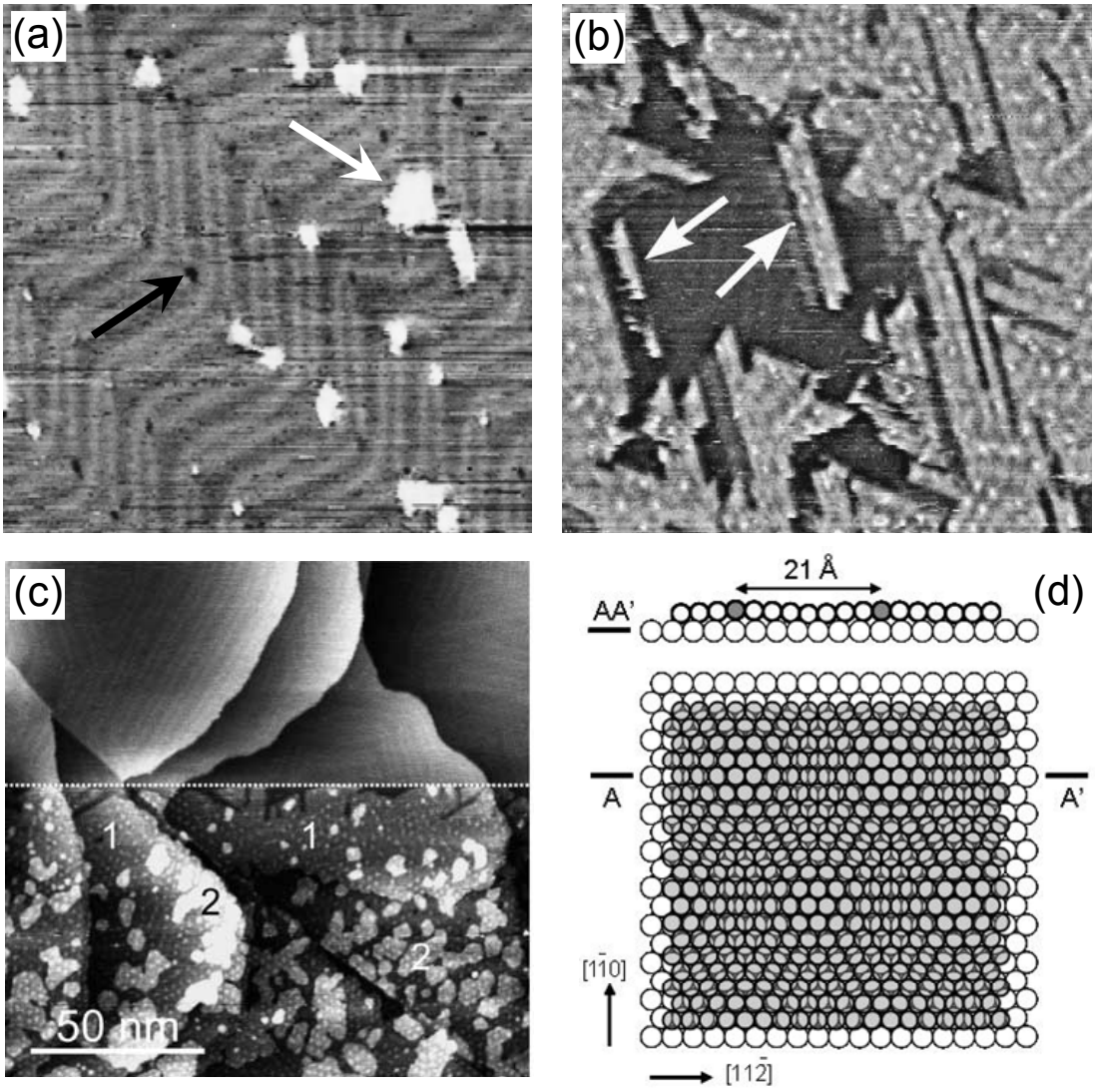

Figure 4.9: Series of STM images recorded on Au(111) showing (a) the slow nucleation and growth of Ni islands at the elbows of the herringbone reconstruction after 2 min at U_{dep} = -1.04 V and (b) the growth of Ni needles at U_{dep} = -1.08 V. STM images (71 x 71 nm²) were obtained in modified Watts electrolyte (10^{-2} M H_3BO_3 + 10^{-4} M HCl + 10^{-3} M $NiSO_4$). (c) STM image (150 x 150 nm²) showing the early stages of Ni growth at U_{dep} = -1.2 V in 0.1 M K_2SO_4 + 1 mM H_2SO_4 + 1 mM KCl + 1 mM $NiSO_4$. Numbers in images are the local thickness in ML. (d) Atomic model for 1 ML-thick Ni layer on Au(111). Cross sections AA' indicates that both atomic layers are assumed to have the same stacking. Adapted from Refs. [4, 17].

The excellent 2D wetting of the surface by Ni adatoms is rather surprising since Ni has a higher surface energy than Au(111): γ_{Ni} = 2.69 J.m^{-2} and γ_{Au} = 1.61 J.m^{-2} [46]. Therefore, 3D growth should be favored from a pure thermodynamic viewpoint. One likely explanation of the growth behavior is attributed to the presence of an H-adsorption layer on the Ni islands (hydrogen is evolved during deposition) which reduces the surface energy and probably favors surface adatom self-mobility as reported in the case of Ni/Ni(100) in the UHV [47]. The step

flow growth of the first layer observed at low η is probably due to selective direct deposition (no surface diffusion) at the substrate steps and at the rim of the metal islands. The incoming Ni^{2+} cations are preferentially discharged at such sites of larger coordination number. At larger η the discharge is irreversible and the adatoms diffuse on the surface and the growth is described by classical mean field theory of nucleation and growth [48]. Subsequent layer-by-layer growth stems from a favorable surface mobility on the H-terminated deposit and from a favorable interlayer transport.

On top of the Ni monolayer (Figs. 4.9b and c), it can be observed a long-range hexagonal pattern, named moiré structure. In the absence of rotation in the Ni overlayer relative to the Au(111) substrate lattice, the period of the moiré pattern can be expressed by $P = \frac{a_{Au} \times a_{Ni}}{(a_{Au} - a_{Ni})}$ [49] from which the deposit lattice parameter can be calculated taking a_{Au} = 2.88 Å. Fig. 4.9d presents the atomic model of the Ni /Au(111) interface for 1 ML-thick deposit (see cross section AA' in Fig. 4.9d). Under the above defined conditions, the presence of hexagonal symmetry of the moiré structure means that nickel grows (111) while the value of the moiré period ~ 21-22 Å indicates that a_{Ni} = 2.53 Å, which is 1.5% larger than the bulk distance ($a_{Ni,bulk}$ = 2.49 Å). The nickel layer is therefore essentially unstrained. Ex situ low incidence X-ray diffraction (XRD), after capping the film with Cu or Au, confirms that fcc Ni(111) is in epitaxy with Au(111).

Cobalt: There are fewer studies of Co/Au(111) growth [17, 23]. At very low overpotential, place exchange occurs [17]. Increasing sufficiently the overpotential makes the growth layer by layer as it is shown in Figure 4.10 [17]. Though the mechanism looks very similar to that of nickel at comparable overpotential [17], there are significant structural differences: the first cobalt layer is actually *biatomic* in height (it is 3.4 Å thick as measured by STM with respect to the gold surface) and next layers are monatomic (2 Å thick as measured by STM with respect to cobalt). The discrepancy between the apparent height and the real thickness of two atomic layers arises from variation of the tunneling barrier, which is larger on Co than on Au. A second difference with respect to Ni concerns the hex moiré pattern. It is 28 ± 1 Å on the bilayer and a 24 ± 1 Å on a trilayer film. Assuming that the moiré is not rotated with respect to the gold lattice and using the above formula yields to a strain amount equal to 4.6% in the Co bilayer and 2.5% in the trilayer.

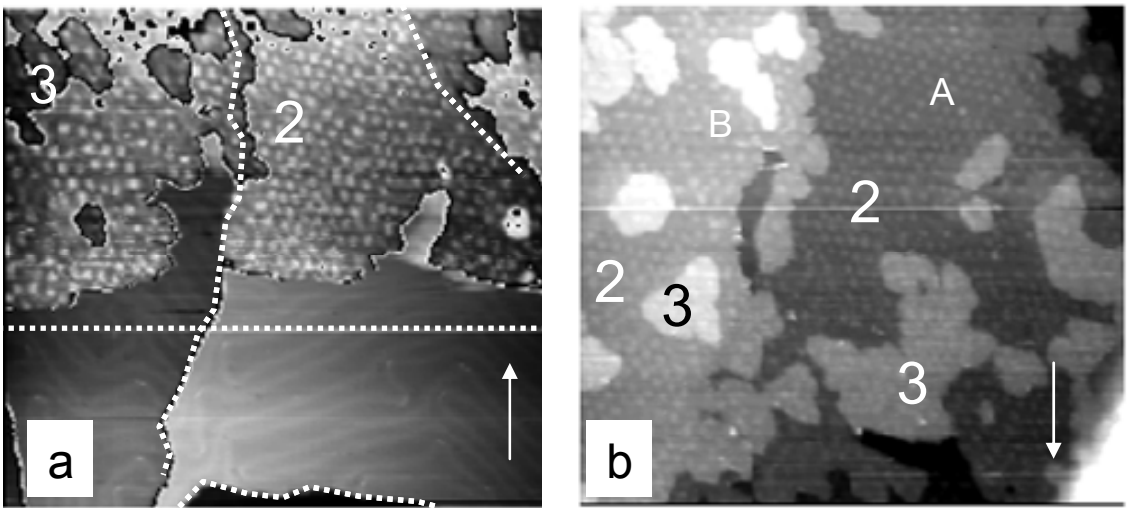

Figure 4.10: Sequence of STM images (100 x 90 nm²) showing the early stages of Co growth at U_{dep} = -1.30 V in 0.1 M K_2SO_4 + 1 mM H_2SO_4 + 1 mM KCl + 1 mM $CoSO_4$. Note the moiré structure on the bilayer and on the 3rd layer. Images were recorded 50 s apart. Numbers in images are the local thickness in ML. Adapted from Ref. [17].

4.3.2 Nucleation and monolayer growth of Ni on *bimetallic* Pd/Au(111) surface

As detailed in Chapter 3, the bimetallic Pd/Au(111) substrate was prepared in situ by electrodeposition of Pd on Au(111) at 0 V during 40 s in a 0.1 M H_2SO_4 + 0.05 mM H_2PdCl_4 solution. In these deposition conditions, the resulting bimetallic Pd/Au(111) substrate, as observed by in situ STM in Fig. 4.11a, consists of Au terraces decorated with ~ 0.5 ML of wide atomically flat Pd monolayer islands, which have mainly nucleated along the Au monoatomic high steps and also in the centre of large Au terraces. There is a pronounced height difference between Pd islands and the Au steps, which allows one to easily identify the Au/Pd boundary. The black dotted lines were used as landmark to locate the monoatomic step edges of the Au terraces while white dotted lines highlight the rims of Pd islands. The Au(111) substrate covered with 0.4-0.6 ML of Pd displays morphological features very well-suited to make comparative growth study.

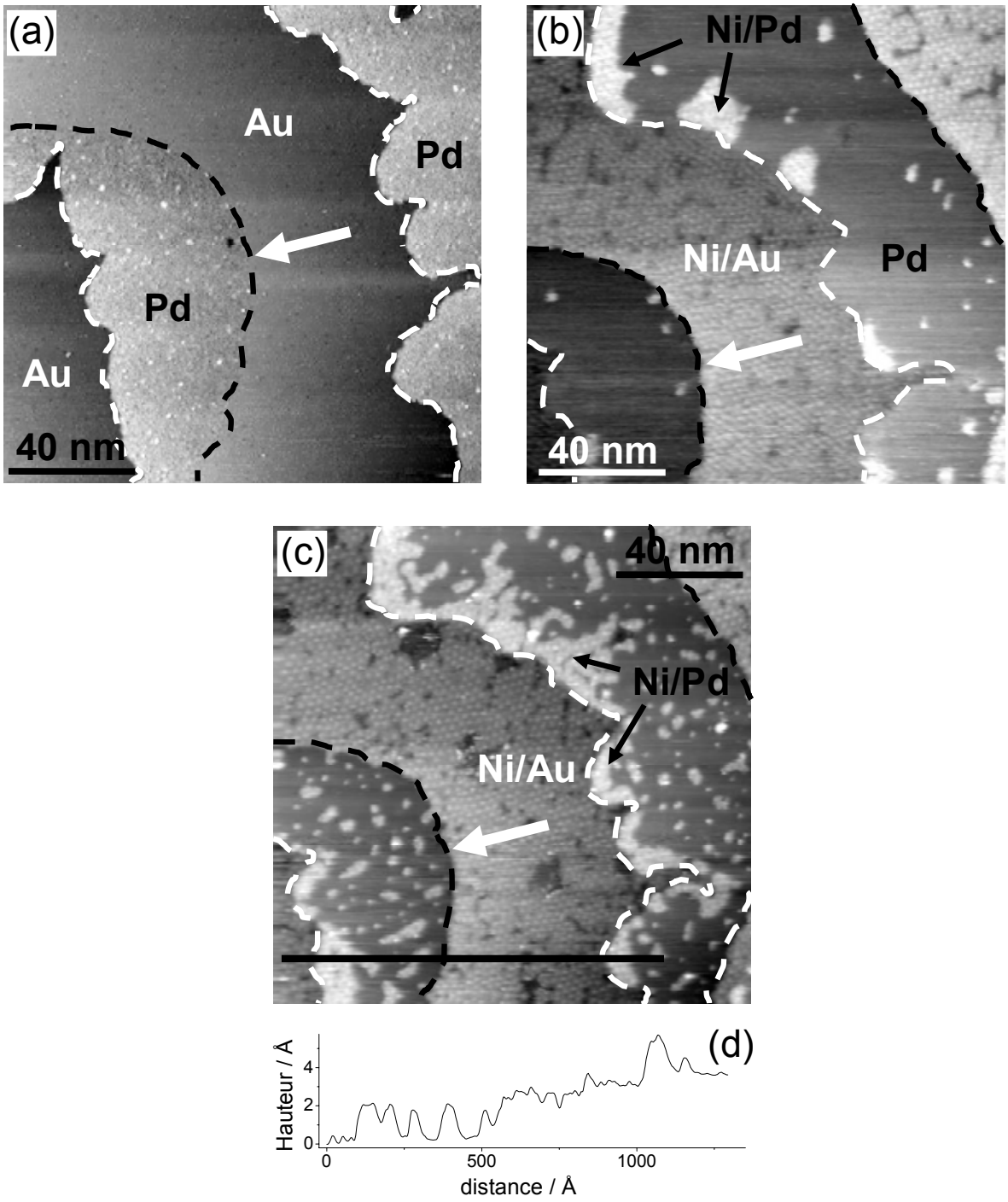

Figure 4.11: (a) STM image of the bare bimetallic PdAu surface recorded at U = -0.6 V. Dotted lines served as landmark to localize Pd islands. (b-c) STM images (151 x 151 nm^2), recorded at U_{stab} = -1.07 V, illustrating selective growth of Ni on the same surface spot at U_{dep} = -1.44 V for 0.6 s (b) and U_{dep} = -1.34 V for 2 s (c) in 0.1 M K_2SO_4 + 1 mM H_2SO_4 + 1 mM KCl + 1 mM $NiSO_4$. White arrows can be used as landmark to facilitate comparison despite the presence of a lateral drift. (d) Profile representing the cross-section along the black line at the bottom of (c).

Figs. 4.11b and 4.11c show the morphology of Ni electrodeposited on the same spot of the bare bimetallic substrate presented in Fig. 4.11a at U_{dep} = -1.44 V for 0.6 s (Fig. 4.11b) and U_{dep} = -1.34 V for 2 s (Fig. 4.11c) in 0.1 M K_2SO_4 + 1 mM H_2SO_4 + 1 mM KCl + 1 mM $NiSO_4$. In the Ni deposition potential range, Pd islands, unlike Au(111), are covered by an absorbed hydrogen layer [14] (see also Sec. 4.2). Ni was deposited with the STM tip withdrawn to avoid tip shielding effects during deposition and the Ni film is stripped off between successive experiments. The Ni monolayer can be identified by the long-range hexagonal pattern (moiré structure). It is straightforward to observe that Ni coverage ($\theta_{Ni/S}$ with S = Au(111) or Pd monoatomic islands) is not uniform throughout the bimetallic surface. Pd upper step edges appeared to be the preferential nucleation sites for Ni islands, which exhibit regular, compact shapes and relatively smooth perimeters. According to the profile presented in Fig. 4.11d, the Ni islands are monoatomic (1.74 Å ± 0.08 Å high). It can be noticed that preferential nucleation and growth at the Pd/Au boundary sites (see white arrows in Fig. 4.11a) is very limited. To be more quantitative, the Ni coverage was measured. The analysis consists, first, in calculating the respective surface occupied by Ni islands on Au terraces and on Pd islands and in dividing them by the initial bare surfaces of Au and Pd islands, which finally gives the corresponding Ni monolayer coverage on Au(111) ($\theta_{Ni/Au}$) and on Pd islands ($\theta_{Ni/Pd}$). In Figs. 4.11b and 4.11c, $\theta_{Ni/Au}$ = 0.95 with the total absence of second layer islands. In contrast, $\theta_{Ni/Pd}$ is only 0.1 in Fig. 4.11b and 0.3 in Fig. 4.11c.

We checked that the above selectivity occurs also at larger overpotential. Fig. 4.12 shows that Ni is still preferentially electrodeposited on the Au(111) surface at U_{dep} = -1.5 V (deposition time 20 and 40 s). The Ni concentration was reduced (0.25 mM) to obtain a submonolayer Ni coverage on Au(111). The Pd islands remain only marginally covered with nickel: $\theta_{Ni/Au}$ = 0.35 and $\theta_{Ni/Pd}$ = 0.1 in image (a); $\theta_{Ni/Au}$ = 0.72 and $\theta_{Ni/Pd}$ = 0.2 in image (b). The characteristics of the Ni monolayer are the same as in Fig. 4.11.

Hence, these STM images show that Ni growth is kinetically hindered on the Pd monatomic islands as compared to Ni/Au(111). This observation fits very well with electrochemical characterizations on monometallic Au(111) and Pd(1ML)/Au(111) surfaces (see Sec. 4.2.2). Fig. 4.11 further demonstrates that the Ni growth on the Au terraces of the bimetallic Pd/Au(111) substrate is also 2D and the Ni monolayer is essentially unstrained (P ~ 21 Å). Further STM observations at very low overpotential point out that noticeable Ni deposition on Pd islands requires applying $U_{dep} \leq$ -1.10 V = $\phi_{Deposition}^{Ni/Pd/Au(111)}$, which is 90 mV more negative than the Ni deposition onset on Au(111) ($\phi_{Deposition}^{Ni/Au}$ = -1.01 V).

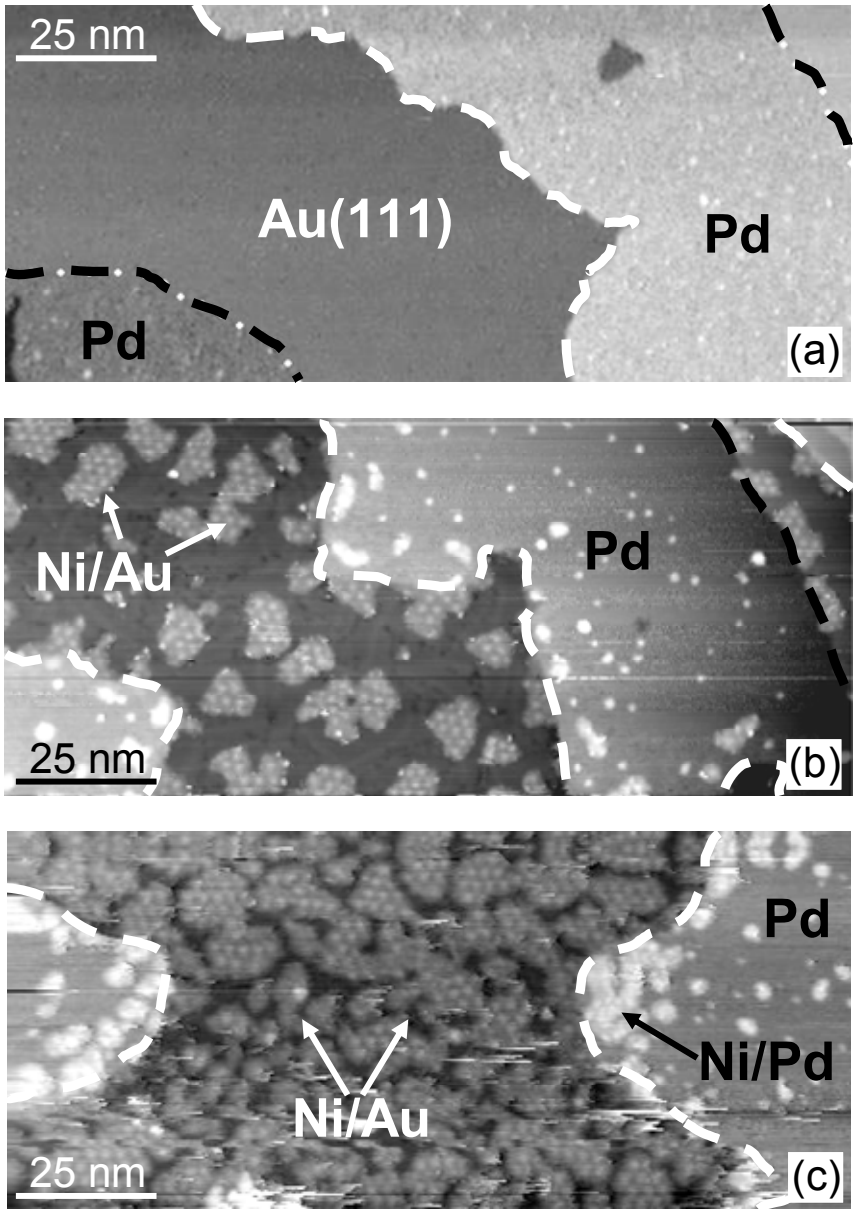

Figure 4.12: Sequence of STM images (150 x 70 nm²) showing the early stages of Ni growth at U_{dep} = -1.50 V in 0.1 M K_2SO_4 + 1 mM H_2SO_4 + 1 mM KCl + 0.25 mM $NiSO_4$ during (a) 20 s and (b) 40 s. Images were recorded at U = -1.07 V.

Fig. 4.13 presents another series of STM images of Ni growth process on bimetallic substrate. They were obtained after Ni deposition on Pd(0.6ML)/Au(111) at U_{dep} = -1.24 V, for increasing deposition times (5, 9 and 13 s). Fig. 4.13a shows that Ni islands on Pd monoatomic islands are preferentially localized close to the Pd step edges although a non negligible number of Ni islands are found in the centre of Pd islands. Then, by increasing the deposition time (Figs. 4.13b and 4.13c), the completion of the 1st Ni layer on Pd islands occurs via lateral growth from the step edges to the centre of the Pd islands. This indicates that Ni/Pd growth is also 2D as on Au(111). During Ni monolayer growth on Pd islands for which $\theta_{Ni/Pd}$ increases from 0.42 to 0.95,

Ni coverage on Au(111) slightly varies between 0.85 and 0.96 and the growth of the second Ni layer on Au is rather limited indicating that the growth rate is much faster in the submonolayer regime than in the multilayer regime. According to these results, the monolayer deposition rate is 0.18 $ML.s^{-1}$ for Ni on Au(111) and 0.07 $ML.s^{-1}$ for Ni on Pd islands, which is in qualitative agreement with electrochemical measurements performed on *monometallic* substrates (Sec. 4.2). Hence, the bimetallic Pd/Au(111) surface can be uniformly covered by a full Ni monolayer due to the existence of slower multilayer growth kinetics on both Pd islands and Au(111).

Fig. 4.14a shows that Ni monolayer on Pd monoatomic islands also exhibits a moiré structure with a period of 21-22 Å, which is equal to the one found for Ni/Au(111). This demonstrates that the Ni monolayer is relaxed across the whole bimetallic surface and that the underlying Pd monolayer remains *pseudomorphic* with the Au(111) substrate even upon Ni deposition. Consequently, the Ni selective growth observed on Au(111) from STM experiments as well as electrochemical measurements, cannot be attributed to different in-plane stress of the Ni layer. Moreover, zooming on the surface (see Fig. 4.14b) reveals that the moiré pattern of Ni/Pd displays an unusual unit cell composed of dark triangular-shaped holes surrounded by three triangular-shaped bright mounds whereas on Ni/Au, the unit cell has a single bright one. Interestingly, such a shape has never been observed for Ni monoatomic thick layers deposited under UHV on Pt(111) [50], Ru(111) [51] as well as under electrochemical conditions on Ag(111) [37]. The origin of this specific moiré pattern shape might be of electronic nature and directly linked to the Ni/substrate interaction.

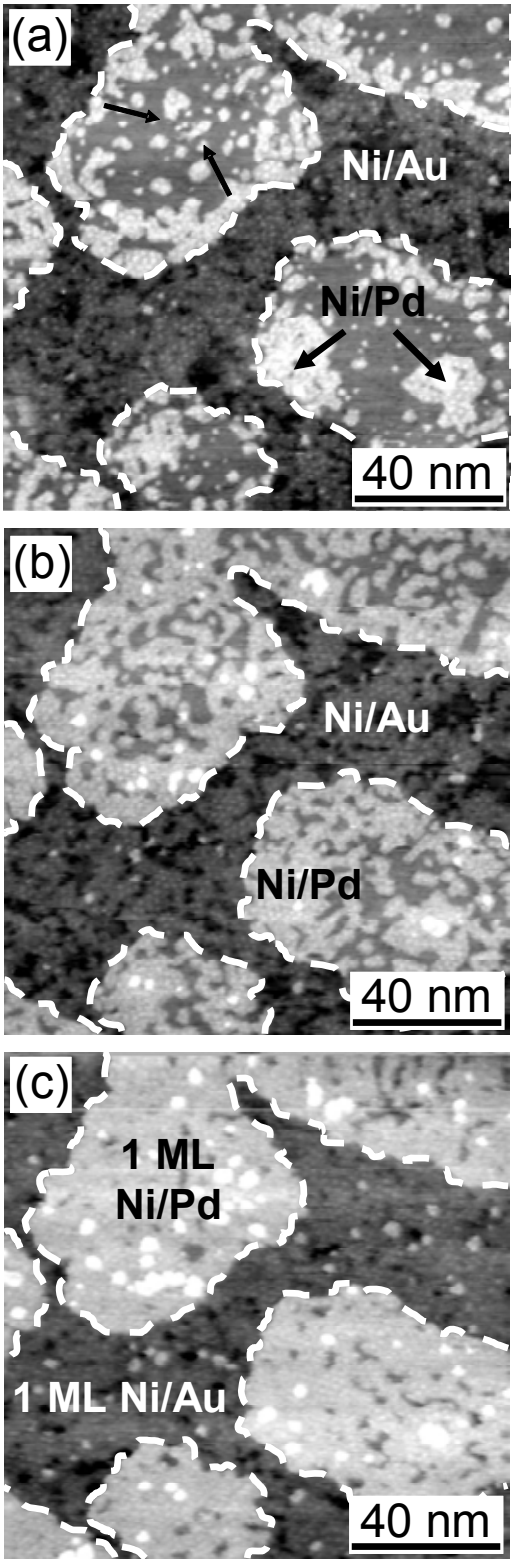

Figure 4.13: Series of STM images (136 x 136 nm²) showing selective growth of a complete Ni monolayer on the same surface spot of the bimetallic PdAu surface. Ni deposits were successively deposited at U_{dep} = -1.24 V in 0.1 M K_2SO_4 + 1 mM H_2SO_4 + 1 mM KCl + 1 mM $NiSO_4$ for (a) 5 s, (b) 9 s and (c) 13 s. The images were recorded at U_{stab} = -1.07 V.

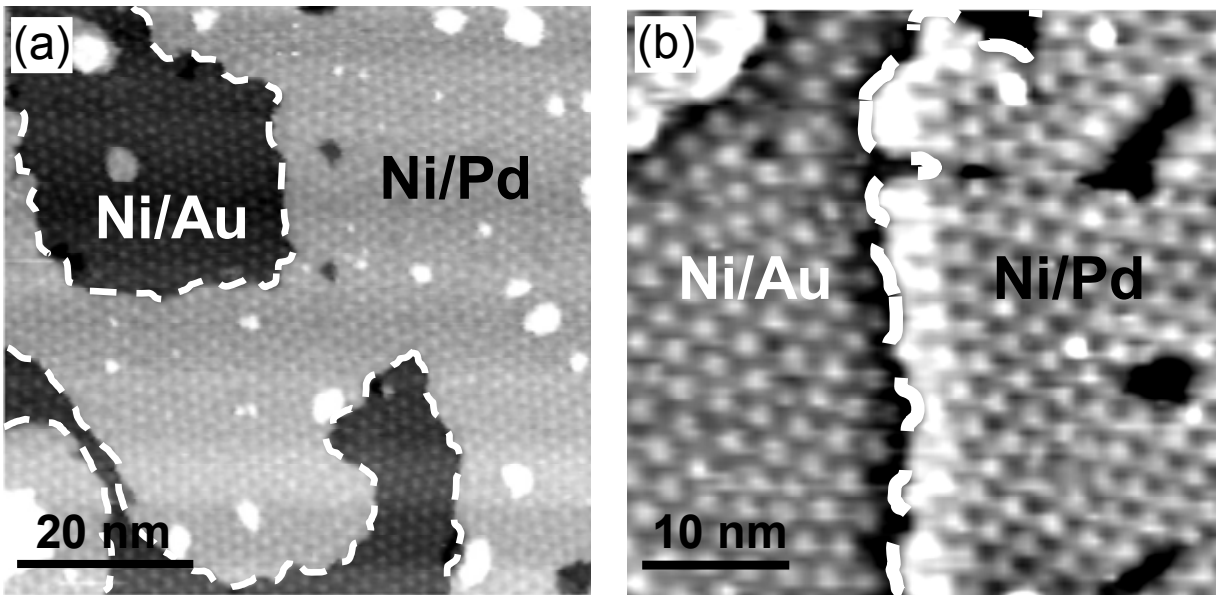

Figure 4.14: (a) STM image (100 x 100 nm²) of the complete Ni monolayer deposited on bimetallic PdAu surface at U_{dep} = -1.24 V for 20 s, and recorded at U_{stab} = -1.07 V. (b) Filtered STM image (40 x 40 nm²) of the boundary region between Au(111) substrate and Pd islands covered by a Ni monolayer. The period of the hexagonal moiré structure on Ni(1ML)/Au(111) is identical to that on Ni(1ML)/Pd(1ML)/Au(111) (21-22 Å).

4.3.3 Multilayer Ni growth on *bimetallic* Pd/Au(111) surface

Fig. 4.15 shows the morphology of multilayer Ni films deposited on bimetallic substrate at -1.34 V on Pd/Au(111) for two different deposition times (30 and 45 s). In Fig. 4.15a, second Ni layer islands have grown on the smooth Ni-monolayer-covered terraces of Au(111) and Pd surfaces, and exhibit isotropic and rounded edge shapes. Also a very small amount of third layer islands have nucleated on the larger second layer islands. For longer deposition time (Fig. 4.15b), growth of the second layer is almost completed on Pd while islands of the third atomic planes have grown. On the Au surface, Ni second layer coverage is not complete. Hence, multilayer Ni film morphologies are in agreement with a layer-by-layer growth morphology on Au(111) as well as on Pd monoatomic islands in this thickness range. Besides, second and third Ni atomic plane are ~ 2 - 2.2 Å high, independently of the surface. Similar value was reported for multilayer Ni films on Au(111) [4, 17]. Also, moiré patterns are well ordered on both surfaces and can be resolved on the bi- and tri-layer. The periodicity of the moiré pattern for Ni (2^{nd} and 3^{rd} ML) is equal to 21-22 Å on both surfaces. The moiré of the second Ni layer on Ni(1ML)/Pd islands does no longer exhibit the unusual unit cell described above and is now similar to the one for Ni(2^{nd} ML) on Au(111). The corrugation of the modulation decreases with increasing Ni thickness, especially on for layers deposited on Pd substrate.

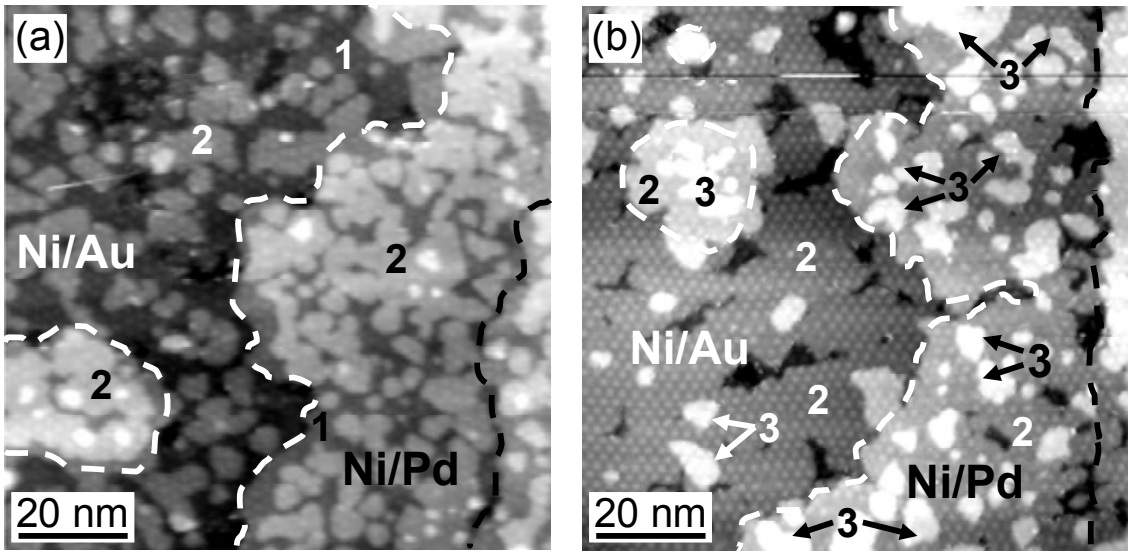

Figure 4.15: STM images (100 x 100 nm²) showing the morphology of multilayer Ni films, deposited on bimetallic PdAu surface at U_{dep} = -1.34 V in 0.1 M K_2SO_4 + 1 mM H_2SO_4 + 1 mM KCl + 1 mM $NiSO_4$ for (a) 30 s and (b) 60 s. The images were recorded at U_{stab} = -1.07 V. Figures N inside images are the local number of Ni atomic monolayers.

4.3.4 Quantitative analysis of Ni growth on *bimetallic* Pd/Au(111) surface

STM image analysis of numerous deposition experiments was conducted to get quantitative insights into the growth process on bimetallic substrate. Fig. 4.16 compares the variation of Ni coverage on Au(111) ($t_{Ni/Au}$) and Pd monoatomic islands ($t_{Ni/Pd}$) as a function of the nickel *average* thickness t_{Ni} during the growth process (black filled symbols in Fig. 4.16). The open symbols in Fig. 4.16 correspond to the electrochemical measurements (dissolution) performed on *monometallic* substrates, i.e. Au(111) and Pd(1ML)/Au(111) (see Sec. 4.2). Note that the data are corrected for the H adsorption in the case of Pd.

Within the Ni monolayer growth regime, a clear selectivity between Pd islands and Au(111) is observed. This phenomenon is reproducible and independent of the deposition potential. In the early stages of Ni growth, the 1st Ni layer coverage on Au(111) increases rapidly up to ~ 1 while Ni coverage on Pd stays negligible. Above ~ 0.4 ML, $\theta_{Ni/Au}$ levels off close to 1 while $\theta_{Ni/Pd}$ slowly increases up to 1. It is straightforward to see that the complementary electrochemical measurements are consistent with the STM observations.

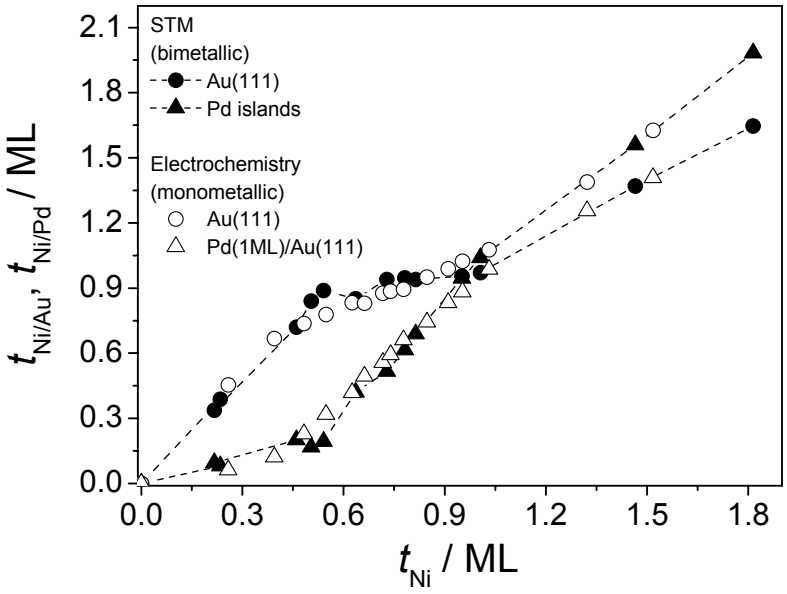

Figure 4.16: Variation of Ni thickness on Pd monoatomic islands ($t_{Ni/Pd}$) and Au(111) ($t_{Ni/Au}$) vs. the average Ni thickness t_{Ni}. Data are derived from quantitative STM image analysis recorded during Ni deposition (black filled symbols) of a Ni monolayer on bimetallic Pd(0.5ML)/Au(111) surface. Open symbols refer to macroscopic electrochemical measurements on *monometallic* surfaces (see Sec. 4.2).

In the multilayer regime (t_{Ni} > 1ML) the growth selectivity is much smaller. The slight difference between $\theta_{Ni/Au}$ and $\theta_{Ni/Pd}$ for t_{Ni} > 1ML is not considered as significant for several reasons. (*i*) The nucleation of the next Ni layers is affected by defects in the first monolayer, which induces uncontrolled local variations. (*ii*) Image analysis becomes much more difficult and less numerous sequences could be analyzed.

The excellent agreement obtained between the macroscopic (electrochemical) measurements and the microscopic (STM) observations demonstrates that the selective deposition observed by STM does not arise from interlayer transport of Ni adatoms from the Pd islands onto the Au terraces. Therefore, the origin of the selective growth of Ni on *bimetallic* Pd/Au(111) substrate can not be explained in terms of difference in Ni adatom surface mobility. It has to be mentioned that the good agreement between the electrochemical measurements and the STM observations in Fig. 4.16 is only obtained if we consider that the H adsorbed on Pd, before Ni deposition, desorbs upon Ni deposition and re-adsorbs on Pd upon Ni dissolution.

4.3.5 Co deposition on *bimetallic* Pd/Au(111) surface

This system was very briefly investigated to compare the film morphology on both surfaces. Fig. 4.17 shows in situ STM images of a Pd/Au(111) surface before (image a) and after (image b) the growth of a cobalt film at U_{dep} = -1.3 V for 5 s in 0.1 M K_2SO_4 + 1 mM H_2SO_4 + 1 mM KCl + 1 mM $CoSO_4$. The initial bimetallic surface (image a corresponds to the area contained in the dashed rectangle of image b) presents Pd monatomic islands which have nucleated at the gold steps but also somewhat homogeneously on Au(111) terraces. Co deposition (image b) does not modify the overall morphology of the surface because the cobalt film perfectly replicates the entire surface structure. Height measurements in the few vacancy islands in the film indicate that a Co biatomic layer is formed on both Au (apparent height 3.4 Å) and Pd (apparent height 3.5 Å). The measured height by STM is therefore similar on both surfaces. The fact that it is smaller than expected from crystallographic considerations is assigned to variation of the tunneling barrier across the surface. This change was quantitatively accounted in the case of Co/Au(111) [17]. In image (c), the film is dissolved by applying a positive ramp of potential (sr = 10 $mV.s^{-1}$) while scanning the STM tip. No peculiar kinetic difference was observed during the dissolution, in agreement with electrochemical data (Sec. 4.2). Finally, on the scale of images, the surface morphology looks identical before (image a) and after Co deposition/stripping sequence (image c), suggesting that no major interface alloying has occurred on the time scale of the experiment. At higher magnification, Figs. 4.17e-f show the existence of a moiré structure of periodicity equal to 25 Å on Au(111) and 22 - 23 Å on Pd(1ML)/Au(111). This difference means that the Co bilayer is a bit less strained on the Pd monolayer. This point was not studied into more details.

Even if the above STM observations are not fully complete, they enable one to prove that the values of ~ 2 ML found for the crossover thicknesses $t^*_{Co/Au}$ and $t^*_{Co/Pd}$ in Fig. 4.4 are consistent with STM observations. Indeed, Fig. 4.10 demonstrates that the next atomic planes nucleate after the completion of the bilayer over the entire bimetallic surface. This fact is well known for Co/Au(111) [17], not for Co/Pd(111). To the best of our knowledge, Co/Pd growth has never been studied. For Co coverage close to the unity, the above sequence of STM images tend to demonstrates that there is no selective process in case of Co deposition, in conditions similar to those used for Ni. For Co submonolayer coverage (not shown), series of STM images show that Co deposition/dissolution occurs at a similar rate on Au(111) and Pd islands in agreement with electrochemical measurements.

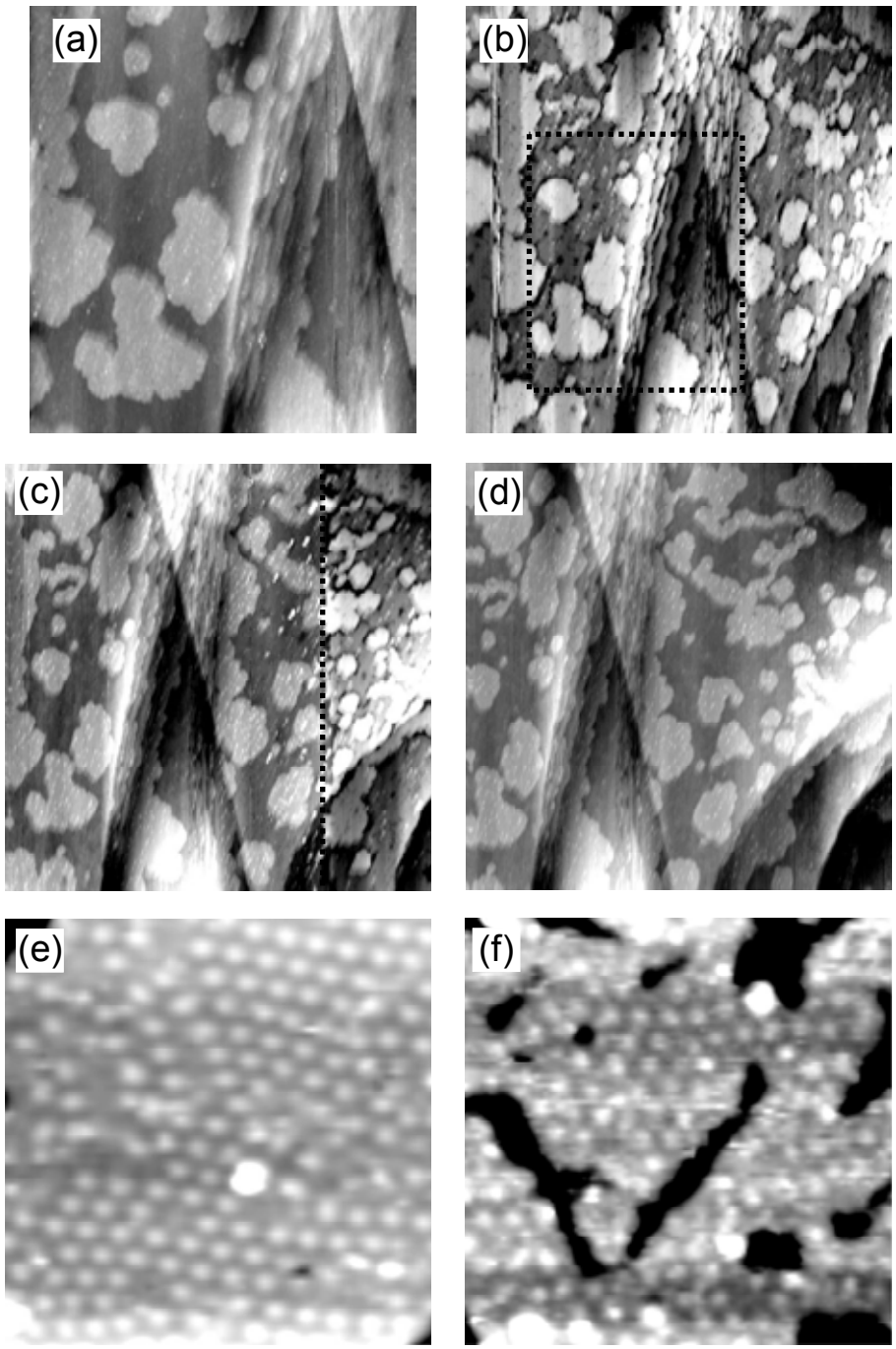

Figure 4.17: (a-d) Series of STM images showing the growth and the dissolution of a complete Co bilayer on the same surface spot of the bimetallic Pd/Au(111) surface. Co was deposited at U_{dep} = -1.30 V in 0.1 M K_2SO_4 + 1 mM H_2SO_4 + 1 mM KCl + 1 mM $CoSO_4$ for 5 s and dissolved by a ramp of potential (sr = 10 mV.s^{-1}). (a) (200 x 180 nm^2), (b-d) (500 x 500 nm^2). (e-f) STM images (33 x 33 nm^2) showing the moiré structure on Co(2ML)/Au(111) (left) and Co(2ML)/Pd(1ML)/Au(111) (right). Images were recorded at U_{stab} = -1.14 V.

Contrary to the case of nickel, the rates of cobalt deposition and dissolution are equal on Au(111) and Pd(1ML)/Au(111). At first sight this difference looks strange because Ni and Co present strong similarities in terms of physical and chemical properties. Their metallurgy with Au or Pd are not such dissimilar. From an experimental viewpoint, the only obvious difference is that Co growth begins, both on Au(111) and Pd(1ML)/Au(111) (see Sec. 4.3), with the formation of a *biatomic* layer and not by one single atomic monolayer (Fig. 4.4 and 4.5). It can be postulated that the presence of the second Co atomic layer on top of the first one stabilizes it and therefore reduces the influence of Co-Pd interactions on deposition or dissolution. It means that these processes should be mainly governed by the activation energy to break (respectively form) the Co-Co bond rather than the Co-S bond with S = Au or Pd, leading to $\Delta\phi^{Co}_{Dissolution} = \phi^{Co/Au(111)}_{Dissolution} - \phi^{Co/Pd/Au(111)}_{Dissolution} = 0$. The analogy with multilayer growth/dissolution finds nevertheless some limit since it remains very intriguing that the Co bilayer growth rate is much faster than that of next atomic planes.

4.4 Ni dissolution process on *bimetallic* Pd/Au(111) surface

4.4.1 Dissolution of Ni monolayer on *bimetallic* Pd/Au(111) surface

In order to prove the existence of a shift in the Ni dissolution onset potential between Pd and Au substrates found from electrochemical measurements, we performed in situ and time-resolved STM measurements of the Ni dissolution process under electrochemical steady state conditions as close as possible to the equilibrium.

Fig. 4.18 shows a sequence of STM images illustrating the dissolution of 1 ML Ni film homogeneously covering the bimetallic substrate. Fig. 4.18a displays the Ni monolayer deposited at U_{dep} = -1.24 V during 20 s and imaged at U_{stab} = -1.07 V. The 1st Ni layer coverage is $\theta_{Ni/Pd}$ = 0.96 and $\theta_{Ni/Au}$ = 0.92. Between Fig. 4.18a and Fig. 4.18b, the electrode potential was gradually increased up to -1.02 V. At this potential, the dissolution begins exclusively at the edges of the few vacancy islands contained in the Ni monolayer deposited on Pd islands (black arrows). In Fig. 4.18c, recorded 17 min later at the same potential, dissolution has obviously progressed from the Ni edges without any noticeable dissolution of Ni deposited on Au(111), despite the presence of vacancy islands in the Ni/Au(111) layer. After 38 min (Fig. 4.18d), half of Ni layer deposited on Pd monolayer islands has been dissolved ($\theta_{Ni/Pd} < 0.5$) with no dissolution in the Ni layer on Au(111). At this potential, complete *selective* dissolution of Ni monolayer from Pd islands was

achieved after 55 min leaving Ni layer exclusively present on Au(111) (not shown here due to loss of the tip resolution).

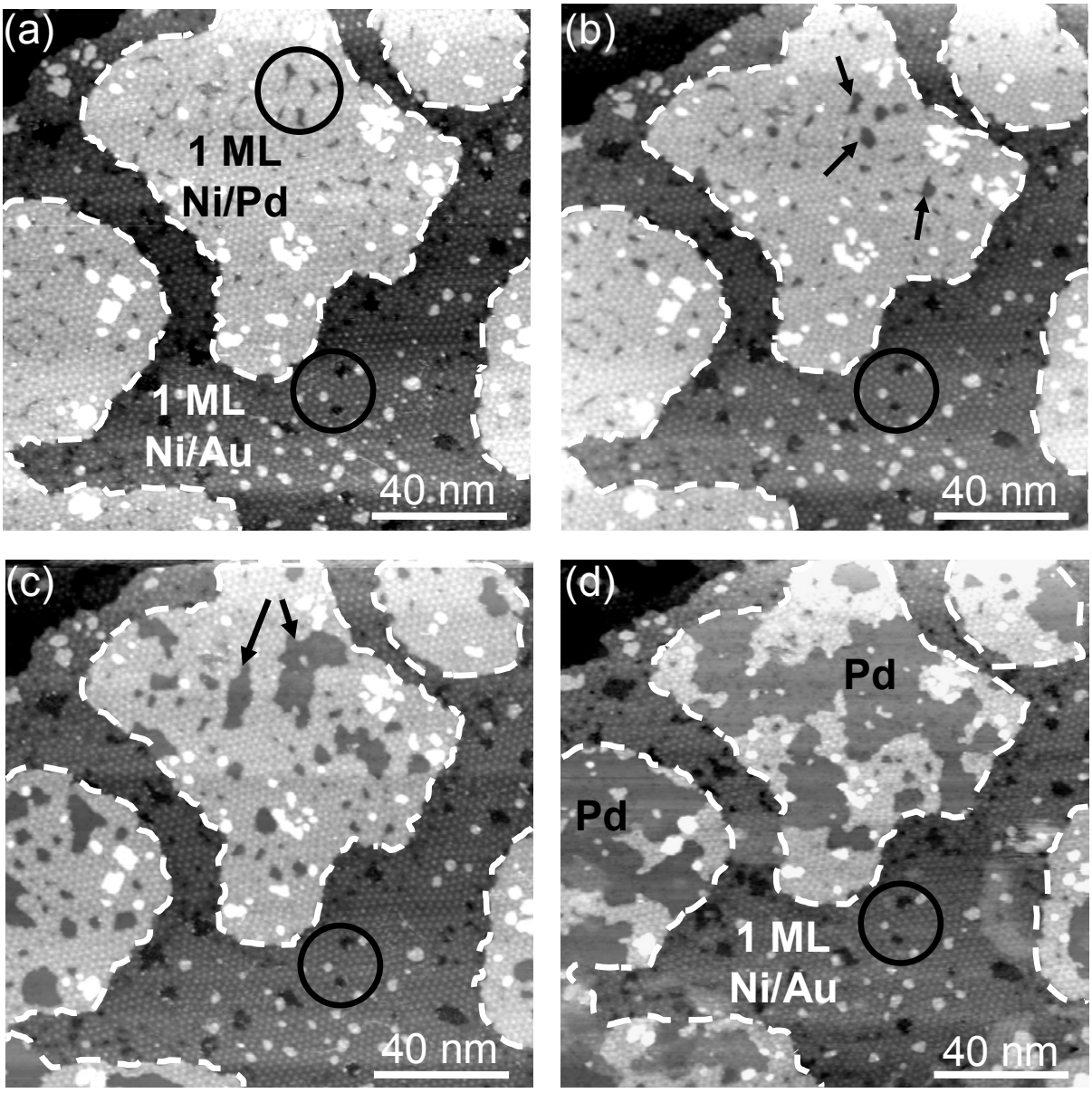

Figure 4.18: Series of STM images (155 x 155 nm²) showing the dissolution of a full Ni monolayer ($\theta_{Ni/Pd} = \theta_{Ni/Au} \sim 1$) which was deposited on Pd(0.5ML)/Au(111) at U_{dep} = -1.24 V for 20 s. Images were recorded (a) at U_{stab} = -1.07 V and successively at U = -1.02 V after (b) 4, (c) 17 and (d) 38 min.

Indeed, selective dissolution of Ni can be achieved by careful adjustment of the electrode potential. The result of this selective dissolution process is illustrated for another series of Ni dissolution experiment shown in Fig. 4.19 for which the Pd/Au(111) surface was initially covered by one complete monolayer of Ni. After 59 min at $\phi_{Dissolution}^{Ni/Pd/Au(111)}$ = -1.02 V (Fig. 4.19a), the Ni

coverage on Au is still close to unity ($\theta_{Ni/Au}$ = 0.94) while the Pd islands are *completely* bare. Dissolution of the Ni monolayer on Au(111) required increasing the electrode potential to $\phi_{Dissolution}^{Ni/Au(111)}$ = -0.98 V. In Fig. 4.19b, the Ni monolayer is totally removed from the Au surface. One also notices some coarsening of the islands left on Pd. The nm monatomic islands left after dissolution (equivalent coverage < than 5 %) are probably Pd islands since they are electrochemically stable. Their origin remains unclear. One possible might be interface alloying.

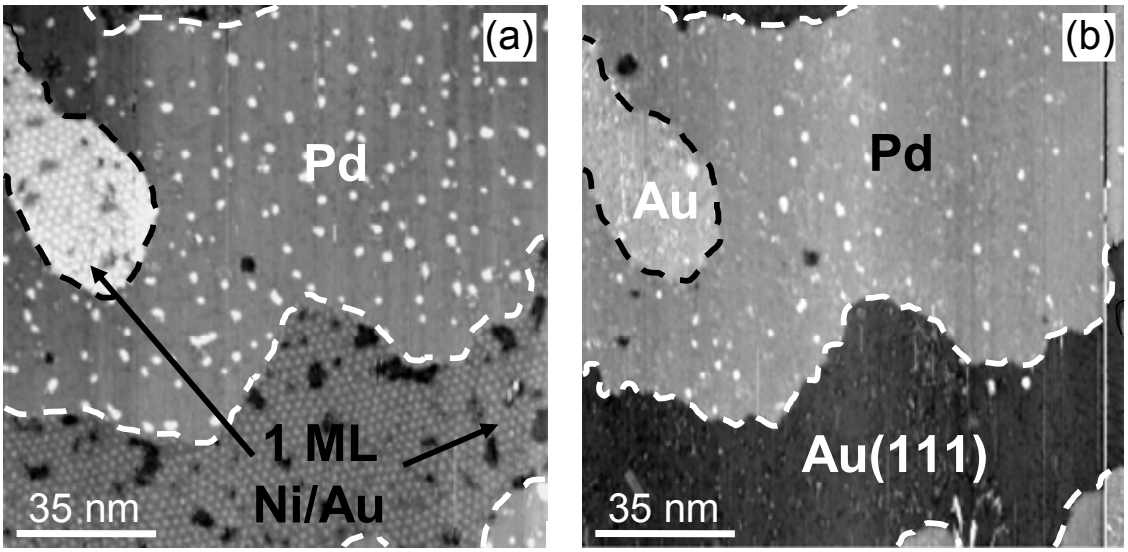

Figure 4.19: STM images (136 x 136 nm^2) showing (a) the results of the complete selective dissolution of Ni from Pd islands achieved after 59 min at U = -1.02 V in 0.1 M K_2SO_4 + 1 mM H_2SO_4 + 1 mM KCl + 1 mM $NiSO_4$, leaving Ni monolayer exclusively present on Au(111) ($\theta_{Ni/Au}$ = 0.94) and (b) the bare bimetallic surface after Ni dissolution on Au(111).

Given the selective dissolution process observed in Fig. 4.18 and the final state of the surface at -1.02 V (Fig. 4.19a) we infer that the dissolution onset potential is $\phi_{Dissolution}^{Ni/Pd/Au(111)}$ = -1.02 V, since at this potential, complete *selective* dissolution of Ni monolayer from Pd islands is achieved while the Ni monolayer remains intact on Au(111). Therefore, by comparing the results for Ni dissolution on Pd islands and on Au terraces, we conclude that there exist a shift of the dissolution onset potential $\Delta\phi_{Dissolution}^{Ni} = \phi_{Dissolution}^{Ni/Au(111)} - \phi_{Dissolution}^{Ni/Pd/Au(111)} = 40 \pm 10$ mV. This result confirms the existence of a shift $\Delta\phi_{Dissolution}^{Ni}$ detected from electrochemical measurements on monometallic substrates. However, the value measured from STM is almost two times smaller than the one found from electrochemical measurements. The probable origin of such discrepancy will be discussed later on.

4.4.2 Influence of anions

As metal dissolution can be significantly influenced by the presence of specifically adsorbed anions on the electrode surface [52, 53], the following section will be devoted to the study of the possible influence of anion adsorption on the existence of selective process during the dissolution of Ni from Pd/Au(111).

Previous investigations of the Ni deposition and dissolution mechanisms by means of electrochemical [54-60] and X-ray scattering [61] techniques strongly support the presence of a coadsorbed species on top of the Ni deposit. Hydrogen, OH^-, SO_4^{2-}/HSO_4^{2-} or water, and Ni^+ species were suggested as possible adsorbates. Unfortunately, imaging by STM such small adsorbates on a metallic surface is very challenging unless adsorbates profoundly alter the local density of states. Most often adlayer is "transparent" in usual tunneling condition and one visualizes the metal surface [53]. Therefore it will be even more difficult to obtain indication on the chemical identity of the adsorbates [4, 17].

In our case, the supporting electrolyte (SE: 0.1 M K_2SO_4 + 1 mM H_2SO_4 + 1 mM KCl) contains mainly sulfates (SO_4^{2-}) and chloride (Cl^-) in much lower concentration. Both anions are known to possess a weakly bound solvation shell, which can be easily striped to form a direct chemical bond with the metal surface, resulting in an ionic surface concentration that exceeds that given by pure electrostatic interactions. For instance, the role of Cl^- in the breakdown of the passive film on Ni surface [62, 63] and in the dissolution of Cu in HCl solution [64] have been clearly established. In the latter case, it involves the formation of a Cl_{ads} intermediate species and Cu is dissolved as $CuCl_2^-$. Sulfate (SO_4^{2-}) is less specifically adsorbed than Cl^- although it was shown in early studies that SO_4^{2-} considerably affects the electrochemical responses of metal electrode such as of Au and Pt single crystals [65, 66]. Thus, one may wonder whether specific adsorption of SO_4^{2-} and/or Cl^- on top of the Ni monolayer is at the origin of the observed selective dissolution of Ni from Pd islands.

The Ni dissolution experiment was therefore repeated in other electrolytes in order to change the nature of the contained ionic species. First, the chloride was removed from the electrolyte. With the aim of removing any trace impurity of Cl^-, the Pd deposition has been performed by using $PdSO_4$ salt rather than K_2PdCl_4 salt i.e. in 0.1 M H_2SO_4 + 0.05 mM $PdSO_4$. Then, the study of the Ni deposition and dissolution processes were carried out in 0.1 M K_2SO_4 + 1 mM H_2SO_4 + 1 mM $NiSO_4$. Fig. 4.20a shows that in Cl^- free solution *complete* selective Ni dissolution from Pd is still observed at -1.02 V, similar to the one shown in Fig. 4.19. Second, in order to discard any influence of specific adsorption from SO_4^{2-} on the existence of selective dissolution process, SO_4^{2-} were replaced by perchlorate (ClO_4^-), which are well known to be not

specifically adsorbed on metal electrode [67]. The electrolyte used in that case corresponds to 0.1 M $KClO_4$ + 1 mM $HClO_4$ + 1 mM $Ni(ClO_4)_2$. Fig. 4.20b shows again that complete selective dissolution occurs at -1.02V. Using strongly adsorbed ions (Cl^- and SO_4^{2-}) or weakly adsorbed ions (ClO_4^-) had no significant impact on the dissolution selectivity, excluding thus the contributions of the anions to this behavior.

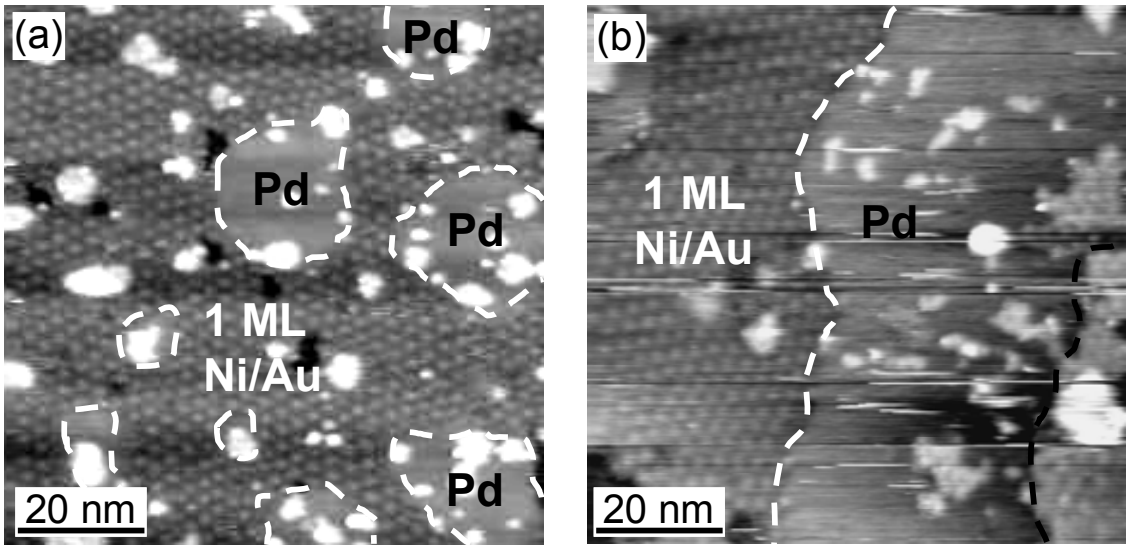

Figure 4.20: STM images (85 x 85 nm²) showing the complete selective dissolution of Ni from Pd islands in other electrolytes. (a) Sulphate electrolyte: first, Pd was deposited from 0.1 M H_2SO_4 + 0.05 mM $PdSO_4$ and, then, the deposition and dissolution processes of Ni were performed in 0.1 M K_2SO_4 + 1 mM H_2SO_4 + 1mM $NiSO_4$. (b) Perchlorate electrolyte: first, Pd was deposited from 0.1 M H_2SO_4 + 0.05 mM K_2PdCl_4, and then the deposition and dissolution processes of Ni were performed in 0.1 M $KClO_4$ + 1 mM $HClO_4$ + 1 mM $Ni(ClO_4)_2$.

4.4.3 Dissolution of multilayer Ni films on *bimetallic* Pd/Au(111) surface

Fig. 4.21 shows the dissolution of a multilayer Ni film (deposited at -1.34 V for 45 s) where the bimetallic surface is initially covered by a total Ni amount of 2 ML on Pd islands and 1.5 ML on Au(111). Difference in Ni amount on Pd islands vs. Au(111) is consistent with observations made in Sec. 4.3.3. Noticeable dissolution begins at potentials between -0.94 ± 0.01 V (slightly positive to the calculated Nernst potential), for which the process is limited to the uncovered first Ni monolayer, the one in contact with the substrate. In a multilayer Ni film, selective dissolution of the uncovered first monolayer has also been observed in favor of Ni/Pd (but at a higher potential than in the case of the monolayer). Then, lateral growth of pits occurred from the lower edges towards the centre of terraces producing bi-layer step edges, while higher layer islands are still unmodified. This clearly indicates that the dissolution rate is smaller for the

second and third Ni layers. At slightly more positive potential, -0.91 V, dissolution of the second Ni layers starts but exclusively at the exposed bi-layer step edges and proceeds by simultaneous removal of the bi-layers, as noted by white and black arrows in Figs. 4.21b - 4.21c. Similar dissolution mechanism was observed on Au(111) and on Pd islands, and is in agreement with Ni dissolution experiments done on Ag(111) for similar film thickness [38]. However, for longer dissolution time at -0.91 V (Fig. 4.21c), it appears that the distribution of the non-dissolved Ni islands strongly varies over the bimetallic substrate and is dependent to the substrate nature (i.e. the dissolution rate is inhomogeneous). Indeed, dissolution of Ni on Au is almost completed, contrary to Ni film on Pd surface which is still covered by more than 70% of Ni. The remaining Ni islands on Pd are, at least, two-layer thick with an almost completed second-layer (90%) as can be observed in Figs. 4.21c and 4.21d. Finally, complete dissolution of the Ni layer was achieved by increasing the electrode potential from -0.89 V (Fig. 4.21d) up to -0.75 V. Fig. 4.21e displays the bare bimetallic substrate after complete Ni dissolution.

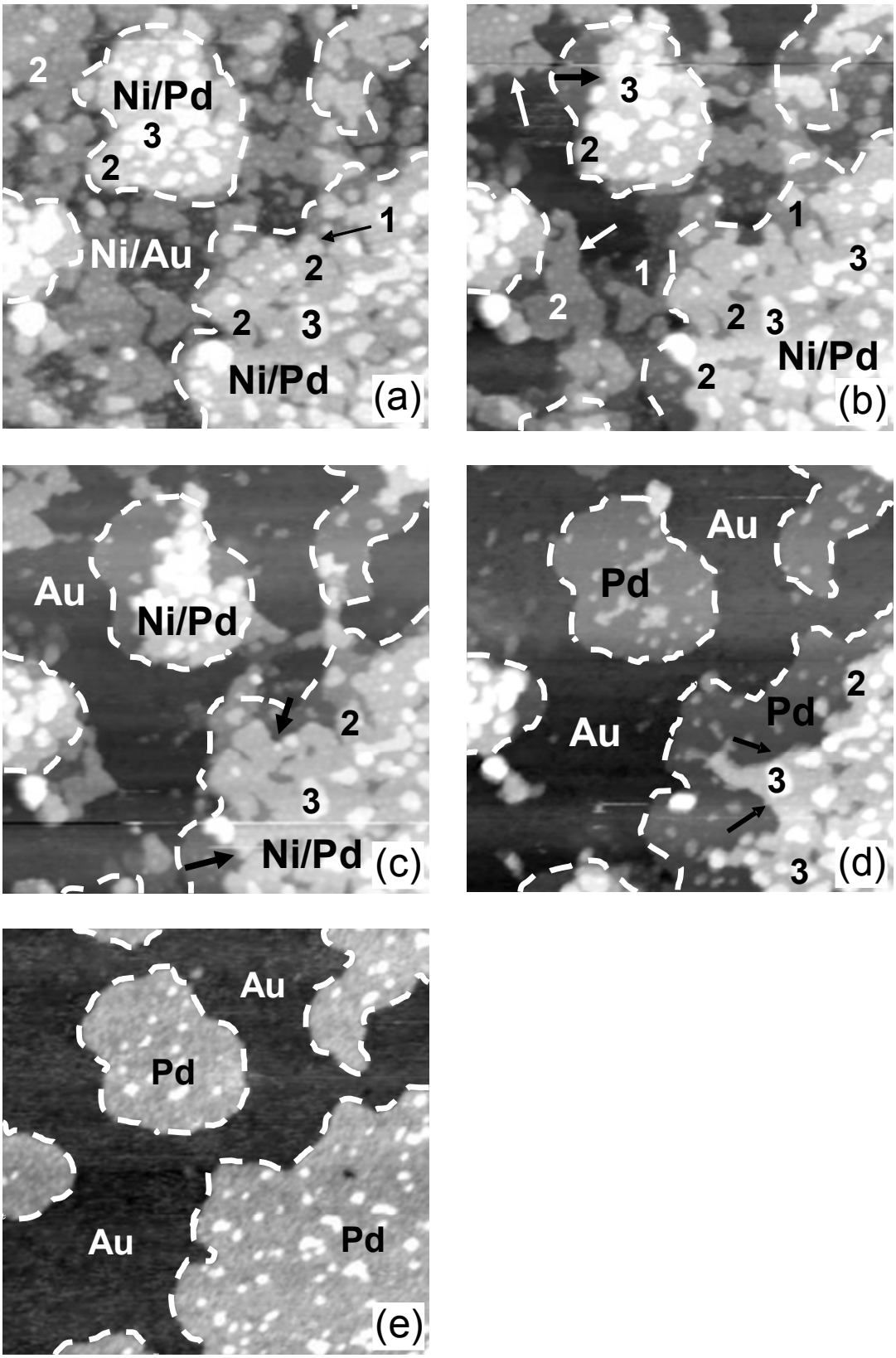

Figure 4.21: Series of STM images (100 x 100 nm²) showing the dissolution process of a multilayer Ni film ($t_{Ni/Pd}$ = 2 ML and $t_{Ni/Au}$ = 1.5 ML) deposited on Pd(0.5ML)/Au(111) at U_{dep} = -1.34 V for 45s in 0.1 M K_2SO_4 + 1 mM H_2SO_4 + 1 mM KCl + 1 mM $NiSO_4$, and recorded successively at (a) -1.07 V, (b-c) -0.91 V, (d) -0.89 V and (e) -0.6 V.

4.4.4 Quantitative analysis of Ni dissolution on *bimetallic* Pd/Au(111) surface

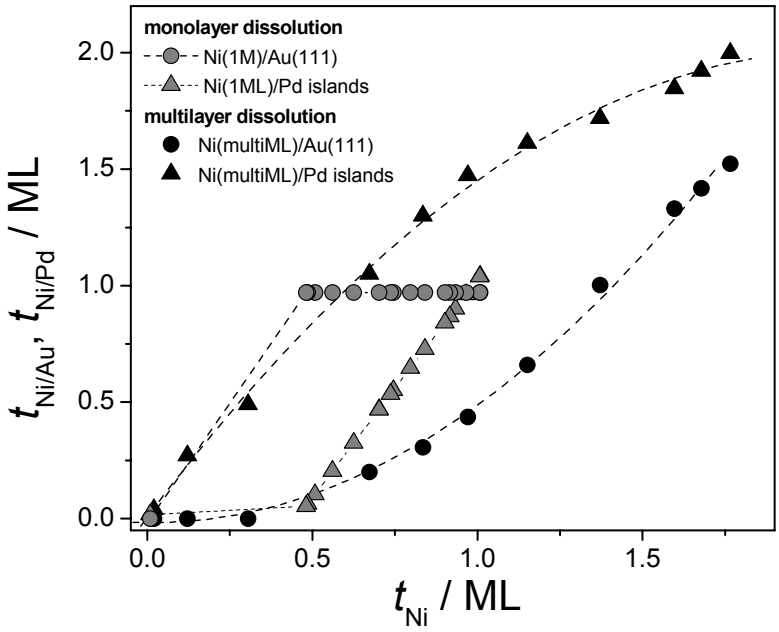

Figure 4.22: Variation of Ni thickness on Pd monoatomic islands ($t_{Ni/Pd}$) and Au(111) ($t_{Ni/Au}$) vs. the average Ni thickness t_{Ni}. Data are derived from quantitative STM image analysis recorded during dissolution of a Ni monolayer (gray filled symbols) or multilayer Ni film (black filled symbols) on bimetallic Pd(0.5ML)/Au(111) surface in 0.1 M K_2SO_4 + 1 mM H_2SO_4 + 1 mM KCl + 1mM $NiSO_4$.

Similarly to the growth study, quantitative analysis of the STM images linked to the dissolution process was conducted and results are presented in Fig. 4.22. Gray filled symbols are related to the Ni monolayer dissolution while black filled symbols correspond to multilayer film dissolution. It can be clearly observed that, for each process, the variation of $t_{Ni/Pd}$ strongly differs from the one of $t_{Ni/Au}$.

In the case of monoatomic thick Ni layer, the variations of the 1st layer coverage ($\theta_{Ni/Pd}$ and $\theta_{Ni/Au}$) express the fact that the Ni can be selectively dissolved at -1.02 V from the Pd surface, whereas the Ni monolayer is totally stable on Au(111). As mentioned above, dissolution of the Ni monolayer from Au(111) surface requires one to shift the electrode potential towards more positive potential, at U = -0.98 V.

For the multilayer film dissolution, a selective process is also observed but in favor of Ni film deposited on Au(111). This point is quite surprising and must be assigned to the initial film morphology. The second Ni layer coverage was initially significantly larger on Pd islands (0.85)

than on Au(111) (0.6). The origin of this reverse selective process is most likely linked to the thickness dependence of the Ni dissolution rate. Actually, the dissolution rate of the second and third Ni layers is found much smaller than the one of the first Ni layer.

4.5 Discussion

The STM observations allowed one to get valuable information to interpret the electrochemical data. Especially, they provide crucial results to the interpretation of t^*-values measured in the thickness - time plots (Figs. 4.4 and 4.5). In case of Ni growth on Au(111), the value $t^*_{Ni/Au}$, found close to 1 ML, agrees with the fact that the 1st Ni monolayer is completed on Au(111) before the second one significantly nucleates. Besides, for Ni growth on Pd/Au(111), the excellent agreement between values of the corrected $t^*_{Ni/Pd}$ (also ~ 1 ML) and the 2D monolayer growth of Ni on Pd monatomic islands observed by STM gives strong support to the fact that the H-desorption process occurs upon adlayer deposition. Finally, in the case of Co, we found that $t^*_{Co/Au} \sim t^*_{Co/Pd} \sim 2$ ML which is in agreement with the initial growth of a biatomic layer and the 2D growth morphology found on both Au and Pd substrates (Fig. 4.17).

Concerning the selective processes observed during the monolayer growth and dissolution of Ni, quantitative analysis of STM images on *bimetallic* surfaces are in agreement with the electrochemical measurements performed on *monometallic* surfaces (Figs. 4.16 and 4.22). The agreement between the two types of measurements is *quantitative*, which is quite surprising considering the different scales of observation. This can be explained by the fact that in our deposition and dissolution conditions, the two processes are, at the atomic scale, the reverse of one another. Namely Ni deposition corresponds to the incorporation of atoms at islands edges whereas Ni monolayer dissolution corresponds to the detachment of Ni atoms from island edges (see Figs. 4.13 and 4.18).

Regarding the deposition and dissolution of Ni *multilayer* films on Pd/Au(111), we also found a smaller selectivity which seems opposite to the one determined in the monolayer range (see again Figs. 4.16 and 4.22). There is still a reasonably good agreement between both electrochemical data and STM observation. However, the selectivity observed in the multilayer range (Figs. 4.15 and 4.21) is not considered as significant. During the deposition process, it could arise from variations of the density of nucleation site for the 2nd monolayer which induce local variations of coverage during of the growth of the 2nd Ni atomic layer. A direct consequence of this is that, in the case of Ni dissolution, the comparison of the electrochemical data and the STM images is not really relevant since the total amount of material is not equal on each

substrate. The STM experiments indeed demonstrate that the dissolution rate of the Ni monolayer is smaller than that of 2 and 3 ML-thick islands. Studying the dissolution selectivity of multilayer films would require preparing Ni layers with identical coverage on Au and Pd, which is difficult. Therefore, we consider that the apparent selectivity is a direct consequence of the nucleation and growth/dissolution processes of the second Ni ML, i.e. governed by the Ni-Ni interactions, and not due to the interaction with the substrate.

In Sec. 4.2.4, we showed, on the one hand, that the H-monolayer adsorbed on Pd reduces the Ni^{2+} electrochemical discharge and thereby contributes to the selective deposition/dissolution processes of Ni monolayer on Pd monolayer. On the other hand, any thermodynamic contributions to these selective processes have not been entirely considered so far. However, the selective growth (Fig. 4.11) and dissolution (Fig. 4.18) observed *under steady state conditions of polarization* strongly suggest that the Ni-substrate interactions could play a key role. We found a significant shift of $\Delta\phi^{Ni}_{Deposition} = \phi^{Ni/Au(111)}_{Deposition} - \phi^{Ni/Pd/Au(111)}_{Deposition} = 70$ mV during the growth process as well as a shift $\Delta\phi^{Ni}_{Dissolution} = 40 \pm 10$mV for the dissolution one. In the case of Co, no selectivity has been observed.

The following sub-sections will discuss (*i*) the origin of those shifts of onset potential in the case of Ni monolayer and (*ii*) the absence of selective processes for Co bilayer.

4.5.1 Interpretation of the substrate dependence of the Ni monolayer deposition/dissolution onset potential

a) Theoretical considerations

The existence of non zero values of $\Delta\phi^{Ni}_{Deposition} = \phi^{Ni/Au(111)}_{Deposition} - \phi^{Ni/Pd/Au(111)}_{Deposition} = 70$ mV and $\Delta\phi^{Ni}_{Dissolution} = 40 \pm 10$mV (as measured by STM under steady state conditions) constitutes a clear indication that there is a shift of the Nernst potential of the electrochemical reaction as a function of the substrate. To the best of our knowledge such a phenomenon has never been reported so far for overpotential deposition (OPD). Such a phenomenon has however been known for a long time in the case of UPD (underpotential deposition) layers. In fact the potential of the electrochemical reactions associated with monolayer deposition/dissolution may strongly depend on the underlying substrate. Numerous theoretical works tried to interpret the occurrence of UPD. In one recent work, the position of UPD peaks was used to derive the adsorption energy

of the adlayer on its substrate [68]. For this purpose, authors used a thermodynamic cycle described in Fig. 4.23 [68].

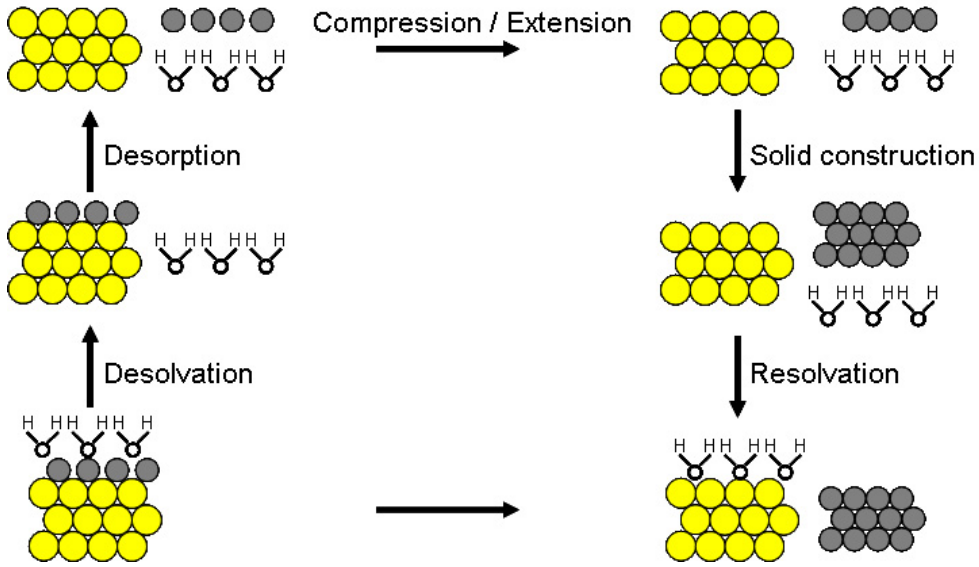

Figure 4.23: Thermodynamic cycle employed to explain the dissolution process. From Ref. [68].

From this cycle we derive the following expression in the case of Ni monolayer dissolution:

$$\phi_{Dissolution}^{Ni/Au} - \phi_{Nernst}^{Ni} = \frac{1}{ze_0}\left(E_{coh}^{Ni} - E_{coh}^{Ni\ monolayer} - E_{lm}^{Ni} + E_{bind}^{Ni/Au}\right) \qquad \text{(Eq. 4.9)}$$

$$\phi_{Dissolution}^{Ni/Pd} - \phi_{Nernst}^{Ni} = \frac{1}{ze_0}\left(E_{coh}^{Ni} - E_{coh}^{Ni\ monolayer} - E_{lm}^{Ni} + E_{bind}^{Ni/Pd}\right) \qquad \text{(Eq. 4.10)}$$

In these expressions, $E_{bind}^{Ni/S}$ (S = Au or Pd) is the Ni-substrate binding energy (by convention, $E_{bind}^{Ni/S}$>0), E_{coh}^{Ni} is the cohesive energy of the Ni metal, $E_{coh}^{Ni\ monolayer}$ is the cohesive energy of the Ni monolayer in vacuum, E_{lm}^{Ni} the energy necessary to expand or compress the deposited Ni monolayer to bring it from its equilibrium structure on the substrate to that in vacuum. In these equations E_{coh}^{Ni} and $E_{coh}^{Ni\ monolayer}$ are independent of the substrate. In addition E_{lm}^{Ni} is also the same for both substrates since the Ni monolayer presents the same amount of strain on both surfaces (see discussion about the moiré pattern observed in Fig. 4.14). Therefore, the difference $\Delta\phi_{Dissolution}^{Ni}$ simplifies to:

$$\Delta\phi_{Dissolution}^{Ni} = \phi_{Dissolution}^{Ni/Au(111)} - \phi_{Dissolution}^{Ni/Pd/Au(111)} = \frac{-1}{ze_0}\left(E_{bind}^{Ni/Pd/Au(111)} - E_{bind}^{Ni/Au(111)}\right) \qquad \text{(Eq. 4.11)}$$

As $\Delta\phi^{Ni}_{Dissolution} = 40 \pm 10\text{mV}$, the difference in the binding energies between Ni-Pd/Au(111) and Ni-Au(111) is $\Delta E^{Ni}_{bind} = \left(E^{Ni/Pd/Au(111)}_{bind} - E^{Ni/Au(111)}_{bind}\right) = -80 \pm 20$ meV (z = 2), i.e. Ni is ~ 80 meV more strongly bound to Au(111) than to Pd islands.

It should be noted that the above cycle predicts that $\Delta\phi^{Ni}_{Deposition} = \Delta\phi^{Ni}_{Dissolution}$. Experimentally, we find $\Delta\phi^{Ni}_{Deposition}$ = 70 mV, which is 30 mV greater than $\Delta\phi^{Ni}_{Dissolution}$. This discrepancy may be assigned to a different Ni nucleation process on Au(111) and on Pd islands. Indeed, at low overpotential, Ni nucleation on Au(111) takes place at the surface dislocation of the Au(111) reconstruction pattern a phenomenon which has no equivalent on pseudomorphic unreconstructed Pd monatomic islands [42]. Hence, the use of $\Delta\phi^{Ni}_{Deposition}$ to interpret the adlayer-substrate interactions is restricted to the case where the nucleation stages occurred on surface presenting similar atomic structure. At the opposite, the electrochemical dissolution, i.e., desorption of a full Ni monolayer at potentials close to the equilibrium offers the advantages to be mainly sensitive to Ni-substrate interactions since the Au(111) surface reconstruction is lifted by the Ni monolayer growth [4, 17].

b) Discussion of E_{bind}

From embedded atom calculations in the case of relaxed Cu adlayer, Sanchez et al. [68, 69] found that the difference in the binding energies (ΔE^{Cu}_{bind}) varies between 70 and 610 meV as a function of the substrate. Unfortunately, Ni adlayer was not considered in this work and no trend correlating the binding energies with the substrate properties (such as atomic size, electronic configuration…) was proposed.

Rodriguez and Goodman established such a correlation in selected UHV studies [70, 71]. They combined thermal desorption spectroscopy (TDS) and X-ray photoemission spectroscopy (XPS) to investigate the surface metal-metal bond of Ni, Pd and Cu films supported on several transition metal substrates such as Ta(110), Mo(110), W(110), Ru(0001). XPS allowed them to measure the core level of the adlayer while TDS enabled them to estimate the overlayer-substrate binding energy through the determination of the thermal desorption temperature (for a review on this technique see Ref. [11] and references cited therein). By using these two experimental techniques, they demonstrated that the overlayer-substrate binding varies linearly with the substrate valence *d* band occupation and is stronger on substrates with a lower occupation. This trend may also be formulated as the difference of overlayer-substrate binding energies, when two substrates are compared, depends on the difference of the substrate *d* band filling. The existence

of such correlation was theoretically confirmed by Yang and Wu [72, 73] by means of first-principles calculations. In the case of Ni adlayer, the linear dependence of the binding energies on the occupancy of the *d* band is plotted in Fig. 4.24 for Ta [74], W [75], Mo [76] and Ru [77].

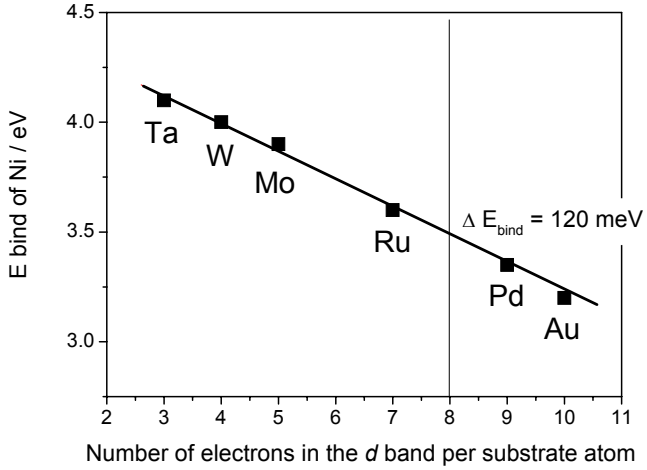

Fig. 4.24: Variation of the Ni-substrate binding energies as a function of the occupancy of the d band of different metal substrates: Ta [74], W [75], Mo [76] and Ru [77].

It can be observed that $\Delta E_{bind}^{Ni} = 120$ meV for Ta(110) and W(110) substrates (*d* band filling increases by one electron per atom), and $\Delta E_{bind}^{Ni} = 470$ meV for Ta(110) and Ru(0001) (*d* band filling increases by four electrons per atom). Hence, in analogy with the above trends and considering that Pd has a *d* band filling one electron lower than Au, one expected $\Delta E_{bind}^{Ni} = +120$ meV , i.e. Ni is more strongly bound to Pd, which contrasts with our results ($\Delta E_{bind}^{Ni} = -80$ meV).

Can the discrepancy be attributed to the fact that we deposit the Ni monolayer on monatomic Pd islands? In our case, the *d* band occupation of Au(111) must rather be compared to the one of strained pseudomorphic Pd islands. Sellidj and Koel [78] used ultraviolet photoemission spectroscopy (UPS) to investigate the electronic properties of the Pd/Au(111) surface. Fig. 4.25 (obtained from Ref. [78]) displays several angle-integrated UPS spectra taken from Pd films of various thicknesses deposited on Au(111) at 125 K by molecular beam epitaxy (MBE) in UHV. It can be observed that the Pd 4*d* band of a pseudomorphic Pd monolayer on Au(111) has a maximum well below the Fermi level (at -1.6 eV) with a minor contribution to the density of states (DOS) at the Fermi level. This indicates that the valence *d* band of Pd islands is most probably fully occupied, with a DOS at the Fermi level similar to that of clean Au(111). On the contrary, the valence 4*d* band of bulk Pd film (~ 5 ML) is only partially occupied. Hence, these spectra clearly demonstrate that the electronic configuration of Pd islands differ from that

of bulk Pd(111) and is very similar to the one of Au(111). In view of these results, we would expect ΔE_{bind}^{Ni} close to zero in our case. The fact that the Pd surface is a strained monolayer on Au(111) is therefore not sufficient to account for our observations.

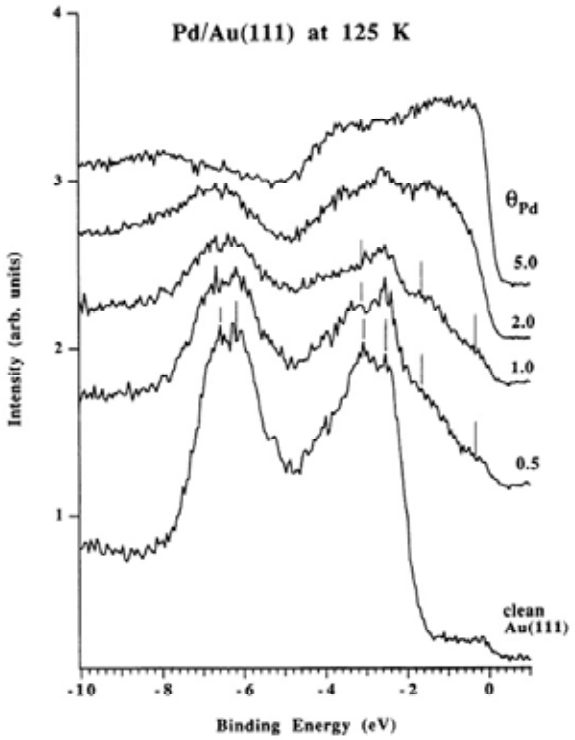

Fig. 4.25: Ultra violet Photoelectron Spectra (UPS) obtained from Pd films of various thicknesses (as indicated at the right hand side), deposited under UHV on Au(111) at 125 K. A Helium lamp emitting at 40.8 eV was used as UV photon source (from Ref. [78]).

c) Role of the H-monolayer adsorbed on the Pd islands

As explained above, Ni deposition occurs on H-terminated Pd surface. The question is now to understand if such adsorbed layer could modify the prediction established for *bare* surfaces, including the Pd one.

The presence of a H monolayer at the Ni/Pd interface could be considered since such sandwich layer would explain a smaller binding energy between the adlayer and the substrate. We have nevertheless showed several facts which are all in favor of H-desorption from the Pd surface in the course of Ni deposition (see Sec. 4.2.4). Therefore an intimate Ni/Pd interface is expected and other reasons must be taken into account to explain the negative value of ΔE_{bind}^{Ni} (-80 meV).

One possible explanation is hydrogen. Although our results are consistent with the absence of H between the Ni layer and Pd islands, the Pd regions that are bare of Ni are covered

by hydrogen (see Fig. 4.18) while the Au surface remains free of adsorbates. As the dissolution process of Ni monolayer took places exclusively at the edges of the vacancy islands contained in the Ni monolayer, the H-atoms (on the Pd islands) which are in the close proximity of the Ni atoms might *locally* destabilize the Ni-Pd bonds and or Ni-Ni bonds. This could be due to subtle local variations of the surface electronic properties and/or of the in-plane strain at the rims of Ni islands.

4.5.2 Explanation of the absence of selective Co deposition/dissolution process

Is it possible to explain the absence of a selective Co deposition/dissolution process on Pd/Au bimetallic surface using the above mentioned considerations? The case of Co is at first sight very similar to that of Ni. Although the Co layer is partially relaxed only, the characteristic length of its moiré pattern is similar on Pd/Au and on Au. Moreover, Co and Ni are neighbors in the periodic table, suggesting close electronic properties. For example, they have almost identical cohesive energies (~ 4.4 eV). The major difference between Ni and Co is that, in our deposition conditions, Ni grows as monolayer islands whereas Co islands are exclusively bilayer. Although this difference may have a minor influence only on the selectivity process, it complicates to a large extent the analysis and the energy balance. For example, in order to rewrite Eqs. 4.9 and 4.10 in the case of Co, one has to figure out what is the limiting process at the atomic scale. If the limiting process is the dissolution of step atoms of the first Co monolayer, then one might expect the dissolution process to be sensitive to the substrate chemical nature. The experimental non selective behavior suggests in this case that $E_{bind}^{Co/Pd/Au(111)} \sim E_{bind}^{Co/Au(111)}$. On the other hand, if the limiting process is the dissolution of the second layer atoms, i.e., breaking a Co−Co bond, then the influence of the substrate is expected to be minor and no conclusion may be drawn on the relative values of $E_{bind}^{Co/Pd/Au(111)}$ and $E_{bind}^{Co/Au(111)}$. Moreover, the limiting process might not be the same for Co dissolution and for Co deposition. Consequently, selective dissolution process is not necessary accompanied by a deposition selectivity. In sum, in spite of the experimental absence of deposition and dissolution selectivity in the case of Co, it is not possible to conclude on the difference between Co binding energy to Au and that to Pd/Au.

4.6 Conclusion

First, our electrochemical measurements performed on *monometallic* substrates clearly show that Ni deposition and dissolution processes, in the first monolayer regime, strongly depend on the substrate chemical nature, i.e. Pd(1ML) or Au(111) contrary to the case of Co bilayer. We found that Ni deposition on Au(111) is more favorable than on Pd monoatomic surface. Intriguingly, rigorous studies of the dissolution curves also show that Ni dissolution is more favorable on Pd islands than on Au(111).

Second, by using *bimetallic* Pd/Au(111) surface, we have demonstrated on the basis of STM observation under steady state condition close to equilibrium condition that the selective processes in the electrochemical deposition/dissolution of Ni monolayer films arises from a smaller binding energy of Ni adatoms on the Pd surface as compared to the Au surface. The difference in binding energy between Ni-Pd and Ni-Au has been estimated to 80 meV, Ni binding more strongly to Au. However, the reason for the smaller Ni-Pd binding energy as compared to that of Ni-Au remains unclear. One possible explanation is the H monolayer on the Pd surface. Theoretical modeling could help in understanding the observed behavior.

References

1. Nichols, R.J., Ross, R.N., and Lipkowski, J., *Imaging metal electrocrystallization at high resolution*, in *Imaging of surfaces and interfaces*. 1999, VCH: New York.
2. Gewirth, A.A. and Niece, B.K., *Electrochemical applications of in situ scanning probe microscopy.* Chemical Reviews, 1997. **97**: p. 1129-1162.
3. Allongue, P. and Maroun, F., *Metal electrodeposition on single crystal metal surfaces mechanisms, structure and applications.* Current Opinion in Solid State and Materials Science, 2006. **10**(3-4): p. 173-181.
4. Möller, F., Kintrup, J., Lachenwitzer, A., Magnussen, O.M., and Behm, R.J., *In-situ STM studies of the electrodeposition and anodic dissolution of ultrathin, epitaxial Ni films on Au(111).* Physical Review B, 1997. **56**(19): p. 12506-12518.
5. Magnussen, O.M. and Behm, R.J., *Structure and growth in metal epitaxy on low-index Au surfaces - a comparison between solid-electrolyte and solid-vacuum interfaces.* Journal of Electroanalytical Chemistry, 1998. **467**: p. 258-269.
6. Herrero, E., Buller, L.J., and Abruna, H.D., *Underpotential Deposition at Single Crystal Surfaces of Au, Pt, Ag and Other Materials.* Chemical Reviews, 2001. **101**(7): p. 1897-1930.
7. Möller, F., Magnussen, O.M., and Behm, R.J., *In situ STM studies on the Cu underpotential deposition on Au(100) in the presence of sulfate and chloride anions.* Physical Review B, 1995. **51**: p. 2484-2490.
8. Oviedo, O.A., Leiva, E.P.M., and Rojas, M.I., *Energetic and entropic contributions to the underpotential/overpotential deposition shifts on single crystal surfaces from lattice dynamics.* Electrochimica Acta, 2006. **51**(17): p. 3526-3536.
9. Brune, H., *Creating Metal Nanostructures at Metal Surfaces Using Growth Kinetics*, in *Handbook of Surface Science*, E. Hasselbrink, Editor. 2008, Elsevier: Amsterdam. p. 761-786.
10. Kolaczkiewicz, J. and Bauer, E., *Thermal desorption spectroscopy of Ni, Cu, Ag and Au from W(110).* Surface Science, 1986. **175**(3): p. 508-519.
11. Brune, H., *Metals on Metals*, in *Landolt Börnstein series: Physics of Covered Solid Surfaces*, H.P. Bonzel, Editor. 2001, Springer: Berlin. p. 217-258.
12. Brown, W.A., Kose, R., and King, D.A., *Femtomole Adsorption Calorimetry on Single-Crystal Surfaces.* Chemical Reviews, 1998. **98**(2): p. 797-831.
13. Kibler, L.A., Kleinert, M., Randler, R., and Kolb, D.M., *Initial stages of Pd deposition on Au(hkl) part I: Pd on Au(111).* Surface Science, 1999. **443**: p. 19-30.

14. Baldauf, M. and Kolb, D.M., *A hydrogen adsorption and absorption study with ultrathin Pd overlayers on Au(111) and Au(100).* Electrochimica Acta, 1993. **38**(15): p. 2145-2153.
15. Naohara, H., Ye, S., and Uosaki, K., *Electrochemical layer-by-layer growth of palladium on an Au(111) electrode surface: Evidence for important role of adsorbed Pd complex.* Journal of the Physical Chemistry B, 1998. **102**(22): p. 4366-4373.
16. Chierchie, T. and Mayer, C., *Voltammetric Study of the Underpotential Deposition of Copper on Polycrystalline and Single Crystal Palladium Surfaces.* Electrochimica Acta, 1988. **33**: p. 341-345.
17. Allongue, P., Cagnon, L., Gomes, C., Gundel, A., and Costa, V., *Electrodeposition of Co and Ni/Au(1 1 1) ultrathin layers. Part I: nucleation and growth mechanisms from in situ STM.* Surface Science, 2004. **557**(1-3): p. 41-56.
18. Gomez, J., Pollina, R., and Valles, E., *Nickel electrodeposition on different metallic substrates.* Journal of Electroanalytical Chemistry, 1995. **386**: p. 45-56.
19. Bard, A.J. and Faulkner, L.R., *Electrochemical Methods: Fundamentals and Applications, 2nd Edition.* 2001, New York: John Wiley & Sons.
20. Lachenwitzer, A. and Magnussen, O.M., *Electrochemical quartz microbalance studies on the kinetics of Ni monolayer and multilayer electrodeposition on (111)-oriented Au films.* Journal of the Physical Chemistry B, 2000. **104**: p. 7424-7430.
21. Cagnon, L., Gundel, A., Devolder, T., Morrone, A., Chappert, C., Schmidt, J.E., and Allongue, P., *Anion effect in Co/Au(111) electrodeposition: structure and magnetic behavior.* Applied Surface Science, 2000. **164**(1-4): p. 22-28.
22. Cagnon, L., Devolder, T., Cortes, R., Morrone, A., Schmidt, J.E., Chappert, C., and Allongue, P., *Enhanced interface perpendicular magnetic anisotropy in electrodeposited Co/Au(111) layers.* Physical Review B, 2001. **63**(10): p. 104419.
23. Kleinert, M., Waibel, H.F., Engelmann, G.E., Martin, H., and Kolb, D.M., *Co deposition on Au(111) and Au(100) electrodes: an in situ STM study.* Electrochimica Acta, 2001. **46**(20-21): p. 3129-3136.
24. Heusler, K.E. and Gaiser, L., Electrochimica Acta, 1968. **13**: p. 59.
25. Matulis, J. and Slizys, R., Electrochimica Acta, 1964. **9**: p. 1177.
26. Ives, A.G., Edington, J.W., and Rothwell, G.P., Electrochimica Acta, 1970. **15**: p. 1797.
27. Epelboin, I., Gabrielli, C., Keddam, M., Takenouti, H., Bockris, J.O.M., Conway, B.E., Yeager, E., and White, R.E., *The study of the passivation process by the electrode impedance analysis*, in *Electrochemical materials science.* 1981, Plenum Press: New York. p. 151-149.
28. Epelboin, I. and Wiart, R., *Mechanism of the Electrocrystallization of Nickel and Cobalt in Acidic Solution.* Journal of the Electrochemical Society, 1971. **118**(10): p. 1577-1582.

29. Pourbaix, M., *Atlas of electrochemical equilibria in aqueous solutions*. Atlas of electrochemical equilibria in aqueous solutions. 1966, London: Pergammon Press. 387.
30. Saraby-Reintjes, A. and Fleischmann, M., *Kinetics of electrodeposition of nickel from watts baths.* Electrochimica Acta, 1984. **29**(4): p. 557-566.
31. Bockris, J.O.M. and Reddy, A.K.N., *Modern Electrochemistry 1*. 1970, New York: Plenum/Rosetta.
32. Epelboin, I., Joussellin, M., and Wiart, R., *Impedance measurements for nickel deposition in sulfate and chloride electrolytes.* Journal of Electroanalytical Chemistry, 1981. **119**(1): p. 61-71.
33. Trasatti, S., in *Advances in Electrochemistry and Electrochemical Engineering*, H. Gerischer and C.W. Tobias, Editors. 1977, Wiley Interscience: New York. p. 213-321.
34. Kolb, D.M., *Reconstruction phenomena at metal-electrolyte interfaces.* Progress in Surface Science, 1996. **51**(2): p. 109-173.
35. Langkau, T. and Baltruschat, H., *The point of zero charge of adsorbed monolayers: Pt(111) covered by Ag.* Electrochimica Acta, 2002. **47**(10): p. 1595-1599.
36. El-Aziz, A.M., Kibler, L.A., and Kolb, D.M., *The potentials of zero charge of Pd(1 1 1) and thin Pd overlayers on Au(1 1 1).* Electrochemistry Communications, 2002. **4**(7): p. 535-539.
37. Morin, M., Lachenwitzer, A., Möller, F.A., Magnussen, O.M., and Behm, R.J., *Comparative in situ STM studies on the electrodeposition of ultrathin nickel films on Ag(111) and Au(111) electrodes.* Journal of the Electrochemical Society, 1999. **146**(3): p. 1013-1018.
38. Lachenwitzer, A., Morin, S., Magnussen, O.M., and Behm, R.J., *In situ STM study of electrodeposition and anodic dissolution of Ni on Ag(111).* Physical Chemistry Chemical Physics, 2001. **3**(16): p. 3351-3363.
39. Hamelin, A., Vitanov, T., Sevastyanov, E., and Popov, A., *The electrochemical double layer on sp metal single crystals. The current status of data.* Journal of Electroanalytical Chemistry, 1983. **145**: p. 225-264.
40. Lachenwitzer, A. and Magnussen, O.M., *Electrochemical Quartz Crystal Microbalance Study on the Kinetics of Nickel Monolayer and Multilayer Electrodeposition on (111)-Oriented Gold Films.* Journal of Physical Chemistry B, 2000. **104**(31): p. 7424-7430.
41. Conway, B.E. and Jerkiewicz, G., *Relation of energies and coverages of underpotential and overpotential deposited H at Pt and other metals to the `volcano curve' for cathodic H2 evolution kinetics.* Electrochimica Acta, 2000. **45**(25-26): p. 4075-4083.
42. Möller, F., Magnussen, O.M., and Behm, R.J., *Overpotential-controlled nucleation of Ni island arrays on reconstructed Au(111) electrode surfaces.* Physical Review Letters, 1996. **77**: p. 5249-5252.

43. Möller, F., Magnussen, O.M., and Behm, R.J., *Two-dimensional needle growth of electrodeposited Ni on reconstructed Au(111).* Physical Review Letters, 1996. **77**(15): p. 3165-3168.
44. Meyer, J.A., Baikie, I.D., Kopatzki, E., and Behm, R.J., *Preferential island nucleation at the elbows of the Au(111) herringbone reconstruction through place exchange.* Surface Science, 1996. **365**: p. L647-L651.
45. Lachenwitzer, A., Vogt, O., Magnussen, O.M., and Behm, R.J., *Electrodeposition of Ni on Cu(100): An in-situ STM study.* Surface Science, 1997. **382**: p. 107-115.
46. Skriver, H.L. and Rosengaard, N.M., *Surface energy and work function of elemental metals.* Physical Review B, 1992. **46**(11): p. 7157-7168.
47. Haug, K., Zhang, Z., John, D., Walters, C.F., Zehner, D.M., and Plummer, W.E., *Effects of hydrogen in Ni(100) submonolayer homoepitaxy.* Physical Review B, 1997. **55**(16): p. R10233-R10236.
48. Chambliss, D.D., Wilson, R.J., and Chiang, S., *Ordered nucleation of Ni and Au islands on Au(111) studied by scanning tunneling microscopy.* Journal of Vacuum Science and Technology B, 1991. **9**(2): p. 933-937.
49. Toney, M.F., Gordon, J.G., Borges, G.L., and Melroy, O.R., *Comment on "Superstructures on Pb monoleyers electrochemically deposited on Ag(111)".* Physical Review B, 1994. **49**(11): p. 7793-7794.
50. Kitchin, J.R., Khan, N.A., Barteau, M.A., Chen, J.G., Yakshinskiy, B., and Madey, T.E., *Elucidation of the active surface and origin of the weak metal-hydrogen bond on Ni/Pt(1 1 1) bimetallic surfaces: a surface science and density functional theory study.* Surface Science, 2003. **544**(2-3): p. 295-308.
51. Meyer, J.A., Schmid, P., and Behm, R.J., *Effect of layer-dependent adatom mobilities in heteroepitaxial metal film growth: Ni/Ru(0001).* Physical Review Letters, 1995. **74**(19): p. 3864-3867.
52. Marcus, P. and Oudar, J., *Corrosion mechanisms in theory and practice.* Corrosion technology. 1995, New York: Marcel Dekker.
53. Magnussen, O.M., *Ordered Anion Adlayers on Metal Electrode Surfaces.* Chemical Reviews, 2002. **102**: p. 679-725.
54. Chassaing, E., Jousselin, M., and Wiart, R., *The kinetics of nickel electrodeposition inhibition by adsorbed hydrogen and anions.* Journal of Electroanalytical Chemistry, 1983. **157**: p. 75-88.
55. Saraby-Reintjes, A. and Fleischmann, M., *Kinetics of electrodepostion of nickel from watts baths.* Electrochimica Acta, 1984. **29**(4): p. 557-566.

56. Wiart, R., *Elementary steps of electrodeposition analysed by means of impedance spectroscopy.* Electrochimica Acta, 1990. **35**(10): p. 1587-1593.

57. Proud, W.G. and Müller, C., *The electrodeposition of nickel on vitreous carbon: impedance studies.* Electrochimica Acta, 1993. **38**(2/3): p. 405-413.

58. Proud, W.G., Gomez, E., Sarret, E., Vall,s, E., and M□ ller, C., *Influence of pH on nickel electrodeposition at low nickel(II) concentrations.* Jounal of Applied Electrochemistry, 1995. **25**: p. 770-776.

59. Skuratnik, Y.B., Kozachinskii, A.E., Pchelnikov, A.P., and Losev, V.V., *Effect of the absorption of hydrogen by nickel on its anodic dissolution and corrosion in acidic solutions.* Journal of Electroanalytical Chemistry, 1994. **366**: p. 311-316.

60. van der Wekken, C.J., *Adsorbed species on nickel in electrolyte solutions.* Journal of the Electrochemical Society, 1986. **133**(11): p. 2293-2295.

61. Magnussen, O.M., Scherer, J., Ocko, B.M., and Behm, R.J., *In-situ x-ray scattering study of the passive film on Ni(111) in sulfuric acid solution.* Journal of the Physical Chemistry B, 2000. **104**: p. 1222-1226.

62. MacDougall, B., *Effect of chloride ion on the localized breakdown of nickel oxide films.* Journal of the Electrochemical Society, 1979. **126**(6): p. 919-925.

63. Lei, K.S., Macdonald, D.D., Pound, B.G., and Wilde, B.E., *Breakdown of the passive film on polycrystal and single crystal (100) nickel by chloride.* Journal of the Electrochemical Society, 1988. **135**(7): p. 1625-1632.

64. Vogt, M.R., Lachenwitzer, A., Magnussen, O.M., and Behm, R.J., *In-situ STM study on the initial stages of corrosion of Cu(100) electrodes in sulfuric and hydrochloric acid solution.* Surface Science, 1998. **399**: p. 49-80.

65. Scherson, D.A. and Kolb, D.M., *Voltammetric curves for Au(111) in acid media: a comparison with Pt(111) surfaces.* Journal of Electroanalytical Chemistry, 1984. **176**: p. 353-357.

66. Clavilier, J., *The role of anion on the electrochemical behaviour of a (111) platinum surface; an unusual splitting of the voltammogram in the hydrogen region.* Journal of Electroanalytical Chemistry, 1980. **107**: p. 211-216.

67. Clavilier, J. and Nguyen van Huong, C., *Etude de l'interface de l'or polycristallin au contact de solutions aqueuses de perchlorate de potassium et d'acide perchlorique* Journal of Electroanalytical Chemistry, 1977. **80**: p. 101-114.

68. Sanchez, C.G., Del Pópolo, M.G., and Leiva, E.P.M., *An embedded atom approach to underpotential deposition phenomena.* Surface Science, 1999. **421**(1-2): p. 59-72.

69. Rojas, M.I., Sanchez, C.G., Del Pópolo, M.G., and Leiva, E.P.M., *Erratum to: "An embedded atom approach to underpotential deposition phenomena": [Surf. Sci. 421 (1999) 59].* Surface Science, 2000. **453**(1-3): p. 225-228.

70. Rodriguez, J.A. and Goodman, D.W., *The Nature of the Metal-Metal Bond in Bimetallic Surfaces* Science, 1992. **257**: p. 897-903.

71. Campbell, R.A., Rodriguez, J.A., and Goodman, D.W., *Chemical and electronic properties of ultrathin metal films: The Pd/Re(0001) and Pd/Ru(0001) systems.* Physical Review B, 1992. **46**(11): p. 7077.

72. Yang, Z. and Wu, R., *First-principles studies on bonding mechanism at Ni/X bimetallic interfaces (X=Ta, W, Re and Ru).* Surface Science, 2000. **469**(1): p. 36-44.

73. Wu, R. and Freeman, A.J., *Bonding mechanism at bimetallic interfaces: Pd overlayer on various substrates.* Physical Review B, 1995. **52**(16): p. 12419.

74. Campbell, C.T., *Ultrathin metal films and particles on oxide surfaces: structural, electronic and chemisorptive properties.* Surface Science Reports, 1997. **27**: p. 1-111.

75. Berlowitz, P.J. and Goodman, D.W., *The adsorption of H2 and CO on strained Ni overlayers on W(110) and W(100).* Surface Science, 1987. **187**(2-3): p. 463-480.

76. He, J.W., Shea, W.L., Jiang, X., and Goodman, D.W., *Surface chemistry of monolayer metallic films on Re(0001) and Mo(110).* Journal of Vacuum Science & Technology A: Vacuum, Surfaces, and Films, 1990. **8**(3): p. 2435-2444.

77. Berlowitz, P.J., Houston, J.E., White, J.M., and Wayne Goodman, D., *Properties of monolayer and multilayer Ni films on the Ru(0001) surface.* Surface Science, 1988. **205**(1-2): p. 1-11.

78. Sellidj, A. and Koel, B.E., *Electronic and CO chemisorption properties of ultrathin Pd films vapor deposited on Au(111).* Physical Review B, 1994. **49**(12): p. 8367.

Chapter 5

Growth and Dissolution of Two-Dimensional Binary Ultrathin Alloy Films on Au(111)

In the present chapter, we investigate the electrochemical growth/dissolution of two-dimensional, monolayer thick Ni_xPd_{1-x} and Ni_xAu_{1-x} alloys on Au(111). The aim is first, to determine the morphology of these alloys for given deposition conditions as a function of the stoichiometry; second, to get better insight into the influence of the NiAu and NiPd interaction energies and surface diffusion on the dissolution morphology by studying the initial stages of the selective dissolution of the less noble metal (Ni). We are particularly interested in determining the influence of the local atomic environment on the dissolution kinetics. We also studied the dissolution process by Monte Carlo simulations, allowing us to support the conclusions derived from the experimental results.

In the following section 5.1, we will start with a brief overview of the alloy growth in UHV and in the electrochemical environment. We will also describe the main features of the dissolution of binary alloys. Then, in section 5.2, we will present our experimental results concerning the growth of NiPd and NiAu alloys. Section 5.3 will be dedicated to the selective Ni dissolution from monolayer thick NiPd and NiAu alloys. In section 5.4, the results of Monte Carlo simulations of monolayer alloy dissolution will be presented. The growth and the dissolution of the alloys will be discussed in section 5.4. The chapter conclusions will be presented in section 5.6.

5.1 Introduction

The surface of an alloy and the preparation of ultrathin alloy layers have attracted increasing interest in the last few years as well-defined model systems, which allow one to correlate the surface stoichiometry (i.e. composition) with the physico-chemical properties [1, 2]. A prerequisite for such correlations is the preparation of atomically flat surfaces on a large scale (to avoid the influence of step atoms on the studied property) and the control of the alloy composition of the topmost atomic layer. The latter is quite difficult with bulk single crystal alloys for which surface segregation (surface enrichment or depletion) may occur during surface preparation [3]. On the other hand, ultrathin alloy layers deposited on different substrates allow a

better control of the surface composition and offer the possibility of varying the (average) lattice constant of the film by choosing different substrate materials as an additional degree of freedom. Indeed, it has been demonstrated that the strain plays an important role in the catalytic [4] and magnetic properties [5] of a thin layer. For these reasons, studying the growth of ultrathin alloy layers has attracted a lot of interest since 3 decades.

The growth of ultrathin layer alloys

In the major part of the alloy film studies, the thin films are generally prepared in UHV conditions [6, 7]. They may be obtained using two experimental procedures. First, by depositing one metal on the surface of a second metal and subsequent annealing resulting in intermixing of the deposited and the substrate atoms [8-18]. This leads to the formation of monolayer alloy localized near the film-substrate interface. Second, by depositing *two* different metals, with a total coverage of typically one monolayer, onto a substrate that does not form alloys with either species. Then, subsequent annealing allows one to get atomically smooth and dispersed surface alloy monolayer. Most of the reported cases using this approach have used Ru(0001) or W(110) as substrate which have a positive mixing enthalpy with most of the metals [19-26]. In all these studies, the close correlation between the alloy surface composition and its properties was made possible thanks to the high resolution scanning tunneling microscopy (STM) measurements with chemical contrast which enable one to identify each atom of the alloy and thus determine the atomic ensembles of the alloy surface and its composition (see for example [19, 27]).

In the electrochemical environment, studies related to the growth of ultrathin alloy films down to the atomic scale are much less numerous than in UHV, although electrodeposition is widely used to produce thick metallic alloy films on various substrates such as gold, copper or carbon. The typical deposition procedure for preparing bimetallic alloy films is to *co-deposit* both atoms from a solution containing both metallic cations. The alloy composition is controlled more often by adjusting the relative metallic cation concentration and in some cases by the applied overpotential. In the latter case, the control of the alloy composition is more delicate because the deposition rate has usually an exponential dependence on the overpotential. In these conditions, thick alloy films were prepared. Among them, a significant amount of research has been done on Ni-based alloys, such as NiCu, NiCo and NiFe, due to the wide variety of applications (corrosion, catalysis and magnetism) [28-31]. In these studies, the bulk structure of the alloy films is usually determined by X-ray diffraction (XRD), the film morphology is investigated by scanning electronic microscopy (SEM) while the surface composition is usually examined by Auger electron spectroscopy (AES) or X-ray fluorescence (XRF). Few studies are related to the

electrodeposition of Ni alloys containing a noble metal such as Pd [32] or Pt [33]. In such a deposition procedure, it is possible to control the average alloy of a relatively thick film (thicker than typically ~ 3-5 ML, depending on the cation concentrations). Below 3-5 ML, the deposition rates of both metals are time dependent and consequently, the alloy composition is different from the average one of the thick layer. Moreover, the growth of the first alloy monolayer might be also different, because of the possible presence of specific interactions between the metals and the substrate leading for example to an exclusive growth of one of the metals. Finally, the flatness at the atomic scale in these deposition conditions is often not guarantied. For all these reasons, this deposition method is not appropriate to prepare ultrathin alloy film.

Maroun et al. [34] deposited ultrathin (0-3 ML) PdAu alloy films on Au(111) in conditions analog to those used in UHV (see Sec. 2.2), i.e., where both metallic cations are deposited in diffusion-limited conditions and at slow deposition rates. In these conditions, the prepared alloy films are atomically flat at all alloy compositions. Using in situ STM with chemical contrast allowed them to determine the atomic arrangement. The close correlation they did between the atomic ensembles and the catalytic activity (determined from electrochemical measurements) as well as the adsorption sites of CO (determined by infra red spectroscopy), allowed them to determine the minimum Pd ensembles to adsorb H and CO. Allongue et al. [35] used similar electrodeposition procedure to form ultrathin FeNi films (1-2 ML) with different composition to investigate and tune their magnetic properties. Before the work of Maroun et al., the ultrathin (< 3 ML) alloy films were prepared ex situ under UHV conditions and then transferred into the electrochemical environment. For instance, Hayden et al. [36] produced well-ordered surface alloys of Pt(111)/Sn(2x2) and Pt(111)/Sn($\sqrt{3}$x$\sqrt{3}$)*R*30° under UHV by metal vapor deposition and, then, transfer the surface alloys in the electrochemical cell to study electro-oxidation of carbon monoxide. Such procedure, although often successful, is time consuming and the transfer from UHV to the electrochemical cell might be delicate especially if the alloy contains a non noble metal (e.g. Ni).

From the thermodynamic point of view, the sign and the amplitude of the enthalpy of mixing allows one to determine the equilibrium configuration of an alloy, solid solution (Fig. 5.1b) or phase segregated (Fig. 5.1c) [37]. Ordered alloy (Fig. 5.1a) is a special configuration of a solid solution which is observed for some specific alloy compositions. The two systems of interest in this chapter are NiPd and NiAu alloys. NiPd system is characterized by the fact that the two metals are miscible ($\Delta H_{mix} < 0$) i.e. the internal energy of the system is reduced by increasing the number of Ni-Pd bonds [38]. For a miscible alloy, and following the Vegard's law at constant temperature, a linear relation is expected between the lattice parameter of the alloy

and its composition such that, in the case of NiPd, $a_{Ni_xPd_{1-x}} = x \times a_{Ni} + (1-x) \times a_{Pd}$ [39]. However, the lattice parameter of the NiPd system is known to follow a non-linear curve with a positive deviation from the Vegard's law [38]. The NiAu system is characterized by the fact that the two metals are immiscible ($\Delta H_{mix} > 0$). Therefore, phase separation of the atoms into Ni-rich and Au-rich clusters is expected.

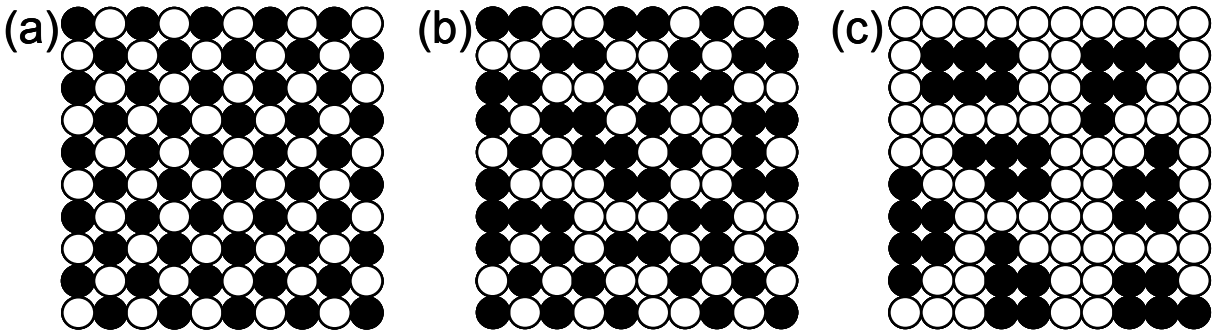

Figure 5.1: Bulk truncation models for the surface structure of the (100) face of fcc type alloys. Schematic representation of solid solutions: (a) ordered substitutional (long-range order), (b) random solution, (c) clustering. Adapted from Ref. [37].

In the case of ultrathin alloy films, the Gibbs free energy is modified because of the interactions with the substrate. Moreover, the presence of strain in the alloy film can strongly modify the tendency for alloy formation [40-42]. In addition to these important elastic-energy effects, it is expected that interface modifications to the surface-alloy electronic structure may also affect the energetic of mixing and ordering [16, 41]. For these reasons, bulk thermodynamic data do usually not apply for ultrathin films, and atoms which are immiscible in the bulk, may become miscible in an ultrathin layer. Such behavior has been reported for Au on Ni(110) [15, 16], Ag on Pt(111) [13, 14] or for AgCu films co-deposited on Ru(0001) [20-22].

In the first part of this chapter, we study the growth of NiPd and NiAu alloys on Au(111) to determine their intermixing properties in the ultrathin limit. In this respect, these two systems have opposite behaviors, bulk NiPd being a miscible system whereas bulk NiAu is an immiscible one. Moreover, our choice to mix a "small atom" (Ni) and a "big atom" (Pd or Au) and deposit them on a "big atom" susbtrate (Au) is motivated by our interest to investigate the influence of strain on the intermixing behavior and on the alloy morphology. Finally, the fact that Ni is significantly less noble than Pd and Au allows one to study the influence of the alloying on the Ni dissolution, without any interference from Pd or Au dissolution.

The electrochemical dissolution of binary alloys

The electrochemical dissolution process of binary alloys, which is commonly called dealloying, has also been largely discussed in the literature [43]. In the case where the alloy components possess large differences in their Nernst potentials, selective dissolution of the less noble metal takes place during anodic polarization leaving behind an intricate nanoporous structure made almost entirely from the noble component. The linear voltammogram of binary alloy dissolution exhibits two different regimes for the current density evolution. The potential defining the transition between these two regimes is known as the critical potential U_c [44]. At potentials below U_c, the dissolution current density is very small because of the formation of an ultrathin *surface* passivation layer, composed of the noble species. This current density is much smaller than that in the case of the pure less noble metal at the same potential. Above U_c, the current density increases sharply due to the breakdown of the passivation layer leading to a *bulk* dealloying process that produces nanoporous layers of the noble component. It has been shown that U_c strongly depends on the alloy composition but also, for a given alloy, on the nature of the anions contained in the electrolyte. For instance, addition of chloride to pure sulfate electrolyte decreases the value of U_c [45]. Such a dealloying process at potentials above U_c has been thoroughly studied and observed for binary alloys like CuAu [43, 46], AgAu [47], and also for NiCu alloys [29]. The high surface area of dealloyed materials also makes them potentially useful as catalysts [48] or sensors [49]. A variety of mechanisms have been proposed to explain the breakdown phenomenon and to predict all of the characteristic features of dealloying including the pore size of the final structures and the concentration-dependent values of U_c [50-53].

In the potential regime of passivation, i.e. below U_c, the recent development of in situ surface and structure sensitive techniques such as STM [45, 54-58] or XRD (surface X-ray scattering (SXS)) [59-61] used in the electrochemical environment allowed one to get better insight into the initial stages of the dealloying. According to STM studies performed on thick alloy films composed of AgAu [54-56] or CuAu [45, 57, 58], the dissolution of the active atoms, i.e. Ag or Cu, proceeds from terraces forming monoatomic deep vacancies which coalesce with one another due to surface diffusion of Au atoms. During the selective dissolution of the topmost alloy layer, the vacancy islands allow the second topmost layer to be in contact with the solution. Consequently, the second topmost layer undergoes also selective dissolution of the active atoms, and vacancy islands form in the second topmost layer, allowing the dissolution of the third topmost layer, etc… The diffusion of most noble metal (Au) and its interlayer transport allow progressive filling of the vacancy islands, and at some point the alloy surface is exclusively covered by the most noble metal, thus forming a passive layer [57, 58]. Renner et al. [59-61]

gained insight into the atomic structure, morphology, and chemical composition of the formed passive layers by studying the initial dealloying process of $Cu_3Au(111)$ below U_c by means of in situ XRD. They found that the structure and morphology of the formed passive layers below U_c depends on the dissolution potentials. In addition, they showed that the dealloying process and the resulting nanoporous structure also depend on the rate at which the potential is increased. At the very beginning of the selective dissolution of Cu (i.e. low overpotentials), they observed the formation of an ultrathin, about 3 ML thick, strained Au-rich layers which contains about 40% Cu, while at slightly higher overpotentials a 10-20 ML thick (2-5 nm) pure, relaxed Au islands is observed. Moreover, the formed passive layers exhibit an inverted stacking sequence of the (111) layers compared to the substrate that requires diffusion within the topmost layers of Au adatoms either on surface or from the bulk. In parallel with these experimental studies, theoretical calculations have been performed by Karma and coworkers. They succeeded in reproducing the porous morphology of AuAg alloy after Ag dissolution, as well the general shape of the current to voltage curve and the presence of a critical potential U_c [53]. Other calculations performed by Greeley and Norskov [62] focused on the determination of the dissolution potential of a solute atom in a host substrate. They presented a simple formalism for estimating trends in the thermodynamics of binary surface alloy dissolution in acidic media from Density Functional Theory (DFT) calculations. They analyzed the resulting trends in terms of the surface segregation energies of these surface alloys.

In the second part of this chapter, we will focus on the selective dissolution of Ni from monolayer thick NiPd and NiAu alloys deposited on Au(111). As the alloy thickness is one monolayer, Ni dissolution takes place in a potential range more negative than the critical potential U_c defined above for thick alloy layers. To the best of our knowledge, this dissolution regime has not been investigated in previous investigations. We will study the dissolution morphology as a function of the alloy composition. We will compare the experimental morphologies to ones obtained by Monte Carlo simulations.

5.2 Growth of Ni-based ultrathin alloy films

The objective is to characterize the morphology of NiPd and NiAu alloys electrodeposited on Au(111) and get information on the local structure by using in situ STM measurements. We will try to answer the following questions: What are the structure and the morphology of ultrathin NiPd and NiAu films? Do they form clusters or solid solution? In the latter case, can we estimate the inter-atomic distance as a function of the alloy composition? Is

the structure in agreement with the thermodynamics of bulk alloys? We will start with the results related to the formation of NiPd alloys, and then present those of NiAu alloys. The respective alloy compositions are determined by estimating, from STM images, the noble metal surface coverage (wrote θ_M with M = Pd or Au) left on the Au(111) surface after the Ni selective dissolution (see Sec. 3.3 for details).

5.2.1 Growth of Ni_xPd_{1-x} ultrathin films

a) Morphologies of Ni_xPd_{1-x} monolayer alloys

Following the 2nd procedure described in Sec. 3.3, a variety of different Ni_xPd_{1-x} thin films with Pd contents varying between 10% and 75% were prepared and investigated. With this procedure, the adsorbed $PdCl_4^{2-}$ is first discharged yielding Pd monoatomic thick islands on Au(111) surface (step 1). The Pd island coverage increases with increasing $PdCl_4^{2-}$ concentration. Then, the alloy electrodeposition occurs on this bimetallic Pd/Au(111) substrate (step 2). In the STM images, the Pd islands may be identified either as regions of the deposit smoother than the alloy corrugation, or as compact islands with a rounded shape after the Ni selective dissolution (see Sec. 5.3.1). To ease their identification in the subsequent STM images, they are surrounded with dashed lines of white or black color depending on the image contrast. The alloy deposition time was adjusted to get an average thickness of foreign metals on Au(111) ranging from 1 to 1.3 ML. The morphology of the NiPd surface alloys representative for a selection of compositions with 12%, 30%, 40%, and 75% surface Pd atoms are presented in the series of STM images in Fig. 5.2. The resulting alloy films exhibit a flat morphology independently of the Pd content and cover completely the Au substrate. This flat morphology of the NiPd monolayer alloys on Au(111) is not surprising because monolayer deposition of pure Pd [63] as well as Ni growth [64, 65] proceed two-dimensionally on this substrate even at large overpotentials.

In Fig. 5.2a, the monoatomic thick Pd islands resulting from the deposition step 1 are clearly visible. They mainly wet the ascending Au step edges and few islands are also present within the $Ni_{88}Pd_{12}$ monolayer. Using a tunneling current of ~ 1 nA and a tip bias of ~ 0.4 V, the apparent height of the Pd monolayer islands (measured with respect to Au substrate) is 1.71 ± 0.03 Å, similar to that of NiPd layer is 1.71 ± 0.24 Å. In the latter case, the large standard deviation value is due to the modulation pattern amplitude (see below). Interestingly, the surface coverage of this Ni-rich alloy ($\theta_{Ni_{88}Pd_{12}}$) is lower on top of the Pd monolayer islands than on the Au(111) terraces, in agreement with the kinetic study made in Chapter 4. The STM image in Fig. 5.2b shows a monolayer of $Ni_{70}Pd_{30}$. In addition to full alloy monolayer which grew on the

Au(111) surface, two types of bright alloy islands can be observed. First, the large ones correspond to the 1st alloy monolayer which grew on top of Pd monoatomic thick islands. Second, the small ones correspond to the beginning of the 2nd atomic layer which grew on top of the 1st alloy monolayer. In Figs. 5.2c and 5.2d, both types of islands are present but exhibit larger sizes.

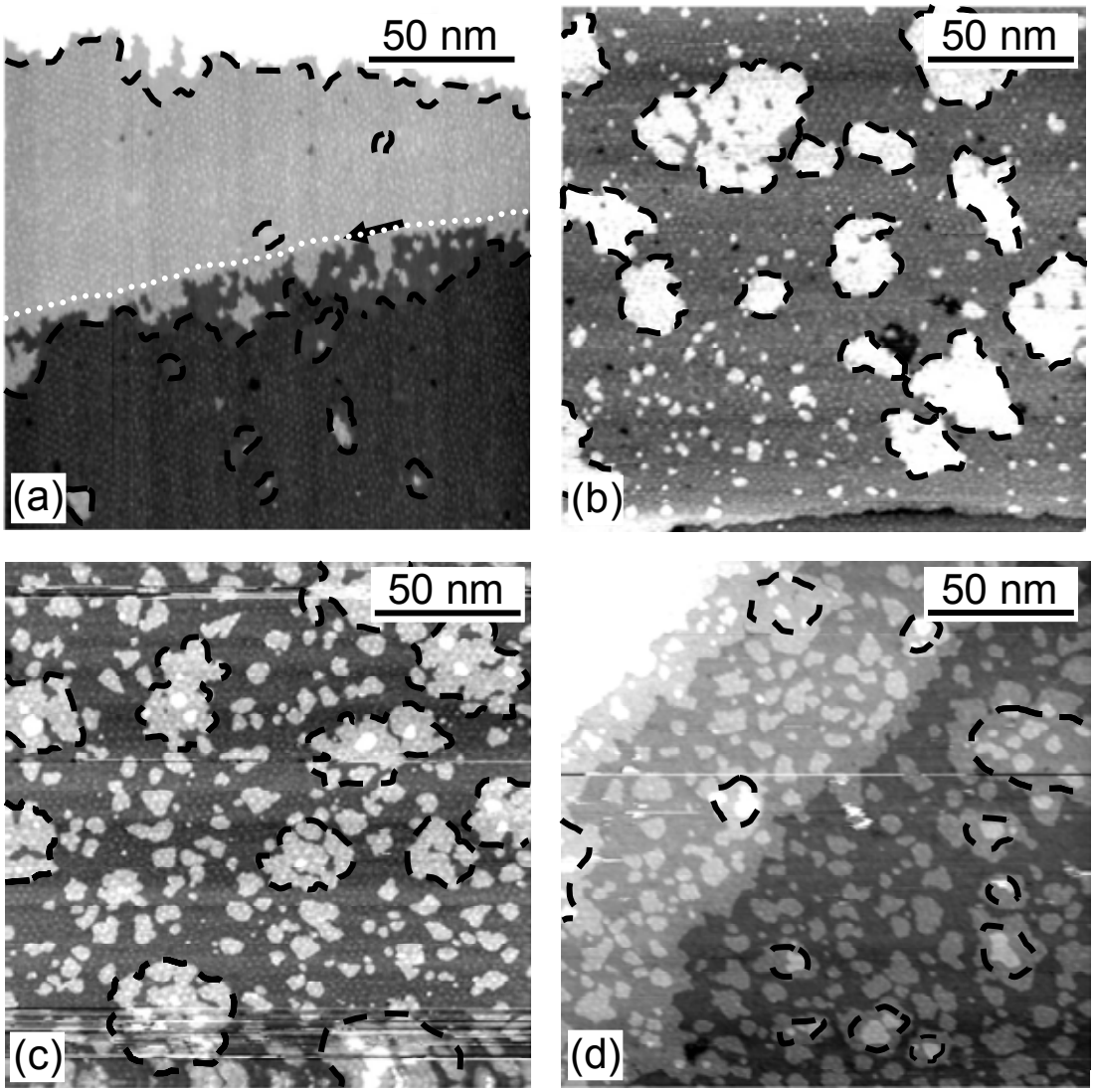

Figure 5.2: Series of STM images (180 x 180 nm²) showing the morphology of NiPd surface alloys deposited on Au(111) representative for a selection of compositions with (a) 12%, (b) 30%, (c) 40%, and (d) 75% surface Pd atoms. The surface alloys were deposited at U_{dep} = -1.24 V in 0.1 M K_2SO_4 + 1 mM H_2SO_4 + 1 mM KCl + 0.125 mM $NiSO_4$ + y mM K_2PdCl_4 with y = 0.01 (a), 0.02 (b), 0.035 (c) and 0.05 (d) during different t_{dep} ranging from 80 to 120 s. The average thickness varies between 1 and 1.3 ML. Images were recorded in the blanked supporting electrolyte at U_{stab} = -1.06 V. Black dashed lines are used as a landmark to localize Pd islands electrodeposited during the 1st step of the alloy electrodeposition.

b) Moiré structure of the NiPd alloys

A closer look to the NiPd alloy corrugation (Fig. 5.3, 50 x 50 nm^2) reveals the presence of a surface modulation, which has a hexagonal symmetry when it is ordered (in the case of Ni-rich alloys). It is clearly visible in the case of $Ni_{88}Pd_{12}$ (Fig. 5.2b) and $Ni_{70}Pd_{30}$ (Fig. 5.2c), to a smaller extent for $Ni_{60}Pd_{40}$ (Fig. 5.2d) and quasi-absent for $Ni_{51}Pd_{49}$ (Fig. 5.2e), and $Ni_{30}Pd_{70}$ (Fig. 5.2f). The modulation pattern (moiré) of pure Ni is shown in Fig. 5.2a for comparison. In the latter case, the moiré structure is caused by the mismatch between Au and Ni adlattices (see Sec. 4.3.1). Its periodicity is 21 - 22 Å and its corrugation is 0.5 - 0.6 Å. The value of its periodicity indicates that Ni layer is relaxed i.e. adopts the Ni bulk adlattice when deposited on Au(111).

STM observations show that the moiré structure, observed for pure Ni monolayer on Au(111), is strongly affected by increasing the Pd content in the alloy films. Compared to pure Ni monolayer, the presence of 12% of Pd atoms within the Ni monolayer (Fig. 5.3b) induces an increase of the moiré periodicity from 21 to 24 Å while the moiré structure remains well ordered. The modulation amplitude is found analogous to the one of pure Ni monolayer i.e. equal to 0.5 - 0.6 Å. Then, by increasing the Pd content to 30% (Fig. 5.3c) and 40% (Fig. 5.3d), the moiré structure remains visible, relatively ordered with a periodicity of 34 Å and 38 Å respectively, while the corrugation of alloy layer decreases to 0.3 - 0.4 Å. For Pd content higher than 50% (Figs. 5.3e and 5.3f), the moiré structure is no longer visible and Pd-rich monolayer alloys display a rather smooth surface characterized by a slight corrugation equal to 0.1 ± 0.05 Å.

Fig. 5.4 (right Y-axis) shows the variation of the moiré structure periodicity of Ni_xPd_{1-x} as a function of Ni content (in %). It may be well fitted by a line. If one assumes that the alloy forms a single phase, the alloy in-plane lattice parameter ($a_{Ni_xPd_{1-x}}$) can be directly deduced from the expression $P(x) = \frac{a_{Au} \times a_{Ni_xPd_{1-x}}}{(a_{Au} - a_{Ni_xPd_{1-x}})}$ (a_{Au} = 2.88 Å) [66]. A similar expression was used in the case of monometallic Ni adlayers on Au(111) (see Sec. 4.3.1). Results are depicted in Fig. 5.4 (left Y-axis). $a_{Ni_xPd_{1-x}}$ varies linearly from 2.53 Å for x = 100 to 2.68 Å for x = 50. The linear relationship between the alloy lattice parameter ($a_{Ni_xPd_{1-x}}$) and the Ni content proves that our experimental data follow the Vegard's law ($a_{Ni_xPd_{1-x}} = x \times a_{Ni} + (1-x) \times a_{Pd}$) using a value of a_{Pd} of 2.88 Å instead of 2.75 Å (the inter-atomic distance of bulk Pd) [39]. The Vegard's law has also been plotted in Fig. 5.4 taking a_{Pd} = 2.75 Å. The value of 2.88 Å is almost identical to the Au in-plane lattice parameter. Although this result is coherent with the fact that pure Pd grows pseudomorphically with Au(111) [67-69], it is quite surprising. Indeed, while the presence of a

moiré structure suggests a partial or full in-plane strain relief, it indicates that, even in the case of Ni-rich alloy, the Pd-Pd distance is that of Au.

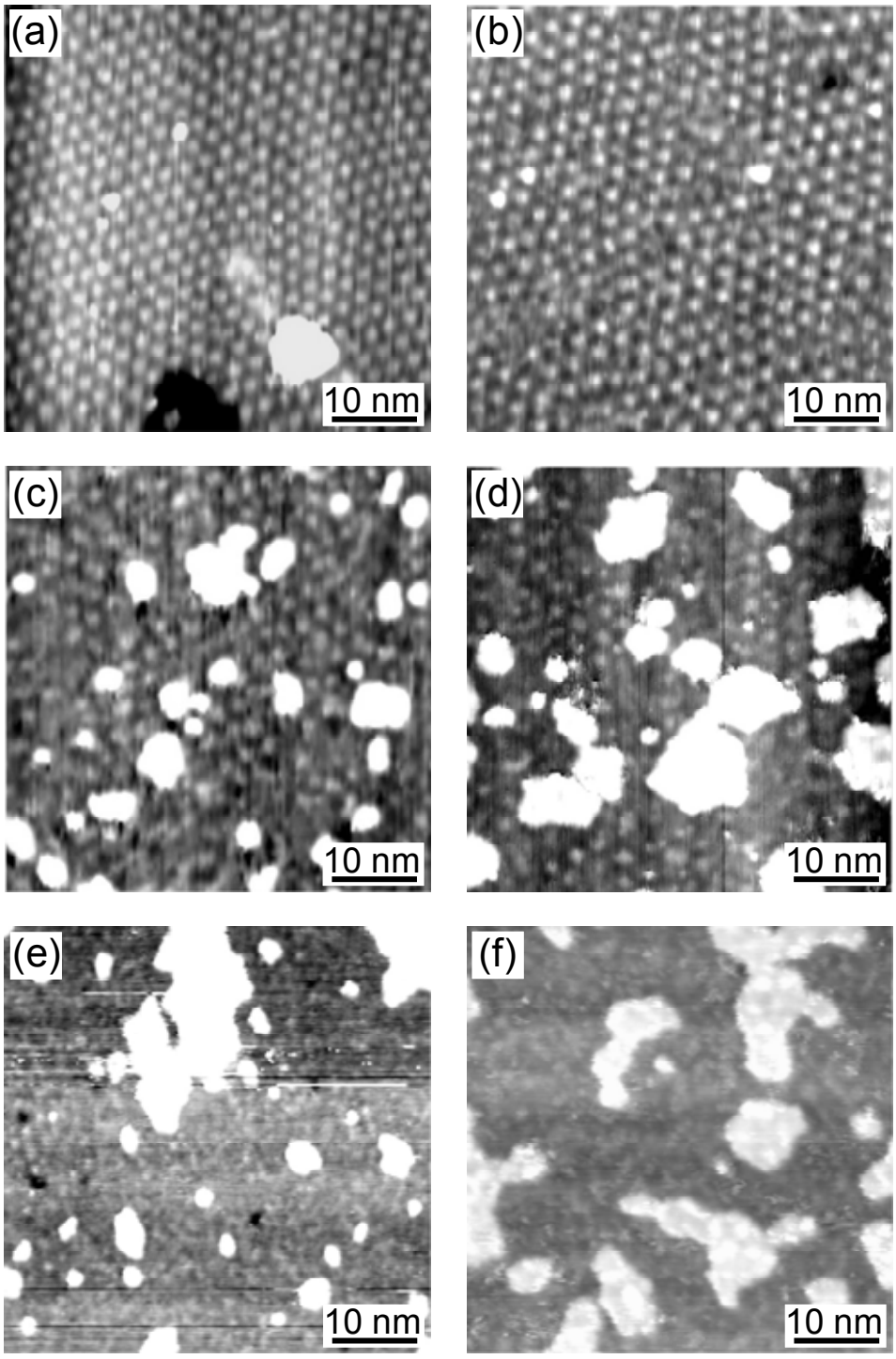

Figure 5.3: Series of STM images (50 x 50 nm²) of monolayer NiPd surface alloys deposited on Au(111) showing the variation of the moiré structure in function of the Pd content: (a) pure Ni, (b) $Ni_{88}Pd_{12}$, (c) $Ni_{70}Pd_{30}$, (d) $Ni_{60}Pd_{40}$, (e) $Ni_{51}Pd_{49}$ and (f) $Ni_{30}Pd_{70}$. The surface alloys were deposited at U_{dep} = -1.24 V in 0.1 M K_2SO_4 + 1 mM H_2SO_4 + 1 mM KCl + 0.125 mM $NiSO_4$ + y mM K_2PdCl_4 with y ranging from 0.01 to 0.05 (d) during different t_{dep} included between 80 and 120 s. Images were recorded in the blanked supporting electrolyte at U_{stab} = -1.06 V.

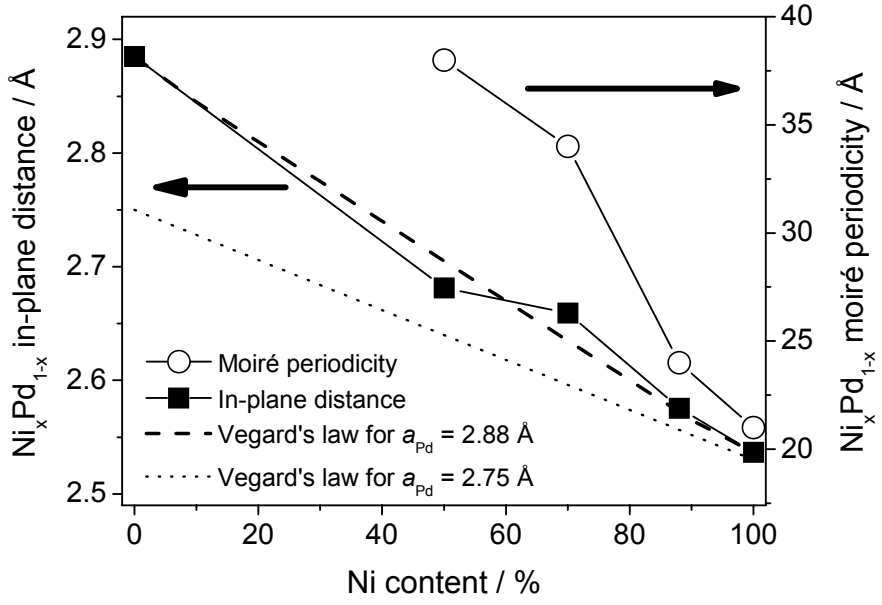

Figure 5.4: Variation of the moiré periodicity (right-hand side axis) and the in-plane distance (left-hand side axis) as a function of the Ni content in the monolayer NiPd alloy films.

c) Conclusion

If no moiré were observed, it would have been difficult to conclude about the alloy phase. Indeed, the apparent height of pure Pd (1.71 Å), pure Ni (1.74 Å) and NiPd alloys (1.71 Å) are almost identical. Therefore, in the absence of a moiré pattern, it is impossible to separate a Ni island, from a Pd island and to conclude on the presence of segregation or solid solution. The presence of a moiré pattern for Ni-rich alloys allowed us to gain invaluable information regarding the alloy phase. Its presence and its linear dependence on the Ni content suggest the presence of a single phase (solid solution, where Ni and Pd atoms are randomly arranged at the atomic scale) with one lattice parameter. The absence of moiré pattern for Ni content lower than 50%, prevents us to conclude on the alloy phase for Pd-rich NiPd alloys. As we will see in Sec. 5.3.1, more information will be gained by studying the NiPd alloy dissolution and by comparing with Monte Carlo simulations (Sec. 5.4).

The subsequent section will be dedicated to the investigation of NiAu monolayer thick alloys electrodeposited on Au(111). Similarly to the above study, stress will be made on the deposit morphology by means of STM investigations.

5.2.2 Growth of Ni_xAu_{1-x} ultrathin films

Contrary to NiPd, the NiAu system is immiscible in the bulk form leading to the clustering of atoms into Ni-rich and Au-rich groups to maximize the number of Ni-Ni and Au-Au bonds. However, recent experimental results under UHV reveal that NiAu surface alloy could be stabilized by elastic contributions due to lattice mismatch between the substrate and constituents [15]. Under electrochemical conditions, the elastic contributions should not be decisive since the Ni grows essentially unstrained on Au(111) which is not the case in UHV environment.

a) Morphology of Ni-rich alloy

STM image in Fig. 5.5a shows the typical morphology of NiAu surface alloy obtained by using the same procedure as for NiPd deposition. This ultrathin alloy film has been electrodeposited on Au(111) at U_{dep} = -1.24 V in SE + 0.125 mM $NiSO_4$ + 0.035 mM $HAuCl_4$ during 85 s. In these experimental growth conditions, the Au(111) substrate is not completely covered and the surface coverage of monoatomic thick NiAu alloy (θ_{NiAu}) is equal to 0.7. The completion of the NiAu monolayer is obtained for longer deposition time, $t_{dep} \geq 120$ s (Fig. 5.5b). Moreover, estimating θ_{Au} after Ni dissolution yields a surface content of Au into the alloy equal to 0.4 i.e. alloy monolayer corresponds to $Ni_{60}Au_{40}$. According to Fig. 5.5a-b, the deposit exhibits a 2D morphology with the absence of 2nd atomic layer islands. The large and bright alloy islands in the STM images correspond to the 1st alloy monolayer which grew on top of wide Au islands originating from the $AuCl_4^-$ anion discharge at 0 V. The small bright islands in Fig. 5.5b correspond to the beginning of the alloy 2nd layer growth. The corrugation of NiAu monoatomic layer displays a modulation, which shape and spatial distribution can be irregular or, on the contrary, ordered similarly to a moiré pattern. An example of the irregular modulation may be seen in the top of Fig. 5.5c (which corresponds to a 25 x 25 nm^2 zoom of Fig. 5.5a) where bright spots with different sizes (1 to 3 nm) are randomly distributed. In addition, peculiar shapes (indicated by arrows) forming ring (semi-circular) or worm-like ("zigzag") patterns may also be observed. Their apparent height is 2.22 ± 0.07 Å. In the lower part of Fig. 5.5c, an ordered modulation is present, with an apparent height of 1.95 ± 0.17 Å. Surface profiles in Figs. 5.5d and 5.5e show clearly this modulation which is characterized by an amplitude of 0.6 Å and periodicity of 26-27 Å. In the case of sub-monolayer alloy deposit (Fig. 5.5a), alloy islands are surrounded by discontinuous bright islands characterized by a string like shape of around 30 Å long, as the ones marked by white arrows. The cross section in Fig. 5.5d reveals that they are 2.25

± 0.05 Å high, similarly to the irregular forms within the alloy islands. Finally, small isolated islands, with a typical size of 3 to 5 nm, are also present in the sub-monolayer deposit (see the encircled island in Fig. 5.5a). Their height is inhomogeneous, with a darker area in their core compared to the edge (~ 2.25 Å), caused by a height difference of ~ 0.5 Å between the border and center.

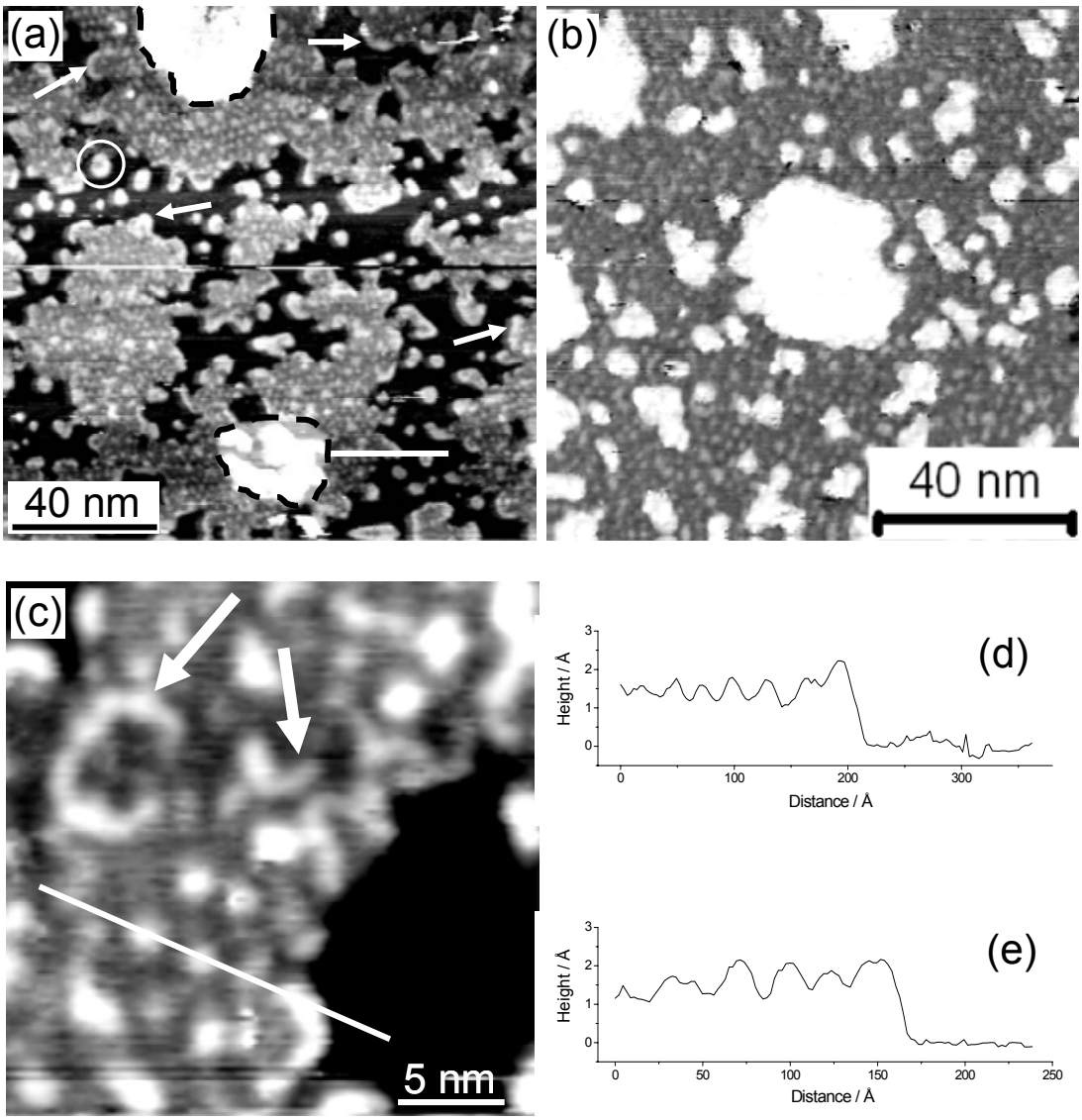

Figure 5.5: (a) STM image (147 x 147 nm^2) illustrating the morphology of submonolayer coverage of $Ni_{60}Au_{40}$ deposited on Au(111) at -1.24 V during 85 s in 0.1 M K_2SO_4 + 1 mM H_2SO_4 + 1 mM KCl + 0.125 mM $NiSO_4$ + 0.035 mM $HAuCl_4$. Image recorded at U_{stab} = -1.04 V. (b) STM image (110 x 110 nm^2) illustrating the morphology of a full monolayer of $Ni_{60}Au_{40}$ (c) Zoom (25 x 25 nm^2) in STM image taken in other area of the surface showing different types of structures. (d) and (e) cross-sections at the positions of the black lines in (a) and (c) which illustrate the height of those structures. Black dashed lines are used as a landmark to localize Au islands electrodeposited during the 1st step of the alloy electrodeposition.

The morphology of $Ni_{60}Au_{40}$ surface alloy tends to demonstrate the existence of spatial inhomogeneities in the dispersion of Ni and Au atoms. Indeed, the height of some of the observed structures (~ 2.25 Å) is much larger than that of pure Ni monolayer on Au(111) (1.74 Å) but very close to that of Au monoatomic step height (2.35 Å). Hence, these structures might correspond to Au-rich clusters. If one assumes that all these protrusions correspond to Au clusters, their total coverage should be in proportion of the alloy composition. Such estimation is very delicate because it strongly depends on the baseline correction and on the chosen threshold. We found that the coverage of these protrusions is in the range 30-45%, in reasonable agreement with the alloy composition. On the other hand, the ordered modulation patterns, which periodicity is 26-27 Å, may be attributed to a single phase NiAu alloy. A similar analysis to that done for NiPd alloys yield an average in-plane lattice parameter is equal to 2.65 Å. This value is consistent with a $Ni_{60}Au_{40}$ solid solution. Therefore, it is difficult to conclude on the alloy phase. Other experiments (especially with lower Au content), which we couldn't do because of the lack of time, would have been useful.

b) Morphology of Au-rich alloy

Au-rich alloy films were deposited on Au(111) using the 1st procedure (see Sec. 3.3) in order to get lower deposition rates (~ 20 times lower than that using the 2nd procedure) and a better control of the alloy composition. Fig. 5.6a shows STM image illustrating the morphology of $Ni_{10}Au_{90}$ thin films. The Au(111) substrate is not completely covered by the alloy films. The coverage of the 1st ML is equal to 0.88 and the 2nd one to 0.35 indicating that, in these growth conditions, the 2nd alloy layer has begun to grow before the 1st ML finished growing. It is straightforward to notice that nanometric dark areas cover uniformly the surface of $Ni_{10}Au_{90}$ layers. The presence of these inclusions is directly linked to Ni deposition. Indeed, Fig. 5.7a shows the morphology of a deposit prepared in the same conditions as those of $Ni_{10}Au_{90}$ in a Ni free solution. The resulting Au islands have compact shape with the absence of any inclusions (see cross-section in Fig. 5.7c). The remaining corrugation (which amplitude has been enhanced for the upper part of the middle island) is that of the Au(111) partial reconstruction. This morphology clearly differs from that of a $Ni_{10}Au_{90}$ island at the same scale (Fig. 5.7b) as also shown in the profile of Fig. 5.7d.

The inclusions observed in the $Ni_{10}Au_{90}$ deposits have various shapes and sizes. Some of them are rather round with a diameter ranging from a fraction of nm to several nm while others exhibit elongated shapes with a typical width of ~ 1 nm and length up to 7 nm. Atomic scale images of the $Ni_{10}Au_{90}$ deposit are shown in Figs. 5.6c-d. Even though the Au lattice is clearly

resolved, we couldn't image any defined features within the dark inclusions. However, we could confirm more precisely that their typical width is ~ 1nm (inclusion marked with an arrow in Fig. 5.6c). We could also show the presence of smaller inclusions down probably to a single atom. Indeed, in Fig. 5.6d, some single *protrusions* (indicated with arrows) correspond most probably to adsorbates on atomic inclusions.

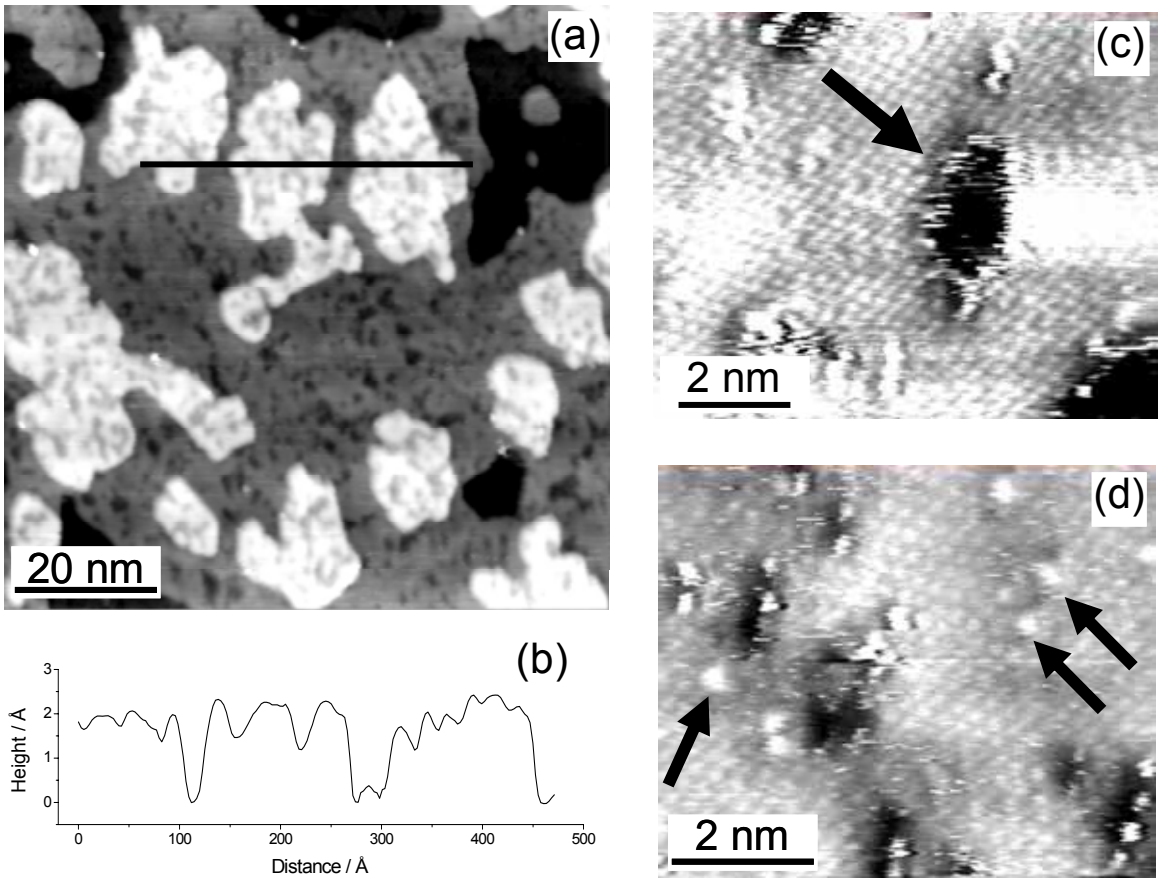

Figure 5.6: STM image (85 x 85 nm²) showing the morphology of $Ni_{10}Au_{90}$ deposited on Au(111) at -1.50 V during 30 min in 0.1 M K_2SO_4 + 1 mM H_2SO_4 + 1 mM KCl + 2. 25 µM $NiSO_4$ + 6.75 µM $HAuCl_4$. Image recorded at U_{stab} = -1.02 V in the blanked supporting electrolyte. (b) Surface profile across islands of the 2nd alloy atomic layer along the line shown in (a). (c) and (d) atomic scale resolution of the $Ni_{10}Au_{90}$ alloy showing the hexagonal lattice of Au(111) and dark or bright features associated with the presence of Ni.

The surface profile in Fig. 5.6b of islands of the 2nd atomic layer reveals that their height is around 2.35 Å while the depth of the inclusions inside the film is in average 0.93 ± 0.2 Å relative. Similar dimensions were found for the 1st ML alloy layer. Thus, the height of the two deposited layers is exactly that of the pure Au steps confirming that the alloy film is mainly made of Au adatoms. In addition, the inclusion height with respect to the lower terrace equals to ~

1.42 Å. This value is very close to the height of the needlelike Ni islands which are equal to 1.4 Å [70]. We therefore attribute these inclusions to Ni islands in the Au layer. The small measured height of Ni inside the island could be explained by the fact that Ni atoms are under strain as in the case of needlelike islands which undergo uniaxial contraction and do not exhibit moiré pattern.

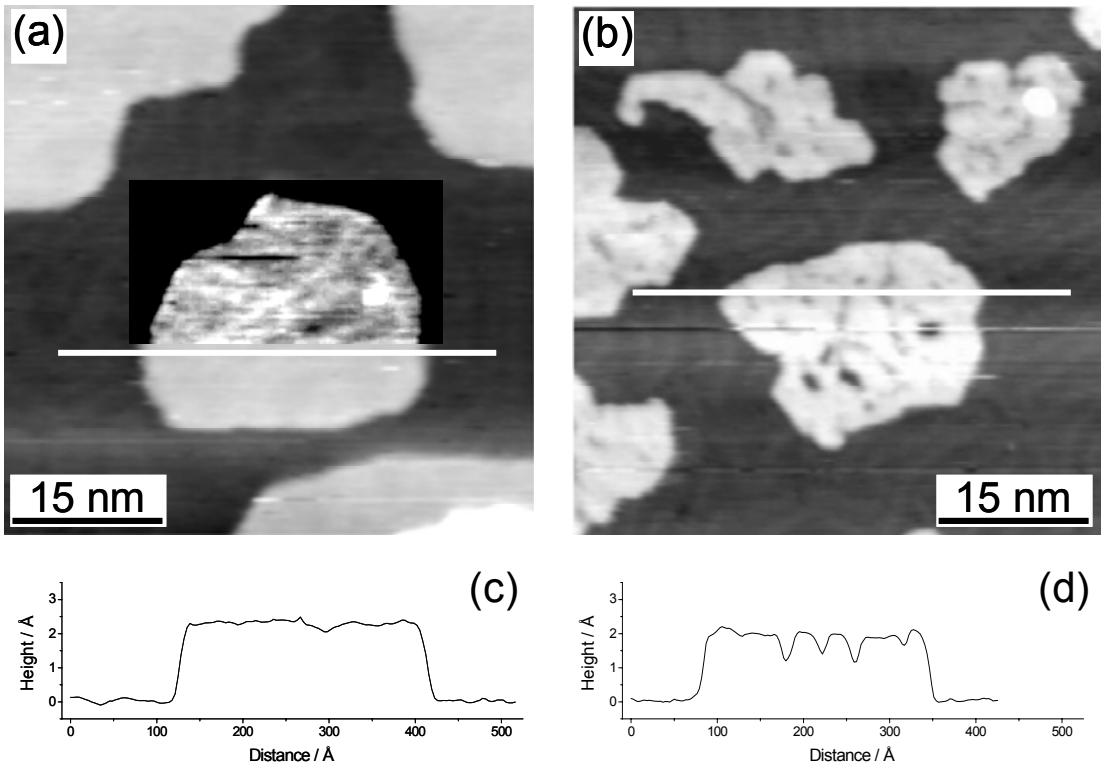

Figure 5.7: STM image (53 x 53 nm²) comparing the morphology of (a) pure Au islands with the one of (b) $Ni_{10}Au_{90}$ islands. Submonolayer coverage films has been deposited on Au(111) at -1.50 V during 30 min in 0.1 M K_2SO_4 + 1 mM H_2SO_4 + 1 mM KCl + 2.25 μM $HAuCl_4$ without (a) and with 0.75 μM $NiSO_4$ (b). Image recorded at U_{stab} = -1.04 V in the blanked supporting electrolyte. The line scans (c) and (d) are taken along the bars in image (a) and (b) respectively.

c) Conclusion

As a brief conclusion, atomically flat and monolayer thick NiAu ultrathin alloys have been successfully prepared by electrodeposition on Au(111) with two stoichiometries $Ni_{10}Au_{90}$ and $Ni_{60}Au_{40}$. The Ni-rich alloy films have a strong surface modulation which may be regularly arranged resembling to a moiré pattern, or irregularly in size and shape. The periodicity of the regular modulation is in agreement with a $Ni_{60}Au_{40}$ solid solution, in opposition to the thermodynamic data for bulk NiAu alloys. The Au-rich alloy films reveal the presence of

nanometric inclusions which may be as small as a single atom or may have an elongated shape with ~ 1 nm wide and up to ~ 7 nm long. The rest of the layer has the characteristic height of Au(111). We attribute the inclusions to Ni islands embedded in the Au layer, implying that the $Ni_{10}Au_{90}$ alloy is most probably phase segregated at the nanometer scale.

5.3 Selective dissolution of Ni from NiAu and NiPd ultrathin alloy films

As mentioned above, STM observations of the morphology of electrodeposited NiPd and NiAu monolayer alloys enable us to partially conclude about the structure of these monolayer alloys. In the following sections, the selective dissolution of the less noble metal i.e. Ni from monolayers of NiAu and NiPd alloys will be studied by STM as a function of time and potential, to get better insight into the atomic structure of these alloys and into the influence of alloying on the dissolution potential of Ni. In addition, the time-resolved experiments will allow us to follow the surface diffusion of the more noble metal, during the selective dissolution of Ni. Results related to the dissolution of NiPd alloys will be presented first, followed by the ones concerning NiAu.

5.3.1 Dissolution of Ni from NiPd ultrathin films

This section deals with the dissolution processes of ultrathin NiPd alloy films studied by STM. The Ni_xPd_{1-x} monolayer alloys were electrodeposited by using the 2nd procedure detailed in Sec. 3.3 for which the substrate corresponds to a bimetallic Pd/Au(111) surface. In the following STM images, the Pd monoatomic thick islands deposited on Au(111) during the 1st step of the procedure are surrounded by dashed lines of white or black color depending on the image contrast. The morphologies of the monolayer NiPd alloys used here have already been presented in Sec. 5.2.1. In the following, Ni dissolution results from Ni_xPd_{1-x} will be presented starting with the Ni-rich alloys.

a) Dissolution of $Ni_{88}Pd_{12}$ monolayer alloy

Fig. 5.8 shows the dissolution process of a monolayer of $Ni_{88}Pd_{12}$ alloy. As explained in Sec. 5.2.1, the alloy surface morphology exhibits a moiré structure of periodicity equal to 24 Å and modulation amplitude of 0.6 Å (Fig. 5.8a). In order to induce the beginning of the

dissolution process, the electrode potential (U) was gradually increased from the stabilization potential U_{stab} = -1.06 V. By increasing U up to -0.96 V, the NiPd monolayer remains completely stable. The beginning of the dissolution starts when the electrode potential was stepped from -0.96 V to -0.90 V, as shown in Fig. 5.8b recorded 6 min after the potential step. At this potential, the dissolution begins exclusively at the edges of the few vacancy islands contained in the alloy monolayer as can be observed by comparing Figs. 5.8a and 5.8b (see black circles for instance). Besides, the dissolution of the NiPd alloy deposited on Pd islands is kinetically more favorable than that of NiPd deposited on Au (see within the black dashed line). In Fig. 5.8c, acquired after 12 min at the same potential, the selective dissolution of Ni from the deposited alloy on Au(111) has obviously progressed from the edges of the vacancy islands. The removal of Ni results in the appearance of small islands of ~ 1.7 Å high on Au(111) and of ~ 2.1 Å on Pd monolayer islands. Complete dissolution of Ni is achieved after 19 min at U = -0.90 V (not shown) while the increase of the electrode potential up to -0.2 V has no effect on the small islands left over the two surfaces, which indicates that they correspond to Pd islands originating from the Pd atoms from the NiPd alloy. Moreover, the height difference measured between the Au terraces and the Pd islands corresponds to that of hydrogenated Pd (see Chapter 4). In Fig. 5.8d recorded at U = -0.80 V, the uniform distribution of the Pd islands on both substrates indicates a homogeneous alloy stoichiometry on the 10 nm scale which is in agreement with the formation of random solid solution.

It is interesting to notice that the onset potential of Ni selective dissolution from $Ni_{88}Pd_{12}$ deposited on Au(111) is in the range between -0.96 V and -0.90 V, which is significantly more positive than the onset of dissolution of pure Ni monolayer deposited on Au(111) (-0.98 V) or on Pd(1ML)/Au(111) (-1.02 V) (Chapter 4). Hence, it indicates that even a small proportion of Pd dispersed among Ni entails a variation of its onset dissolution potential independently of the chemical nature of substrate.

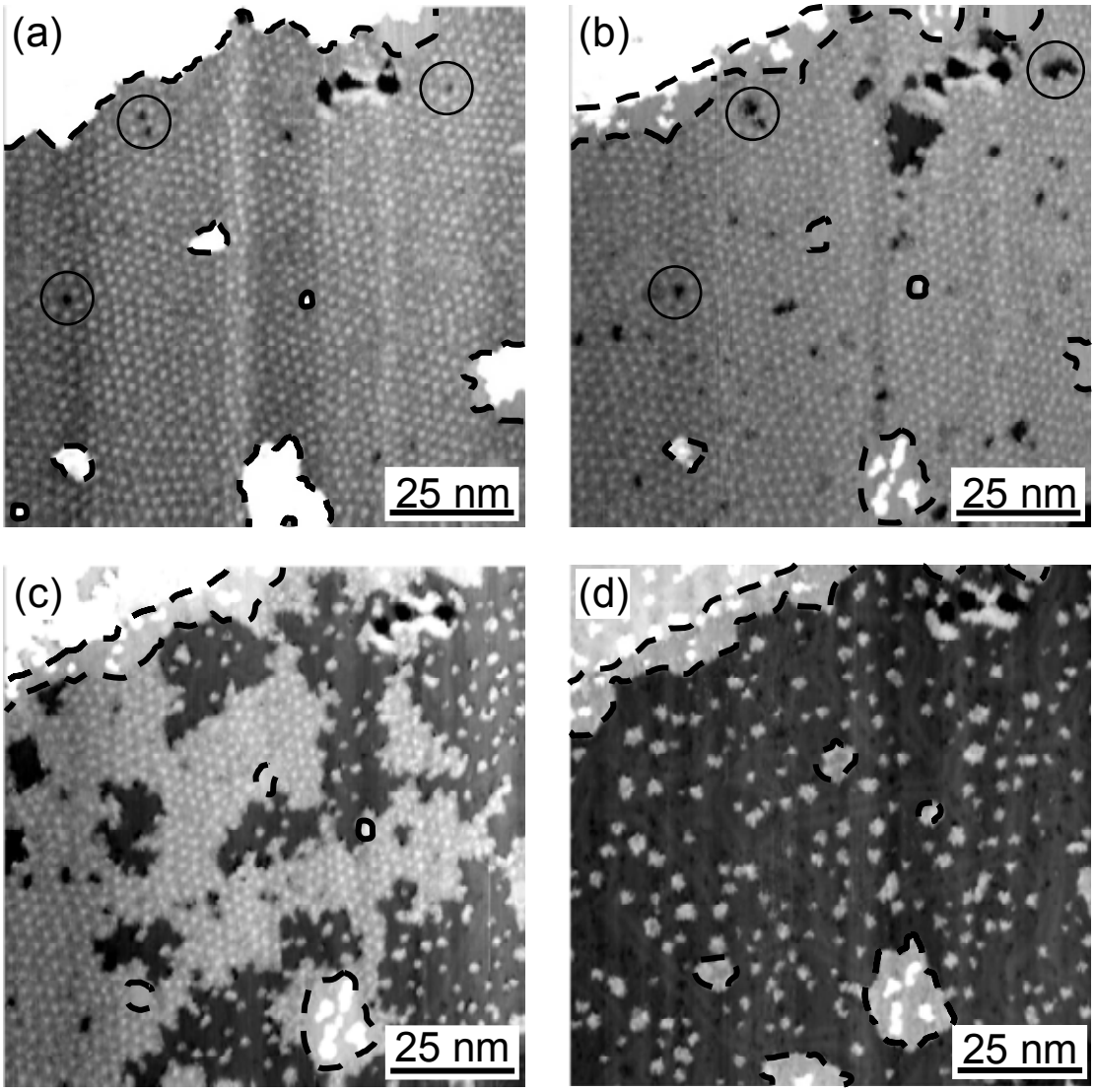

Figure 5.8: Series of STM images (105 x 105 nm^2) showing the dissolution process of $Ni_{88}Pd_{12}$ monolayer alloy deposited on Au(111) at -1.24 V during 120 s in 0.1 M K_2SO_4 + 1 mM H_2SO_4 + 1 mM KCl + 0.125 mM NiSO4 + 0.01 mM K2PdCl4. Images were recorded at (a) U = -1.06 V, at U = -0.90 V after (b) 6 min, (c) 12 min and (d) 36 min. Black dashed lines are used as a landmark to localize Au islands electrodeposited during the 1st step of the alloy electrodeposition.

b) Dissolution of $Ni_{70}Pd_{30}$ monolayer alloy

Fig. 5.9 shows the dissolution process of $Ni_{70}Pd_{30}$ monolayer alloy. As for $Ni_{88}Pd_{12}$, the alloy monolayer remains stable up to U = -0.96 V (Fig. 5.9a) then the potential was stepped to U = -0.90 V where the dissolution process began. In Fig. 5.9b recorded after 6 min at U = -0.90 V, the dissolution has taken place at the edges of small vacancy islands initially present in the alloy film (white circles in Fig. 5.9a). In addition, regions with darker contrast, which characteristic size equals ~ 10 nm, can be observed (black arrows in Fig. 5.9b). These domains appeared

simultaneously with the beginning of the dissolution process (they are absent in Fig. 5.9a) and correspond to areas where the local monolayer height decreases by around 0.4 - 0.5 Å. We carefully checked that they are not the result of the plane correction of the image. In the centre of each vacancy island formed by Ni dissolution, small Pd islands remain on the Au(111) surface as observed in the case of $Ni_{88}Pd_{12}$. After 9 min at the same potential (Fig. 5.9c), the dissolution continues from the step edges of vacancy islands (see white circles), Ni dissolution taking preferentially place from the dark domains mentioned above. In Fig. 5.9d, it can be observed than the size of the remaining alloy islands on Au(111) is not homogeneous. In addition to small rounded-shape islands which have sometimes coalesced, larger islands are still present on the Au surface as the one enclosed in the white rectangle. These islands appear irregular in height, with the presence of darker areas. Then, after 21 min at U = -0.90 V (see Fig. 5.9e), the morphology of the alloy layer does not evolve any further, and few large islands remain on the Au(111) surface. Noticeable changes in the alloy morphology is obtained by increasing the electrode potential up to U = -0.80 V (Fig. 5.9f), which results in the formation of vacancy islands within the remaining large islands of Fig. 5.9e. No changes are observed upon increasing the potential furthermore.

In order to quantitatively analyze these observations, we plotted in Fig. 5.10 the variation of the alloy surface coverage (θ) on Au(111) and the alloy Ni content as a function of the dissolution time. The potential is also indicated in the upper part of the graph. θ has been determined from the quantitative analysis of STM images. The Ni content was calculated as the difference between the actual coverage and the final coverage (after complete Ni dissolution) divided by the actual coverage. At U = -0.90 V, θ decreases rapidly from 1 to 0.4 during the first 15 min, which corresponds to the dissolution of 86% of the Ni present in the alloy, and then reaches a plateau at θ = 0.4 - 0.35. Further decrease of θ is possible by increasing the electrode potential to -0.85 V and then to -0.80 V, where θ reaches its final value of 0.30, corresponding to the Pd coverage initially contained in the alloy. Thus, the kinetics of the dissolution process seems to level off at U = -0.90 V. At this point, the Ni content within the alloy film diminished from 70% to 20%. The remaining 20% of Ni content necessitates applying more positive potentials.

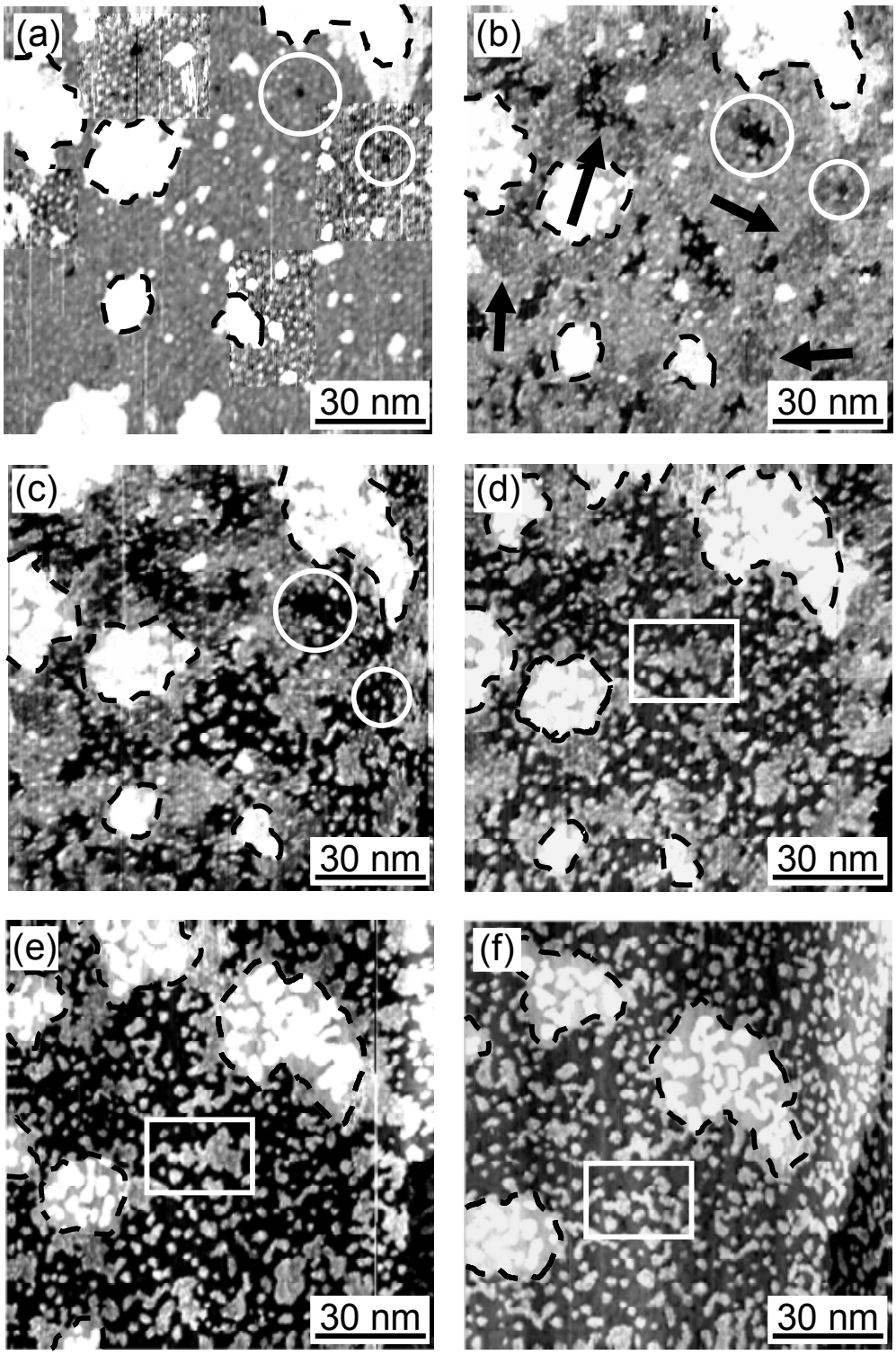

Figure 5.9: Sequence of STM images (116 x 116 nm^2) illustrating the dissolution process of $Ni_{70}Pd_{30}$ monolayer alloy deposited on Au(111) at U_{dep} = -1.24V during 110 s in 0.1 M K_2SO_4 + 1 mM H_2SO_4 + 1 mM KCl + 0.125 mM $NiSO_4$ + 0.02 mM K_2PdCl_4. Images were recorded at (a) U = -0.96 V, at U = -0.90 V after (b) 6 min, (c) 9 min, (d) 12 min and (e) 21 min and finally (f) at U = -0.80 V after 26 min from the beginning of the dissolution process. Black dashed lines are used as a landmark to localize Au islands electrodeposited during the 1st step of the alloy electrodeposition. White circles indicate the regions where dissolution starts. White rectangle are used as landmark to allow following one specific alloy island.

It is interesting to note that, in addition to the shift of the Ni dissolution onset observed also for $Ni_{88}Pd_{12}$, more positive potentials are necessary for the complete dissolution of Ni. According to the STM images shown in Fig. 5.9, the remaining Ni atoms after the dissolution at -0.9 V are mainly located in the center of alloy islands surrounded by a Pd rim. This suggests that the Pd rims passivate the remaining Ni atoms. Finally, the appearance of the dark regions at the dissolution onset is intriguing, and has not been observed in the case of $Ni_{88}Pd_{12}$. Their apparent height with respect to the Au substrate is close to that of pure needlelike Ni deposit. However, these areas definitely contain Pd atoms, as indicated by the Pd islands left on the surface after their dissolution. They might correspond to Ni-rich domains. Indeed, a careful examination of the location of these areas in Fig. 5.9a (areas with enhanced image contrast), shows that they correspond to regions with relatively well ordered moiré pattern. As the ordering of the latter is related to the Pd content in the alloy (Sec. 5.2.1), it seems that these areas have a lower Pd content than the rest of the film.

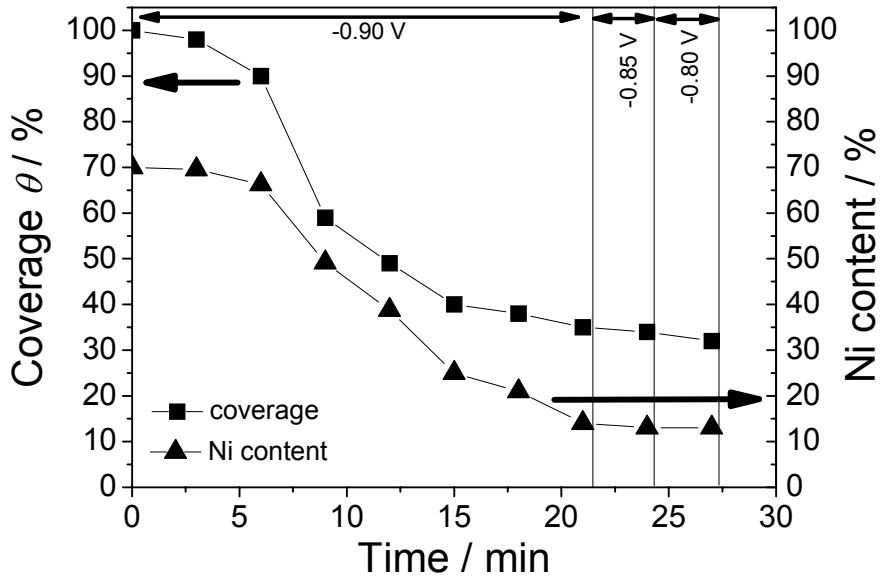

Figure 5.10: Variation of the surface coverage of $Ni_{70}Pd_{30}$ monolayer alloy on Au(111) and the Ni content embedded in the remaining alloy islands during the dissolution experiment shown in Fig. 5.9.

c) Dissolution of $Ni_{51}Pd_{49}$ monolayer alloy

We also studied the Ni selective dissolution for the $Ni_{51}Pd_{49}$ alloy, for which no defined surface modulation is observed. Fig. 5.11 shows a series of STM images illustrating the dissolution process. Fig. 5.11a shows the morphology of $Ni_{51}Pd_{49}$ film recorded at U = -0.95 V where the alloy is stable. Fig 5.11b was recorded 10 min after stepping the potential to -0.9 V.

Similarly to the case of $Ni_{88}Pd_{12}$ (Fig. 5.8) and $Ni_{70}Pd_{30}$ (Fig. 5.9), the removal process of Ni occurs exclusively at the step edges of small vacancy holes originally contained in the alloy film. The edges of these vacancy islands are characterized by the presence of bright islands which could be composed of Pd atoms. We also observe the dark areas (depletions of around 0.4 - 0.5 Å) in case of $Ni_{70}Pd_{30}$, although in the present case, their size is much smaller (see for example regions with enhanced image contrast in Fig 5.11b and also in Fig 5.11c). Such domains are still visible after stepping back the electrode potential to -1.00 V, which indicates that their appearances are not caused by a change in the imaging conditions but are rather induced by the selective dissolution of Ni. The removal of Ni atoms takes place preferentially in these areas.

Fig 5.11c shows the dissolution morphology 20 min after stepping the potential to -0.9 V. The hole average size remains rather small considering the dissolution time of 20 min indicating that the dissolution kinetics of $Ni_{51}Pd_{49}$ at U = -0.90 V is much slower than the one found in the case of $Ni_{70}Pd_{30}$. Stepping the electrode potential to -0.88 V (Fig. 5.11d) results in increasing the dissolution rate (after it became negligible at -0.9 V), revealing large monoatomic thick alloy islands in which the dissolution has not yet begun (as the one enclosed by the white rectangle in Fig. 5.11d). The spatial distribution of the vacancy islands is rather inhomogeneous. Fig. 5.11e shows the morphology of the remaining alloy film at U = -0.84 V after 43 min from the commencement of the dissolution process. At this potential, the dissolution of Ni leads to the appearance of (*i*) vacancy stripes within the large islands which started at the step edges in direction to the centre and, in a lower extent of (*ii*) vacancy holes embedded in the islands (see inside the white rectangle for instance). Finally, at U = -0.72 V (Fig. 5.11e), the selective dissolution of Ni is completed. It should be noted that the remaining Pd islands are not inter-connected, but forms large (larger than 10 nm) aggregates separated by nanometric Pd islands.

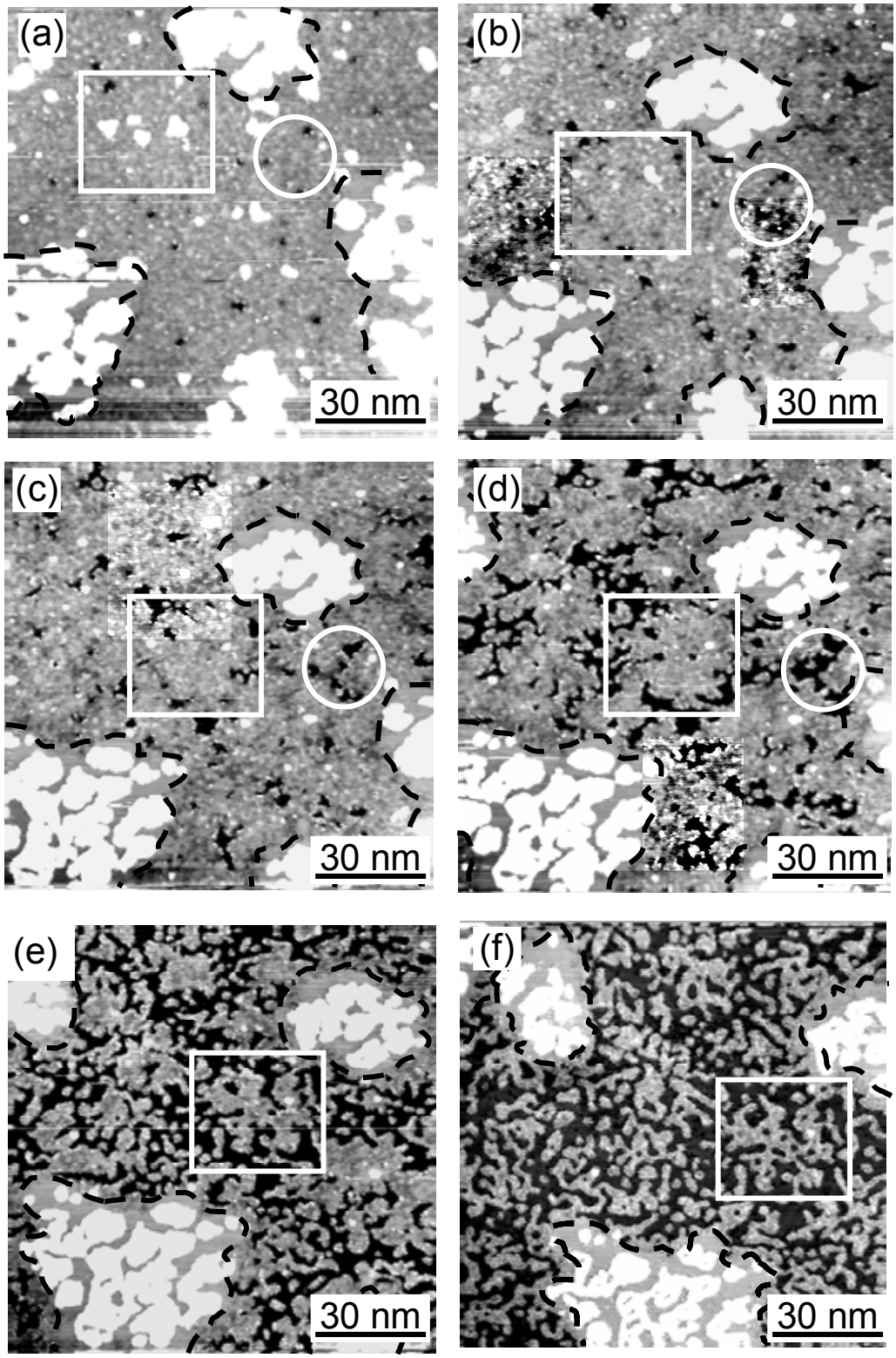

Figure 5.11: Series of STM images (116 x 116 nm^2) showing the selective dissolution of Ni from $Ni_{51}Pd_{49}$ monolayer alloy deposited on Au(111) at -1.24 V during 90 s in 0.1 M K_2SO_4 + 1 mM H_2SO_4 + 1 mM KCl + 0.125 mM $NiSO_4$ + 0.035 mM K_2PdCl_4. Images were recorded at (a) U = -0.95 V, (b) U = -0.90 V after 10 min, (c) U = -0.90 V after 20 min, (d) U = -0.88 V after 31 min, (e) U = -0.84 V after 43 min, and (f) U = -0.72 V after 69 min from the beginning of the dissolution process. Black dashed lines are used as a landmark to localize Pd islands electrodeposited during the 1st step of the alloy electrodeposition.

Fig. 5.12 displays the variation of surface coverage during the dissolution of $Ni_{51}Pd_{49}$. It can be observed that each small increase of the electrode potential leads to a rapid increase of the dissolution rate followed by a saturation, a behavior similar to that observed for $Ni_{70}Pd_{30}$. However, in the present case, the complete dissolution of Ni necessitates applying a significantly more positive potential (> -0.8 V). If we apply the same reasoning as for the $Ni_{70}Pd_{30}$ alloy, we come to the conclusion that different passivation steps take place during the dissolution of Ni from $Ni_{51}Pd_{49}$.

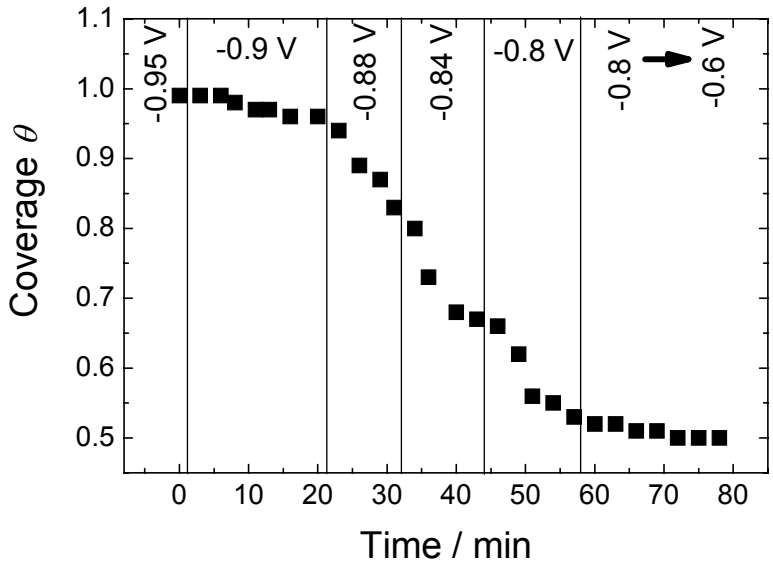

Figure 5.12: Variation of the surface coverage of $Ni_{51}Pd_{49}$ monolayer alloy on Au(111) during the dissolution experiment shown in Fig. 5.11.

d) Dissolution of $Ni_{24}Pd_{76}$ monolayer alloy

The dissolution of $Ni_{24}Pd_{76}$ ultrathin alloy is shown in Fig. 5.13. It starts at -0.9 V (Fig. 5.13b) and necessitates applying -0.65 V (Fig. 5.13f) to remove all the Ni atoms. The dissolution rate is slower than that of $Ni_{51}Pd_{49}$ at similar potentials. During the dissolution process, the coarsening of the vacancies formed upon Ni removal yields labyrinth shapes (see Fig. 5.13c-d), which increase in size and connectivity as a function of time and potential. On the other hand, the last dissolution stage (see Fig. 5.13e-f) is characterized by the formation of nanometric holes in the layer, which remain separated from each other and from the large void labyrinths. It is interesting to note the presence of these two characteristic vacancy islands: the large labyrinth and the nanometric holes.

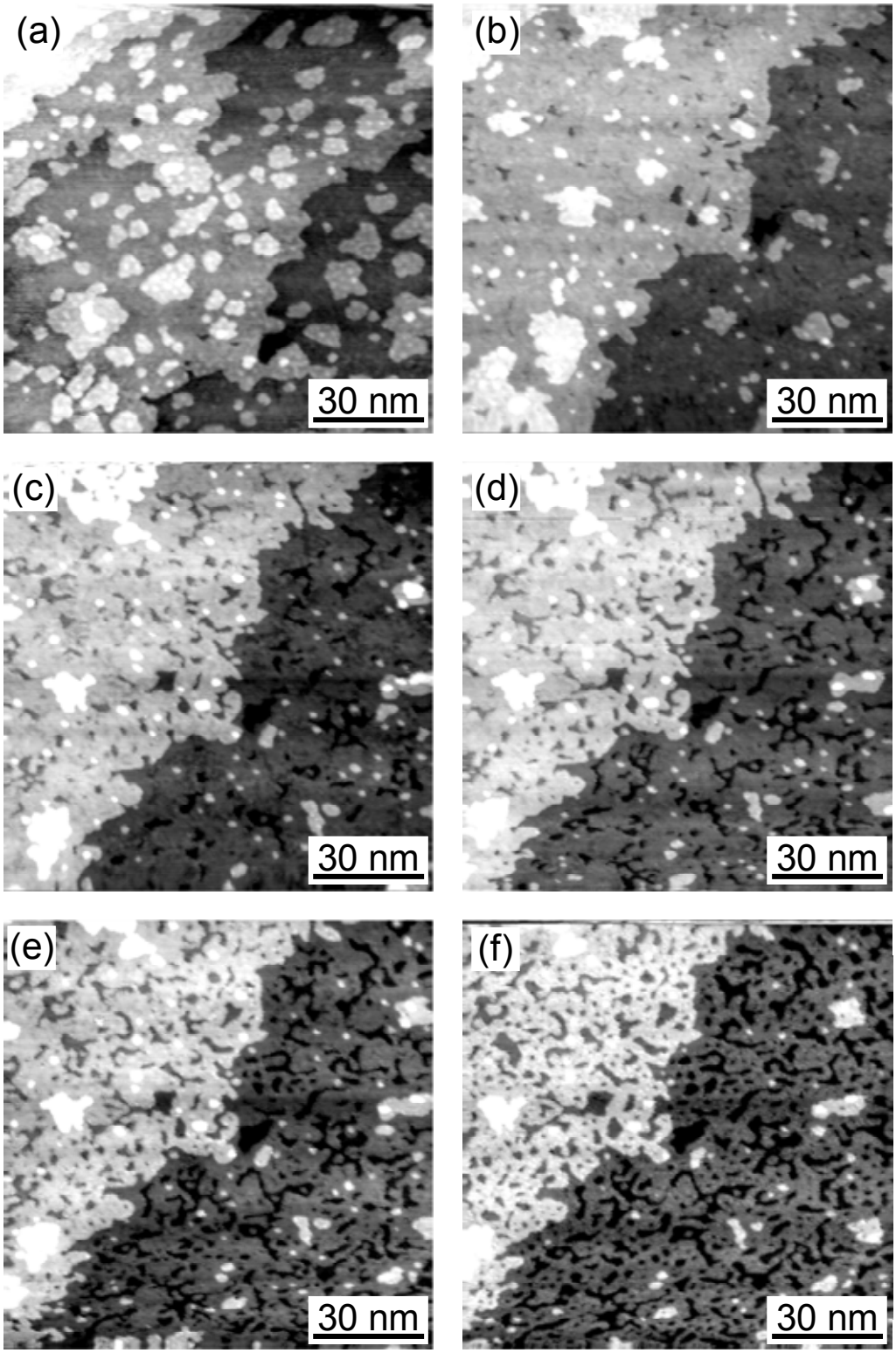

Figure 5.13: Sequence of STM images (116 x 116 nm^2) illustrating the dissolution of $Ni_{24}Pd_{76}$ monolayer alloy deposited on Au(111) at -1.24 V during 75 s in 0.1 M K_2SO_4 + 1 mM H_2SO_4 + 1 mM KCl + 0.125 mM $NiSO_4$ + 0.05 mM K_2PdCl_4. Images were recorded at (a) U = -1.00 V, (b) U = -0.88 V after 17 min, (c) U = -0.82 V after 28 min, (d) U = -0.78 V after 36 min, (e) U = -0.75 V after 41 min, and (f) U = -0.65 V after 53 min from the beginning of the dissolution process. Black dashed lines are used as a landmark to localize Pd islands electrodeposited during the 1st step of the alloy electrodeposition.

e) Conclusions

Studying the dissolution of NiPd alloys with different compositions give evidence of the pre-existence or the formation (during Ni dissolution) of Ni-rich regions, where the dissolution takes place preferentially. These regions appear at the dissolution onset potential and remain until the complete removal of Ni. The morphology of the Pd layer at the end of the dissolution process is inhomogeneous: Pd islands with two characteristic sizes and shapes for $Ni_{51}Pd_{49}$ and vacancy islands with also two characteristic sizes and shapes for $Ni_{24}Pd_{76}$. Finally, although the dissolution onset potential is quasi-independent of the alloy composition (-0.9 V), increasing Pd content of the alloy decreases the dissolution rate and increases the potential allowing complete Ni dissolution (up to -0.65 V for $Ni_{24}Pd_{76}$).

5.3.2 Dissolution of Ni from NiAu ultrathin films

a) Dissolution of Ni-rich alloy

Fig. 5.14 shows a series of STM images of the dissolution process of Ni from $Ni_{60}Au_{40}$ alloy electrodeposited on Au(111) by using the 2nd procedure. The submonolayer coverage alloy film shown in Fig. 5.14a corresponds to the same deposition experiment than the one described in Fig. 5.5 (see Sec. 5.2.2). STM image of Fig. 5.14a was recorded at U = -1.01 V where no dissolution occurs, and shows the presence of wide monoatomic thick alloy islands. Ni dissolution begins at U = -0.98 V which is equal to the dissolution potential found in the case of pure Ni monolayer deposited on Au(111) (see Sec. 4.4). In each STM image, white rectangle encloses the same NiAu island to facilitate comparison during the dissolution process. In Fig. 5.14b, recorded after 11 min at U = -0.98 V, dissolution has obviously progressed from the edges of NiAu islands. During the dissolution process of Ni, some islands are left on the Au(111) surface. These islands are 2.35 Å high indicating that they correspond to pure Au islands. After 30 min at the same potential (Fig. 5.14c), the density of these Au islands increases. Moreover, Au atoms accumulate at the edges of the alloy islands as indicated by white arrows in Fig. 5.14c. At U = -0.98 V, most of the dissolution of Ni from NiAu islands was achieved after 50 min (not shown). However, in the last dissolution stage, some Ni atoms remain trapped within Au-rich islands as the ones indicated by white arrows in Fig. 5.14d. The dissolution of the remaining Ni atoms requires applying potentials in the range between -0.97 and -0.75 V. Such wide potential range is probably related with the local atomic environment of the remaining Ni atoms. This behavior is similar to the passivation of Ni by Pd observed during NiPd dissolution. However, in

the present case, this passivation takes place for Ni coverage (< 0.5%) and Ni content (< 1%) which are much smaller than that in the case of NiPd.

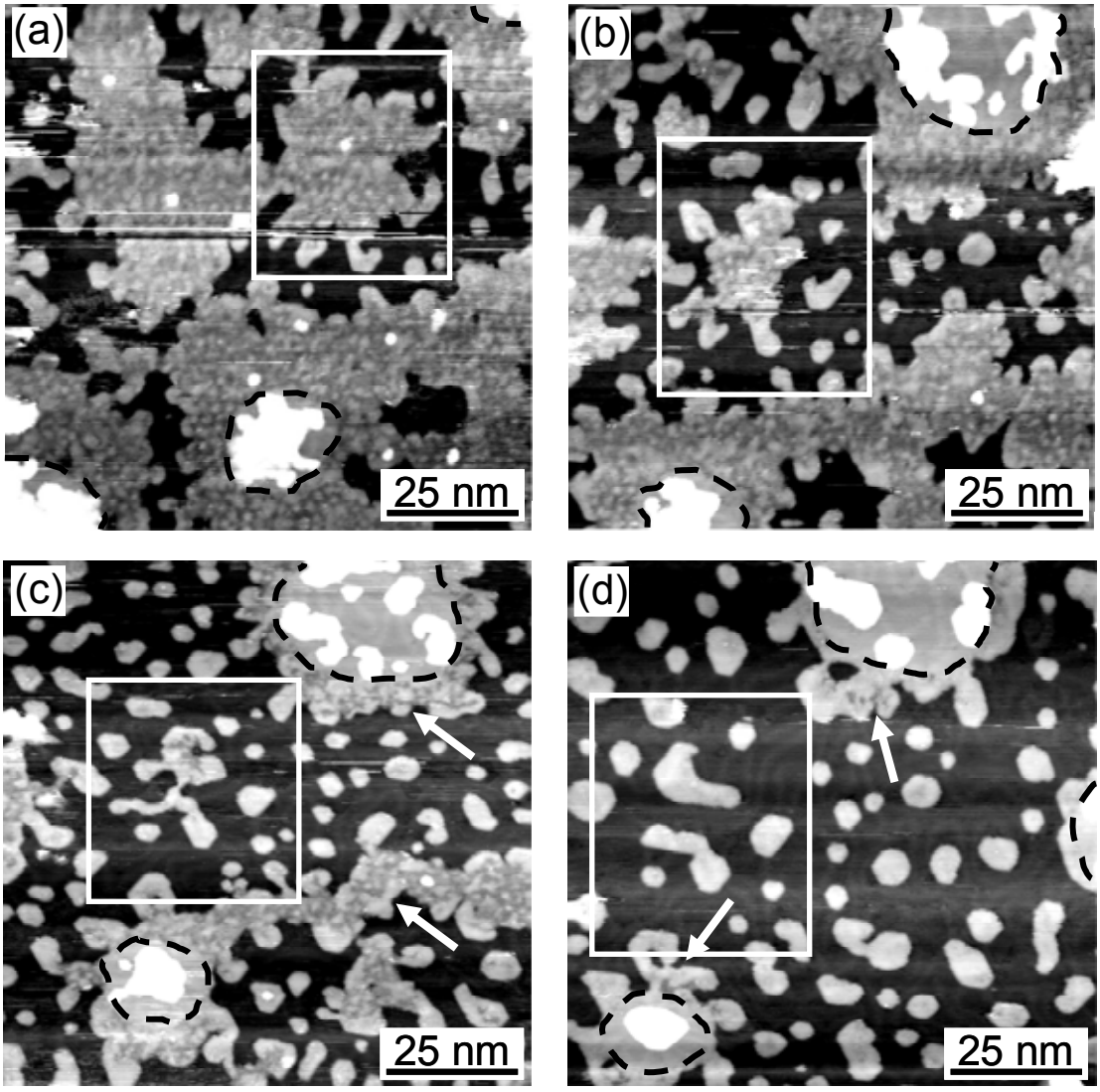

Figure 5.14: Sequence of STM images (100 x 100 nm^2) showing the selective dissolution of Ni contained into submonolayer coverage of $Ni_{60}Au_{40}$ which was deposited on Au(111) at -1.24 V during 85 s in 0.1 M K_2SO_4 + 1 mM H_2SO_4 + 1 mM KCl + 0.125 mM $NiSO_4$ + 0.035 mM $HAuCl_4$. Images were recorded at (a) U = -1.01 V and successively at U = -0.98 V after (b) 11 min, (c) 30 min and at (d) U = -0.93 V after 100 min from the beginning of the dissolution process. White rectangles enclose one of the NiAu islands to facilitate comparison during the dissolution process despite the presence of lateral drift. Black dashed lines are used as a landmark to localize Au islands electrodeposited during the 1st step of the alloy electrodeposition.

In order to analyze in more details the dissolution process, we will focus on one island (white rectangle in Fig. 5.14) and follow its dissolution as a function of time (Fig. 5.15). Fig. 5.15a displays its initial shape at U = -1.01 V in which patterns formed by bright mounds are clearly

discernable, especially in the center part of the island. We marked some of them by black dots to ease their identification during the dissolution process. Fig. 5.15b was recorded after 11 min at *U* = -0.98 V at which the selective dissolution of Ni had begun. At this potential, the dissolution takes place exclusively at the edges of NiAu island. After 14 min at this potential (Fig. 5.15c), the number of spotted mounds decreased. Meanwhile, a dark area is starting to form in the upper part of the island (see dotted lines in Fig. 5.15c and Fig. 5.15e). This area is relatively large (~ 2 x 10 nm^2), much larger than the expected separation between two modulations within a moiré pattern, and its apparent height is 0.7 - 0.8 Å smaller than that of the surrounding Au clusters. It may therefore consist in a pure Ni phase. This Ni phase was not present in Fig. 5.15a, and was formed during the dissolution process. Figs. 5.15d and 5.15e point out different dissolution kinetics between the bright mounds and the surrounding layer which has been assigned to a Ni phase. For example, the feature marked by the white arrows (quoted A in Figs. 5.15d-f) is not affected by the dissolution process, although it is located at the island edge. Between Figs. 5.15e and 5.15f, it can be noticed that the mound indicated by the arrow A seems to have moved to join the Au located in its vicinity (see white arrow in Figs. 5.15f). Meanwhile, a second spotted mound has diffused to a neighborhood Au island (process B) as can be seen by comparing the area enclosed in the black ellipse in Fig.5.15e and in Fig. 5.15f. Subsequently, similar surface diffusion processes arise during the end of the selective dissolution of Ni and correspond to the ones noted C and D in Figs. 5.15g and 5.15h. Finally, after 50 min (Fig. 5.15k), the selective dissolution of Ni seems to be completed (the surface coverage reaches a saturation value) and dark areas that we assigned to a Ni phase is no longer visible. On the Au(111) surface remains the Au islands resulting from the Ni removal. In Fig. 5.15l recorded 25 min after Fig. 5.15k at the same potential, the surface morphology is almost unchanged, although the Au islands remaining on the surface slowly evolved to their 2D hexagonal shape. The behavior described above is not specific to the chosen area. Indeed, similar characteristic morphologies may be observed in different areas as the one shown in Fig. 5.16.

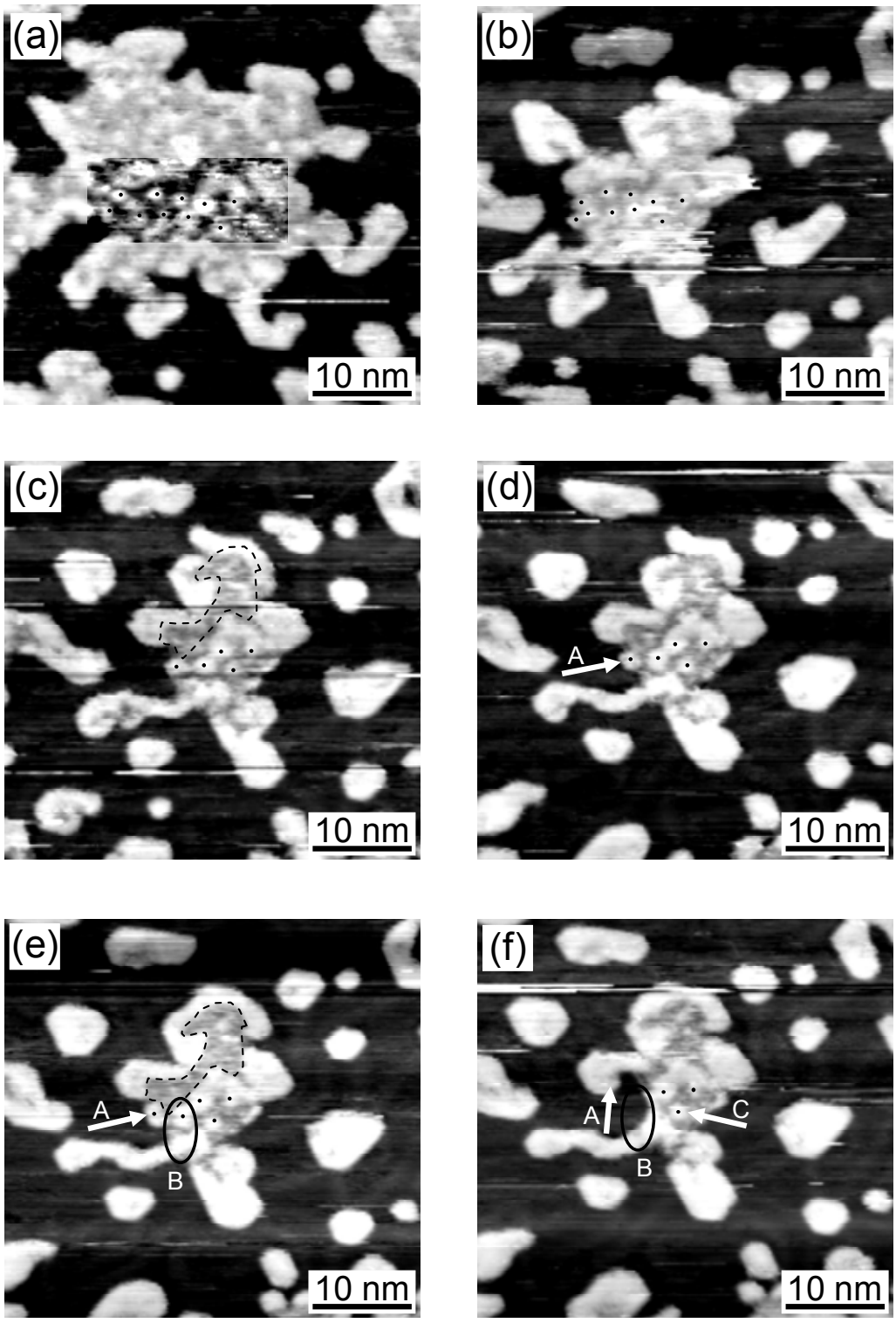

Figure 5.15: Series of 12 STM images (42 x 40 nm²) showing the selective dissolution of Ni from $Ni_{60}Au_{40}$ island. Images focus on the island enclosed by white rectangle in Fig. 5.14. They were recorded at (a) U = -1.01 V and successively at U = -0.98 V after (b) 11 min, (c) 14 min, (d) 20 min, (e) 23 min and (f) 26 min. Lateral drift present in images of Fig. 5.14 has been corrected.

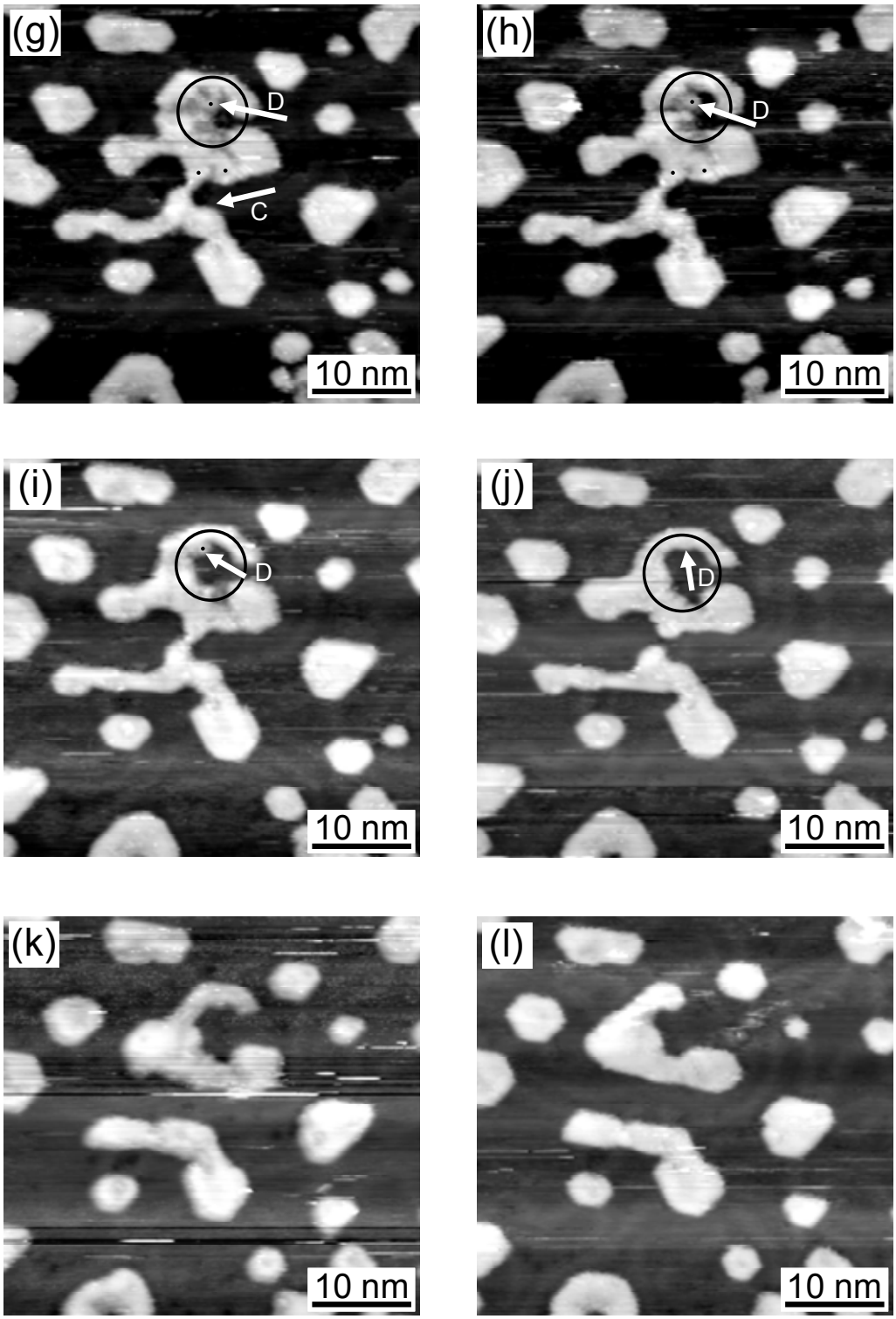

Figure 5.15: Selective dissolution of Ni from $Ni_{60}Au_{40}$ island continued (42 x 40 nm²). Images were recorded successively at U = -0.98 V after (g) 34 min, (h) 37 min, (i) 40 min, (j) 42 min, (k) 50 min and (l) 75 min.

The presence of the relatively large areas which we assign to a Ni phase, suggest that the protrusions of the NiAu alloys are most probably pure Au clusters. As explained in Sec. 5.2.2, their coverage is in agreement with the Au content in the alloy. These facts are in favor of a

phase separated $Ni_{60}Au_{40}$ alloy. This is in agreement with thermodynamic data of bulk NiAu alloys, and kinetically possible thanks to the large Au adatom mobility in this potential range [71, 72] and its probable increase in the presence of chloride [73-75]. Nevertheless, the ordering of the observed protrusions in some areas of the alloy layer is rather intriguing. Further investigations would be helpful for a better understanding of the observed morphology.

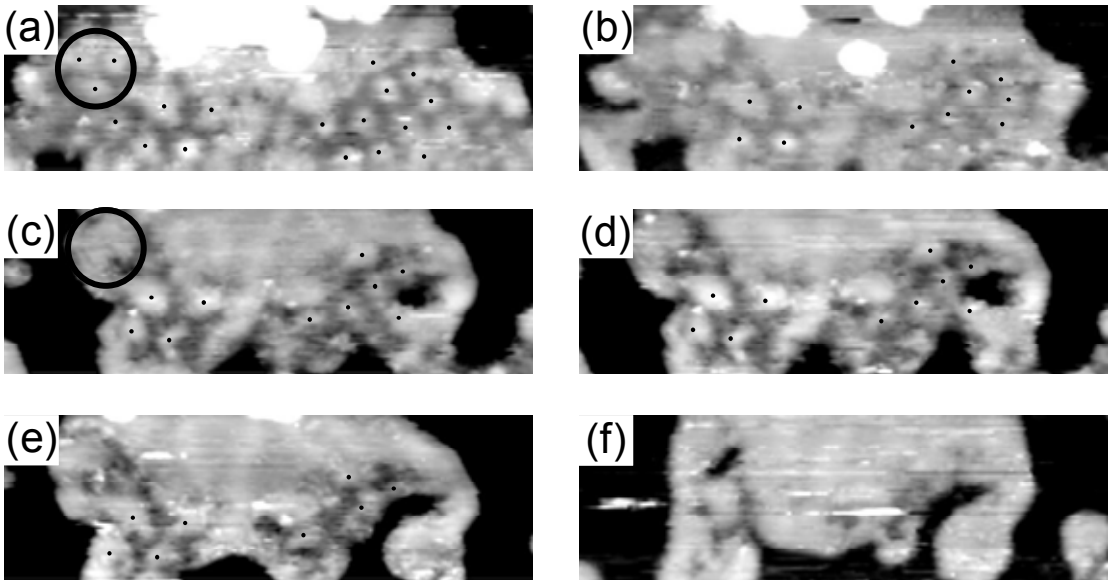

Figure 5.16: Series of STM images (37 x 12 nm^2) illustrating the selective dissolution of Ni from $Ni_{60}Au_{40}$ island for which the long-ranged quasihexagonal ordered patterns are well resolved. Some of them are spotted by small black dots to make their identification easier during the dissolution process. Images were recorded at (a) U = -1.01 V and successively at U = -0.98 V after (b) 8 min, (c) 23 min, (d) 26 min, (e) 40 min and (f) 63 min.

b) Dissolution of Au-rich alloy

Fig. 5.17 presents a series of STM images showing the dissolution process of $Ni_{10}Au_{90}$ alloy layer, deposited using the 1st procedure (see Sec. 3.3). The alloy layer grew around a pre-existing Au island. The latter is surrounded by a dashed line. In addition, Au(111) reconstruction is also visible inside this Au island (Figs. 5.17c-f). We do not show large scale images because, first, we found similar dissolution morphologies in the different areas and the morphology evolution takes place at a small scale. A first specific feature of Au rich NiAu alloy is the dissolution potential range, which spreads between -0.9 V and -0.6 V. This characteristic has been observed for Ni rich NiAu alloy, in the last dissolution stage. Such wide dissolution potential range is most probably due to the special morphology of the alloy, which consists in nanometer Ni inclusions in the Au lattice (Fig. 5.17a). The dissolution of these inclusions begins essentially at -0.85 V (Fig. 5.17b), where small vacancy islands (indicated by grey colored arrows) start to be

formed exclusively in the inclusions regions. However, the vacancy island formation does not appear to be faster in case of large inclusion area. Indeed, a hole is not observed by STM in the large inclusion, which is surrounded by a white circle, until Fig. 5.17e. The following dissolution steps are observed while the potential is gradually increased from -0.8 V (Fig. 5.17c) to -0.6 V (Fig. 5.17f), where the major part of the Ni inclusions are transformed into vacancy islands. However, even at -0.6 V, some inclusions (the smallest) are still present. The hole density increases gradually with decreasing Ni content, and no significant island coarsening was observed.

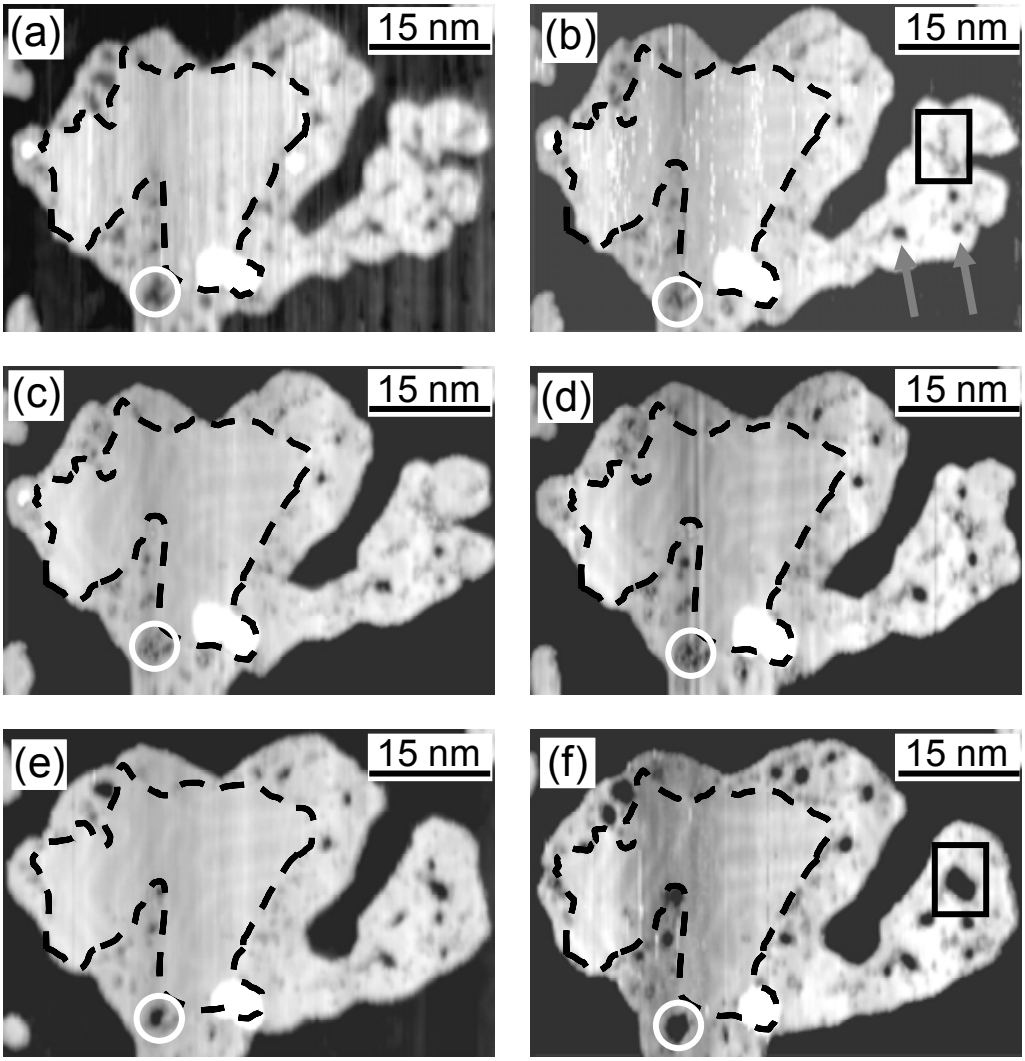

Figure 5.17: Series of STM images (61 x 41 nm²) illustrating the selective dissolution of Ni from a $Ni_{10}Au_{90}$ island which grew around a pre-existing Au island. The latter is highlighted by a dashed line. The dissolution of a specific part of the island is indicated by a white circle. Images were recorded at (a) U = -0.9 V, (b) U = -0.85 V, (c) U = -0.8 V, (d) U = -0.8 V, (e) U = -0.7 V and (f) U = -0.6 V. Black dashed lines are used as a landmark to localize a pure Au island.

It is interesting to compare between the initial area of an inclusion and that of the hole formed at the same location after selective dissolution of Ni. Such comparison is particularly

instructive in the case of inclusion showing an elongated shape, as the one highlighted by the black rectangle in Fig. 5.17b. The area of the hole formed after Ni dissolution (black rectangle in Fig. 5.17f) divided by the length of the inclusion before dissolution yields an inclusion width of ~ 1 nm. This value is close to the one obtained in Sec. 5.2.2, but significantly smaller than the inclusion apparent width in the STM image. In the same way, smaller inclusions, which appear nanometric in size, probably consist in few Ni atoms or even a single atom. In such small inclusions, the lateral neighbors of Ni atoms are mainly Au atoms. This specific environment of Ni atoms is probably responsible for their stability up to -0.6 V. Finally, the area of the vacancy islands in Fig. 5.17f is very close to that of the inclusions in Fig. 5.17a.

c) Conclusions

Studying the Ni selective dissolution from $Ni_{60}Au_{40}$ alloy layer allowed us to show that Ni dissolution takes place at the same potential than the one found for pure Ni monolayer on Au(111). Hence, the presence of Au adatoms embedded in Ni monolayer does not modify the potential at which Ni atoms are removed. Then, by following the dynamic processes during Ni dissolution, the features we observed suggest that the protrusions correspond to pure Au clusters embedded into a pure Ni layer. In other terms, the $Ni_{60}Au_{40}$ alloy films are phase segregated at the nanometer scale. Similar conclusions may be drawn from the study of $Ni_{10}Au_{90}$ alloy dissolution, although in this case, it takes place at more positive potentials because the Ni phase form nanometric inclusions in the Au layer.

5.4 Monte Carlo simulations of alloy dissolution

Monte Carlo simulations of the dissolution of one monolayer of an alloy AB have been performed in order to check whether it is possible to reproduce the experimentally observed morphology of the bimetallic alloys during their dissolution with one set of simulation parameters. Such investigation is rather ambitious, first due to the large number of atomic scale events that are necessary for a realistic description of the dissolution process; second because the available STM data are at the nanometer scale but rarely at the atomic scale. Other groups are specialized in such calculations (see for example [76]). Therefore, the aim of these simulations is not to determine the atomic parameters but to find whether the morphologies observed by STM as a function of the alloy composition correspond to those of a solid solution or a segregated alloy.

5.4.1 Model description

In order to simulate correctly the alloy dissolution process, one needs to define two sets of parameters: one for the dissolution step and one for the surface diffusion step. These steps are calculated on a square lattice (instead of a hexagonal lattice) for the sake of simplicity. Therefore, some of the morphology features of the simulated dissolution will reflect the square surface symmetry. Consequently, one should be careful when comparing the calculated morphology and those obtained from the STM experiments.

a) Dissolution step

A complete set of parameters defining the dissolution step should include the desorption probabilities of the less noble metal (A) as a function of the atomic site, i.e., as a function of the number of neighbors and their chemical nature (A or the more noble metal B). This leads to 15 parameters in the case of a square lattice with maximum 4 nearest neighbors. However, in practice, only few of these parameters are relevant. Indeed, most of the STM dissolution experiments have been performed at a very slow dissolution rate. In this case, it has been experimentally observed that the desorption of A takes place mainly at the deposit step edge and only rarely in the middle of the deposit terrace. This indicates that, in spite of the large number of atoms A in sites with 4 neighbors at the beginning of the alloy dissolution, the desorption probability of A in such a site may be neglected. Similar reasoning leads also to give a small value to the desorption probability of A in a 3 neighbor site. Nevertheless, we still need to fix 6 parameters (5 relatively to one of them), i.e., the dissolution probability of A with 0 neighbor, with 1 neighbor (A, or B), with 2 neighbors (AA, AB or BB). One expects that the desorption probabilities of A with 2 A neighbors is different from those with 2B neighbors. However, this different influence on the dissolution morphology may be neglected in a first approximation, because the diffusion step will smooth it out. Indeed, the random diffusion of atoms A and B will attenuate the effect of the initial desorption position of the atom A on the final deposit morphology. This smoothening is effective because of the small dissolution rate allowing a relatively long diffusion step. Therefore, in the present simulations, one set of desorption probabilities was considered which is independent of the nature of the neighbors. The desorption probabilities are listed below and are referenced to that with 0 neighbors:

Number of neighbors	Desorption probability
0	1
1	1
2	0.1
3	0.01
4	$1\ 10^{-7}$

It is important here to briefly discuss how these values have been chosen. They are not the result of any ab initio calculation which is far beyond the scope of this work. They have been determined (in order of magnitude) to account for the experimentally obtained morphology (see details in the following sections). The reason for the significantly smaller desorption probability for the site with 4 neighbors with respect to the other desorption probabilities is the following: one has to bear in mind that to determine whether an atom A with a specific number of neighbors will desorb, these desorption probabilities have to be multiplied by the number of available sites. In practice, during the dissolution of 1 ML of alloy, the number of A with 0 neighbor is very small (see diffusion step), whereas, there exists a large number of A with 4 neighbors (all terrace sites). This very small desorption probability of A with 4 neighbors has been chosen to allow simulating correctly the rare experimental observation of pit formation in the alloy terraces. Finally, as we will see in the diffusion step description, the diffusion step duration is inversely proportional to the desorption probability. Therefore, in order to study the influence of the diffusion step duration on the dissolution morphology, the chosen set of desorption probabilities was allowed to increase (respectively decrease) by a factor of 10. This results in a decrease (respectively increase) of the diffusion step duration by a factor of 10.

b) Diffusion step

The set of parameters necessary to describe properly the diffusion step contains also a large number of parameters. Indeed, one has to take into account the atomic diffusion as a function of the number of neighbors, the chemical nature of the neighbors (A or B) and the difference of surface mobility of A and B. Again, we end up with a large number of parameters. However, one should expect that diffusion probabilities are significant for atoms with 2 or less neighbors only, and that diffusion towards a site with fewer neighbors is less favorable than towards a site with equal or larger number of neighbors. In order to take into account in a simple way these differences in diffusion probabilities, we considered that the diffusion probability for atoms with 2 or less neighbors depends exponentially ($e^{-\alpha \Delta n}$, with a multiplying factor α typical

values equals 1 to 5) on the *difference* Δn of the number of neighbors of the final site and that of the initial site (i.e., no dependence on the actual initial and final site type). For example, the diffusion probabilities in the case of an atom with n neighbors to a site with n+1, n, or n−1 neighbors are respectively >1, =0.22, or =0.01, using $\alpha = 3$ (see Fig. 5.18). Such simplifications (exponential form, independence on the site type) are most probably crude for the proper description of the atomic diffusion processes, but as we will show, we are only interested in a qualitative description of the obtained morphologies, with no aim to obtain atomic parameters out of these simulations. We allowed this exponential factor to depend on A (α_A) and B (α_B). However, we found out that the influence of α_A on the obtained morphology is much less significant than that of α_B. Therefore, we will consider $\alpha_A = \alpha_B$ in the following. Moreover, as mentioned above, the diffusion probability should in principle depend on the local atomic environment, i.e., whether the neighbors are A or B. Indeed, one way to understand the formation of a segregated alloy is to consider a larger diffusion probability for an atom with neighbors with different chemical nature (A surrounded by B, or B surrounded by A). We took into account this phenomenon by adding an adjustable parameter β allowing one to increase artificially the number of neighbors if the atom and its neighbors are of the same chemical nature. The typical value of this number of neighbor change is 0.5−1.5 per neighbor. If this factor is larger than 1 (1.2 in Fig. 5.18), then an A atom with B neighbors will have a larger probability to diffuse than an A atom with A neighbors. This factor was applied only to the initial site and not to the final diffusion site. In addition, in order to take into account the probable difference between the surface overall diffusion coefficient of A and B, the diffusion probability was allowed to vary as a function of the chemical nature of the diffusing atom (typically by a factor 10−100). However, as mentioned above, the diffusion coefficient of A has little influence on the dissolution morphology, and thus it will be considered equal to that of B. Finally, we considered that the probability of vacancy formation in the deposit terraces resulting from vacancy diffusion from the step is negligible. Practically, we excluded vacancy diffusion from the step to into the terrace.

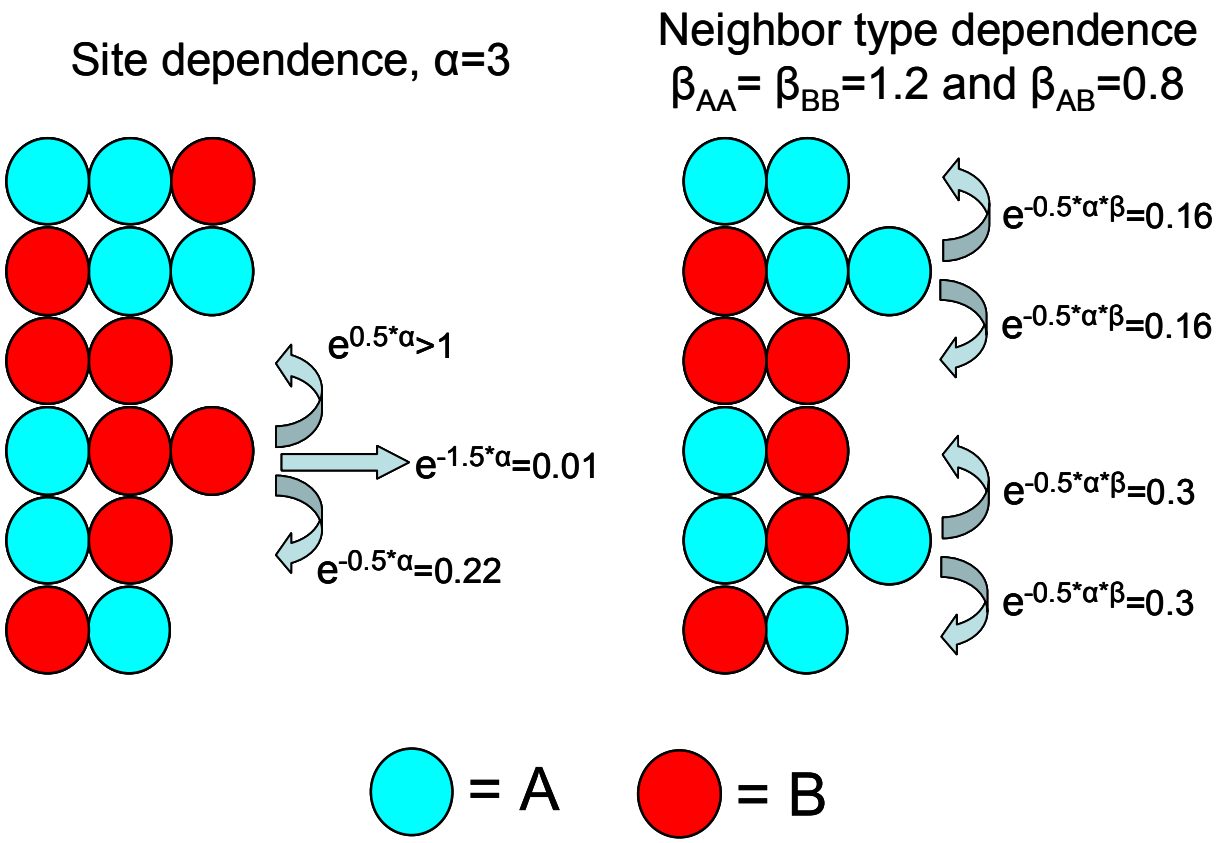

Figure 5.18: Schemes illustrating the different diffusion probabilities of atoms A (blue balls) and atoms B (red balls) as function of the local environment and the values of the diffusion parameters α , β_{AA}, β_{BB}, β_{AB}.

c) A brief description of the program

A typical dissolution simulation is performed as follows:

- The construction of a full monolayer of a random solid solution A_xB_{1-x} alloy which is represented by a matrix. The matrix element values may be 1 (atom A, the less noble metal) or 2 (atom B). In the dissolution process, a vacancy will be represented by 0. It was found useful to construct a second matrix which contains the number of neighbors of each atom (4 at the beginning). A typical matrix size is 100 x 100 (more rarely 200 x 200 atoms), which correspond to STM image sizes of ~ 25 nm x 25 nm (~ 50 nm x 50 nm).
- In a while loop, the dissolution and the diffusion steps are achieved sequentially, until no A atoms are available. In the dissolution step, A atoms are sorted as a function of their probability to desorb multiplied by the number of A atoms in a similar site. Then one of the A atoms with a large probability to desorb is removed, and the number of neighbor matrix is updated. In the second step, all atoms (A and B) with a number of neighbors between 0 and

3 are listed. These atoms are then allowed to hop to an available neighboring position, with a diffusion probability which depend on the number of neighbors in the initial and the final site, and the initial site environment (mostly A, or mostly B). The atom and neighbor number matrixes are then updated. The number of times the diffusion step is achieved after the desorption of one A atom is inversely proportional to the desorption probability (see table above) of the most probable atom in the preceding dissolution step.

- We considered periodic conditions at the cell borders.

5.4.2 Simulation results

a) Summary of the characteristics of the experimental alloy dissolution morphology

Similarly to former studies [53], we will compare the experimental alloy final morphology, i.e., after the desorption of all the surface atoms of the less noble metal, to simulations. However, as the whole dissolution process has been studied by means of the STM experiments, we have access to the intermediate morphologies during the dissolution. This information is invaluable to refine the values of the parameters used in the simulations. Therefore, we will use this information but to some extent only, because a comprehensive study is out of the scope of this work. Moreover, a particular experimental behavior specific to the NiPd alloys, consists in a significant slowing down of the dissolution reaction, taking place at a specific alloy coverage and composition. As we will see in the discussion section, we attribute this to the passivation of all of the alloy step sites by Pd atoms, i.e., no more Ni atoms at the alloy step edge are available for dissolution. This passivation process may be determined experimentally, by detecting the moment where the dissolution becomes much slower and increasing the sample potential is necessary to continue the dissolution process. This specific behavior may be easily determined in the simulations as an abrupt decrease in the dissolution rate. We will also compare the values of the coverage and the A content at passivation obtained experimentally to those from the simulations.

In the following, we will detail the dependence of the calculated morphology on the different parameters in the case of random alloys (solid solution). We will then consider segregated alloys as well as alloys layers with some defects (vacancies) in the initial state.

b) Dependence of the calculated morphology on the simulation parameters

A typical simulation sequence is shown in Fig. 5.19 for $A_{70}B_{30}$. The image size is ~ 25 nm x 25 nm (100 x 100 atoms). Atoms A (less noble metal) are in blue and atoms B in red. In this sequence we considered non selective diffusion ($\beta_{AA} = \beta_{BB} = \beta_{AB} = 1$), and a multiplying factor $\alpha = 3$ in the exponential determining the diffusion probabilities. Starting from a randomly distributed A and B atoms, a small number of dissolution pits are formed in the alloy terrace and grow in size. The pit density is function of the desorption probability of an A atom with 4 neighbors fixed in the preceding section. This pit density is close to the one we typically observe by STM for $Ni_{70}Pd_{30}$, indicating that our choice of the simulation parameters allows one to describe correctly the alloy dissolution process. During the dissolution of A, some B rich islands with rounded shape are formed (see white circle in image i). The final morphology after complete selective dissolution of A is island like with half of them with rounded shape and the other half with an elongated shape (image l). From these images, the total coverage (red curve) and the A proportion (white curve) as a function of time may be plotted (Fig. 5.19m). As explained in the preceding section, the time step is proportional to the inverse of the desorption probability of the actually desorbed atom. Two dissolution regimes are clearly visible: a fast dissolution rate at the beginning down to a coverage of ~ 0.4, followed by a significantly slower one. The first regime corresponds to the dissolution rate when A atoms are still available at the deposit steps. The second one corresponds to the dissolution rate when A step atoms are no longer available, the steps being completely decorated by B atoms ("passivation"). In this case, available A atoms have 4 neighbors and the dissolution rate is therefore smaller. The transition from the first to the second regime takes place, in the present case, at a coverage of ~ 0.4 and A content of ~ 0.2. We carefully checked that these values are reproducible and do not depend significantly on the cell size. However, as we will see below, they depend on the system parameters, in particular the diffusion probabilities.

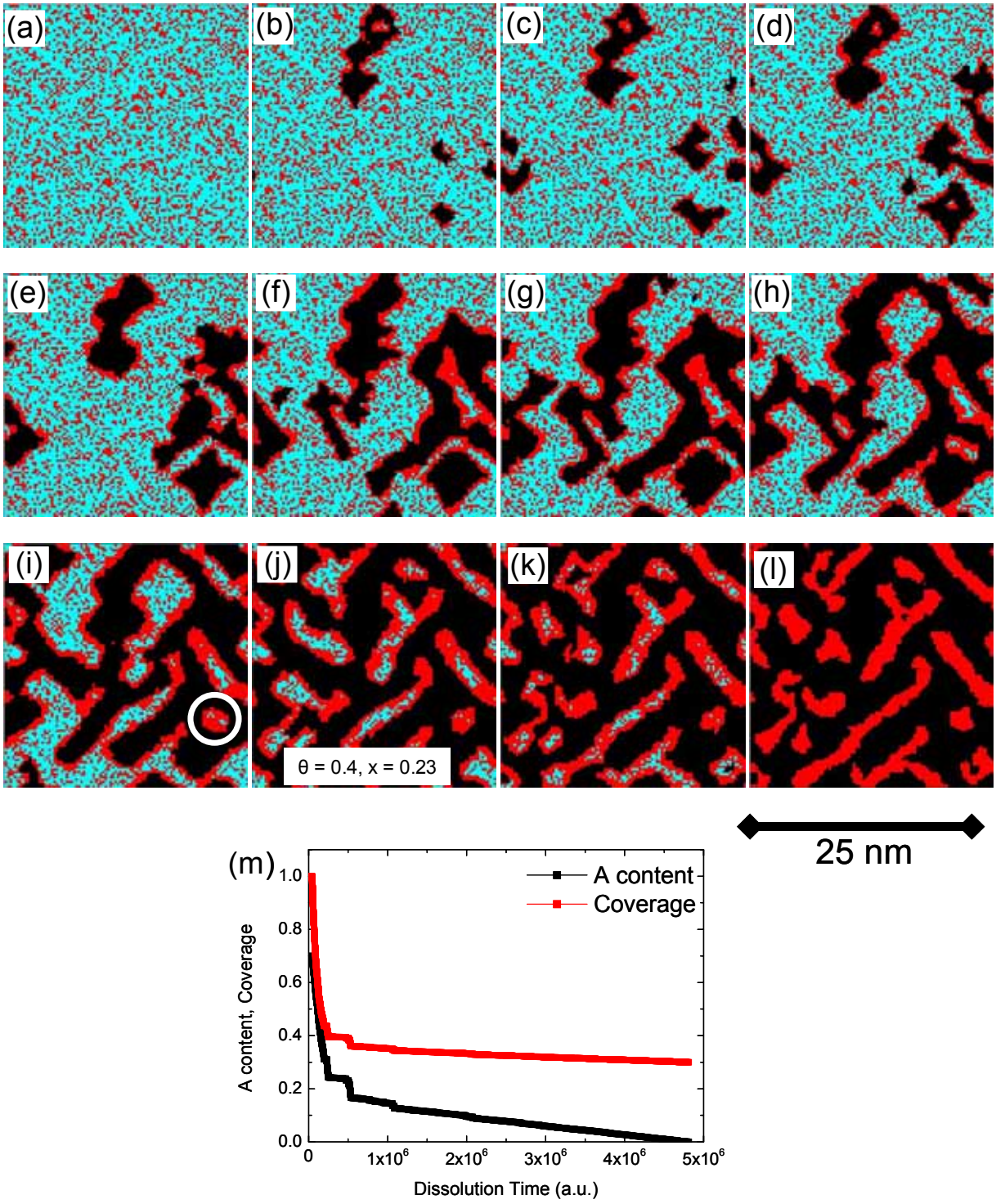

Figure 5.19: (a) to (l) simulation results of the dissolution morphologies of $A_{70}B_{30}$ monolayer alloy film, using A = 3 , $\beta_{AA} = \beta_{BB} = \beta_{AB} = 1$. Blue is A, red is B, and black is void. The simulation cell size is 100 x 100 atoms. Notice the passivation of the alloy islands by B rims in image (j). (m) the evolution of the A content (black curve) and total coverage (red curve) as a function of the dissolution time.

It is interesting to compare the morphology of the final state as a function of the alloy composition (Fig. 5.20). The remaining B atoms form separated islands for A content of 0.9 and 0.7 (Fig. 5.20a−b) whereas, for A content of 0.5 and 0.3, they form a connected network which contains vacancy islands with a homogeneous spatial distribution (Fig. 5.20c−d). This difference is significant and does not depend on the cell size. It is also independent of the diffusion and desorption parameters (see below). The experimentally observed morphologies of NiPd alloys with Ni content larger than 0.5 are similar to those obtained by the simulations. However, the agreement is very poor for Ni content lower than 0.5. The consequences of this disagreement will be analyzed in details in the discussion section.

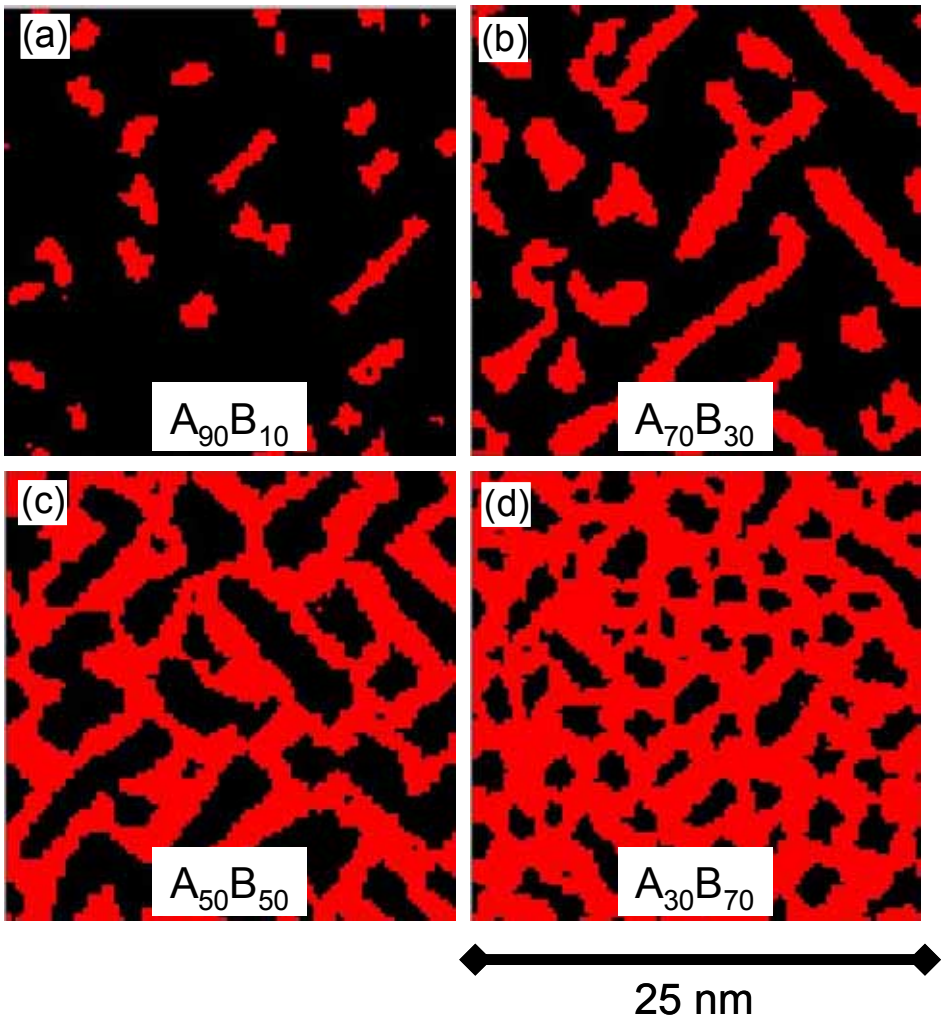

Figure 5.20: simulation results of the dissolution morphologies after complete A removal from (a) $A_{90}B_{10}$ m (b) $A_{70}B_{30}$ (c) $A_{50}B_{50}$ and (d) $A_{30}B_{70}$ monolayer alloy film, using α=3 , $\beta_{AA}=\beta_{BB}=\beta_{AB}$=1. Red is B, and black is void.

In Fig. 5.21, the final state after the complete dissolution of A is presented for three values of the exponential factor α (2, 3 and 4) of the diffusion probabilities and for different alloy compositions. An indirect consequence of changing the α value is an overall change of the diffusion probabilities. To avoid this problem, we normalized the diffusion probabilities by the sum of the diffusion probabilities of changing by 1, 0, and -1 the neighbor number in the final state. Using a smaller α value (i.e., lower influence of the number of neighbors on the diffusion probabilities) the island density is smaller, although their shape remains elongated. The transition from a fast to low dissolution rates takes place at lower coverage and at lower A content. Using a larger α value, the trend is exactly the opposite (smaller islands and transition at larger coverage and at larger A content). The dependence of the coverage and A content at the transition is linear with the exponential factor. The same trends are observed at different alloy compositions: $A_{90}B_{10}$ (Fig. 5.21a−c) and $A_{70}B_{30}$ (Fig. 5.21d−f). For $A_{50}B_{50}$, the deposit morphology resembles that of a network of elongated pores, the pore density increasing with increasing the coefficient α. For α=4, we notice that the pore connectivity increases while their size decreases. This behavior matches well with the smaller diffusion probability.

Similarly, if one increases by a factor of 10 the diffusion coefficient of A and B, or, equivalently, decrease by a factor of 10 the desorption probabilities, an increase of the island size is observed for A content larger than 0.5 (Fig. 5.22a−f). Similar trends are observed regarding the pore size dependence on the diffusion time for A content larger than 0.5 (Fig. 5.22g−l). However, for all alloy compositions, reducing the diffusion time affects much more the final morphology than increasing it. It is particularly visible for A contents larger than 0.5.

Finally, if the diffusion step is made selective, i.e., $\beta_{AA} = \beta_{BB} > 1$ and $\beta_{AB} < 1$ (or the opposite), the resulting morphology of the final state is shown in Fig. 5.23 for different alloy compositions. The clearly visible effect of a change in the diffusion selectivity is a change in the island (respectively pore) density for A content larger (respectively smaller) than 0.5. These changes are very similar to those obtained by varying the diffusion time (Fig. 5.22). This similarity is not surprising because, when the diffusion selectivity increases, the AA and BB bond is artificially weakened or strengthened, which effect is to change the overall diffusion. Therefore, it is delicate to separate the effect of the diffusion selectivity and the diffusion time. Moreover, if the diffusion is selective during the dissolution process, it will be selective also during the alloy growth, which might yield segregated alloy. However, in our experimental conditions of NiPd growth, the alloy deposition is typically ~ 10 times faster than its dissolution, which reduces the effect of selective dissolution on the growth process. Nevertheless, we will discuss the dissolution of segregated alloys in the next sub−section.

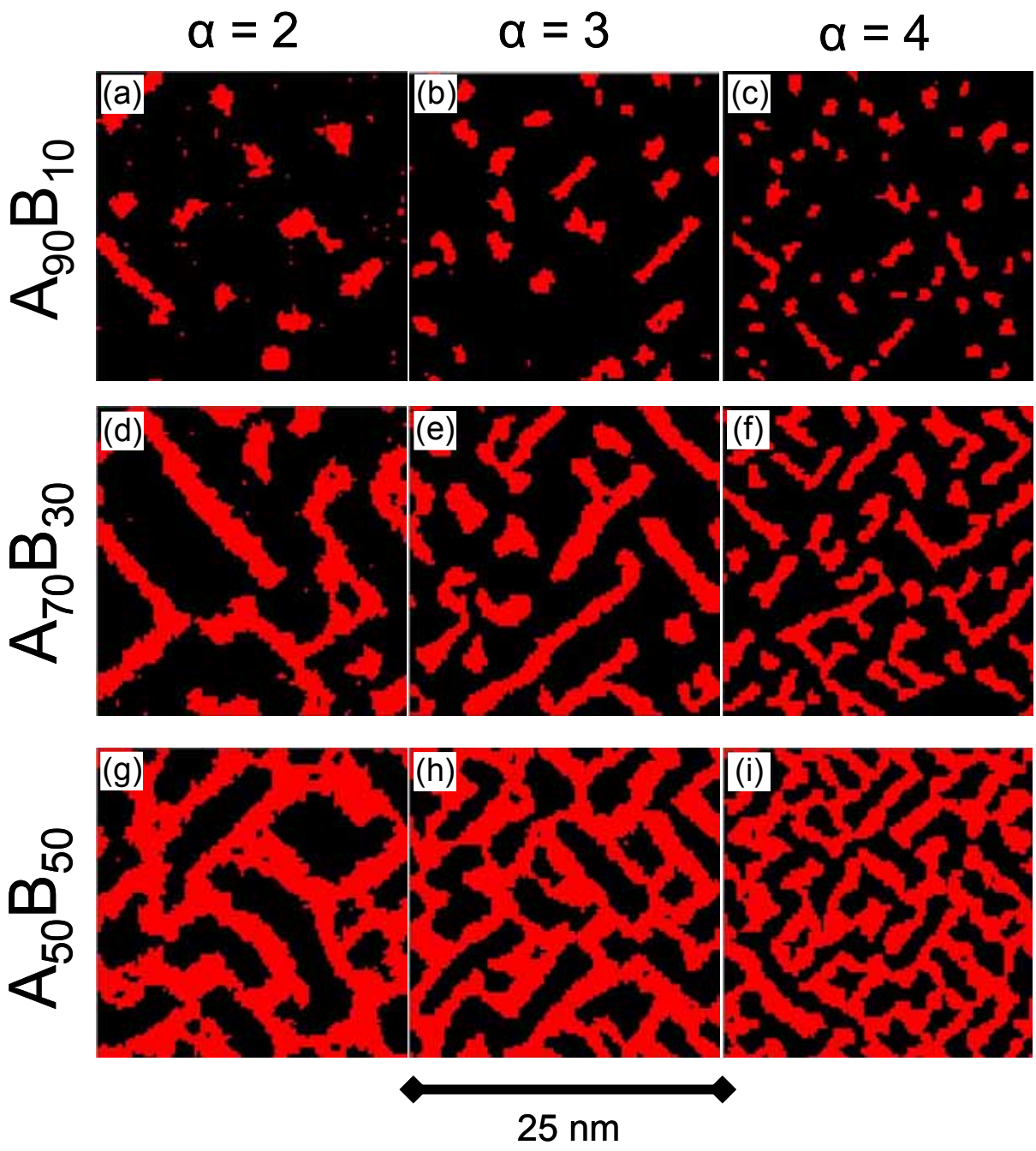

Figure 5.21: Simulation results of the dissolution morphologies after complete A removal from (a-c) $A_{90}B_{10}$ (d-f) $A_{70}B_{30}$ and (g-i) $A_{50}B_{50}$ monolayer alloy film, and for different values of α. Red is B, and black is void.

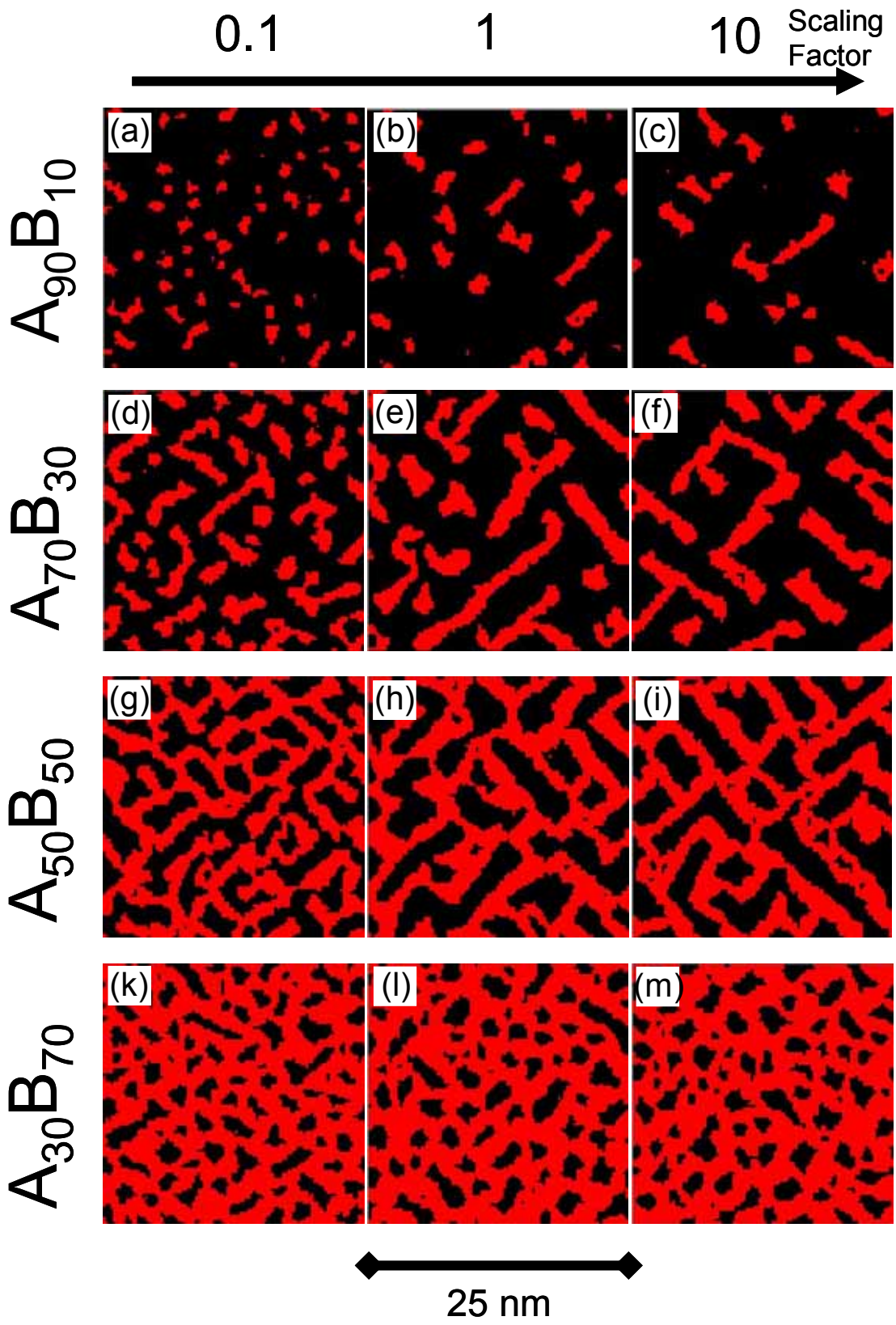

Figure 5.22: Simulation results of the dissolution morphologies after complete A removal from (a-c) $A_{90}B_{10}$ (d-f) $A_{70}B_{30}$, (g-i) $A_{50}B_{50}$ and (j-l) $A_{30}B_{70}$ monolayer alloy films, for different values of the diffusion time. Red is B, and black is void.

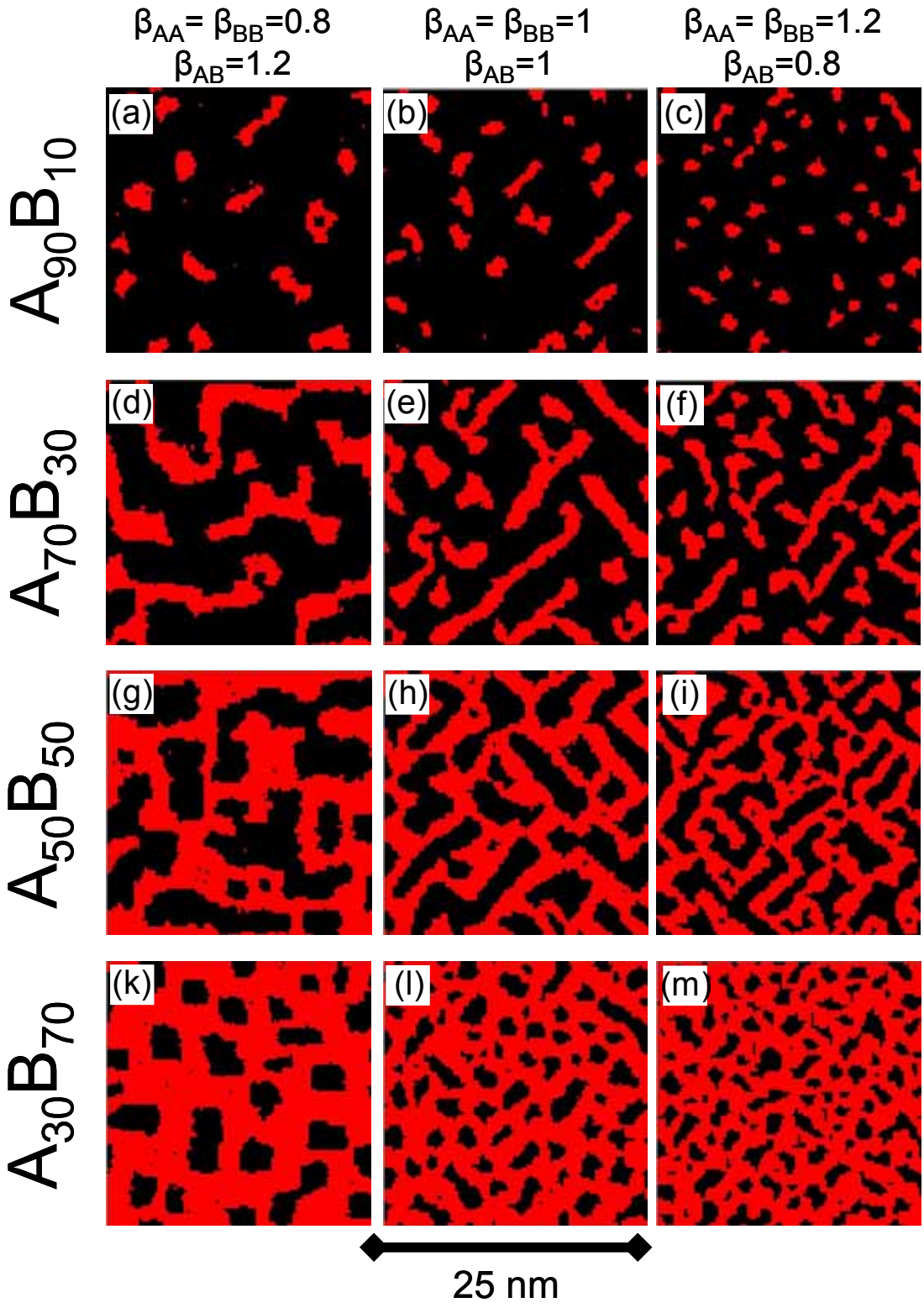

Figure 5.23: Simulation results of the dissolution morphologies after complete A removal from (a-c) $A_{90}B_{10}$ (d-f) $A_{70}B_{30}$, (g-i) $A_{50}B_{50}$ and (j-l) $A_{30}B_{70}$ monolayer alloy films, for different values of the selective diffusion parameter β. Red is B, and black is void.

One mean to have an overall view of the above presented results is to plot the island density of B atoms in the final state, as a function of the different parameters and for different alloy compositions (Fig. 5.24). We also added in these plots the island densities obtained experimentally by STM for NiPd alloys (dashed lines). One may easily notice that the island density varies quasi−linearly with the different parameters. Its values are relatively small (≤ 11 per 625 nm^2) for an A content of 0.5, which is coherent with the porous layer presented above for this alloy composition. These values are overestimated due to the influence of the cell borders in the case of small island density. On the other hand, the island density may be as large 80 per 625 nm^2 for A content larger than 0.5. Finally, for a fixed set of parameters, the island density generally decreases with decreasing A content.

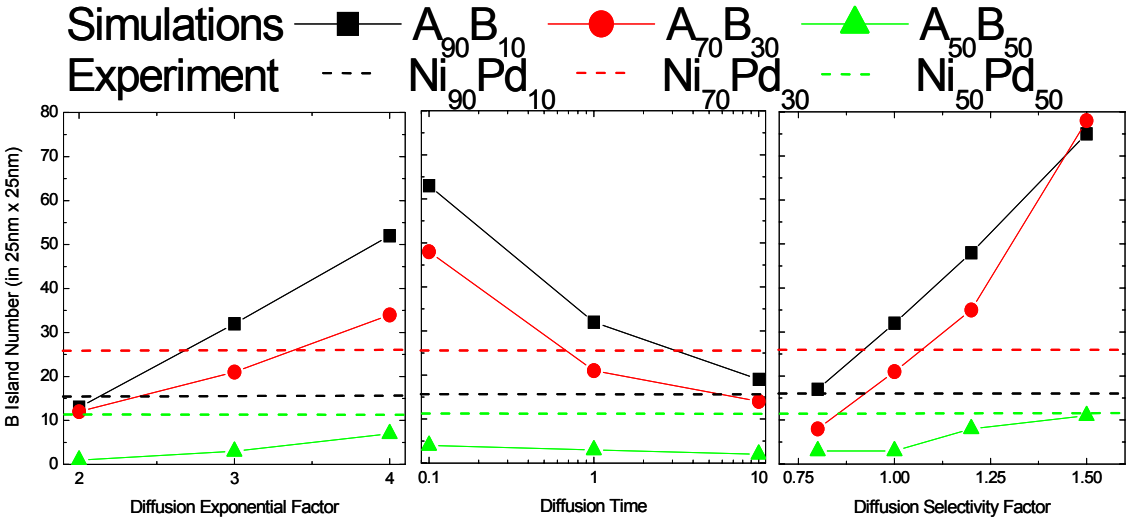

Figure 5.24: Variations of the B island density after complete A removal from $A_{90}B_{10}$ (black curves) $A_{70}B_{30}$, (red curves) and $A_{50}B_{50}$ (green curves) as a function of simulation parameters. Dotted lines correspond to experimental values.

In addition to the morphology of the final state, we may also study the variation of the A content at passivation as a function of the different parameters (Fig. 5.25). Experimental values for NiPd are represented by dashed lines. In the case of $Ni_{90}Pd_{10}$, we couldn't measure this value, because it lies below our measurement uncertainty. Indeed, if A content is below 0.1 in one monolayer thick $Ni_{90}Pd_{10}$, then the difference between the deposit coverage at passivation and the one after complete A dissolution is of the order of ~ 0.01, which is difficult to evaluate from STM images. We find typical trends for different alloy compositions: linear as a function of the diffusion exponential factor and a rough bell shape as a function of the diffusion time and the

diffusion selectivity. These variations might appear peculiar but may be explained simply. For example, the bell shape as a function of the diffusion time may be understood in the following way: at low diffusion time, the B atoms do not have enough time to diffuse and passivate the alloy islands. At large diffusion time, B atoms have enough time to diffuse to a favorable site (maximum number of neighbors), thus leaving A steps undecorated. We are not going to analyze in details the different behaviors, but would like to point out that the parameter values giving significantly different values of A content at passivation for different alloy compositions and fitting reasonably well with experimental values (for alloys with A content larger than 0.5) are: diffusion exponential factor $\alpha = 3$, diffusion time = 1 and diffusion selectivity = 1 (i.e., no diffusion selectivity).

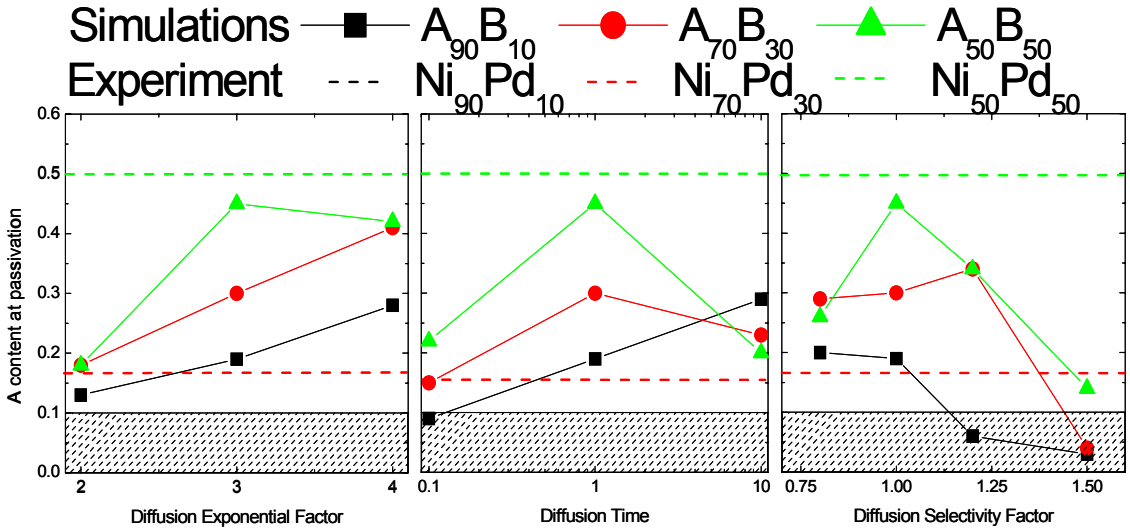

Figure 5.25: Variations of the A content at passivation during the dissolution of $A_{90}B_{10}$ (black curves) $A_{70}B_{30}$, (red curves) and $A_{50}B_{50}$ (green curves) as a function of simulation parameters. Dotted lines correspond to experimental values.

c) Dissolution of segregated alloys

It is worth considering the case of the dissolution of segregated alloys, because, as we will see in the discussion section, different experimental results suggest that NiAu and NiPd alloys have a tendency to phase separation for some alloy compositions. Therefore, calculating the dissolution morphology of a segregated alloy would be useful. Indeed, if the obtained morphology of the final state is closer to the experimental one than the calculated morphology

with a solid solution, the segregation hypothesis would then be more plausible. The difficulty in treating segregated alloys is fixing the segregation scale. In the case of a solid solution, A and B atoms are randomly distributed. In the case of phase segregation, the segregation scale may vary from few atoms to islands as large as the simulation cell. The large segregation scale is relatively obvious, and we are sure that it is not the case of our NiAu and NiPd alloys. Consequently, we will focus on small segregation scale (typically few nanometers). Moreover, the segregation may be *partial* resulting in an inhomogeneous composition distribution instead of separated islands of A and B. We will not consider the case of partial segregation (i.e. spatially inhomogeneously distributed alloy composition) which is more complex and will most probably yield results half way between those with solid solutions and those with *total* segregation.

In order to obtain segregated alloys with different segregation scales, we used a program similar to that used for the dissolution simulation, in which the dissolution step is replaced by a deposition step where A and B atoms are deposited randomly with a relative deposition rate identical to the relative alloy final composition. In order to obtain segregation, the diffusion step is made selective and its duration longer. The diffusion selectivity and duration were increased to obtain larger segregation scales. We varied the average size of B atom pattern between 10 to 100 atoms.

In the case of $A_{70}B_{30}$ with an average B island size of 10 atoms, the effect of the segregation is not significant, except a change in the island density of the final state of the segregated alloy (compare Fig. 5.26 and Fig. 5.20). For $A_{90}B_{10}$ the effect of segregation is invisible (not shown). This behavior is not surprising because for this A content, the A morphology is largely interconnected whatever the segregation scale is. Furthermore, the segregation scale does not seem to affect significantly the final morphology for $A_{70}B_{30}$ and $A_{50}B_{50}$, except for the largest investigated scale where the final morphology resembles the B atom arrangement of the initial alloy. However, it seems to reduce the A content at passivation (by to a factor of two) for the largest scale, which is due to the interconnected network of A atoms at this segregation scale. For the smaller scales, the trends are less clear, and they might be related to the actual morphology of the segregated alloy as a function of the segregation scale. Therefore, they are difficult to interpret.

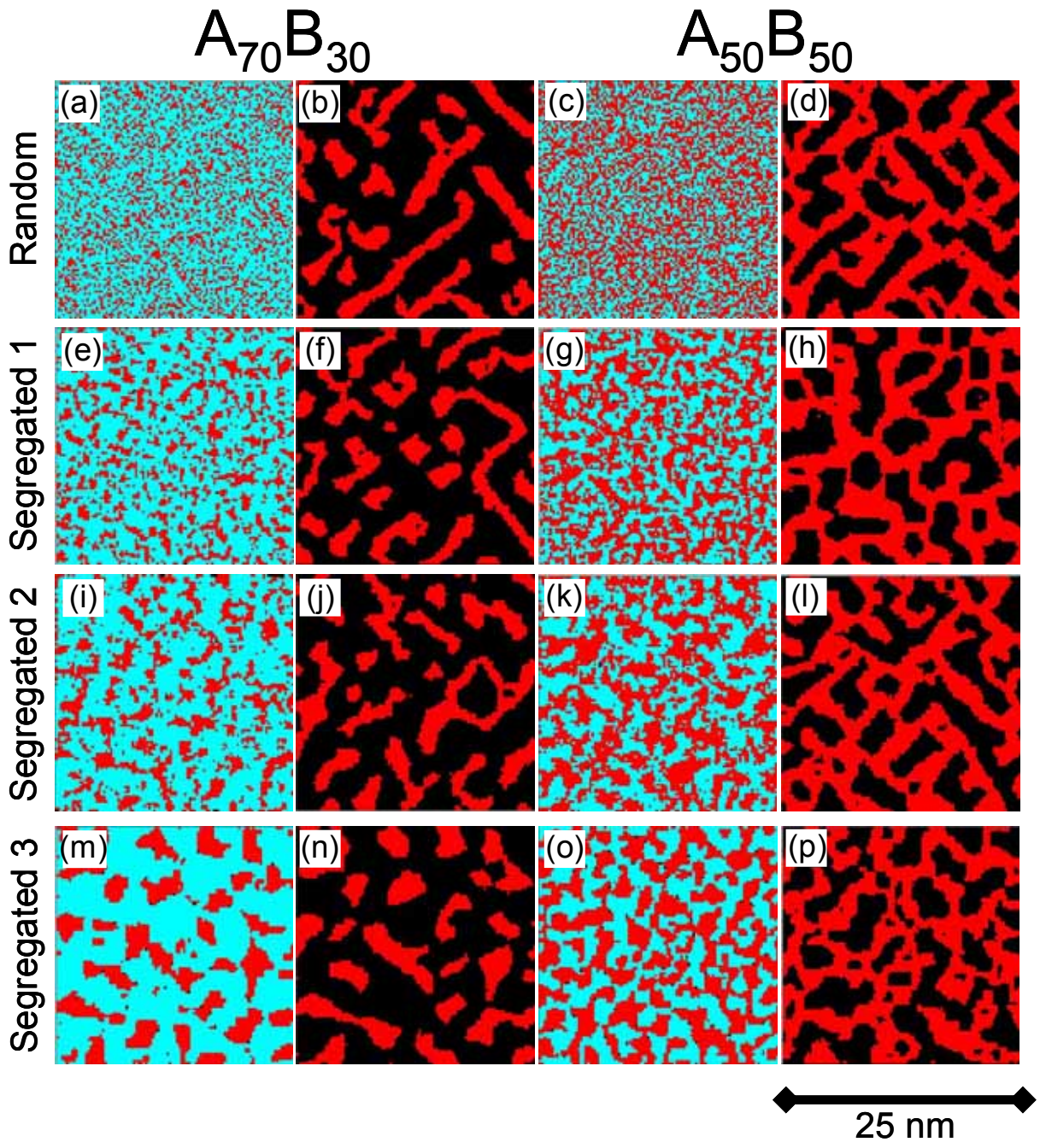

Figure 5.26: Simulation results of the dissolution morphologies after complete A removal from (a, b, e, f, i, j, m, n) $A_{90}B_{10}$ and (c, d, g, h, k, l, o, p) $A_{70}B_{30}$ monolayer alloy films, for different segregation morphologies of the alloys. Blue is A, red is B, and black is void.

d) The influence of defects in the alloy layer

The alloy layers that we showed in the experimental results contained a very small density of vacancy islands. They are thus comparable to the defect free alloy monolayers that we used in the simulations. However, it is difficult to exclude the presence of atomic scale defects. For example, the alloy layer is formed via the nucleation and the growth of existing nuclei. At the intersection of two growing alloy islands, one may expect the presence of defects. They may be very small vacancy islands, which are difficult to observe by STM at this scale, or atoms in a less favorable position, or small alloy areas with locally larger in−plane strain. These different defects are probably the exclusive favorable sites for dissolution because we performed the dissolution experiments at small overpotentials, i.e., at very low dissolution rates.

In order to check whether the presence of defects in the alloy layer influences the dissolution morphology, we performed dissolution simulations with a specific defect density in the alloy layer before dissolving it. The defects in our simulations consist in vacancies which are arranged along a large cross in the middle of the simulation cell. We also considered that the cell is surrounded by vacancies (equivalently, the cell correspond to an alloy island), i.e., the border atoms have 3 neighbors instead of 4. This well defined defect arrangement allows one to check easily whether the final dissolution morphology contains a reminiscence of the defects and their initial position.

In Fig. 5.27, we present the calculated morphology without defects (images a and b) and that with the defects (images c and d). Intriguingly, the final dissolution morphology in the presence of defects (image d) does not present reminiscence of the defect positions, except those at the cell borders, which is not surprising because the vacancy distribution around the cell is equivalent to consider the cell as an alloy island. Moreover, although the final morphologies with and without defects are slightly different, their vacancy islands have similar shape and characteristic size. Thus, the presence of defects does not seem to alter the final dissolution morphology.

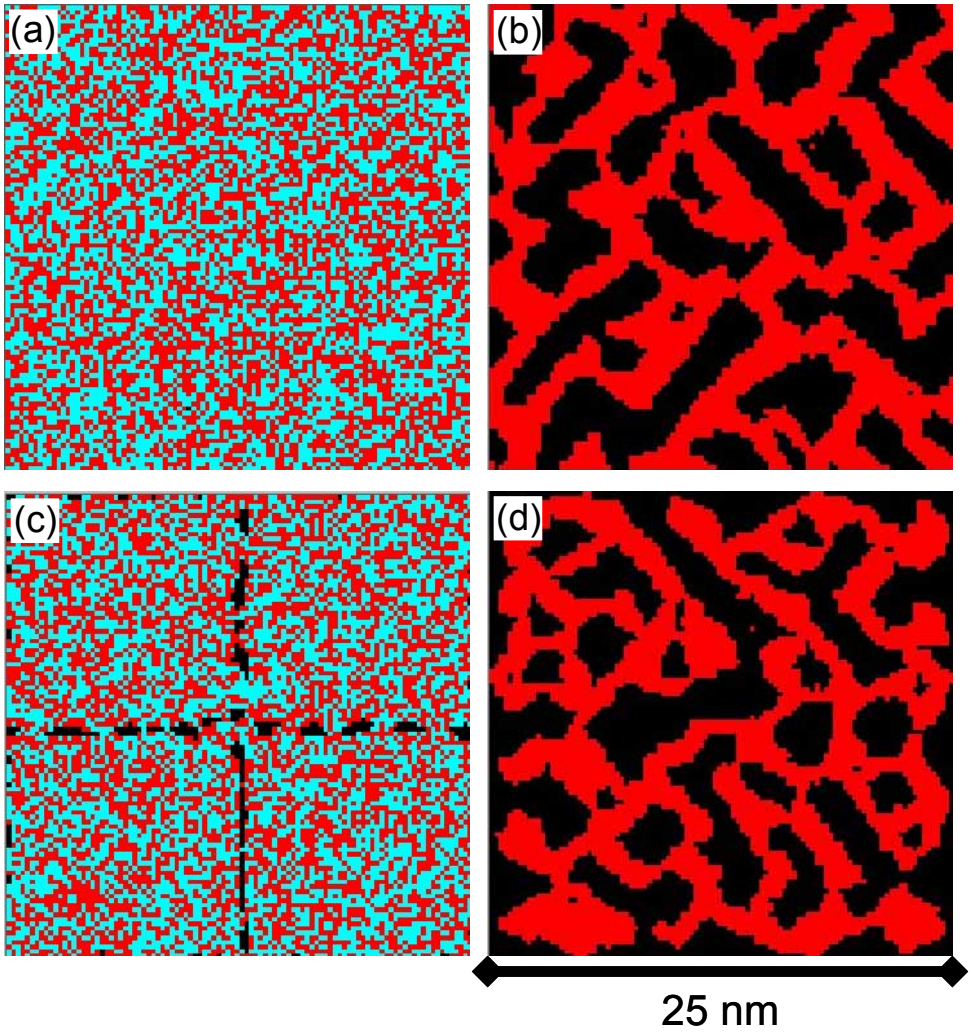

Figure 5.27: Simulation results of the dissolution morphologies after complete A removal from $A_{90}B_{10}$ (a, b) in the absence and (c, d) in the presence of defects (vacancies) in the monolayer alloy films.

5.4.3 Conclusion

The simulations we performed allowed us to determine the typical dissolution morphologies for different alloy compositions, using dissolution probabilities allowing one to reproduce reasonably well the experimental observations. The influence of the different diffusion parameters on the final morphology as well as on the A content at passivation has also been investigated. The comparison with experiment results of NiPd alloys enabled us to determine a set of diffusion parameters allowing a reasonable agreement for alloys with A content larger than 0.5. We also studied the influence of alloy segregation and the presence of defects on the final dissolution morphology. The latter does not seem to be significantly influenced by these changes.

5.5 Discussion

5.5.1 General remarks

The morphology of an alloy layer and its phase (solid solution or segregated) is directly related to the sign of the energy balance $W = E_{interaction}^{AA} + E_{interaction}^{BB} - 2E_{interaction}^{AB}$, where $E_{interaction}^{XY}$ is the interaction energy (or the binding energy) between atom X and atom Y. If $W < 0$, then the alloy will phase segregate at equilibrium (as it is the case for bulk NiAu alloys), whereas if $W > 0$, the equilibrium configuration is a solid solution (as it is the case for bulk NiPd alloys). These considerations are valid if thermodynamic equilibrium is reached, i.e., the system had enough time to reach the equilibrium state. Moreover, if one considers alloy thin film instead of bulk alloys, the interaction energy of the film with the substrate may induce strain in the film plane which energy should be taken into account in the energy balance. These two facts should be considered in our alloy film because (*i*) they are ultrathin (one monolayer thick), (*ii*) they have a lattice parameter different from that of the substrate, which might induce strain, and (*iii*) their growth conditions are most probably not those allowing to reach thermodynamic equilibrium. In the following, we will try to analyze our results concerning NiPd and NiAu ultrathin film alloys taking into account the above mentioned considerations. We will start with the NiAu alloys followed by the NiPd alloys.

5.5.2 NiAu monolayer alloys

The case of NiAu alloys is in principle simpler than that of NiPd alloys, because the system consists in two metals, Ni (in the alloy film) and Au (in the alloy film and the substrate), whereas, in the case of NiPd, three metals are involved Ni and Pd (both in the alloy), and Au (the substrate). Our STM observations of the electrodeposited Ni rich ($Ni_{60}Au_{40}$) layers showed protrusions which have in general irregular spatial distribution and are regularly ordered (moiré like) in some regions of the film. Although the characteristic distance (~ 2.7 nm) of these moiré regions is in agreement with a single phase, i.e., a $Ni_{60}Au_{40}$ solid solution, the possibility of having phase segregation at the same scale could not be ruled out. The Ni selective dissolution experiments of $Ni_{60}Au_{40}$ shed new light on the alloy phase: (*i*) the dissolution potential is identical to that of pure Ni, and (*ii*) STM images clearly showed the formation of relatively large areas which height may be attributed to pure Ni only. These two observations suggest that the $Ni_{60}Au_{40}$ monolayer film is phase segregated. The observed protrusions are thus attributed to pure Au

clusters, and the segregation scale is thus typically ~ 3 nm. Consequently, the ultrathin layer geometry of NiAu alloy does not seem to change the energy balance *W* of bulk NiAu alloy which is in favor of phase segregation.

It is however important to figure out the origin of this particular segregation scale. First, let us examine the film strain. The Au clusters should not induce in plane strain because the underlying substrate is also Au, unless they have different crystallographic orientation, which is highly improbable (pure Ni grows also 111 on Au(111)). The Ni areas do not show any height modulation, as the typical moiré pattern of pure Ni deposits on Au(111), even when these areas are larger than the characteristic length of the moiré. Moreover, the apparent height of these areas is close to that of needlelike Ni islands on Au(111), which are pseudomorph with the Au(111) substrate along the needle and relaxed perpendicularly to the needle. These observations suggest that the Ni contained in the NiAu alloy is most probably expanded and strained. Is there a relationship between this strain and the segregation scale? One way to explain the segregation scale without taking into account the film strain is the interplay between the segregation kinetics and the deposition rate. However, in the case of $Ni_{10}Au_{90}$ monolayer alloy, although the deposition rate is 20 times smaller than for $Ni_{60}Au_{40}$, the Ni inclusions have also a typical width of the order of 1-2 nm. On the other hand, a way to relieve the Ni strain is to add Au clusters in the Ni layer, and the characteristic size of a stable strained Ni islands should be close to the width of the Ni needlelike islands, i.e., n x 1.1 nm [64]. Consequently, positioning a Au cluster every few nanometers appears as a preferred way for Ni to accommodate the strain. One might however argue about the possibility of having large Au domains separated by large Ni domains, in which the strain is completely relieved by the presence of the moiré pattern. Indeed, this configuration should be energetically more favorable in a phase segregated alloy. The absence of such configurations in our case might be due to the interplay between the segregation kinetics and the deposition rate. However, the $Ni_{60}Au_{40}$ dissolution morphology clearly demonstrates that the Au adatoms released upon Ni dissolution remain principally at the step edges of the alloy islands, wetting Au as well as Ni areas. This observation, together with the relatively small segregation scale, indicates that the energy balance *W* is not far from zero, i.e., the tendency of NiAu *monolayer* alloy for phase segregation is relatively weak.

5.5.3 NiPd monolayer alloys

As explained above, the case of NiPd monolayer alloys deposited on Au(111) is in principle more complicated, because of the presence of an additional metal (Pd). The STM observations of Ni-rich electrodeposited NiPd layers clearly showed the presence of a moiré pattern. Its regularity decreases and its characteristic length increases linearly with increasing Pd content. Such observations allowed us to safely conclude that NiPd monolayer films with Ni content larger than 50%, form a single phase, namely a solid solution. For smaller Ni content, it was not possible to conclude on the alloy phase because of the absence of a moiré pattern and any other characteristic features in the film morphology. As it was the case for NiAu alloys, STM experiments of Ni selective dissolution from NiPd monolayer films gave insight into the film structure. The dissolution potential is significantly more positive than that of pure Ni on Au(111), even for Pd content as small as 12%. This behavior clearly contrasts with that of NiAu alloys and represents an additional proof that Ni rich NiPd alloys form a solid solution. Moreover, the dissolution rate at a constant potential decays to zero after the dissolution of a part of the Ni atoms (which depends on the alloy composition) (see Figs. 5.10, 5.12). This behavior is characteristic of a passivation process and resembles the one observed during the dissolution of bulk alloys below the critical potential [50, 53, 56]. In that case, the passivation is three dimensional, i.e., upon the dissolution of the less noble metal in the few topmost layers, the noble metal completely covers the less noble one in the lower layers, yielding an alloy surface mainly constituted of the noble metal atoms. On the other hand, the passivation in our case is strictly bi-dimensional, and the 3D analog of covering the less noble metal with the nobler one is the decoration of all the step sites of the alloy islands by the nobler metal. We may therefore consider that before the passivation of our NiPd alloys, the Ni atoms at step edges of the alloy (or vacancy) islands are available for dissolution, and at passivation no Ni atoms are left at the step edges. Further Ni dissolution takes place at Ni sites belonging to the alloy terraces. We observed experimentally that the latter dissolution step necessitates applying more positive potentials. The cross correlation between these two phenomena is a proof that the more neighbors the Ni atom has, the more stable it is and the more positive its dissolution potential is. Such considerations apply also in the case of the dissolution of a pure Ni monolayer, i.e., a Ni atom in a Ni terrace is in principle more stable against dissolution than a Ni atom at the step edge. However, the difference of the dissolution potential of a Ni atom at the step edge and that of a Ni atom in a terrace site is difficult to measure precisely. Indeed, whenever the potential is made positive to

initiate a pit formation in a terrace, the dissolution rate from the step edges becomes generally very high, making STM observations difficult.

The observed morphology of the Pd layer after complete removal of Ni appears somehow not uniform: (*i*) for $Ni_{70}Pd_{30}$ and $Ni_{51}Pd_{49}$ the Pd layer consists in separated islands having two distinct characteristic sizes and shapes, the larger Pd islands being irregular and surrounded by the much smaller ones with round shape; (*ii*) for $Ni_{24}Pd_{76}$ the Pd layer form an interconnected porous layer, and the vacancy islands have also two characteristic sizes and shapes, the larger having labyrinth shape and the smaller being round. These peculiar shapes may be at first sight the result of the interplay between the Ni dissolution rate and the Pd surface mobility. To support this conclusion, we performed Monte Carlo simulations of the dissolution of a monolayer bimetallic alloy. We could correctly reproduce the presence of a passivation process in which the more noble metal atoms completely decorate the rims of the alloy islands (Fig. 5.19j, in the case of $Ni_{70}Pd_{30}$). We also found similar dependence of the dissolution rate on time, i.e., it decays to zero whenever Ni atoms at the step edges are no more available (see Fig. 5.19m). We studied the dissolution morphology as a function of the different simulation parameters for Ni desorption and for Ni and Pd diffusions. We could find a set of parameters for the desorption probabilities (see table in Sec. 5.4.1) and for the diffusion probabilities (α=3, identical diffusion coefficients for both metals, and no diffusion selectivity) yielding morphologies close to the experimental ones for Ni rich alloys in the case of a solid solution. A reasonable agreement may be observed in Figs. 5.24-25, where the island density of the noble metal (after complete dissolution of the less noble metal), and the content of the less noble metal at passivation are plotted as a function of the simulation parameters. It should be noted that the Ni content at passivation in the case of $Ni_{88}Pd_{12}$ could not be measured experimentally because it is lower than our coverage estimation precision (~ 1%). For this reason, the experimental value for this alloy composition in Fig. 5.25 is represented by a filled rectangle instead of a dashed line.

Surprisingly, with this set of parameters, we could not reproduce the Pd morphology after complete Ni removal for $Ni_{51}Pd_{49}$ and for $Ni_{24}Pd_{76}$. Furthermore, we varied the simulation parameters in a wide range but we could not find Pd morphologies close to those obtained experimentally. In all cases, we found for the $A_{50}B_{50}$, after complete removal of A, a continuous B layer with a number of separated vacancy islands (Figs. 5.21-23). We also performed similar simulations in the case of a segregated alloy with different segregation scales and still, we could not obtain the experimental morphologies (Fig. 5.26). Finally, we suspected that the presence of defects in the experimental alloy layers to be the origin of these peculiar morphologies. For this purpose, we did the same simulations with an initial alloy layer containing a significant number of

vacancy islands (Fig. 5.27). Nevertheless, we could not obtain the experimental morphologies. This discrepancy between the simulations and the experimental observations calls for reconsidering the alloy structure obtained by electrodeposition. Let us analyze once more the dissolution morphology of $Ni_{51}Pd_{49}$, in particular the area marked by a white rectangle in Fig. 5.11, which is represented in Fig. 5.28. Obviously, Ni dissolution takes place preferentially close to the image borders as evidenced in Fig. 5.28b-c, although most of the dissolved areas were free of apparent vacancy islands in Fig. 5.28a. Meanwhile, only few small vacancy islands are visible in the middle of the image in Fig. 5.28c. The difference in the dissolution rate between the image borders and its centre is surprising. Furthermore, a careful analysis of the Pd local coverage after the complete removal of Ni (Fig. 5.28f) clearly evidences larger coverage in the image centre as compared to the image borders. These two observations suggest that local Pd content in the alloy monolayer is not homogeneous on the 10 nm scale, or, equivalently, Ni content is larger on the image borders and smaller in the middle. This implies that the alloy composition is inhomogeneous, and that the alloy structure consists in Pd rich areas surrounded by Ni rich ones. With such an alloy composition, one expects that Pd islands in the Ni rich areas after Ni removal to resemble those of a NiPd alloy with lower Pd content, for example $Ni_{70}Pd_{30}$. Indeed, their shape and size are similar to those in Fig. 5.9f. In the same way, the dissolution potential of Ni rich areas in $Ni_{51}Pd_{49}$ should be close to that of $Ni_{70}Pd_{30}$, whereas the dissolution potential of Pd rich areas should be more positive. Indeed, the Ni is dissolved at -0.9V in the Ni rich areas, i.e., at the same potential as for $Ni_{70}Pd_{30}$, whereas more positive potentials are necessary to dissolve Ni in the Pd rich areas. These observations lead us to an interesting conclusion: the larger the Pd content in the NiPd alloy, the more positive the Ni dissolution potential is. In other words, the dissolution potential and the stability of a Ni atom is not only dependent on its number of neighbors, but also, and to a large extent on whether they are Ni or Pd atoms.

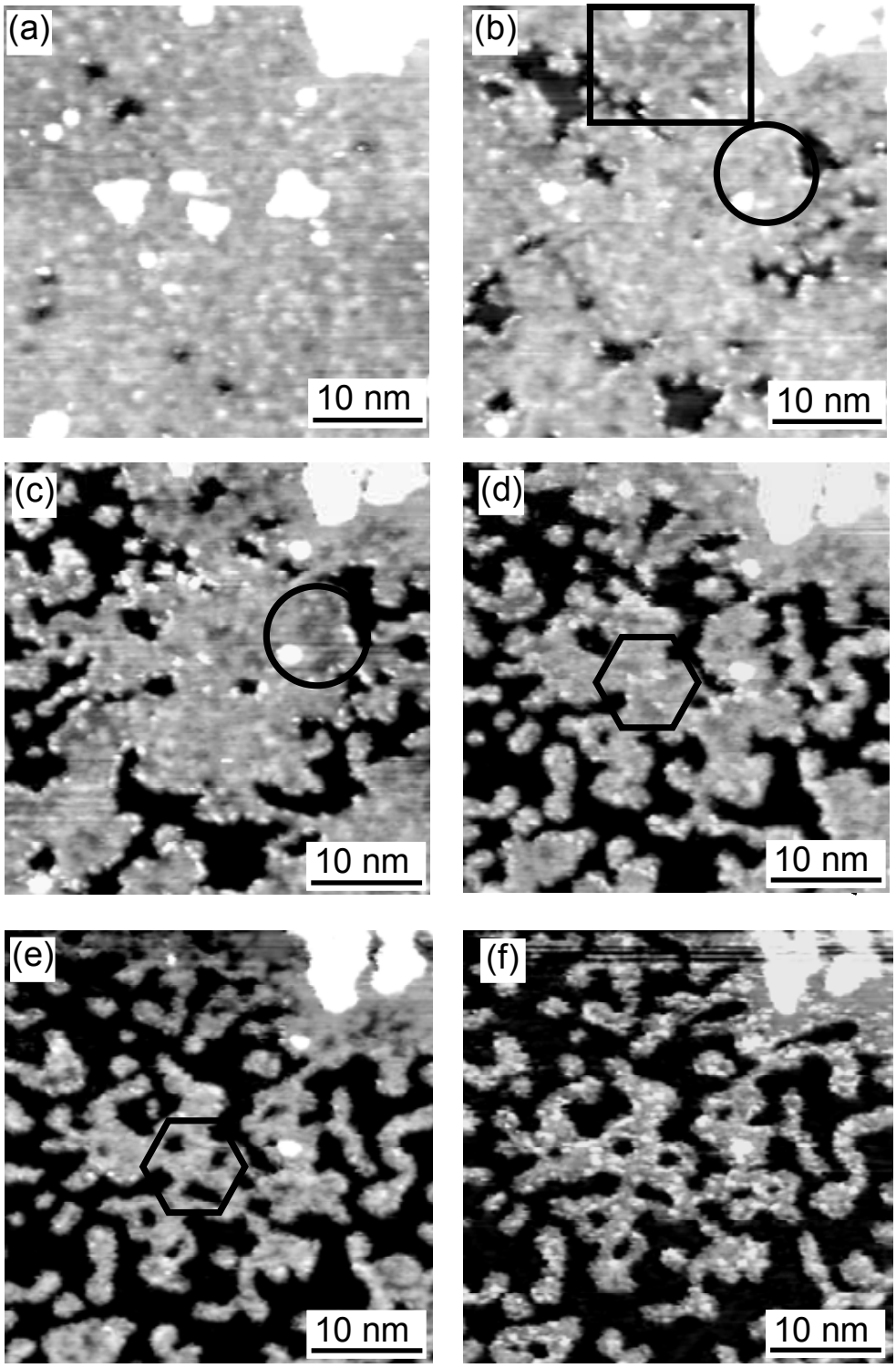

Figure 5.28: Series of STM images (45 x 45 nm²) showing the selective dissolution of Ni from $Ni_{51}Pd_{49}$ monolayer alloy deposited on Au(111) at -1.24 V during 90 s in 0.1 M K_2SO_4 + 1 mM H_2SO_4 + 1 mM KCl + 0.125 mM $NiSO_4$ + 0.035 mM K_2PdCl_4. Images were recorded at (a) U = -1.00 V, (b) U = -0.90 V after 20 min, (c) U = -0.88 V after 31 min, (d) U = -0.84 V after 43 min, (e) U = -0.78 V after 51 min, and (f) U = -0.72 V after 69 min from the beginning of the dissolution process. The area represented in these images is that inside the white rectangle in Fig.5.11.

Such variation in the alloy composition may be due to the presence of a driving force for phase separation associated with a relatively large Ni and Pd adatom mobility. The driving force may be the decrease of the layer in-plane strain, although it is not straightforward that phase separation would reduce the strain. Moreover, Ni and Pd surface mobilities are not expected to be particularly large: for instance, the shape of Pd islands after complete Ni removal from $Ni_{70}Pd_{30}$ and $Ni_{51}Pd_{49}$ alloys (Fig. 5.9f and Fig. 5.11f) is much more irregular than that of Au islands after Ni removal from a $Ni_{60}Au_{40}$ alloy (Fig. 5.14d). In the case of Ni, the pits formed during the dissolution of a pure Ni monolayer deposited on Au(111) or on Pd/Au(111) have also an irregular shape (Chapter 4). Therefore, if a driving force for phase separation is present, it is highly improbable that the Ni and Pd surface mobilities are large enough to yield the observed alloy composition variations. Another possible explanation of the variable alloy composition would be the alloy growth mechanism. The NiPd alloy were grown using the 2nd deposition procedure, i.e., Ni is grown at a small overpotential (kinetically limited) whereas Pd is grown in a diffusion limited regime. Consequently, although the Pd deposition rate is expected to be constant as a function of time, the Ni growth rate may be sensitive to the surface structure, for example the presence of many step sites and defects. Then, a possible growth mechanism would be as follows: Pd is deposited at a constant rate forming islands increasing the surface step site density, while the Ni growth rate increases gradually with increasing step site density. If this explanation is correct, such reduced Ni growth during the first growth stage should not take place at the step edges of pure Pd islands formed during the first deposition step (three of these Pd islands are indicated by dashed lines in Fig. 5.11e). In other words, the Ni content of the alloy in the vicinity of these pure Pd islands should be larger than in the middle of the white rectangle. Indeed, in Fig. 5.11e, the local coverage of the vacancy islands is larger close to these Pd islands than that in the centre of the white rectangle. In conclusion, the variation of the alloy composition seems to be the result of step dependent Ni growth rate when the 2nd deposition procedure is used. It would have been interesting to undergo similar studies on NiPd monolayer films deposited using the 1st procedure (Ni and Pd deposited in a diffusion limited regime). Unfortunately, all the experiments done in these conditions resulted in a peculiar adsorption layer, which probably consists in a Ni hydroxide. Such Ni hydroxide species is indeed favored in the 1st procedure because of the large hydrogen evolution current taking place in parallel with the alloy deposition, resulting in a local pH increase.

Following the above mentioned considerations, it appears that the NiPd monolayer alloys form a solid solution for all alloy composition, similarly to bulk NiPd alloys. The inhomogeneous local variation of the alloy composition seems to be due to the deposition conditions and not to a

change in the energy balance (W) sign. Moreover, although the NiPd layers seem to be strained in-plane (the average NiPd distance is larger than expected, Fig. 5.4), strain does not seem to play a significant role in determining the alloy phase. Furthermore, the interaction of the alloy with the Au(111) substrate (especially that of Pd with Au) does not seem to influence to a large extent the energy balance in favor of phase segregation.

Finally, it is interesting to find out the origin of the dark areas that appear on the alloy surface during the Ni dissolution, one of these being indicated by a black rectangle in Fig. 5.28b. These areas are usually absent before the Ni dissolution onset (see Fig. 5.28a), although some dark features located in the same region are present. They form at different potentials (compare the areas marked by black circles in Fig. 5.28b and Fig. 5.28c), and Ni dissolution takes place preferentially within these areas. They seem to be mainly formed of Ni, because the resulting vacancy island surface is close to that of the corresponding initial dark area (compare the areas within the black hexagons in Fig. 5.28d and Fig. 5.28e). The question is when and how these pure Ni areas form? These areas appear shortly before the Ni dissolution within their perimeter, and they mainly consist in Ni atoms, whereas, before they become visible, the same areas consist in Ni and Pd atoms. Therefore, it seems that there exists mass transfer within the alloy layer and a driving force for phase segregation slightly before Ni dissolution. Surprisingly, we observed protrusion displacement within NiPd islands during the Ni dissolution. In Fig. 5.29, we present two series (Fig. 5.29a-b, and Fig. 5.29c-d) of two successive STM images where local changes of the terrace corrugation are observed. We marked identical areas in successive images by circles and squares to ease the comparison. We don't have an explanation about the mechanism of this mass transfer, but it seems to take place. Consequently, local phase segregation of the NiPd alloy film is somehow possible. We have also no explanation about the driving force for such phase transition. Such phase transition, from a solid solution to a segregated phase has not been reported on previously and seems very interesting and promising for future studies.

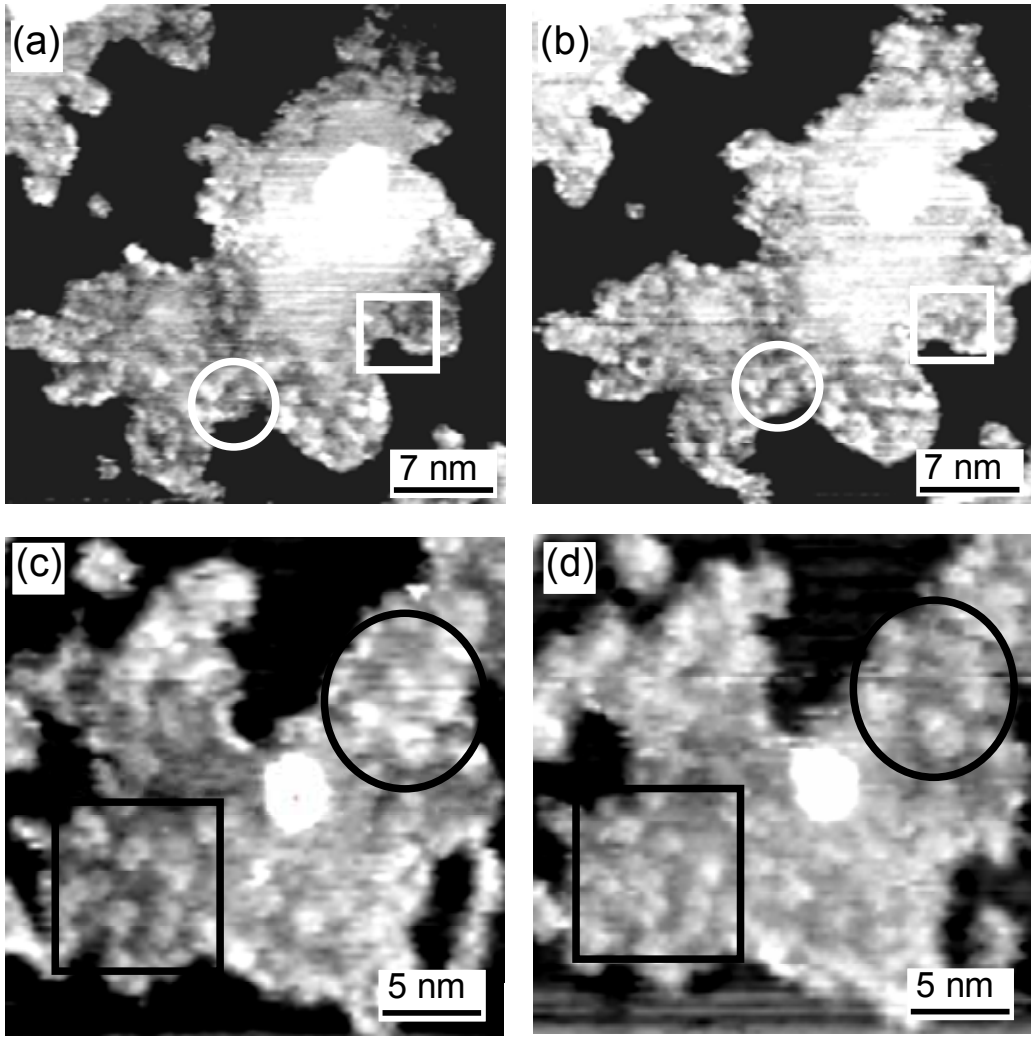

Figure 5.29: Two series of successive STM images ((a-b) 35 x 35 nm^2) ((c-d) 25 x 25 nm^2) showing the movement of features within the $Ni_{60}Pd_{40}$ island deposited on Au(111) at -1.24 V during 80 s in 0.1 M K_2SO_4 + 1 mM H_2SO_4 + 1 mM KCl + 0.125 mM $NiSO_4$ + 0.035 mM K_2PdCl_4. White (black) rectangles and circles mark areas with apparent changes.

5.6 Conclusion

The detailed STM study of the morphology of electrodeposited NiPd and NiAu monolayer alloys and that of the dynamics of their dissolution allowed us to gain invaluable information about the alloy phase and the alloy stability as a function of the alloy composition. In the case of NiAu, phase segregation is expected from thermodynamics of bulk alloys, and we also found that $Ni_{60}Au_{40}$ and $Ni_{10}Au_{90}$ monolayer alloys deposited on Au(111) are both phase segregated. However, we found a very small segregation characteristic scale (~ 1-3 nm), which seems to be driven by partial strain relaxation in the Ni phase and by a slight tendency of the monolayer alloy to form a solid solution. The combination of these two effects yielded interesting

alloy morphology, for example ordered Au clusters in a Ni layer. In the case of NiPd, a solid solution is expected for bulk alloys, and we found that NiPd monolayer alloys deposited on Au(111) form also solid solutions for all alloy compositions. We were able to determine the average inter-atomic distance of the alloy and to correlate it with the alloy Ni content. The detailed analysis of the dissolution morphologies and their comparison with Monte Carlo simulations allowed us to evidence the presence of a composition variation on the 10 nm scale, which seems not to originate from energy minimization of the alloy but from the deposition conditions. We also found evidence for a passivation process taking place every time Ni atoms in a step edge site are no longer available, i.e., when all step edges are decorated by Pd atoms. This phenomenon is similar to the passivation below the critical potential of 3D alloys, except that in our case it is bi-dimensional. We also succeeded in establishing a close correlation between the dissolution potential of a Ni atom and the number of its Pd neighbors. Finally, we also observed the formation of dark areas preceding Ni dissolution, which we attribute to Ni areas resulting from a local phase segregation of the NiPd alloy. Indeed, we found evidence for mass transfer within the alloy layer taking place in the Ni dissolution potential range.

References

1. Besenbacher, F., Pleth Nielsen, L., and Sprunger, P.T., *Surface alloying in heteroepitaxial metal-on-metal growth*, in *The Chemical Physics of Solid Surfaces and Heterogeneous Catalysis*, D.A.K.a.D.P. Woodruff, Editor. 1997, Elsevier Science Publishers: Amsterdam.
2. Woodruff, D.P., *Surface Alloys and Alloy Surfaces*. The chemical Physics of Solid Surfaces. Vol. 10. 2002, Amsterdam: Elsevier Science Publishers
3. Ruban, A.V., Skriver, H.L., and Norskov, J.K., *Surface segregation energies in transition-metal alloys*. Physical Review B, 1999. **59**(24): p. 15 990-16 000.
4. Mavrikakis, M., Hammer, B., and Norskov, J.K., *Effect of strain on the reactivity of metal surfaces*. Physical Review Letters, 1998. **81**(13): p. 2819-2822.
5. Murayama, A., Hyomi, K., Eickmann, J., and Falco, C.M., *Strain dependence of the interface perpendicular magnetic anisotropy in epitaxial Co/Au/Cu(111) films*. Physical Review B, 1999. **60**(22): p. 15245.
6. Bardi, U., *The atomic structure of alloy surfaces and surface alloys*. Rep.Prog.Phys., 1994. **57**: p. 939-987.
7. Hwang, R.Q. and Bartelt, M.C., *Scanning tunneling microscopy studies of metal on metal epitaxy*. Chemical Reviews, 1997. **97**: p. 1063-1082.
8. Lu, S.H., Wang, Z.Q., Wu, S.C., Lok, C.K.C., Quinn, J., Li, Y.S., Tian, D., Jona, F., and Marcus, P.M., *Structural and electronic properties of a surface alloy of Pd and Cu on Cu(001)*. Physical Review B, 1988. **37**: p. 4296-4298.
9. Wu, S.C., Lu, S.H., Wang, Z.Q., Lok, C.K.C., Quinn, J., Li, Y.S., Tian, D., Jona, F., and Marcus, P.M., *Cu(001)c(2x2)-Pd: an ordered surface alloy*. Physical Review B, 1988. **38**: p. 5363-5370.
10. Rousset, S., Chiang, S., Fowler, D.E., and Chambliss, D.D., *Intermixing and three-dimensional islands in the epitaxial growth of Au on Ag(110)*. Physical Review Letters, 1992. **69**: p. 3200-3203.
11. Murray, P.W., Stensgaard, I., Laegsgaard, E., and Besenbacher, F., *Mechanisms of initial alloy formation for Pd on Cu(100) studied by STM*. Physical Review B, 1995. **52**: p. R14404-R14407.
12. Murray, P.W., Stensgaard, I., Laegsgaard, E., and Besenbacher, F., *Growth and structure of Pd alloys on Cu(100)*. Surface Science, 1996. **365**: p. 591-601.
13. Röder, H., Schuster, R., Brune, H., and Kern, K., *Monolayer-confined mixing at the Ag-Pt(111) interface*. Physical Review Letters, 1993. **71**: p. 2986-2989.

14. Schuster, R., Röder, H., Bromann, K., Brune, H., and Kern, K., *Stress relief via island formation of an isotropically strained bimetallic surface layer: The mesoscopic morphology of the Ag/Pt (111) surface alloy.* Physical Review B, 1996. **54**(19): p. 13476.
15. Pleth Nielsen, L., Besenbacher, F., Stensgaard, I., Laegsgaard, E., Engdahl, C., Stoltze, P., Jacobsen, K.W., and Norskov, J.K., *Initial growth of Au on Ni(110): surface alloying of non miscible metals.* Physical Review Letters, 1993. **71**: p. 754-757.
16. Pleth Nielsen, L., Besenbacher, F., Stensgaard, I., Laegsgaard, E., Engdahl, C., Stoltze, P., and Norskov, J.K., *"Dealloying" phase separation during growth of Au on Ni(110).* Physical Review Letters, 1995. **74**(7): p. 1159-1162.
17. Nagl, C., Haller, O., Platzgummer, E., Schmid, M., and Varga, P., *Submonolayer growth of Pb on Cu(111): surface alloying and de-alloying.* Surface Science, 1994. **321**: p. 237-248.
18. Baddeley, C.J., Barnes, C.J., Wander, A., Ormerod, R.M., King, D.A., and Lambert, R.M., *Surface cristallography of three catalytically important structures in the Au(111)-Pd system.* Surface Science, 1994. **314**: p. 1-12.
19. Hoster, H.E., Filonenko, E., Richter, B., and Behm, R.J., *Formation and short-range order of two-dimensional Cu_xPd_{1-x} monolayer surface alloys on Ru(0001).* Physical Review B, 2006. **73**(16): p. 165413-11.
20. Stevens, J.L. and Hwang, R.Q., *Strain stabilized alloying of immiscible metal in thin films.* Physical Review Letters, 1995. **74**(11): p. 2078-281.
21. Thayer, G.E., Ozolins, V., Schmid, A.K., Bartelt, N.C., Asta, M., Hoyt, J.J., Chiang, S., and Hwang, R.Q., *Role of Stress in Thin Film Alloy Thermodynamics: Competition between Alloying and Dislocation Formation.* Physical Review Letters, 2001. **86**(4): p. 660.
22. Thayer, G.E., Bartelt, N.C., Ozolins, V., Schmid, A.K., Chiang, S., and Hwang, R.Q., *Linking Surface Stress to Surface Structure: Measurement of Atomic Strain in a Surface Alloy using Scanning Tunneling Microscopy.* Physical Review Letters, 2002. **89**(3): p. 036101.
23. Ling, W.L., Hamilton, J.C., Thürmer, K., Thayer, G.E., de la Figuera, J., Hwang, R.Q., Carter, C.B., Bartelt, N.C., and McCarty, K.F., *Herringbone and triangular patterns of dislocations in Ag, Au, and AgAu alloy films on Ru(0 0 0 1).* Surface Science, 2006. **600**(9): p. 1735-1757.
24. Schmid, A.K., Hamilton, J.C., Bartelt, M.C., and Hwang, R.Q., *Surface alloy formation by interdiffusion across a linear interface.* Physical Review Letters, 1996. **77**(14): p. 2977-2980.
25. Pratzer, M. and Elmers, H.J., *Structural and Magnetic Properties of Co-Fe Binary Alloy Monolayers on W(110).* Physical Review Letters, 2003. **90**: p. 077201.

26. Pratzer, M. and Elmers, H.J., *Heteroeptiaxial growth of $Co_{1-x}Fe_x$ alloy monolayers on W(110).* Journal of Crystal Growth 2005. **275** p. 150-156.
27. Hebenstreit, E.L.D., Hebenstreit, W., Schmid, M., and Varga, P., *$Pt_{25}Rh_{75}$(111), (110), and (100) studied by scanning tunnelling microscopy with chemical contrast.* Surface Science, 1999. **441**: p. 441-453.
28. Orinakova, R., Turonova, A., Kladekova, D., Galova, M., and Smith, R.M., *Recent developments in the electrodeposition of nickel and some nickel-based alloys.* Journal of Applied Electrochemistry, 2006. **36**: p. 957-972.
29. Chang, J.-K., Hsu, S.-H., Sun, I.-W., and Tsai, W.-T., *Fomation of nanoporous nickel by selective anodic etching of the nobler copper component from electrodeposited nickel-copper alloys.* Journal of Physical Chemistry C, 2008. **112**: p. 1371-1376.
30. Kazeminezhad, I., Blythe, H.J., and Schwarzacher, W., *Alloys by precision electrodeposition.* Applied Physics Letters, 2001. **78**: p. 1014.
31. Correia, A.N. and Machado, S.A.S., *Anodic linear sweep voltammetric analysis of Ni-Co alloys electrodeposited from dilute sulfate baths.* Journal of Appled Electrochemistry, 2003. **33**: p. 367-372.
32. Grden, M. and Czerwinski, A., *EQCM studies on Pd-Ni alloy oxidation in basic solution.* Journal of Solid State Electrochemistry, 2008. **12**: p. 375-385.
33. Mallett, J.J., Svedberg, E.B., Bonevich, J.E., Shapiro, A.J., Egelhoff, W.F., and Moffat, T.P., *Compositional control in electrodeposited Ni_xPt_{1-x} films.* Journal of the Electrochemical Society, 2008. **155**: p. D1-D9.
34. Maroun, F., Ozanam, F., Magnussen, O.M., and Behm, R.J., *The role of atomic ensembles in the reactivity of bimetallic electrocatalysts.* Science, 2001. **293**(5536): p. 1811-1814.
35. Allongue, P., Maroun, F., Jurca, H.F., Tournerie, N., Savidand, G., and Cortes, R., *Magnetism of electrodeposited ultrathin layers: Challenges and opportunities.* Surface Science, 2009. **603**: p. 1831-1840.
36. Hayden, B.E., Rendall, M.E., and South, O., *Electro-oxidation of Carbon Monoxide on Well-Ordered Pt(111)/Sn Surface Alloys.* Journal of the American Chemical Society, 2003. **125**: p. 7738-7742.
37. Porter, D.A. and Easterling, K.E., *Phase Transformations in Metals and Alloys, 2nd Edition.* 1992, London: Chapman & Hall.
38. Hansen, M., *Constitution of binary alloys*. Metallurgy and metallurgical engineering series. 1958, New York: McGraw-Hill.

39. Denton, A.R. and Ashcroft, N.W., *Vegard's law.* Physical Review A, 1991. **43**: p. 3161-3164.
40. Tersoff, J., *Surface-confined alloy formation in immiscible systems.* Physical Review Letters, 1995. **74**: p. 434-437.
41. Christensen, A., Ruban, A.V., Stoltze, P., Jacobsen, K.W., Skriver, H.L., Nørskov, J.K., and Besenbacher, F., *Phase diagrams for surface alloys.* Physical Review B, 1997. **56**(10): p. 5822.
42. Ozolins, V., Asta, M., and Hoyt, J.J., *Elastic relaxations in ultrathin epitaxial alloy films.* Physical Review Letters, 2002. **88**: p. 096101.
43. Pickering, H.W. and Wagner, C., *Electrolytic dissolution of binary alloys containing a noble metal.* Journal of the Electrochemical Society, 1967. **114**: p. 698-706.
44. Pickering, H.W., *Characteristic features of alloy polarization curves.* Corrosion Science, 1983. **23**: p. 1107-1120.
45. Moffat, T.P., Fan, F.R.F., and Bard, A.J., *Electrochemical and scanning tunneling microscopic study of dealloying of Cu3Au.* Journal of the Electrochemical Society, 1991. **138**: p. 32243235.
46. Fritz, J.D. and Pickering, H.W., *Selective anodic dissolution of Cu-Au alloys: TEM and current transient study.* Journal of the Electrochemical Society, 1991. **138**: p. 3209-3218.
47. Li, R. and Sieradzki, K., *Ductile-brittle transition in random porous Au.* Physical Review Letters, 1992. **68**: p. 1168-1171.
48. Liu, H., He, P., Li, Z., and Li, J., *High surface area nanoporous platinum: facile fabrication and electrocatalytic activity* Nanotechnology, 2006. **17**: p. 2167-2173.
49. Jia, F., Yu, C., Ai, Z., and Zhang, L., *Fabrication of nanoporous gold film electrodes with ultrahigh surface area and electrochemical activity.* Chemistry of Materials, 2007. **19**: p. 3648-3653.
50. Sieradzki, K., Dimitrov, N., Movrin, D., McCall, C., Vasiljevic, N., and Erlebacher, J., *The dealloying critical potential.* Journal of the Electrochemical Society, 2002. **149**: p. B370-B377.
51. Erlebacher, J., *An atomistic description of dealloying: porosity evolution, the critical potential, and rate-limiting behavior.* Journal of the Electrochemical Society, 2004. **151**: p. C614-C626.
52. Rugolo, J., Erlebacher, J., and Sieradzki, K., *Length scales in alloy dissolution and measurement of absolute interfacial free energy.* Nature Materials, 2006. **5**: p. 946-949.
53. Erlebacher, J., Aziz, M.J., Karma, A., Dimitrov, N., and Sieradzki, K., *Evolution of nanoporosity.* Nature, 2001. **410**: p. 450-453.
54. Oppenheim, I.C., Trevor, D.J., Chidsey, C.E.D., Trevor, P.L., and Sieradzki, K., *In situ scanning tunneling microscopy of corrosion of silver-gold alloys.* Science, 1991. **254**: p. 687-689.
55. Newman, R.C. and Sieradzki, K., *Metallic corrosion.* Science, 1994. **263**: p. 1708-1709.

56. Wagner, K., Brankovic, S.R., Dimitrov, N., and Sieradzki, K., *Dealloying below the critical potential.* Journal of the Electrochemical Society, 1997. **144**: p. 3545-3555.
57. Chen, S.J., Sanz, F., Ogletree, D.F., Hallmark, V.M., Devine, T.M., and Salmeron, M., *Selectice dissolution of copper from Au-rich Cu-Au alloys: an electro chemical STM study.* Surface Science, 1993. **292**: p. 289-297.
58. Stratmann, M. and Rohwerder, M., *A pore view of corrosion.* Nature, 2001. **410**: p. 420-423.
59. Renner, F.U., Stierle, A., Dosch, H., Kolb, D.M., Lee, T.L., and Zegenhagen, J., *Initial corrosion observed on the atomic scale.* Nature, 2006. **439**(7077): p. 707-710.
60. Renner, F.U., Stierle, A., Dosch, H., Kolb, D.M., and Zegenhagen, J., *The influence of chloride on the initial anodic dissolution of $Cu_3Au(111)$.* Electrochemistry Communications, 2007. **9**: p. 1639-1642.
61. Renner, F.U., Stierle, A., Dosch, H., Kolb, D.M., Lee, T.L., and Zegenhagen, J., *In situ x-ray diffraction study of the initial dealloying and passivation of $Cu_3Au(111)$ during anodic dissolution.* Physical Review B, 2008. **77**: p. 235433.
62. Greeley, J. and Nørskov, J.K., *Electrochemical dissolution of surface alloys in acids: Thermodynamic trends from first-principles calculations.* Electrochimica Acta, 2007. **52**(19): p. 5829-5836.
63. Naohara, H., Ye, S., and Uosaki, K., *Electrochemical deposition of palladium on an Au(111) electrode: effects of adsorbed hydrogen for a growth mode.* Colloids and Surfaces A: Physicochemical and Engineering Aspects, 1999. **154**: p. 201-208.
64. Möller, F., Kintrup, J., Lachenwitzer, A., Magnussen, O.M., and Behm, R.J., *In-situ STM studies of the electrodeposition and anodic dissolution of ultrathin, epitaxial Ni films on Au(111).* Physical Review B, 1997. **56**(19): p. 12506-12518.
65. Allongue, P., Cagnon, L., Gomes, C., Gundel, A., and Costa, V., *Electrodeposition of Co and Ni/Au(1 1 1) ultrathin layers. Part I: nucleation and growth mechanisms from in situ STM.* Surface Science, 2004. **557**(1-3): p. 41-56.
66. Toney, M.F., Gordon, J.G., Borges, G.L., and Melroy, O.R., *Comment on "Superstructures on Pb monoleyers electrochemically deposited on Ag(111)".* Physical Review B, 1994. **49**(11): p. 7793-7794.
67. Kibler, L.A., Kleinert, M., Randler, R., and Kolb, D.M., *Initial stages of Pd deposition on Au(hkl) part I: Pd on Au(111).* Surface Science, 1999. **443**: p. 19-30.
68. Naohara, H., Ye, S., and Uosaki, K., *Electrochemical layer-by-layer growth of palladium on an Au(111) electrode surface: Evidence for important role of adsorbed Pd complex.* Journal of the Physical Chemistry B, 1998. **102**(22): p. 4366-4373.

69. Takahasi, M., Hayashi, Y., Mizuki, J., Tamura, K., Kondo, T., Naohara, H., and Uosaki, K., *Pseudomorphic growth of Pd monolayer on Au(111) electrode surface.* Surface Science, 2000. **461**(1-3): p. 213-218.

70. Möller, F.A., Magnussen, O.M., and Behm, R.J., *Two-Dimensional Needle Growth of Electrodeposited Ni on Reconstructed Au(111).* Physical Review Letters, 1996. **77**(15): p. 3165.

71. Sibert, E., Ozanam, F., Maroun, F., Behm, R.J., and Magnussen, O.M., *Diffusion-limited electrodeposition of ultrathin Au films on Pt(1 1 1).* Surface Science, 2004. **572**(1): p. 115-125.

72. Krug, K., Stettner, J., and Magnussen, O.M., *In Situ Surface X-Ray Diffraction Studies of Homoepitaxial Electrochemical Growth on Au(100).* Physical Review Letters, 2006. **96**(24): p. 246101-4.

73. Nichols, R.J., Magnussen, O.M., Hotlos, J., Twomey, T., Behm, R.J., and Kolb, D.M., *An in-situ STM study of potential-induced changes in the surface topography of Au(100) electrodes.* Journal of Electroanalytical Chemistry, 1990. **290**: p. 21-31.

74. Ikemiya, N., Nishide, M., and Hara, S., *Potential dependence of the surface self-diffusion coefficient on Au(100) in sulfuric acid solution meaured by atomic force microscopy.* Surface Science, 1995. **340**: p. L965-L970.

75. Kubo, K., Hirai, N., and Hara, S., *Decay of nano-islands on Au(1 0 0) electrode in sulfuric acid solution with Cl- anions.* Applied Surface Science, 2004. **237**(1-4): p. 301-305.

76. Lequien, F., Creuze, J., Berthier, F., Braems, I., and Legrand, B., *Superficial segregation, wetting, and dynamical equilibrium in bimetallic clusters: A Monte Carlo study.* Physical Review B (Condensed Matter and Materials Physics), 2008. **78**(7): p. 075414-10.

Chapter 6

Conclusion

In the first part of the work, we studied the influence of the substrate chemical nature on the heteroepitaxial deposition/dissolution reactions in the absence of UPD process. For this purpose, we compared the deposition and dissolution of ultrathin films of nickel (Ni) and cobalt (Co) on two different substrates: Au(111) and Pd/Au(111). The Pd/Au(111) substrate consists of a Au(111) surface modified by monoatomic Pd overlayers of various coverage ranging from few islands up to the monolayer completion. Depending on the Pd coverage deposited on Au(111), this substrate can be considered as *monometallic* (Pd(~1ML)/Au(111)) or as *bimetallic* (Pd(<1ML)/Au(111)) and exhibit the same in-plane lattice parameters than bare Au(111).

Electrochemical measurements on *monometallic* surfaces

By using cyclic and linear sweep voltammetry, we characterized the electrochemical behaviors of Ni and Co on *monometallic* Au(111) and Pd(1ML)/Au(111). Compared to Au(111), Ni and Co growth occurs on a hydrogenated Pd(1ML)/Au(111) surface since the H-adsorption on this surface takes place at potentials more positive than Ni or Co Nernst potential.

We found the existence of two different growth kinetic regimes for Ni and Co on both substrates. The first regime corresponds to the growth of the first Ni monolayer (resp. Co biatomic layer) and is characterized by a high growth rate, followed by the second regime which corresponds to the growth of the second Ni monolayer (resp. the third Co monolayer) with a significantly lower growth rate. For Ni monolayer, we showed that the growth kinetics strongly depends on the substrate chemical nature since the Ni monolayer growth is *slower* on Pd(1ML)/Au(111) than on Au(111). For Co bilayer, we demonstrated, on the contrary, that the growth kinetics was independent of the nature of substrates by measuring similar growth rates on both Au(111) and Pd(1ML)/Au(111). In the multilayer range, the growth rate is not dependent on the substrate for Ni and Co.

Intriguingly, studies of the dissolution process of Co bilayer and Ni monolayer revealed that the dissolution kinetics of those overlayers was dependent on the nature of the substrate. We found that the dissolution process was *slower* on Pd(1ML)/Au(111) than on Au(111). Moreover, in the specific case of Ni monolayer, we found that the

dissolution process begins preferentially on Pd(1ML)/Au(111). In the multilayer range, the dissolution of Ni (resp. Co) multilayer films was found *slower* than the monolayer (resp. bilayer) dissolution process.

Finally, our results strongly suggest that the H-monolayer was *desorbed* from the Pd surface upon Ni or Co deposition.

STM measurements on *bimetallic* surfaces

We performed in situ STM investigations at the nanometer scale on *bimetallic* Pd/Au(111) surface in order (*i*) to characterize the growth process of Ni and Co on Pd monoatomic islands and (*ii*) to confirm the existence (or absence) of selective behaviors (determined by electrochemical measurements) from direct comparison of the deposition/dissolution processes on these two different surfaces.

Nickel:

At low overpotential (i.e. close to equilibrium), we observed that noticeable Ni deposition on Pd islands requires applying $U_{dep} \leq$ -1.10 V = $\phi_{Deposition}^{Ni/Pd/Au(111)}$, which is 90 mV more negative than the Ni deposition onset on Au(111) ($\phi_{Deposition}^{Ni/Au}$ = -1.01 V). At large overpotential, Ni growth appeared to be kinetically hindered on the Pd monatomic islands as compared to Au(111) terraces for which preferential Ni monolayer growth took place. These results confirmed the existence of selective process during Ni growth. For longer deposition time, the bimetallic Pd/Au(111) surface can be uniformly covered by a full Ni monolayer demonstrating that the Ni/Pd growth is also 2D as on Au(111). Then, a layer-by-layer growth morphology was recorded at least up to the 3rd layer on both substrates. Moreover, we showed that the Ni monolayer on Pd also exhibits a moiré structure with a period of 21-22 Å, which is equal to the one found for Ni/Au(111). This demonstrates that the Ni monolayer is relaxed on Pd monolayer as well as on Au(111) terraces and that the underlying Pd monolayer remains *pseudomorphic* with the Au(111) substrate even upon Ni deposition. Consequently, the Ni selective growth observed on Au(111) cannot be attributed to different in-plane stress of the Ni layer.

The microscopic (STM) observations fit very well with the macroscopic (electrochemical) measurements. Therefore, the origin of the selective growth of Ni on *bimetallic* Pd/Au(111) substrate can not be explained in terms of difference in Ni adatom surface mobility.

In the multilayer regime, the selective growth process seemed to be reversed compared to the one observed for the monolayer case. However, the growth selectivity is much smaller and this slight difference is not considered as significant.

Concerning the dissolution, STM measurements performed under steady state condition close to equilibrium condition also reveal that a Ni monolayer covering the entire bimetallic surface may be completely dissolved from the Pd islands at $\phi_{Dissolution}^{Ni/Pd/Au(111)}$ = -1.02 V, while the Ni(1ML)/Au(111) film remains unaltered up to $\phi_{Dissolution}^{Ni/Au(111)}$ = -0.98 V. Therefore, we conclude that there exist a shift of the dissolution onset potential ($\Delta\phi_{Dissolution}^{Ni} = \phi_{Dissolution}^{Ni/Au(111)} - \phi_{Dissolution}^{Ni/Pd/Au(111)}$) equal to 40 ± 10 mV. This result confirms the existence of a shift $\Delta\phi_{Dissolution}^{Ni}$ detected from electrochemical measurements on monometallic substrates.

Cobalt:

We found the initial growth of a biatomic layer and the 2D growth morphology on the Pd monolayer similarly to Co/Au(111). On top of the bilayer, we observed the existence of a moiré structure of periodicity equal to 25 Å on Au(111) and 22 - 23 Å on Pd(1ML)/Au(111), indicating that the bilayer is less strained on the Pd monolayer. STM images demonstrate that there is no selective process in case of Co during the deposition/dissolution processes, in conditions similar to those used for Ni. These results are in agreement with the electrochemical measurements. The main explanation to the absence of selective behaviors for Co compared to Ni is that Co growth begins, both on Au(111) and Pd(1ML)/Au(111) with the formation of a *biatomic* layer and not by one single atomic monolayer. We postulated that the presence of the second Co atomic layer on top of the first one stabilizes it and therefore reduces the influence of Co-Pd interactions on deposition or dissolution. These processes was thus mainly governed by the activation energy to break (respectively form) the Co-Co bond rather than the Co-S bond with S = Au or Pd, leading to $\Delta\phi_{Dissolution}^{Co} = \phi_{Dissolution}^{Co/Au(111)} - \phi_{Dissolution}^{Co/Pd/Au(111)} = 0$.

<u>Origin of the selective processes observed in the case of Ni monolayer</u>

The selective growth was explained by taking into account kinetic and thermodynamic considerations:

First, we attributed such behavior to a slower Ni^{2+} electrochemical discharge kinetics on Pd islands than on Au(111) terraces. Indeed, the H layer exclusively adsorbed

on Pd is expected to (*i*) reduce the Pd density of states (DOS) near the Fermi level and (*ii*) act as a steric barrier for the approach distance of the Ni^{2+} electrochemical discharge.

Second, by correlating the shift of the dissolution onset potential to the existence of different Ni-substrate interactions, we have demonstrated that the selective processes in the electrochemical deposition/dissolution of Ni monolayer films on bimetallic Pd/Au(111) surface also raised from a smaller binding energy of Ni adatoms on the Pd surface as compared to the Au surface. The difference in binding energy between Ni-Pd and Ni-Au has been estimated to 80 meV. However, the fact that the Ni-Pd binding energy is smaller than that of Ni-Au remains unclear. Experiments suggest that the H monolayer on the Pd surface must play a key role.

Finally, this work demonstrates that the developed experimental approach is sensitive enough to measure small difference in binding energy and open up perspectives to determine small differences in binding energies for other adsorbate/substrate couples.

In the second part of this work, after comparing the vertical Ni-Pd and Ni-Au interaction energies (i.e. the binding energies), we investigated the lateral interaction energies between NiAu and NiPd (i.e. the pairwise energies). For this purpose, we studied the growth and dissolution of NiPd and NiAu monolayer alloys on Au(111). We established two different alloy growth procedures while detailed STM study of the film morphology and that of the dynamics of Ni selective dissolution process allowed us to gain invaluable information about the alloy phase and the alloy stability as a function of the alloy composition. The results are summarized below:

<u>NiPd monolayer alloys</u>

In agreement with bulk thermodynamic data, we found that NiPd monolayer alloys deposited on Au(111) form also solid solutions for all alloy compositions. We were able to determine the average inter-atomic distance of the alloy and to correlate it with the alloy Ni content. The detailed analysis of the dissolution morphologies and their comparison with Monte Carlo simulations allowed us to evidence the presence of a composition variation on the 10 nm scale, which seems not to originate from energy minimization of the alloy but from the deposition conditions.

We also found evidence for a passivation process taking place every time Ni atoms in a step edge site are no longer available, i.e., when all step edges are decorated by Pd atoms. This phenomenon is similar to the passivation below the critical potential of 3D alloys, except that in our case it is bi-dimensional.

We found that even a small proportion of Pd dispersed among Ni monolayer entails a positive shift of the Ni dissolution potential. We succeeded in establishing a close correlation between the dissolution potential of a Ni atom and the number of its Pd neighbors.

Finally, we observed the formation of dark areas preceding Ni dissolution, which we attribute to Ni areas resulting from a local phase segregation of the NiPd alloy. Indeed, we found evidence for mass transfer within the alloy layer taking place in the Ni dissolution potential range.

NiAu monolayer alloys

As expected from thermodynamics of bulk alloys, we found that $Ni_{60}Au_{40}$ and $Ni_{10}Au_{90}$ monolayer alloys deposited on Au(111) are both phase segregated. However, we found a very small segregation characteristic scale (~ 1-3 nm), which seems to be driven (*i*) by partial strain relaxation in the Ni phase and (*ii*) by a slight tendency of the monolayer alloy to form a solid solution. The combination of these two effects yielded interesting alloy morphology, for example ordered Au clusters in a Ni layer.

We found that the presence of Au adatoms embedded in Ni monolayer does not modify the potential at which Ni atoms are removed.